TMUP-HEL-701(EXP)

EXPERIMENTAL STUDY OF ANTINEUTRON-PROTON AND ANTIPROTON-PROTON ANNIHILATIONS AT LOW ENERGY *)

by Shoichi KITAMURA

DEPARTMENT OF PHYSICS, FACULTY OF SCIENCE
TOKYO METROPOLITAN UNIVERSITY
Setagayaku, Tokyo, JAPAN

1976

---

*) Submitted to the Graduate School of Tokyo Metropolitan University in partial fulfilment of the requirements for the Degree of Doctor of Science.

ACKNOWLEDGEMENTS

The author wishes to express his appreciation to Professor T. Yamagata for his guidance and suggestions not only in this work but also in the author's graduate study.

Special thanks are due to Mr. T. Emura for his efforts and encouragement throughout this experiment.

The experiment has been done by the author in collaboration with Drs. R. Hamatsu, I. Kita, H. Kohno, S. Matsumoto, K. Takahashi, T. Yamagata, and Messrs. S. Hamada, J. Kishiro, M. Komatsu in Japan. He wishes to express his gratitude for their guidance, discussions and good cooperation. It would have been difficult to succeed in the experiment without skill and efforts of all members.

The author would like to express his gratitude to the foreign collaborators; Drs. B. S. Chaudhary, S. N. Ganguli, A. Gurtu, P. K. Malhotra, U. Mehtani, R. Raghavan, A. Subramanian, (Tata Institute of Fundamental Research); Dr. L. Montanet, (CERN); Drs. M. Bogdanski, E. Jeannet,(Neuchâtel University) for their efforts in data taking and useful communication during the experiment. Their good works have made it possible to perform this experiment with high statistics.

The author is also grateful to Messrs. M. Kimura, H. Kaseno, M. Takanaka, K. Tanahashi and Miss T. Mukohda for their generous assistance during the course of the experiment, and Dr. T. Hirose for his suggestion in data analysis.

This experiment was assisted by a grant of the Japan Society for the Promotion of Science and another one of the Mitsubishi

Fundation.

Finally the author is in debt to staffs of Bubble Chamber Group and Data Handling Division at KEK for their helpful guidance where major part of computations through THRESH, GRIND, and others were carried out with the computer system of HITAC 8700.

CONTENTS

ABSTRACT

About 3,500 events of antineutron-proton annihilation in a hydrogen bubble chamber were analyzed in order to investigate pionic annihilations below 0.8 GeV/c. The antineutrons were produced by the charge exchange of antiprotons in hydrogen. The signature of the event is an occurence of three-, five- or seven-prong star due to an antineutron-proton annihilation associated with an zero-prong vertex in the charge exchange scattering upstream. At the same time about 13,000 events of all antiproton-proton interactions were detected at 0.6-0.8 GeV/c.

For the antineutron-proton annihilations, fractions of resonance production were determined. Phenomenological analyses of $\bar{n}p$ data were performed by the statistical model, the multiperipheral model and the dual model which has recently been developed. A ρ-ω interference effect was observed in the $(\pi^+\pi^-)$ effective mass spectrum for $\bar{n}p \rightarrow 2\pi^+\pi^-\pi^0$ reaction. For the antiproton-proton events, annihilation cross sections into zero, two, four, six, and eight prongs were determined, and results of semi-inclusive reactions were compared with statistical models.

I. Introduction

Existence of antiparticles makes it possible to study interactions of antiparticle-particle within processes called "annihilation" where the initial particle and antiparticle disappear in the final state: For example experimental data of antinucleon-nucleon($\bar{N}N$), antikaon-kaon($\bar{K}K$), and electron-positron (e^-e^+) reactions annihilating into mesons gave opportunity for studying various aspects of the basic reaction mechanisms in the past decade.[1),2),3)]

In particular the $\bar{N}N$ annihilation reactions possess a large amount of energy available to recreate hadrons in the final state, which takes place inside a volume of $\sim 10^{-39}$ cm^3. It is well known that pions are mostly produced in ~90 % of the annihilations and furthermore very large part of these pions is due to resonance production (e.g. ρ, ω, K^*, f and A_2).

An aim of this experiment is to obtain from the available films as much information as possible regarding to antiproton-proton (denoted as $\bar{p}p$ hereafter) charge exchange scattering

$$\bar{p}p \rightarrow \bar{n}n, \qquad \text{(I-I)}$$

and antineutron-proton (denoted as $\bar{n}p$) annihilation

$$\bar{n}p \longrightarrow (n_1+1)\ M \ + n_1M^- + n_2M^0, \qquad \text{(I-2)}$$

$$n_1 = 1,\ 2,\ 3,\ n_2 = 0,\ 1,\ 2,\ \ldots$$

where M represents any meson of given charge, at low energy. A characteristic signature for the events in a hydrogen bubble chamber is a zero-prong $\bar{p}p$ interaction, corresponding to the reaction (1), with the subsequent annihilation of the produced antineutron with proton. The $\bar{n}p$ annihilation produces odd number of charged and any number of neutral mesons corresponding to the reaction (2). The case of $n_1=0$ in (I-2) is excluded because of the large contaminations due to backgroung events.

Another aim is to investigate $\bar{p}p$ annihilation

$$\bar{p}p \longrightarrow n_1M^+ + n_1M^- + n_2M^o, \qquad (I-3)$$

$$n_1 = 0, 1, 2, 3, 4, n_2 = 0, 1, 2, \ldots$$

where M again represents any meson.

The measurement of the total and differential cross section for the $\bar{p}p$ charge exchange scattering (I) has been already made in this experiment based on a sample of about 3,500 events in the 0.7-0.76 GeV/c incident momentum range.5),6)

The purpose of this work is to make a rudimentary study for the reactions (2) and (3) around 0.7 GeV/c.

Characteristics of the $\bar{n}p$ annihilation are that the initial state is purely isotopic-spin 1 and moreover both antineutron and proton are free before the reaction in confrast with the $\bar{p}n$ annihilation as stated below. These facts are very useful to study the $\bar{N}N$ annihilation with respect to isotopic-spin (I) dependence by comparing the $\bar{n}p$ data with $\bar{p}p$ ones in the same energy range since $\bar{p}p$ is a mixture of I=1 and I=0 states.

On the other hand $\bar{n}p$ state is connected with $\bar{p}n$ state by charge symmetry, so that data for $\bar{n}p$ annihilation and those of $\bar{p}n$ one, which are obtained in antiproton-deuteron reactions, should be symmetric. It is not meaningless to ask whether two data mentioned above are symmetric actually, because the neutron in the deuterium is not free, but is bound weakly with the proton (binding energy of 2.23 MeV) accordingly the bound neutron has the Fermi motion whose effect may be significant at low energy.[7)]

Experimental data for $\bar{n}p$ annihilation (1) is very poor because of the difficulty to produce enough antineutron beams to carry out the experiment. The total cross section $\sigma_{tot}(\bar{n}p)$ was measured at antineutron momentum 6.65 GeV/c using antideuteron beams.[8)] The result was that values of the total cross sections $\sigma_{tot}(\bar{n}p)$ and $\sigma_{tot}(\bar{p}n)$ were 59.0 ± 3.0 and 58.8 ± 2.4 mb respectively, and the both values agreed within statistical error. Another experiment was made with bubble chamber films at antineutron momenta about 1.1 GeV/c, and fractions of resonance production were determined.[9)] The method of analysis in the above experiment was basically the same as what is employed in the present experiment.

The $\bar{p}n$ annihilation at intermediate- or low-energy region was investigated experimentally by many authors mostly in a bubble chamber analysis,[10)-26)] and the theoretical consideration was also made.[27)-36)] The results imply that statistical aspects appears to dominate in the $\bar{n}p$ annihilation, but dynamical effects probably emerge in the data for two-particle or three-particle correlations over the phase space factors. In particular, $2\pi^+\pi^-$ and $3\pi^+2\pi^-$ final states, which have no neutral-pions, are interesting in the duality theory as pointed out by Rubinstein.[30),31)]

Measurement of the $\bar{p}p$ annihilation cross section is important espectially from the viewpoint of statistical approach.[27),28)] Moreover it is interesting to search for similarities in data of $\bar{p}p$, e^-e^+, $\bar{K}K$, and off-mass-shell $\bar{p}p$ annihilations without regards to detailed mechanisms.[37),38),39)] Experimental data of the cross sections (or branching ratios) for $\bar{p}p$ annihilation with 0 prong, 2 prongs, 4 prongs ... were obtained in bubble chamber experiments at rest,[4)] 0.43,[40),41)] 0.55,[40),41)] 0.94,[42)] and 1.2 GeV/c.[28)] But the data for 0-prong annihilation are rather poor except the one at rest because the cross sections for the charge exchange are not determined so precisely.

The points studied in this work concerning the $\bar{n}p$ annihilation are i) dynamics of the $\bar{n}p$ annihilation, ii) analysis of the many-pion final states and iii) ρ-ω interference effect. For each of the above points the analyses have been made as follows.

i) Dynamics of the $\bar{n}p$ annihilation

a) determination of cross sections for various final states, and comparison of the results with the statistical model developed by Orfanidis and Rittenberg in which it is assumed that annihilation proceeds by a series of single pion boil-offs from fireballs retaining non-exotic quantum numbers at each stage.[27)]

b) determination of fractions of produced resonances for various final states, and test of application of the CŁA model to the annihilation. The CŁA model, modified by de la Vaissiere, includes production mechanism of resonances and gives qualitatively good fits to data of $\bar{p}p$ annihilation at incident momenta 1 – 7 GeV/c.[43),44)]

c) phenomenological approach by 4-point Veneziano amplitudes[22)] for the final state $2\pi^+\pi^-$ and study of the final state $3\pi^+2\pi^-$ in the dual theory of Rubinstein's standpoint.[30),31)]

ii) Analysis of the many-pion final states

d) study of the annihilation in single particle distributions, charge flows[45] between points, and opening angles between pion pairs of like charge or unlike charges.[46]

e) study of the inclusive reaction in terms of the transverse momentum and missing mass; the former quantity is interesting for the thermodynamical analysis[47] while the latter for the Regge-Müller analysis.[34]

iii) ρ-ω interference effect

f) study of $\bar{n}p$ annihilation in terms of the G-parity conservation law, especially for single-particle distributions in the production c.m. system and for ρ-ω interference effect.[124]

The points concerning to the $\bar{p}p$ annihilation are;

determination of the annihilation cross sections:

a) 0 prong, 2 prongs, 4 prongs, 6 prongs and 8 prongs at 0.7 GeV/c, and comparison of the results with statistical models.[27,28]

b) search for similarities and dissimilarities among $\bar{p}p$, e^+e^-, $\bar{K}K$, and off-mass-shell $\bar{p}p$ annihilations.

This experiment has been carried out under the Bombay-CERN-Neuchâtel-Tokyo collaboration. Films were those of the Saclay 81 cm hydrogen bubble chamber with antiproton beams of momenta 0.7 GeV/c(Exposure I) and 0.75 GeV/c(Exposure II). Numbers of pictures used here were 2.2×10^5(Expo.I) and 4.1×10^5(Expo. II) pictures. The analysis for $\bar{n}p$ annihilation is made with about 3,500 events (Expo. I, II) and that for the $\bar{p}p$ annihilation with about 13,000 events(from Expo. I only). In the latter case topological cross sections are obtained from the beam-count data obtained in every twentieth frame.

In Section II historical background for reactions (1), (2) and (3) are described. Section III includes experimental procedures, namely, scanning, measuring, and computer processing. The method of analysis and interpretation of the results for the $\bar{n}p$ annihilation and for the $\bar{p}p$ annihilation are described in Sections IV and V respectively. Results are summarized in Section VI. Discussion and conclusion are presented in Section VII, and appendices are presented in Section VIII.

II. Historical Background

II-1. $\bar{p}p$ Charge Exchange Scattering

II-1-i. Characteristics of the Reaction

The charge exchange scattering (I-1) itself has some characteristics as follows;

i) The reaction is free from diffraction in contrast to the elastic scattering;

$$\bar{p}p \longrightarrow \bar{p}p \qquad \text{(II-1)}$$

Furthermore the u-channel exchange is exotic with baryon number 2. This fact implies a small backward cross section and is available in search for s-channel resonances.

ii) By combining data on the charge exchange scattering with that of the elastic scattering, one can extract information on the relative importance of isotopic spin.

iii) The $\bar{p}p$ charge exchange scattering is connected with the neutron-proton charge exchange;

$$np \longrightarrow pn \qquad \text{(II-2)}$$

by line reversal. One may therefore expect a similarity in the differential cross section (I-1) and (II-2). In particular, the behavior of the differential cross section in the forward direction of the processes (I-1) and (II-2) are intresting from the viewpoint of the interference between t-channel π exchange term and some kind of "background".

II-1-ii. Counter Experiments

The energy dependence of the cross section for $\bar{p}p$ charge exchange was investigated precisely between incident momenta 0.276 and 3.0 GeV/c by counter experiments for the purpose of searching s-channel resonances.48),49),50) Some structures were found in momentum range 1-3 GeV/c as the result,48),49) but the signals were not clear for evidence of the resonances.58)

Measurements of the differential cross section were made in high statistics by counter technique at 1.8,5,5.5, 6, 7, 7.76, 8,9,25, and 35 GeV/c.52)-56) It is now established experimentally that the differential cross section above 1.8 GeV/c shows a sharp peak in the forward direction due to π exchange. The differential cross section for the np charge exchange (II-2) also shows a sharp peak over incident momentum range 0.6-27.4 GeV/c.68),69),70) Furthermore the data of $\bar{p}p$ charge exchange at 1.8,7.76, and 8 GeV/c indicate that the forward peak of $\bar{p}p$ charge exchange is slightly less pronounced than that of np charge exchange at the same energy.

Theoretically the π exchange itself vanishes in the forward direction. Therefore it needs a real background interfering with the π exchange term59), or a contribution both of a π exchange pole and the opposite-parity pole (called a conspirator pole)16), to produce a sharp peak. Description for the structure of $\bar{p}p$ and np charge exchange processes was tried by several authors in terms of Regge-pole exchange with conspirator.63),64),65) An absorption picture for the charge exchange scattering was proposed by Kane et al., where Regge cuts were introduced as backgrounds interfering with Regge poles.[64),65)] This model was applied to the $\bar{p}p$ charge exchange data at 7.76 GeV/c,[55)] and the magnitudes of the non-interfering and interfering backgrounds were obtained together with slope parameters. The result is that the non-interfering background is non-vanishing in the forward direction, and the slope parameter of the interfering-background term does not exceed typical values found in elastic scattering.[55)] This is in contrast to what was obtained in np charge exchange data by the model of Engler et al.[67)] where the non-interfering background term was found to be negligible and the slope parameter was about twice as large as large as the value obtained for elastic scattering.

II-1-iii. Bubble Chamber Experiments

Bubble chamber experiments for $\bar{p}p$ charge exchange were carried out mainly at low energies ($\lesssim$ 1 GeV/c) with a hydrogen bubble chamber. The differential cross section was obtained at 0.43,[41)] 0.55,[41)] and 1.13,[51)] based on 111, 104, and 2,600 events respectively. Their limited statistics could not established the forward peak,which was found in $\bar{n}p$ charge exchange data over the incident momentum range 0.6-1.7 GeV/c.[68)]

Theoretical predictions for $\bar{N}N$ interactions were given by Bryan and Phillips(BP model), where they used one boson exchange potential(OBE) and phenomenological imaginary potential (independent of spin and isotopic spin) of the Woods-Saxon shape to take care of the strong absorption in $\bar{N}N$ case.[60)] The OBE potential was obtained by fitting the nucleon-nucleon data and was used for $\bar{N}N$ case after changing the sign of contributions from mesons of odd-G parity.

The predicted angular distribution of $\bar{p}p$ charge exchange by the BP model was compared with the experimental data, and the general shape was reproduced.[41),51)] But a characteristic feature of the BP model; i.e. a sharp forward peak followed by a dip-bump structure, was not given in the data at 1.13 GeV/c, and was not conclusive in the data at 0.43, and 0.55 GeV/c. Ohsugi et al.[71)] measured the polarization in the $\bar{p}p$ elastic scattering at 0.7 GeV/c, and they pointed out that the prediction of the BP model was not correct(the predicted value of the polarization was much smaller than the observed one).

Diu proposed a theoretical consideration for np and $\bar{p}p$ charge exchange available for all energies except the very low ones.[61)] The restriction comes from the requirement that the physical t-interval must be wide enough to separate the peak (or dip) linked to π exchange, where t is the momentum transfer between $\bar{p}$ and $\bar{n}$ (or n and p in the np case), that is, the incident momentum should be more than 0.35 GeV/c. To explain the behavior of the differential cross sections in the forward direction, the values at t=0 of three linear combinations of the invariant amplitudes were taken into account in addition to the π exchange in Diu's theory. These combinations were recombined into the amplitudes of interference and non-interference with π exchange term, and a restriction was imposed on these terms from the np charge exchange data. Data for $\bar{p}p$ charge exchange were required at either intermediate or low energies to estimate the magnitude of contribution due to the absorptive part of the amplitude.

II-1-iv. Result at the Present Experiment

The $\bar{p}p$ charge exchange scattering in the 0.7-0.75 GeV/c incident momentum region has been already analyzed,5),6) based on 3,500 events. It has been found that $\sigma_{ce} = 10.7 \pm 0.2$ mb at the average momentum of 0.73 GeV/c. The differential cross section has been characterized by a sharp forward peak and a dip followed by a secondary maximum in the forward direction. The position of the dip has been $|t| \sim m_\pi^2$ (m_π ; pion mass).

The diffraction model of Frahn and Venter72) has been employed to analyze amplitudes of isotopic spin 1 and 0 independently. Simultaneous fit of the model to the data of $\bar{p}p$ charge exchange, $\bar{p}p$ elastic73) scattering, and $\bar{p}p$ polarization71) has been tried, and it has been able to reproduce the observed distribution of charge exchange.

On the other hand, the dip-bump structure was understood by a simple picture by Leader,62) which involves a π exchange and a constant background(for $|t| \lesssim 3m_\pi^2$). It was proposed to explain the dip-bump structure observed in the $\bar{p}p$ charge exchange data at 40 GeV/c.

Further investigation concerning the above-mentioned fact in this experiment will not be discussed in this thesis since this has been presented in ref. 5),6).

II-2. Antinucleon-nucleon($\bar{N}N$) Annihilation and Statistical Models

II-2-i. Fermi Model

In the annihilation reactions, initial particles are destroyed and new forms of matter (hadrons) are created. All this takes place inside the volume of $\sim 10^{-39}$ cm^3. A statistical idea seems more appropriate there than in the case of the nucleon-nucleon collisions. Therefore we will review various types of such ideas in this section.

A statistical model of strong interaction was first proposed by Fermi[74)] to explain multiparticle production processes in high energy collisions. According to the Fermi model, an annihilation process can be visualized as such that , in the first instance, within a certain volume a thermodynamical equilibrium is established, in which the energy will be distributed among the various degrees of freedom according to statistical law. Then the energy will be rapidly dissolved and the particles, into which the energy has been converted, will fly out in all directions. The probability that within the minute interaction volume a certain number of particles will be created with a given energy distrubution can be computed statistically.

II-2-ii. Koba and Takeda Model

A statistical model for $\bar{N}N$ interactions was proposed by Koba and Takeda[75)] by assuming a compound structure for the nucleon and antinucleon, which are considered to be composed by a hard core and a π-meson cloud. The core acts in the $\bar{N}N$ interaction as a perfectly absorbing medium and the characteristic time of its interaction (which is assumed to be of the order of $1/(2m_N)$; m_N is the nucleon mass) is short compared with the period of the pion's oscillation in the cloud. In such way in the annihilation process two different phenomena take place; the short core-core interaction in which π and K-meson emerge, and the emission of the cloud π -mesons which have no longer a center to be bounded.

The number of pions in the cloud was estimated as $<n_\pi>=1.3$, therefore 2.6(=1.3x 2) pions are on the average comming out from the cloud of $\bar{N}N$ pair. Fermi's statistical model was applied to the core annihilation and the pion multiplicity was obtained to be 2.2. Hence, the average multiplicity of pions is 4.8 at rest.

This model seems to explain the $\bar{N}N$ annihilation,but quantitative discussion about experimental data has not been made yet.

II-2-iii. Interaction Volume of $\bar{N}N$ Annihilation

According to the Fermi model, the rate of annihilation into a given final state with n completely independent particles is given by

$$P_n(\Omega) = \left(\frac{\Omega}{V} \right)^n, \qquad \text{(II-3)}$$

where Ω is the interaction volume in which statistical equilibrium is reached and V is the large normalization volume. In the original formulation by Fermi the interaction takes place in a volume

$$\Omega_0 = (4\pi/3)R^3, \; (R=1.4\times10^{-13} \text{ cm}) \qquad \text{(II-4)}$$

multiplied by a Lorentz contraction factor. In the conventional statistical model the transition probability per unit time for a reaction yielding n particles is given by[76)]

$$P = f(i) \prod_{i=1}^{n} [(2s_i+1)m_i \frac{\Omega_i}{\Omega_0}]R_n(E,p). \quad \text{(II-5)}$$

The quantity f(i) is an isotopic statistical weight arising from the assumption of conservation of total isospin I. $R_n(E,p)$ is a Lorentz invariant phase space, E and P are the total energy and momentum of the reaction and m_i, s_i, Ω_i are mass, spin, interaction volume of the particle labeled i in the final state.

McConnell et al.[76)] estimated the interaction volume for π meson (Ω_π) and K meson (Ω_K) from the data of $\bar{p}p$ annihilation in the incident momentum range 0-1.99 GeV/c from the above equation. The results are $\Omega_\pi \simeq 5\Omega_0$, $\Omega_K \simeq 0.1\Omega_\pi$ which tend to dim physical significance.

II-2-iv. Bose-Einstein Statistics

Goldhaber et al. introduced the influence of Bose-Einstein (BE) statistics for pion pairs of like charge into a statistical model for $\bar{p}p$ annihilation.[46)] To this end suitable symmetrized wave functions for like-charged-pion pairs are used. The total rate R_n of annihilation into $n\pi$ state is given by

$$R_n \simeq \int \cdots \int \frac{dp_1 \cdots dp_n}{\omega_1 \cdots \omega_n} P_n(\rho, p_1 \cdots p_n)\delta(W - \sum_{i=1}^{n} \omega_i)\delta(\sum_{i=1}^{n} p_i), \quad \text{(II-6)}$$

where W is the available annihilation energy and p_i, ω_i are momentum and energy of i-th pion. $P_n(\rho, p_1 \cdots p_n)$ is the probability to find n free pions, which depends on the radius ρ of the interaction volume.

P_n is a product of correlation function ψ for like-charged pion pions. For example in the case of four pion final state

$$\bar{p}p \longrightarrow 2\pi^+ \, 2\pi^- , \qquad \text{(II-7)}$$

labeling $\pi^+\pi^+\pi^-\pi^-$ as 1,2,3,4, R_4 is given by

$$R_4(2^+2^-) \approx \int \frac{dp_1 \cdots dp_n}{\omega_1 \cdots \omega_n} \psi(12)\psi(34)\delta(W - \sum_{i=1}^{4} \omega_i)\delta(\sum_{i=1}^{4} p_i), \qquad \text{(II-8)}$$

For two identical particles having momenta p_1 and p_2, the corresponding $\psi(12)$ can be written as

$$\psi(12) = \int\int |\phi^s(12)| dr_1 dr_2. \qquad \text{(II-9)}$$

It should be integrated twice over a sphere $\Omega = \frac{4}{3}\pi\rho^3$. $\phi^s(12)$ is given by

$$\phi^s(12) = (\frac{1}{\sqrt{2}V})\{\exp[i(p_1r_1+p_2r_2)]+\exp[i(p_2r_1+p_1r_2)]\}, \qquad \text{(II-10)}$$

where V is a large normalization volume.

Goldhaber et al. used a Gaussian-shaped volume instead of a spherical one. This replacement simplifies some computations without significant change in the results.

$\psi(12)$ thus obtained is

$$\psi(12) = 1 + \exp(-\lambda x_{12}), \qquad \text{(II-11)}$$

where

$$x_{12} = (p_1 - p_2)^2 - (w_1 - w_2)^2,$$

and the radius ρ of the interaction volume is related to λ as

$$\rho = 2.15\ \lambda^{1/2}. \qquad \text{(II-12)}$$

ρ is a free parameter in this model and should be determined to fit multiplicities. But the results were inadequate physically as mentioned in II-2-iii, so that the value of about 3/4 times the π Compton wave length(1.4×10^{-13} cm) is used hereafter as the ρ which is a reasonable order of magnitude for strong-interaction volume.

One can see from the correlation function that the opening angles between pions of like charge tend to be smaller than those of unlike charge, which is called GGLP effect.

This effect was observed experimentally in $\bar{p}p$ annihilation by many authors,[77)-82)] and it is now established that we need a description of modified statistical models including not only experimentally found resonance production rates but also the BE symmetrization to explain the data.

II-2-v. Hagedorn Model

Statistical thermodynamics of strong interactions at high energies was proposed by Hagedorn.[47)] The essential idea is that a thermodynamical system is established at high-energy collisions, and the system consisting of more or less excited hadrons(fire ball or resonance) is itself nothing else than a highly excited hadron. It was shown[47)] that the above idea combined with usual formalism of statistical thermodynamics leads to the following predictions;

i) The number of hadronic state of mass between m and m+dm is given by

$$\rho(m)dm \xrightarrow[m \to \infty]{} \frac{\text{const.}}{m^{5/2}} \exp[m/T_0]dm.$$

ii) When the energy density becomes large, the temperature tends rapidly to a finite limit T_0.

The existence of the highest temperature can be anticipated by an imagination as follows: In the fireball gas, not only one but an infinity of different kinds of particles can be created freely. In this situation, a creation of new particles leads to a much larger increase of the number of quantum states than would an increase of the kinetic energy of the existing particles; with increasing total energy, the new particles swallow more and more energy, and in the limit the kinetic energy per particle tends to remain constant: $T \rightarrow T_0$ for $E \rightarrow \infty$ (practically for $E \gtrsim$ a few GeV).

This temperature T_0 governs the transverse momentum distribution of the outgoing particles, because this distribution will not be affected by any kinematical effect caused by relative motion of incident particles and targets.

The probability that a particle of mass m chosen at random will have a transverse momentum between p_T and $p_T + dp_T$ is

$$W(p_T)dp_T \simeq \text{const.} p_T \sqrt{p_T^2 + m^2} \; K_1\left(\frac{\sqrt{p_T^2 + m^2}}{T_o} \right) dp_T \quad . \tag{II-13}$$

where K_1 is the second kind modified Hankel function. This equation can be expressed approximately as

$$\begin{aligned} W(p_T)dp_T &\simeq \text{const.} p_T \; T_o \sqrt{p_T^2 + m^2} \exp(- \sqrt{p_T^2 + m^2} / T_o) \\ &\simeq c \; p_T^{3/2} \exp(-p_T / T_o) . \end{aligned} \tag{II-14}$$

The former is for $\sqrt{p_T^2 + m^2} / T_0 \longrightarrow \infty$ and the latter for $p_T >> m$.

Hagedorn estimated the value of the maximum temperature T_0 from experimental data of proton-proton elastic scattering as

$$T_0 = 158 \pm 3 \text{ MeV}. \qquad \text{(II-15)}$$

Ijaz et al. studied[83)] distributions of the transverse momentum of produced pions in $\bar{p}p$ and $\bar{p}n$ annihilation at 3.5 GeV/c. Their result is that the Hagedorn distribution (II-14) fits the data for annihilation well and T_0 varies from 214 MeV to 138 MeV corresponding to the variation of the final states from 3 pions to 6 pions.

II-2-vi. Orfanidis and Rittenberg(OR) Model

Orfanidis and Rittenberg proposed a new statistical model to describe $\bar{N}N$ annihilation into pions.[27)] They suggested from experimental data that a statistical description of many-particle final states of $\bar{N}N$ annihilation seems to be correct up to P_{lab}=5.7 GeV/c. Data of $P_{lab} \gtrsim 5.7$ GeV/c show transverse momentum limitation and non-isotropic angular distribution, which are chracteristic feature of multiperipherality.

In the OR model annihilation proceeds by a series of single pion boiloffs from fireball, the fireball retaining non-exotic quantum numbers at each as shown in Fig. 1(a). The statistical weight, and hence the branching ratio of a given final state, is determined by a number of such linear decay schemes which can yield the particular final state. The number n of pions emitted is taken as having a Gaussian distribution, whilst the mean <n>, and the variance σ^2 are based on the form used in other statistical models.

OR suggested the relations

$$\langle n\rangle = 5.05\left(\frac{s}{4M^2}\right)^{\frac{1}{3}}, \quad \left(\begin{array}{l}\text{M;nucleon mass} \\ \text{s;total energy squared in cms}\end{array}\right),$$

$$\sigma^2 = \frac{1}{4}\langle n\rangle , \qquad \text{(II-16)}$$

and then found good general agreement between the predicted exclusive and inclusive branching ratios and the experimental results for $\bar{p}p$ up to approximately 6 GeV/c, and for $\bar{p}n$ at rest.

The OR model is explained in Appendix A in datail.

Caro et al. confronted the model with data on $\bar{p}n$ annihilation below 1 GeV/c.84) They concluded from the values of inclusive, exclusive branching ratios, correlation coefficients that it continued to give good agreement.

II-2-vii. Lamb Model

Lamb introduced incorporation of SU(3) invariance and resonance production to a statistical model to describe $\bar{N}N$ annihilation (Lamb model).28) In order to incorporate SU(3) invariance, the transition matrix of this model is made so as to be not only isospin invariant but SU(3) invariant as well.

The narrow widths of most resonances indicate that they decay outside the interaction volume which produces the final state. Therefore from the viewpoint of the primary interaction described by the transition matrix, most resonances which are members of SU(3) multiplets, are treated as stable particles. Thus the model can make a possible description of resonance production.

Further explanation of this model is given in Appendix C.

A comparison of predictions of the model with data is made for $\bar{p}p$ and $\bar{p}n$ annihilations up to 3 GeV/c,$^{28)}$ and branching ratios for several final states and cross sections for resonance production are fairly well described.

II-3. $\bar{N}N$ Annihilation and CŁA Model

II-3-i. The model by Chan Hong-Mo et al.

The $\bar{N}N$ annihilations are complex and are far from being well understood. Statistical feature is dominant over the multiperipherality in the experimental data as already mentioned. But there may be a component due to multi-Regge-pole exchange, which is characterized by large effective mass of produced-particle pairs.

To guarantee the existence of the two components (statistical component and multi-Regge exchange one) in πp or Kp case, Chan Hong-Mo et al.[85] Suggested the following parametrization for the multiparticle production amplitude. It is called CŁA model, and the exchange mechanism is given in Fig. 1(b) graphically. the amplitude is given by

$$|A| \sim \prod_{i=1}^{n-1} \left(\frac{g_i s_i + ca}{s_i + a}\right) \left(\frac{s_i + a}{a}\right)^{\alpha_i} \left(\frac{s_i + b_i}{b_i}\right)^{\beta_i t_i} \equiv \prod_{i=1}^{n-1} A_i(s_i, t_i). \tag{II-16}$$

The α_i and β_i are the intercept and slope of the i-th Regge pole respectively (see the Fig. 1(b)). The quantities s_i and t_i are defined as

$$s_i = (p_i + p_{i+1})^2 - (m_i + m_{i+1})^2,$$

$$t_i = (p_A - \sum_{r=1}^{i} p_r)^2,$$

where p_i and m_i are momentum and mass of i-th leg in the Fig.1(b) a and c are the scales for statistical component and are constant parameters.

The g_i plays the role of the coupling constant and b_i indicates the exponential dependence on t_i of the Regge coupling .

In that region of phase space where all s_i's >>a and b_i the above amplitude becomes

$$\prod_i g_i\left(\frac{s_i}{a}\right)^{\alpha_i} \exp[(\beta_i' + \log s_i)\beta_i t_i],$$

with $\beta_i'=-\log b_i$. This has the form of a fully Reggeized multiparticle amplitude.

On the contrary, when any of the s_i's is small, then the corresponding term is replaced by the constant c.

Application of the model to p̄p annihilations was made by several authors at 1.6-7.0[86], 2.32[87],2.5[88),89] and 5.7[90] GeV/c. Adjusting the parameters, production angles, transverse momenta, and longitudinal momenta of pions were described by the model qualitatively over wide range of beam momenta and multiplicity. Clayton et al. pointed out that it was necessary to take into account in the amplitude both nucleon and Δ trajectories for a satisfactory fit.[89]

II-3-ii. Modification of the CŁA model

A point which was left unanswered in the CŁA model is a general method for including resonance formation in the calculation. The point is important for p̄p annihilation because of its large fraction of resonance production.

Ranft[90] proposed a modification of the CŁA model for resonance production. The mothod is that supposing the i-th leg in Fig 1(b) a resonance, then the total amplitude is

$$|A|^2 = (1-r) \prod_{j=1}^{n-1} |A_j^{\mathrm{nonres}}|^2 + r|A_i^{\mathrm{res}} \prod_{\substack{j=1 \\ j\neq i}}^{n-1} A_j^{\mathrm{nonres}}|^2 ,$$

where A_j^{nonres} and A_i^{res} are the CŁA amplitude without resonances and a Breit-Wigner amplitude respectively, and γ is a fraction to produce a certain resonance.

Another mothod is proposed by Plahte and Roberts$^{91)}$. They replaced the clustering constant c occuring in each A_i amplitude in eq.(II-16)by a new constant c' as follows. If the particles i and i+1 in Fig.1(b) are supposed to form a resonance, then

$$c^2 \longrightarrow c'^2 + \gamma_j \ BW_j(s_i)^2 ,$$

where the constant γ_j is a measure of probability for formation of a resonance j and the summation is over all possible resonances.

In both methods mentioned above, a measure of fraction for resonance production is determined empirically or in fitting to data.

Recently de la Vaissiere built a phenomenological model for $\bar{p}p$ annihilation by introducing resonances in the CŁA model in a different way from the above-mentiond modifications.$^{43),44)}$ The de la Vaissiere's idea is that resonances have the same kind of coupling constant with the nucleon trajectory as pions. This model is explained in detail in IV-4.

In this model the weight of Breit-Wigner function for a resonance is introduced to the phase-space integral. The probability to produce a resonance is determined by the strength of the vertex coupling, namely, the strength of the coupling of a certain resonance with the nucleon trajectory. By considering that primary pions are produced at much higher rate than resonances in mind, an assumption is made that the vertex coupling constant G decreases rapidly with increasing mass m of the resonance(or meson). A suitable expression for the G is given as

$$G = D_{I,I_z} H \exp(-m/M_0), \qquad \text{(II-17)}$$

where D_{I,I_z} is the Clebsch-Goldan coefficient between the resonance (or meson) and the coupled nucleon-antinucleon pair of a certain isospin state. M_0 and H are the nucleon mass and a constant parameter to be adjusted, respectively.

This model gives a good approximation for not only single-particle distributions but also two-particle correlations in $\bar{p}p$ annihilation in wide range of incident momentum (1∿7 GeV/c) and multiplicities.44) It may teach us something about physics of annihilation.

II-4. Formation Experiment on $\bar{p}n$ Annihilation

$\bar{p}n$ state has a characteristic of pure-isospin state(I=1). There are many experiments[10),26)] on $\bar{p}n$ annihilation in a deuteron bubble chamber below 3 GeV/c for the purpose of searching s-channel resonances of I=1. In these experiments, energy dependence of the cross section for many final states was investigated carefully. It is interesting that Carroll et al.[92)] observed a structure at mass value 1932 MeV/c^2(probably I=1 state) in $\bar{p}p$ and $\bar{p}n$ total cross sections by a counter experiment.

II-5. Dual Model and $\bar{p}n$ Annihilation

II-5-i. Veneziano Model

The 3-pion final state in $\bar{p}n$ annihilation

$$\bar{p}n \longrightarrow \pi^+\pi^-\pi^- , \qquad \text{(II-18)}$$

was investigated in detail at rest[11),29),32)] and in flight.[22),23)] In the former case the initial state is dominated by the orbital angular momentum zero[93)] state. Furthermore angular-momentum-, parity-, G-parity-, and isospin-conservation laws suggest that the initial state is uniquely I^GJ^P(isospin, G parity, angular momentum, parity)$=1^-0^-$, which are just the same quantum numbers as pion.

Lovelace[29)] analyzed the Dalitz plot of the reaction(II-18) at rest supposing the $\bar{p}n$ state to be a heavy pion, where the one-term Veneziano amplitude of $\pi\pi$ elastic scattering[94)] was employed:

The amplitude is

$$F(s,t) = \beta(0.885(s,t)-0.034)\frac{\Gamma(1-\alpha(s))\Gamma(1-\alpha(t))}{\Gamma(2-\alpha(s)-\alpha(t))}, \qquad \text{(II-19)}$$

with

$$\alpha(s)=0.483+0.885s+i0.28\sqrt{s-4m_\pi^2},$$

where s and t are the Mandelstam variables of the crossed channels, and m_π is the pion mass. The result of this fitting reproduces the general feature of the reaction; a hole in the middle of the Dalitz plot, a pronounce peak at low effective-mass values of $\pi^-\pi^-$ channel, bumps of the $\pi^+\pi^-$ spectrum at about masses of ρ and f mesons.

A 4-point Veneziano amplitude was also fitted to a Dalitz plot of the same reaction obtained at 1.2 GeV/c.[22)] This analysis is equivalent to treating the pions as a decay product from a single J^P state of $\bar{p}n$. In this way thirteen 4-point amplitude were prepared for possible initial states. The result is that the amplitude for $J^P = 2^+$ gives qualitative agreement with the data, which has the following form.

$$A^{ij} = \frac{\Gamma(2-\alpha_\rho(s_{12}))\Gamma(1-\alpha_\rho(s_{23}))}{\Gamma(3-\alpha_\rho(s_{12})-\alpha_\rho(s_{23}))}(p_1^i q^j+p_1^j q^i)-(1\longleftrightarrow 3), \qquad \text{(II-20)}$$

where p_1 and p_3 are the negative pion's momenta in the c.m.system. $q=p_3 x p_1$ and $(1\longleftrightarrow 3)$ indicates the second term obtained from the first one by interchanging particles 1 and 3. $\alpha_\rho(s)$ represents the ρ trajectory and the parameters used are

$$\alpha_\rho(s)=0.65+0.84s+i0.26\sqrt{s-4m_\pi^2}.$$

II-5-ii. Rubinstein Theory for Many-particle Final State

Rubinstein pointed out$^{31),32)}$ based on duality and absence of exotics that the general feature of the 3π reaction (II-18), namely, a threshold-like enhancement in the exotic channel and resonance-like peaks near prominant resonances, should appear even in many-body final states.

The threshold-like enhancement in the reaction (II-18) was solved by Lovelace$^{29)}$ as follows.

The amplitude for the decay of a charged heavy pion into three pions is given by

$$A_{\pi^- \longrightarrow \pi^+\pi^-\pi^-} = F(s,t) \qquad \text{(II-21)}$$

$$A_{\pi^0 \longrightarrow \pi^+\pi^-\pi^0} = 1/4(F(u,t)-F(s,t)-F(u,s)) \qquad \text{(II-22)}$$

$$A_{\pi^0 \longrightarrow \pi^0\pi^0\pi^0} = 1/4(F(s,t)+F(s,u)+F(u,t)) \qquad \text{(II-23)}$$

where s,t,u, are the squares of masses of the final dipion combinations and F is the same form as eq.(II-19). In the case (II-21), the u channel is exotic and the Veneziano amplitude grows with increasing s and t. It is clear that the amplitude attains its maximum at the minimum value of u, because of the relation s+t+u = sum of masses. On the other hand, in the case of (II-22) or (II-23) there are several terms and they have maxima at different values of the variables under study, and this fact smears the structure which leads to phase-space-like distribution in Dalitz plot.

Rubinstein's opinion is that the above effect in the 3π channel should be still operative for annihilations of many-particle final states both at rest and in flight, and it should disappear as a function of increasing number of neutral pions.

One can see that the effect is more operative in $\bar{p}n$ case than in $\bar{p}p$ one since the latter system is neutral initially.

Experimental data for 4-, 5-, 6-, 7-, and 8-pion final states of $\bar{p}n$ and $\bar{p}p$ annihilations both at rest and inflight show the predicted effect in dipion-mass plot (see Fig. 2 in ref. (31)).

II-5-iii. Müller-Regge Analysis for $\bar{p}n$ Annihilation

Rittenberg and Rubistein[34)] suggested that under the assumption of validity of duality and $\bar{p}n$ annihilation via resonant intermediate state, the differential momentum distribution for the reactions

$$\bar{p}n \longrightarrow \pi^+ + \text{"anything"}, \qquad \text{(II-24)}$$

and

$$\bar{p}n \longrightarrow \pi^- + \text{"anything"}, \qquad \text{(II-25)}$$

behaves differently. They described the above inclusive processes by Müller expression[95)] considering a $\bar{p}n$ state decayed into a pion and anything. More details are given in Sec. IV-9-ii. The predicted spectra, as the result, for $\bar{p}n$ annihilation are

$$\frac{1}{p}\frac{d\sigma}{dM^2} = \sum_i \beta_i(0)(M^2)^{\alpha_i(0)}, \quad \text{at rest,} \qquad \text{(II-26)}$$

$$\frac{d^2\sigma}{dM^2dt} = \sum_i \beta_i(t)(M^2)^{\alpha_i(t)}, \quad \text{in flight,} \qquad \text{(II-27)}$$

where p, M^2, and t are the momentum of the detected particle, mass of "anything", and momentum transfer between the incident $\bar{p}$ and each pion of a specific charge respectively. The sum should be over the relevant Regge trajectories α_i that can be exchanged between the $\bar{p}n$ system and a pion, and β_i is the suitable residue function.

A schematic description for the Müller-Regge analysis is given in Fig. 1(c). Looking at the π^+ spectrum, the crossed channel is exotic (see Fig. 1(c)), hence the only possible trajectory is Pomeron. Therefore the following relations are obtained from the equations (II-26) and (II-27) for the π^+ spectrum.

$$\frac{1}{p}\frac{d\sigma}{dM^2} = \beta_P(0)M^2 \text{ , at rest ,} \qquad \text{(II-28)}$$

$$\frac{d\sigma_k}{dM^2} = \int_{\Delta t_k} \frac{d^2\sigma}{dM^2 dt}\, dt = K_k^P M^2 \text{ , in flight,} \qquad \text{(II-29)}$$

with

$$K_k^P = \int_{\Delta t_k} \beta_P(t)dt \text{ (at } t=t_k).$$

These expressions suggest that π^+ spectrum should lie on a straight line with respect to M^2, passing through the origin of the axis, multiplied by $\beta(0)$ or K_k factors. The π^- case is more complicated, since more terms being expected to contribute to the sum in eqs. (II-26),(II-27). If only Pomeron and normal (ρ) trajectories are important in this case, then the π^- spectrum is

$$\frac{1}{p}\frac{d\sigma}{dM^2} = \beta_P(0)M^2 + \beta_\rho(0)M, \text{ at rest ,} \qquad \text{(II-30)}$$

$$\frac{d\sigma}{dM^2} = K_k^P M^2 + K_k^\rho M \text{ , } \qquad \text{in flight.} \qquad \text{(II-31)}$$

The inclusive studies of the reactions (II-24), (II-25) were made both at rest[17)] and in flight[25)] (1.0-1.6 GeV/c) in bubble chamber experiments. The both results were in complete disagreement with the above predictions. Both spectra of π^+ and π^- are around a single curve which is rightly expected from the phase space[96)] for the average multiplicity of $\bar{p}n$ annihilation.

III. Experimental Procedure

III-1. Antiproton Beams

The antiprotons were produced in a Beryllium target (12x3x38 cm) by circulating beams of the CERN PS(Proton Synchro-cyclotron) and were transported to the 81 cm Saclay hydrogen bubble chamber through the beam transport system as shown in Fig. 2.[97] Functions of each part constituting the system (see Fig. 2) are as follows; The bending magnets(BM) and electrostatic separators(Sep) separate out desired particles by selecting the momentum and mass respectively. The quadrupole magnets(Q) focuss beams. The collimators, which are slits made of two blocks of lead, eliminate unwanted particles. The shielding walls (hatched areas in Fig. 2) absorb background particles which may traverse the chamber and spoil the quality of pictures. The bending magnet closest to the chamber(BM vert.) is adjusted in order to have the most convenient image of beams inside the chamber, that is, spread of the incident particles in large in vertical plane(normal to the optical axis of the camera) and narrow in holizontal one.In the exposure of the films used here,about ten antiparticles entered the chamber per burst.

III-2. Operation of Bubble Chamber

A hydrogen bubble chamber, which is a high-pressure vessel with glass windows containing liquid hydrogen, is a useful tool for high-energy physics. It is a detector for charged particles which make strings of bubbles along their paths in the chamber. The principle and operation of a hydrogen bubble chambet are described below.[98]

Any chaged particle moving in a bubble chamber undergoes collisions with atomic electrons and suffers energy loss. The energy left amongst atoms causes localized heating, radiation, or decomposition of H_2 molecules. At this moment the liquid is brought in a critical or superheated state, then the localized boiling along the path of the chaged particle is induced. When the bubbles have grown to reach a suitable size, photographs are taken simultaneously by three or four cameras positioned at intervals in one of the sides of the chamber.

A liquid hydrogen bubble chamber is kept statically in the condition of temperature of 26° K and pressure of 5 atmospheres. During each cycle the chamber is expanded by a piston within $\sim$ 20 m sec where the volume increases by the amount of 0.5-1 % and the pressure decreasesby 3.4 -4 atmospheres.

Fig. 3(a) shows the whole aspect of the Saclay 81 cm hydrogen bubble chamber[99)], and Fig.3(b) the arrangement of cameras and flashes. The light of each flash is focussed outside the cameras, so that the images of bright tracks in a dark field are photographed.

A nearly homogeneous magnetic field is maintained perpendicular to the face of the glass of the bubble chamber (20.7 K Gauss in the Saclay chamber), and that allows a measurement of the momentum of charged particles from curvature of the tracks formed.

In principle the velocity of the particles is reflected in density of the bubbles, therefore the amount of ionization loss (i.e. a measurement of the bubble density) should give a measure of particle masses. In practice, tracks of a proton (or antiproton) can be distinguished from those of a pion clearely, but it is not always sufficient to well define kaon tracks among pion ones in the present situation.

A bubble chamber, when it is used as a particle detector, has the following properties;

i) Interaction points and tracks can be measured more precisely than electronic detectors. For example, a spatial position of an interaction point can be defined within error of a few hundreds microns in the present case (by a hand-measuring machine).

ii) The liquid in a chamber, which forms strings of bubbles, is itself a target exposed to incident beams. By this fact, not only high-energy particles but also low-energy ones(< 0.5 GeV/c) can be detectable without any difficulty.

iii) All tracks are recorded in a photograph even if a reaction forms a complicated topology, that is, a bubble chamber is a 4-π solid-angle detector and suitable for many-particle reactions or cascade ones.

iv) In normal expansion (one expansion per two seconds in general), photographs are taken without reference to reactions. Therefore once photographs have been taken, it is possible to study several problems on the same films depending on physical aspects interesting and feasibility.

III-3. Density of Liquid Hydrogen in an Operating Bubble Chamber

III-3-i. Formulae for Range-Energy Relation

In order to evaluate a cross section for any reaction in a hydrogen bubble chamber, it is essential to determine the liquid-hydrogen density in operating condition. The density of H_2 in the Saclay 81 cm bubble chamber was deduced by means of measurement of muon-track length produced by decay $\pi^+ \longrightarrow \mu^+ + \nu_\mu$.100) The experimental method concerning the above analysis is described briefly in the following.

A basic expression for energy loss per unit path length of a charged particle through matter is given by the Bethe-Bloch equation101)

$$\frac{\partial E}{\partial X} = \frac{2\pi z^2 e^4 NZ}{mc^2 \beta^2 A}\left(\ln \frac{2mc^2\gamma^2\beta^2\, Q_{max}}{I^2} - 2\beta^2 - \frac{2C}{Z} - \delta\right), \tag{III-1}$$

where Q_{max} is the maximum energy that can be transfered per collision and is given by

$$Q_{max} = 2mc^2\gamma^2\beta^2/(1+ 2\gamma m/M + (m/M)^2).$$

The arguments in the above equations mean as follows;

ze, βc, M : charge, velocity, mass of the incident particle respectively.
mc^2 : electron rest energy.
NZ/A : property of medium.
NZ : number of electrons per unit volume.
A : atomic weight.

I is the excitation energy of H_2(20.3 eV)[101] and δ, a correction term which becomes important in the region $\beta \rightarrow 1$. C/Z represents the shell correction term which becomes important in the region of small β or, more precisely, when the β of an incident particle is comparable to the electron velocity in atoms this term is not negligible.

Integrating eq.(III-1) to establish a range-energy relation. the low-nergy region is excluded but uses an experimental value at energy T_0. The range, thus obtained, is expressed as[102]

$$R(T_i,m_i:T_o,I)=\frac{m_i}{m_p}(R(T_o)+\int_{T_o}^{(m_p/m_i)T_i}(\frac{\partial E}{\partial X})^{-1}dE, \quad \text{(III-2)}$$

where m_i is the mass and T_i the kinetic energy of the particle i in question, $R(T_o)$ is the range of a proton of energy T_o in the medium. With T_o = 2 MeV, $R(T_o)$ is taken to be 0.00288 g/cm^2 in liquid hydrogen.[101] For a muon case the range is

$$R_\mu\ (T_\mu = \frac{m_\mu}{m_p} T_o) = \frac{m_\mu}{m_p} R(T_o),$$

in eq.(III-2).

III-3-ii. Experimental Result

The events of the decay $\pi^+ \longrightarrow \mu^+ + \nu_\mu$ followed by $\mu^+ \longrightarrow e^+ + \nu_\mu + \nu_e$, where π^+'s were produced in reactions of $\bar{p}p$ annihilation in the 81 cm Saclay bubble chamber, were measured and reconstructed through THRESH. 128 such events passed the following criteria;

i) point errors: $\Delta x<0.025$, $\Delta Y<0.025$, $\Delta Z<0.12$ (cm).

ii) dip angle of $\mu^+ < 60°$.

iii) laboratory angle between π^+ and μ^+ directions > 90°.

Perhaps the criterion iii) minimizes the background due to the in-flight π^+'s ; the μ^+'s are mostly monoenergetic with kinetic energy $T_\mu = 4.121$ MeV.

The arc lengths of the μ^+ tracks were calculated from the linear distance between two decaying points with correction for the multiple-scattering effect (0.16 %)[101] and the curvature effect (0.8 %). Figure 4 shows a histogram of the muon-track lengths thus obtained for 128 events. The average track length is 1.0527 cm with width 0.0443 cm. The expected width due to straggling is approximately 0.0359 cm.[102]

The liquid-hydrogen density is deduced from eq. (III-2) to b

$$\rho_{H_2} = 0.06266 \pm 0.00011 \text{ g/cm}^3.$$

where the terms of δ and C/Z in eq. (III-1) are neglected.

The density of H_2 in the Saclay chamber had been measured once by CERN-Saclay collaboration; the result is[40] $\rho_{H_2} = 0.0625 \pm 0.0001$ g/cm^3. The two values are in good agreement, and the average value, $\rho_{H_2} = 0.0626$ g/cm^3, is used throughout this experiment.

III-4. Scanning and Measuring

III-4-i. Scanning Criteria.

Having acquired films, the first stage in any experiment is scanning; searching each photograph for events of the required topology. For this purpose films are projected, frame by frame, onto a white topped table. An image of the film is magnified to make identification of the required event easy (20 times magnification at Tokyo). Three views of the photograph are used simultaneously, scanners note down the frame number of each event, if it is found, along with the topology. At the same time scanners also record characteristics of the events under a given rule so as to hold the information necessary for reidentification, classification and measurement of the event.

At Bombay, Neuchatel and Tokyo scanning was carried out for the reaction

$$\begin{array}{l} \bar{p}p \longrightarrow \bar{n}n \\ \qquad\quad \llcorner\!\!\longrightarrow \bar{n}p \rightarrow \text{annihilation.} \end{array} \quad \text{(III-3)}$$

Bombay and Neuchâtel groups used the films of the exposure II (0.75 GeV/c), and Tokyo group the films of the exposure I (0.7 GeV/c)

The event is identified on a scanning table such as a 0-prong vertex associated with an odd-prong star with a positive net charge down stream (photographs of the typical events are given in Fig.5) . The scanning procedure is as follows.

i) Frames which have no beam track or are not illuminated, half illuminated, or very faint are rejected.

ii) All odd-prong stars(3, 5, 7 prongs) are firstly searched. The accompanying $V_0(K^0 \rightarrow \pi^+\pi^-$ decay) or Dalitz pair

($\pi^0 \longrightarrow \gamma e^+e^-$ decay) is also recorded, where the latter is identified by one or two spiralling tracks. Any event of one-prong star is not searched because of large single-track background.

iii) Stars of which a positive track stops in the chamber without any decay product are rejected. They are protons mainly due to background πp elastic scattering.

iv) Stars of which one of the tracks is clearly going to the interacting vertex instead of comming out from it are rejected. They are events of $\bar{p}p$ annihilation induced by off-beam $\bar{p}$ or background πp elastic scattering. This point is checked observing δ - rays (knockon electrons). δ - rays are usually on the right-hand side with respect to the direction of the moving particle in the present case(see Fig.5).

v) The stars of which one of the tracks is heavily ionized may be $\bar{p}p$ annihilation by off-beam $\bar{p}$ or background πp elastic scattering, even if they passed the steps iii) and iv). The number of stars having the ambiguity with $\bar{p}p$ annihilation was 20 (1.3 % of total samples) at Tokyo, and they were judged to be accepted or not by a few veteran physicists with reference of ionization and dip angle of the track in question.

vi) Once a star was found, a 0-prong beam track is searched upstream. The 0-prong, if found, is checked to confirm if the vertex actually stays in the chamber rather than hitting the glass windows of the chamber, since a genuine O-prong reaction occures at middle depth. O-prong tracks suffering a scattering before are not accepted.

III-4-ii. Classification of Samples and Scanning Efficiency

Events obtained on scanning are classified as;

(A) Associated events: There is an odd-prong star associated with a O-prong vertex upstream.

(B) Unassociated events: There is an odd-prong star with a 0 prong downstream or without any 0 prong.

(C) Two 0-p or two odd-p in a frame: There are more than one 0 prong or more than one odd-prong star in one frame. In this case ambiguity for the reaction (III-3) arises, because more than one combination are possible between 0 prong and odd-prong stars.

Events are also classified with respect to the number of prongs or existence of V_0, Dalitz pair at the star vertex. A result is summarized in Tables 1(a), 1(b), and 1(c) corresponding Tokyo's, Bombay's and Neuchâtel's data respectively. Figures 5(a), 5(b) and 5(c) show typical events associated with a 3-prong, 5-prong, or 7-prong star respectively.

Two independent scans were carried out by trained scanning staff or physicists and scanning efficiency was estimated by the following equation.

$$E = \frac{(N_1+N_2-N_{12})N_{12}}{N_1N_2} , \qquad \text{(III-4)}$$

where N_1, N_2 and N_{12} represent number of events (including those of both classes (A) and (C)) found in the first scan, second scan and both scans respectively. The average value of E was 97 % on the three groups, and the result also appears in tables 1(a) - 1(c).

III-4-iii. Super Mangiaspago Type Measuring Projector (SMP)

The purpose of measuring an event obtained in scanning is to determine the positions of vertices and tracks on two or more views, and prepare the information with suitable format for the series of computer programs for spatial reconstruction. The events obtained at Tokyo were measured mostly by a hand measuring machine SMP (Super Mangiaspago Type Measuring Projector). A principle and measurement accuracy of this machine are as follows.

The SMP is,essentially, an image plane digitizer employing two strings which measure a point in a bipolar coordinate system.[103)] A diagram of the device is shown in Fig. 6(a).[104)] Two 200 microns diameter steel music wires have one of their end attached to a "pack" and the others wound around two 10 cm diameter drums. The drum has a spiral groove cut in it and a copper wire wound permanently in the groove. The measuring wires are wound between the turns of the copper wire.

In this way high-precision machining is restricted to the outer surface of the drums and the axial holes only. The wires are kept under constant tension by counter weights connected to the strings wound on the second smaller drums mounted coaxially with the measuring drums.

The drums are mounted directly on the shafts of 8,000 counts per evolution encoders which enable us to read the position of the "pack" in semipolar coordinate.

The coordinate system is not strictly bipolar because the wires lie tangential to the edge of the drum instead of passing through the center. A conversion of the coordinate system to a Cartesian one is performed by an iteration method.

One least count of the encoder is 39μ change in length of the wire. Films are projected on the measuring table with a magnification of 17 times without any mirror in path of light, the overall accuracy of the digitizer is within 4μ on films.

Positions are measured on several reference fiducials, of apecies, and on five or more points spaced evenly along each track. Raw data from the digitizer are arranged for the geometrical-reconstruction program THRESH through the computer program "Pre-THRESH".

To estimate mass resolution for K^o of this machine, 300 events of V^o decay produced in $\bar{p}p$ annihilation were measured, and the result obtained for the K^o mass was

$$(K^o \text{ mass}) = 0.495(\text{GeV}/c^2),$$

with spread 0.011 (GeV/c^2). This is in good agreement with the standard value appearing in Particle Data Group Table (0.4977 GeV/c^2).

III-4-iv. Computer Aided Measuring Projector(CAMP)

The Tokyo data were also measured by CAMP (Computer Aided Measuring Projector) partly. This machine is a semi-automatic film plane digitizer designed by Prof. Yamagata.105),106)

CAMP consists of an automatic measuring device(AMD) and a rough digitizer(supersonic digitizer), and these are controlled by an on-line mini-computer. A block diagram of the device is given in Fig. 6(b).

A film image is magnified ten times and is projected on a desk-top screen on which a supersonic digitizer is provided. A human operator indicates to the computer three points on a track to be measured using the supersonic digitizer. The supersonic digitizer is constructed with an electric-spark pack and three slab-type condenser microphones placed along the edge of the screen. A spark coordinate, a point to be digitized, is determined with the time-of flight of the sonic wave detected by the microphones.

The computer then calculates a circular road connecting these roughly measured points, and drives the stage, where films are mounted, along the circular road with velocity of about 30 mm/sec. The position of the stage is measured by a pair of Moire fringe digitizers with the least count of 2μ.

Digitization along the circular road is made by means of automatic measuring mode or manual mode. In the former case, now in progress for completion, the AMD scans and measures, on fly, track segments which are within 2 mm from the optical axis. The scan is made 100 times per second by a rotating mirror along the track where the stage is driven so as for the track to stay within the scan area. The image of the track to be measured is directed such as to be always parallel to the axis of the rotation mirror and to the slit (20μ wide and 1 mm long) by the Dove prism (see Fig. 6(b)). Data from the AMD are processed and output by the mini-computer.

In the latter case(manual mode) the stage is controlled manually and the coordinates of points on a track are measured by the like method employed at a Vangard-type machine. The monitor displays the neibourhood of the point to be measured on the circular road on a TV screen in 150x magnification. Then a human operator adjusts the point into the cross-hair in the TV screen by two handles regarding to X and Y directions.

K^o mass was obtained to be

$$(K^o \text{ mass}) = 0.496 \ (\text{GeV}/c^2)$$

with spread 0.010 (GeV/c^2) based on 199 events with manual-mode measuring by the CAMP, which was comparable with that by the SMP.

III-4-v. Measuring Machines Used at Bombay and Neuchâtel.

Bombay group used conventional image-plane measuring machines. The characteristics of the machines were studied elsewhere.[107)] Among their results, the point-setting error is 7.5 μ and the peak value of K^o mass is obtained based on 2,153 events as

$$(K^o \text{ mass}) = 0.4925 \ (\text{GeV}/c^2)$$

with full-width at half-maximum being 0.015 (GeV/c^2).

Neuchâtel group used a semi-automatic measuring machine called ENETRA 114A.[108)] 200 V^o events were measured to estimate the actual accuracy and the result was

$$(K^o \text{ mass}) = 0.4980 \ (\text{GeV}/c^2).$$

III-5. Processing by Computer (Pre-THRESH, THRESH)

III-5-i. Pre-THRESH

Events obtained on scanning are measured to deliver the required quantities to THRESH, a program for spatial reconstruction of the measured points and tracks, developed at CERN.[109)] For the purpose of arrangement of the raw data (measured data) for the required input format of the THRESH, a program Pre-THRESH was used at Tokyo. This program, which should be altered depending on sort of experiment and on type of measuring machine, has some functions as follows.

i) It prepares input data for the THRESH after arrangement of measured ones.

ii) A correction due to the optical distortion of a measuring machine is made if necessary.

iii) The order and number of measured points of events are checked.

iv) Measurement errors for the fiducial marks are checked.

For the purpose of the last one, a criterion is made ready as the same way employed in the THRESH. Let (X_i, Y_i) be a coordinate of the fiducial marks projected on the inside face of the chamber window, which is prepared in TITLE card for each view for THRESH run. Let (X_i', Y_i') be the correspoding one obtained by measuring. Then (X_i, Y_i) and (X_i', Y_i') are related by the equations

$$\begin{aligned} X_i &= a_1 + a_3 X_i' + a_5 Y_i' , \\ Y_i &= a_2 + a_4 X_i' + a_6 Y_i' , \end{aligned} \qquad \text{(III-5)}$$

where i=1,2,3,4 in each view (four fiducial marks are measured in practice). The coefficients (a_1, a_2,..., a_6) are obtained by least square method. Using the coefficients, thus obtained, deviations ΔX_i, ΔY_i and a stretch parameter ST are defined as

$$\Delta X_i = | X_i - (a_1 + a_3 X_i' + a_5 Y_i')|,$$

$$\Delta Y_i = | Y_i - (a_2 + a_4 X_i' + a_6 Y_i')|,$$

$$ST = \sqrt{\frac{(a_3 - Sa_6)^2 + (a_5 + Sa_4)^2}{|a_3 a_6 - a_4 a_5|}} \text{ , (III-6)}$$

where i=1,2,3,4 and $S=(a_3a_6-a_4a_5)/|a_3a_6-a_4a_5|$ Figure 7 gives a distribution of ST for each view of the photograph. The following criteria were imposed to measured events.

i) ΔX_i and ΔY_i should be within the limit 0.03 cm.

ii) The value of ST should be lie between 0 and 0.006 in each view.

By these criteria one can find frames, where fiducial marks are not precisely measured or films are stretched badly, before runs of the THRESH.

Positions of the four fiducial marks, a 0-prong interaction point, an apex of the odd-prong star and five points spaced evenly along each tracks were measured on each view. Events which did not pass the above two criteria were remeasured.

III-5-ii. THRESH

In this experiment the mass-dependent THRESH was used which reconstructs apecies and tracks taking into account the effect of energy loss due to ionization, where track parameters(momentum, polar angle, azimuthal angle) are calculated both at beginning point and at end point for one track. It requires the following information in addition to the Pre-THRESH outputs; constant parameters for the events in question and measuring machine (CONS block), the camera coordinates (CAMERA block), the characteristics of the optical media (MEDIA blosk), the coordinates of the standard reference fiducial marks (REFER block), the mass requests for any track (MASHYP block), the range-energy tables (RANGE block), the magnitude of the magnetic field at all points inside the chamber (FIELD block) and other optional blocks. The parameters in the CONS block are explained in Table 2(a) together with the values adopted at Tokyo group.

Spatial position errors for the interaction points (odd-prong star vertices) of the THRESH outputs are given in Fig. 8(a),8(b), and 8(c) corresponding to ΔX, ΔY, and ΔZ respectively. Errors for momentum, dip angle (polar angle) and azimuthal angle of the incident tracks are also given in Fig. 9(a),9(b), and 9(c) respectively, and residues are in Fig. 9(d).

To eliminate poorly measured events, the following criteria were imposed to THRESH outputs and the events which did not pass these criteria were remeasured.

i) Position errors at each vertex should be $\Delta X<0.03$, $\Delta Y<0.03$, and $\Delta Z<0.15$ (cm).

ii) The error code for each track should be less than 1000, this criterion guarantees that a spiral helix is fitted to measured data with convergence.

iii) The residue for each track should be less than 30 μ.

The arrows in Figs. 8 and 9 indicate the upper limit for acceptance of events due to the above criteria. The momentum resolution $\Delta p/p$ for the measured tracks was about 4 % on the average.

Measurement was made three times for the events which did not pass the above criteria, and finally 11 % of all samples failed in reconstruction. The majority of the failed events are those which are difficult to measure precisely enough, because they contain a 0-prong vertex which is hidden by other beam tracks, or a star having a track with large dip-angle or a track of low-momentum pion decaying within the chamber occasionaly.

The results of measurement at Tokyo is summarized in table 1(a). The results at Bombay and Neuchâtel are also summarized in table 1(b) and 1(c) respectively together with their criteria employed for acceptance.

III-6. Test on Coplanarity Angle for 3-prong Stars

III-6-i. Rejection of Background Events

One of the most prominent background contaminating samples is the star-like 3-prong events due to πp(or pp) elastic scattering caused by background pions (or protons rarely) traversing the chamber at random. A striking feature of the above-mentioned events is such that one of the three tracks (or all of the three tracks in pp case) is heavily ionized which corresponds to the recoiled proton. Such a feature also appears in genuine $\bar{n}p$ stars of 3 prongs when one of the tracks has a large dip angle, so that the background cannot be removed a priori in scanning.

All 3-prong events picked up in scanning were checked on coplanarity of the three tracks using the THRESH outputs as follows.

Quantitied CUB and COP are defined as

$$\text{CUB} = |\vec{i}\cdot(\vec{j}\times\vec{k})| \ , \qquad \text{(III-7)}$$

$$\text{COP} = \left|\frac{\vec{i}.(\vec{j}\times\vec{k})}{|\vec{i}|.|(\vec{j}\times\vec{k})|}\right| \ , \qquad \text{(III-8)}$$

where $\vec{i}$, $\vec{j}$ and $\vec{k}$ represent unit vectors along the direction of the three tracks in question. For elastic scattering, the values of both CUB and COP should be compatible with zero taking into account errors on the measured quantities.

In practice, distributions of both CUB and COP showed sharp peaks at ≤ 0.04 and at ≤ 0.05 respectively superimposed on smooth distributions pertaining to genuine $\bar{n}p$ stars (see Figs. 10(a) and 10(b)).

The 3-prong samples with one (or more) heavily ionized track in the region CUB ≤ 0.04 were rejected. In the most case, it was found that the composition of angles between three tracks of the rejected samples was compatible with the hypothesis of the elastic scattering. 174 events were removed from the 3-prong samples (1,134 events), and as the result both CUB and COP distributions became consistent with smooth behavior as seen in Figs.10(a) and 10(b) respectively (In the both figures the shaded area corresponds to the rejected samples).

The samples which failed in spatial reconstruction cannot be checked on coplanarity. In this case the background events were confirmed by a few physicist by refering the information (ionization and composition of the angles of the three tracks) obtained by scanning. 18 events were removed from the failed samples of 3 prongs (119 events).

Ratios of the rejected events to the total ones for the good reconstructed samples and badly measured ones are 174: 1,134 (=0.153:1) and 18:119(=0.151:1), and are in good agreement suggesting that the background in the badly measured samples is rejected fairly well.

III-6-ii. Ratio of 3, 5, 7 prongs to the Total

The pure samples, thus obtained at Tokyo, are summarized in Table 1(a). The numbers of events in the 8-th row in this table give ratios of $\bar{n}p$ annihilation into 3, 5, and 7 prongs to the total (=0.72 : 0.27 : 0.007). The results at Bombay and Neuchâtel are also given in tables 1(b) and 1(c) respectively.

A method of the background rejection employed at Bombay is different from that at Tokyo a little. They cut off the events of CUB ≤ 0.025 and estimated a number of events lost due to this cut by extrapolating a smooth curve at CUB > 0.025 to the region CUB ≤ 0.025.

The ratios obtained at three groups are consistent, and finally the summation of the results of three groups yields

$$\begin{aligned} &3 \text{ prongs}: 5 \text{ prongs}: 7 \text{ prongs} = 2670.33:1077.67:29 \\ &= 0.707 : 0.285 : 0.008, \qquad \text{(III-9)} \end{aligned}$$

where the former gives numbers of events and the latter gives the ratio.

III-7. Processing by Computer (GRIND, Data Summary Tape)

III-7-i. Principle of GRIND

A kinematical state of a particle is completely determined by its relativistic four-momentum, namely its ordinary three momenta and energy, and each component of the four quantities of the particles involved in an event should satisfy relativistic conservation laws during the interaction. Usually kinematical quantities of THRESH outputs do not satisfy these conservation laws because of measurement errors and unobserved neutral particles if any. The GRIND adjusts the data of THRESH outputs for an event to the conservation laws (called constraint equations) with regard of a given physical hypothesis, and puts out fitted quantities together with fitting probability for the given hypothesis.110)

The GRIND requires the following information in addition to the THRESH outputs ; constant parameters used in the fitting procedure (CONS block), the information on controlling the interation procedure of the fitting routine (CONV block), the beam information (BEAM block), the energy-range tables (RANGE block), the magnitude of the magnetic field at all points inside the chamber (FIELD block), a list of hypotheses indicating suitable mass assignment for particles of the event (Hypothesis block). The parameters in the CONS block are explained in Table 2(b) together with the values adopted at Tokyo group.

A set of the four variables to determine a particle is three-momentum components p_x, p_y, p_z, and mass M. Another set is inverse of momentum 1/P, dip angle λ , azimuthal angle ϕ , and mass M. Errors of variables in the latter set distribute more symmetrically than those in the former set, so that the set $(1/P, \lambda, \phi, M)$ is used as the variables in kinematical fitting by the GRIND. These variables can be divided into three groups:

i) Variables evaluated together with errors during the geometrical reconstruction of a track, which are called measured (or well measured) ones. The following definitions are made:

(m_i); vector of well measured variables,
(G^{-1}_{ij}); error matrix for the vector m,
(c_i); vector for correction on the vector m,

where i(j) represents an index corresponding to each variable and varies i(j)=1, 2, ..., 3N; N is the number of tracks with regard.

ii) Variables fixed by a hypothesis, for example, mass of particles.

iii) Variables of badly measured or unmeasured, which corresopond to tracks with difficulty of good measurement or invisible neutral particles respectively. Definitions are made as follows;

(m^*_k); vector of badly measured variables. For unmeasured variables one first guesses to exist.
(G^*_{kl}); inverse error matrix for m^*. The matrix G^* is diagonal since the correlations between badly measured or unmeasured variables have no physical significance. The elements of unmeasured variables are zero.

(c_k^*); vector for correction on the vector m^*.

The constraint equations are given by

$$\Sigma \pm p_x=0, \quad \Sigma \pm p_y=0, \quad \Sigma \pm p_z=0, \text{ and } \quad \Sigma \pm E=0, \qquad \text{(III-10)}$$

where the direction of a track is always pointing away from the interaction point, so that the minus signs in eq. (III-10) are applicable for incoming and target particles.

Vectors c and c^* are determined in fitting procedure under the conditions

$$\chi^2 = c^T G c + c^{*T} G^* c^* = \text{minimum}, \qquad \text{(III-11)}$$

$$f_\lambda \; (m+c, \; m^*+c^*) = 0, (\lambda = 1,2,3,4), \text{(III-12)}$$

where T means transposition and f_λ (λ =1,2,3,4) is each of the constraint equations (III-10). χ^2 is the measure of likelihood of the hypothesis employed to a given event with a number of degree of freedom (= number of constraint equations - number of variables unmeasured or badly measured). A fit to a certain hypothesis is obtained if χ^2 converges.

III-7-ii. Fitting Procedure in GRIND

The hypotheses for the reaction (III-3), i.e.,

$$\bar{p}p \longrightarrow \bar{n}n$$

$$\llcorner\!\!\longrightarrow \bar{n}p \quad \longrightarrow \text{annihilation}, \quad \text{(III-3)}$$

were considered at each vertex as follows.

(1) 0 prong; $\bar{p}p \longrightarrow \bar{n}n$, 0-C fit (III-13)

(2) 3 prongs; $\bar{n}p \longrightarrow 2\pi^+\pi^-$, 4-C fit (III-14)

(3) $\bar{n}p \longrightarrow 2\pi^+\pi^-\pi^o$, 1-C fit (III-15)

(4) $\bar{n}p \longrightarrow 2\pi^+\pi^-M^o$, no fit (III-16)

(5) 5 prongs; $\bar{n}p \longrightarrow 3\pi^+2\pi^-$, 4-C fit (III-17)

(6) $\bar{n}p \longrightarrow 3\pi^+2\pi^-\pi^0$, 1-C fit (III-18)

(7) $\bar{n}p \longrightarrow 3\pi^+2\pi^-M^0$, no fit (III-19)

Here 4-, 1-, 0-C fit and no fit mean that numbers of degree of freedom are 4, 1, 0, and no constraint respectively, and M^0 means multi-π^0 production. At present 7-prong stars are not taken into account because of the poor statistics.

As seen from the above hypotheses, all tracks at the star vertex were considered as pions unless V^0 was associated to the vertex. The reasons why only pions were taken into account are; i) In $\bar{p}p$ annihilation purely pionic final states are dominated (~90 %),4) and this fact suggests the purely pionic-final-state dominance in $\bar{n}p$ annihilation, ii) It is difficult to identify charged kaons definitely from bubble density.

According to 4-C fit, 1-C fit and no fit, the fitting process can be divided into three cases;

i) When an $\bar{n}p$ vertex fits to one of the hypotheses (2),(5), with 3-C (The momentum of $\bar{n}$ is unknown) firstly, then GRIND proceeds 0-prong vertex with hypothesis (1) using the value of momentum of $\bar{n}$ determined previously. It goes back to the $\bar{n}p$ vertex again with the fitted momentum of $\bar{n}$ obtained at 0-prong vertex and tries 4-C fit there. Finally multi-vertex fit is carried out with 4-C.

ii) When an $\bar{n}p$ vertex fits to one of the hypotheses (3), (6), with 0-C (The unknowns are the momentum of $\bar{n}$ and $1/P$, λ, ϕ, of π^0.), the kinematics of this fit gives two solutions for momentum of $\bar{n}$ arising from a small difference of neutron and proton masses. For the 0-prong vertex GRIND now tries both attempts with each solution and determines the fitted momentum of $\bar{n}$. It goes back again to the $\bar{n}p$ vertex with the momentum of $\bar{n}$ and tries 1-C fit there. Finally multi-vertex fit is carried out with 1-C.

iii) When a $\bar{n}p$ vertex does not give any fit, this is the case of (4) or (7), not only single-vertex fit but also multi-vertex one is provided.

Kinematics for $\bar{p}p$ vertex is described in Section V-3-ii in detail. Kinematical quantities of rather multi-vertex fit than single-vertex one were accepted at Tokyo group since the former is given by adjusting overall quantities measured. It was found that there was no significant difference between the quantities obtained at single-vertex fit and multi-vertex fit.

III-7-iii. Kinematical Ambiguity and Classification of Events

One of the most important problem is to solve kinematical ambiguities in the GRIND outputs, that is to clarify kinematical overlaps and to eliminate background contamination entering into fitted samples.

To check the bias which might have been introduced in the fitting procedure, distributions were taken for quantity pull;

$$\text{pull} = \frac{A - A'}{\sqrt{\sigma_A^2 - \sigma_{A'}^2}} , \qquad \text{(III-20)}$$

where A is the measured quantity and A' the fitted one, and $\sigma_A(\sigma_{A'})$ is the standard deviation of $A(A')$. Figures 11(a), (b), and (c) give the pulls of $1/P$, λ, and ϕ of the incident $\bar{p}$'s of fitted events (4C or 1 C) respectively.

Each of these distributions is consistent with a symmetric distribution around zero. The biases, if any, due to the use of the uncorrected magnetic field or due to uncorrected optical distortion of the measuring machine should disturb the symmetric distributions. Figures 11(a), (b), and (c) imply that there is no above-mentioned biases in the present analysis.

It is possible to predict the χ^2 distribution for certain degree of freedom, and hence to calculate the probability that the χ^2 comes out with an actual value provided the three assumptions below are true.111)

i) All measurements are elements of Gaussian distribution.

ii) The error matrix is correctly evaluated.

iii) The hypotheses that the equations of a certain constraints are valid in nature is true.

Therefore χ^2 probability $P(\chi^2)$ is available to eliminate the background contamination. The following criteria were imposed to fitted events.

i) If there were several 0 prongs or odd-prong stars on the same frame, 4-C fit event was accepted when one combination gave 4-C fit and others 1-C or no fit. On the other hand 1-C event was accepted when one combination gave 1-C fit and others no fit. Nothing was accepted when they gave fit with the same degree of freedom or did not give any fit.

ii) 26 events overlapped between 4-C and 1-C fits. Furthermore 17 samples of 1-C fit in these events gave $P(\chi^2) < 10$ %, whereas the samples of 4-C fit gave a random distribution of $P(\chi^2)$. From the above fact and from what mentioned in Section III-7-ii, it can be concluded that the 4-C fit is more reliable than the 1-C fit. Therefore 4-C fit was accepted in the overlapping case.

iii) Figures 12 and 13 give distributions of $P(\chi^2)$ and $(MM)^2$ for the fitted events respectively. The missing-mass squared $(MM)^2$ is defined as

$$(MM)^2 = (E_{in} - E_{out})^2 - (P_{in} - P_{out})^2, \qquad \text{(III-21)}$$

where E_{in} and E_{out} represent the energies of incoming particles ($\bar{n}$ and p) and outgoing ones of measured (assumed to be pions) respectively, while P_{in} and P_{out} represent the momentum values.

One can see from Figure 12 that $P(\chi^2)$ distributions for 4-C fit are consistent with flat distributions, while those for 1-C fit give slightly positive slopes which may be caused by overestimation of the measurement error. The $(MM)^2$ distribution for the 4-C events (see Fig. 13) shows that the events are concentrated very close to zero and nearly symmetric. These facts suggest that background contaminations are small among the fitted events. One restriction was imposed for acceptance of 4-C fit events as

$$-0.16 < (MM)^2 < 0.16\ (\text{GeV})^2, \qquad \text{(III-22)}$$

and only 3 events in the $3\pi^+2\pi^-$ samples were rejected by this cut.

The $(MM)^2$ distribution for $2\pi^+\pi^-\pi^0$ final state is rather broad and significantly deviates from the symmetric one around $m^2_{\pi^0}$($=0.018$ GeV^2) (see Fig. 13). A restriction was imposed to acceptance of 1-C fit events as

$$-0.3 < (MM)^2 < 0.4 \quad (\mathrm{GeV}^2). \qquad \text{(III-23)}$$

Folding the distribution in the region $(MM)^2 < 0.02$ onto the region $(MM)^2 > 0.02$, contaminations due to multi-π^0 production in the $2\pi^+\pi^-\pi^0$ samples were estimated as ~40 %.

Numbers of the fitted events, thus obtained, are classified in Table 3 together with those obtained at Bombay and Neuchâtel. The cut on $(MM)^2$ distributions for the data of the foreign groups is not imposed in the present case because of the lack of $(MM)^2$ quantity on the DST (Data Summary Tapes).

III-7-iv. Data Summary Tape (DST)

The GRIND outputs consist of many words providing the information in the fitting, and a part of these is not used in analyses so long as GRIND proceeds events normally. Therefore it is convenient to make a data summary tape (DST) on which variables are selected for one's purpose and arranged and written on a magnetic tape with suitable format for analyses.

In the present experiment the DST was made at each group with format as given in Table 3, and exchanged among them.

In Figure 14 a flow of events handling at each step (from scan to DST) is shown schematically which was employed at Tokyo.

III-8. Mass Resolution (Measured Width of ω Resonance)

Since the mass resolution in this experiment is expected to be larger than the width of ω resonance, which is established as 10 MeV in Particle Data Group[112)], it is possible to estimate the resolution by measuring the width. Figure 15(a) shows the $(\pi^+\pi^-\pi^o)$ effective mass squared spectrum for the six-pion final state (see III-7-ii) obtained from the data of Exposure I : there are 6 combinations per event. The spectrum shows a sharp peak at the ω mass.

The mass and width of the ω were obtained by a least square fit of the spectrum between 0.4 and 0.9 $(\mathrm{GeV}/c^2)^2$ to the function

$$f = a_o(1+a_1m^2+a_2m^4) + \frac{a_3}{(m^2-M_\omega^2)^2+M_\omega^2\Gamma_\omega^2} , \quad \text{(III-24)}$$

where m is the $(\pi^+\pi^-\pi^o)$ effective mass, and a_o, a_1, a_2, a_3, M_ω, and Γ_ω are parameters to be fitted. The mass M_ω and width Γ_ω, thus obtained, are

$$M_\omega = 0.780 \pm 0.004 \quad \mathrm{GeV}/c^2 , \quad \text{(III-25)}$$

$$\Gamma_\omega = 0.050 \pm 0.013 \quad \mathrm{GeV}/c^2 , \quad \text{(III-26)}$$

with $\chi^2/\ n_D = 45.5/51$. The solid curve in Fig. 15(b) gives the fitted one. The world average for the above quantities is given by the Particle Data Group[112)] as

$$M_\omega^{tr} = 782.7 \pm 0.6 \ \mathrm{MeV}/c^2, \quad \text{(III-27)}$$

$$\Gamma_\omega^{tr} = 10.0 \pm 0.4 \ \mathrm{MeV}/c^2 , \quad \text{(III-28)}$$

One can see that M_ω and M_ω^{tr} are in agreement within statistical errors implying no systematic biases in the present data. Since the value of Γ_ω^{tr}, true width, is small in contrast with that of Γ_ω, the value of Γ_ω obtained gives a measure of the experimental mass resolution.

The Breit-Wigner formula in eq (III-24) suitably represents a resolution function for the experimental responce, therefore the mass resolution for the $3\pi^+2\pi^-\pi^0$ final state , Γ_R, is estimated as [113)]

$$\Gamma_R = \Gamma_\omega - \Gamma_\omega^{tr} = 40 \text{ MeV/c}^2. \qquad \text{(III-29)}$$

IV. General Characteristics of Antineutron-Proton Annihilation

IV-1. Branching Ratios in the Final State

IV-1-i. Branching Ratios and Cross Sections

We now proceed to the discussion of general characteristics of $\bar{n}p$ annihilation observed in our experiments.

The experimental procedure employed at Bombay and Neuchâtel groups was essentially the same as that at Tokyo, so that, the events obtained at the three groups were treated as a set in the analysis for antineutron-proton($\bar{n}p$) annihilation.

For this analysis two criteria were imposed to the sample obtained by the procedure as described in Chapter III;

i) To study the annihilation within a restricted energy region, only stars produced by an antineutron within the momentum interval

$$0.5 < P(\bar{n}) < 0.8 \text{ (GeV/c)} \qquad \text{(IV-1)}$$

are used.

ii) Furthermore only unambiguous stars, i.e. events with one 0 prong and one odd-prong star in a frame, are used to avoid the background contamination due to unassociated stars to 0-prong vertex or vice versa.

Figure 16 gives a distribution of the antineutron momenta of all events passing through the criterion ii), in which two arrows indicate the criteria i). Abnormal excess of events of $\bar{n}$ momentum < 0.002 GeV/c in Fig. 16 is explained below. The momentum distribution is taken from the GRIND outputs for fitted events and from the THRESH outputs for nofit ones. The GRIND gives faked 1-C fit rarely with very low $\bar{n}$ momentum because of the kinematical ambiguity for $\bar{n}$ momentum due to the small mass difference between proton and neutron, and the events in the region $P(\bar{n}) < 0.002$ GeV/c are those ones (The things are described in V-2-ii and the kinematical scheme is given in Figure 62.).

The stars satisfying the above two criteria are subdivided into pion multiplicities in Table 3. Ratios (branching ratios) of number of events, after MM^2 cut (see III-7-iii), for each multiplicity to the total (> 3 prongs) are given in Table 5 which was derived from Tokyo data.

We are unable to calculate the absolute cross sections for each multiplicity since the number and the track lengths for the incident antineutrons are not known if they do not give rise to a star within the fiducial volume. Therefore the cross sections are estimated on the assumption that the cross sections for $\bar{n}p$ annihilation with more than 3 charged prongs should be equal to that for $\bar{p}n$ annihilation (the charge symmetry).

The absolute cross sections for $\bar{p}n$ annihilation ($\geq$ 3 prongs) below 1 GeV/c had been measured in a deuterium bubble chamber experiment by Roma Trieste group.[18)] By fitting an empirical formula to the data to represent the cross section (see V-2-iii) the absolute cross section for $\bar{n}p$ annihilation is deduced as

$$\sigma^{ann}_{\bar{n}p} \;(\geq 3 \text{ prongs}) = 53.4 \pm 0.7 \text{ mb} \quad \text{at } 0.65 \text{ GeV/c}, \tag{IV-2}$$

which is used as a normalization. The cross sections for each pion multiplicity in $\bar{n}p$ annihilation are obtained multiplying $\sigma^{ann}_{\bar{n}p}$ ($\geq$ 3 prongs) by the branching ratios as given in Table 5.

IV-1-ii. Comparison of Branching Ratios for $\bar{n}p$ and $\bar{p}n$ Annihilations

The consequences from the processes of $\bar{n}p$ annihilation are expected as being symmetric to that of $\bar{p}n$ annihilation by the charge symmetry. On the other hand, data of $\bar{p}n$ annihilation are extracted from antiproton-deuteron reactions in which the neutron is not on-mass shell state, whereas those of $\bar{n}p$ annihilation are obtained as a consequence of reactions of a free antineutron on a free proton.

This fact may not guarantee the charge symmetric distribution for produced particles since $\bar{p}d$ reactions suffer more complex mechanism in their interactions.

The data of $\bar{p}n$ annihilation obtained by Roma Trieste group$^{18)}$ gives the average ratio

$$R_{\bar{p}n}(3\text{ prongs}):R_{\bar{p}n}(5\text{ prongs}) = 1 : 0.40\pm0.01$$

$$(\text{at } 9.498\text{-}0.591\text{ GeV/c}), \qquad (\text{IV-3})$$

and that obtained recently by Melbourne group is$^{21)}$

$$R_{\bar{p}n}(3\text{ prongs}) : R_{\bar{p}n}(5\text{ prongs}) = 1:0.36\pm0.03$$

$$(\text{at } 0.404\text{-}0.927\text{ GeV/c}). \qquad (\text{IV-4})$$

The ratio for $\bar{n}p$ annihilation at present experiment is

$$R_{\bar{n}p}(3\text{ prongs}) : R_{\bar{n}p}(5\text{ prong}) : R_{\bar{n}p}(7\text{ prong})$$
$$= 1 : .39\pm0.03 : .013\pm0.004$$

$$(\text{at } 0.65\text{ GeV/c}). \qquad (\text{IV-5})$$

The data by Melbourne group also give the ratios for pion multiplicities.$^{21)}$ The ratios for $\bar{p}n$ annihilation obtained by the two groups are summarized in Table 6 together with those for $\bar{n}p$ annihilation obtained here. Predictions for the branching ratios by Orfanidis-Rittenberg statistical model (see Appendix A) are given in Table 6 which will be discussed later.

IV-2. Resonance Production

IV-2-i. Method of Analysis

Antinucleon-nucleon annihilation is an abundant source of meson resonaces in general4), and this fact holds in $\bar{n}p$ annihilation processes too as mentioned in the following sections. In practice clear enhancements due to ρ or ω meson production over the phase space are observed in effective mass distributions in the present data.

The relative amount of resonance production for the multi-pion annihilation processes is determined by constructing a (model-independent) matrix element for the process and fitting its parameters by maximum likelihood techniques.23),114) The procedure is;

i) Resonance production is parametrized by the Breit-Wigner amplitude

$$R(m) = \Gamma\ /(m^2-m_R^2+im_R\Gamma\ ), \qquad \text{(IV-6)}$$

where m is the effective mass of the pion combination, m_R and Γ are the mass and effective width of the resonance under consideration for two-body resonances with broad width, the width Γ varies with energy roughly as

$$\Gamma \simeq \Gamma_0(q/q_0)^{2l+1}, \qquad \text{(IV-7)}$$

where Γ_0 is the central width, l is the orbital angular momentum of the partial wave of the decay, q is the 3-momentum of each member of the pair in their rest frame and q_0 is its value at resonance.115) This form (IV-7) is used for ρ , f and g mesons in the analysis. The true width of ω resonance is narrower than the measured one obtained in III-8, so that the measured width

(III-26) is used as an effective width. Resonance parameters used here are summarized in Table 7. The amplitude is constructed to hold the symmetric property under like-charge pion interchange required by Bose statistics. For example, labeling the $\pi^+\pi^+\pi^-\pi^o$ of four-pion final state as 1 2 3 4, and letting R(ij) be the Breit-Wigner amplitude evaluated for the ij pion combination with resonance R, the matrix elements for $\rho^-\pi^+\pi^+$ and $\rho^o\pi^+\pi^o$ are given respectively by

$$|M_{\rho^-\pi^+\pi^+}|^2 = |R_\rho(34)|^2 \quad , \qquad \text{(IV-8)}$$

$$|M_{\rho^o\pi^+\pi^o}|^2 = |R_\rho(13)|^2 + |R_\rho(23)|^2 . \qquad \text{(IV-9)}$$

ii) Assuming that the amplitudes of the separate processes add incoherently, the final matrix element for a certain final state is

$$|M|^2 = (1-\sum_i \alpha_i) + \sum_i \alpha_i \frac{|M_i|^2}{N_i} , \qquad \text{(IV-11)}$$

where the first term is due to nonresonant state and the α_i are the fractions of the resonance production to be determined from the likelihood fit. The normalization factor N_i is given by

$$N_i = \int |M_i|^2 \, d\rho \quad , \qquad \text{(IV-12)}$$

where $d\rho$ is the differential phase space, and the above integral is calculated by the Monte Carlo method using the CERN program FOWL.116),117) The method of event generation employed in the FOWL is explained in Appendix B.

iii) The likelihood function for r events of a certain final state is represented as

$$L = \sum_{j=1}^{r} |M|_j^2 \ , \qquad \text{(IV-13)}$$

and it should be maximized with respect to the parameters (percentages) α_i. To minimize -ln L, the CERN program MINUIT[118)] is used, which provides also an estimate of the errors the resulting values of the α_i's.

iv) Once the best-fit parameters α_i are obtained, events are generated according to the optimized matrix element, and then compared to the real events through the effective mass distributions.

IV-2-ii. $\bar{n}p \longrightarrow \pi^+\pi^+\pi^-$ Final State.

A sample of 90 events of the final state

$$\bar{n}p \longrightarrow \pi^+\pi^+\pi^- \ , \qquad \text{(IV-14)}$$

was used. Figure 17 gives the effective mass distributions for $(\pi^+\pi^-)$ and $(\pi^+\pi^+)$ combinations. Two bumps due to ρ^0 and f mesons over the phase space curve (indicated by dashed curves) are clearly observed in the $(\pi^+\pi^-)$ effective mass distribution. The matrix element is built including the following channels:

$$\text{a)}\ \bar{n}p \longrightarrow 2\pi^+\pi^- \text{(phase space)}, \qquad \text{(IV-15)}$$

$$\text{b)}\ \bar{n}p \longrightarrow \rho^0\pi^+ \ , \qquad \text{(IV-16)}$$

$$\text{c)}\ \bar{n}p \longrightarrow f\pi^+ \ , \qquad \text{(IV-17)}$$

$$\text{d)}\ \bar{n}p \longrightarrow g\pi^+ \ . \qquad \text{(IV-18)}$$

The normalization factor N_i (see eq. (IV-12)) for each channel of a)-d) was calculated by the FOWL as given below.

$$N_{a)} = 0.2987 \ , \qquad \text{(IV-19)}$$

$$N_{b)} = 0.5241\text{x}2 \ , \qquad \text{(IV-20)}$$

$$N_{c)} = 0.2149\text{x}2 \ , \qquad \text{(IV-21)}$$

$$N_{d)} = 0.06401\text{x}2 \ , \qquad \text{(IV-22)}$$

The percentage for each channel was determined by the maximum likelihood fit. The result is given in Table 8.

The percentages for the charge symmetric reaction of the above channels were measured between 0.4-0.95 GeV/c by the $\bar{p}d$ experiment (Melbourne group). The result is[146)]

$$\bar{p}n \longrightarrow \rho^0\pi^-: 33 \pm 2\ (\%), \qquad \text{(IV-23)}$$

$$\bar{p}n \longrightarrow f\pi^-: 51 \pm 2\ . \qquad \text{(IV-24)}$$

The percentages for the channels (IV-16),(IV-17) of the $\bar{n}p$ case are (see Table 8):

$$\rho^0\pi^+ : f\pi^+ = 40\pm12 : 47\pm12 \qquad \text{(IV-25)}$$

The above two results are in good agreement within the statistical errors. Solid curves in Figure 17 are the fitted ones.

IV-2-iii. $\bar{n}p \longrightarrow 2\pi^+\pi^-\pi^0$ Final State.

A sample of 529 events of the final state:

$$\bar{n}p \longrightarrow 2\pi^+\pi^-\pi^0\ , \qquad \text{(IV-25)}$$

was used. Figure 18 gives the effective mass distributions for various combinations of the reaction. Phase space distributions are given by dashed curves in this figure. Inspecting the Fig. 18, sizable production of ρ^0 and ρ^+ is observed. The matrix element is built including the following channels:

$$\text{a)}\quad \bar{n}p \longrightarrow 2\pi^+\pi^-\pi^0 \text{(phase space)}, \qquad \text{(IV-26)}$$

$$\text{b)}\quad \bar{n}p \longrightarrow \rho^0\pi^+\pi^0, \qquad \text{(IV-27)}$$

$$\text{c)}\quad \bar{n}p \longrightarrow \rho^+\pi^+\pi^-, \qquad \text{(IV-28)}$$

$$\text{d)}\quad \bar{n}p \longrightarrow \rho^-\pi^+\pi^+, \qquad \text{(IV-29)}$$

$$\text{e)}\quad \bar{n}p \longrightarrow f\pi^+\pi^0\ , \qquad \text{(IV-30)}$$

$$\text{f)}\quad \bar{n}p \longrightarrow \rho^+\rho^0\ , \qquad \text{(IV-31)}$$

$$\text{g)}\quad \bar{n}p \longrightarrow \omega\pi^+\ , \qquad \text{(IV-32)}$$

The normalization factor N_i (see eq. (IV-12) for each of the channels (IV-26)-(IV-31) was calculated as below.

$$N_{a)} = 0.06512, \tag{IV-33}$$

$$N_{b)} = 0.1800\text{x}2, \tag{IV-34}$$

$$N_{c)} = 0.1800\text{x}2, \tag{IV-35}$$

$$N_{d)} = 0.1800, \tag{IV-36}$$

$$N_{e)} = 0.02237\text{x}2, \tag{IV-37}$$

$$N_{f)} = 0.5496\text{x}2, \tag{IV-38}$$

$$N_{g)} = 0.03589\text{x}2. \tag{IV-39}$$

The percentage for each channel was determined by the maximum likelihood method. The result is given in Table 8.

Comparison of the result with the $\bar{p}n$ data is made as follows. The percentages of resonance productions for the charge symmetric reaction of the above channels were also estimated between 0.4-0.95 GeV/c.146) The result is

$$\bar{p}n \longrightarrow 2\pi^-\pi^+\pi^o;\ 34\ (\%), \tag{IV-40}$$

$$\bar{p}n \longrightarrow \rho^o\pi^-\pi^o;\ 18\ , \tag{IV-41}$$

$$\bar{p}n \longrightarrow \rho^-\pi^-\pi^+;\ 16\ , \tag{IV-42}$$

$$\bar{p}n \longrightarrow \rho^+\pi^-\pi^-;\ 12\ , \tag{IV-43}$$

$$\bar{p}n \longrightarrow f\pi^-\pi^o;\ 1\ , \tag{IV-44}$$

$$\bar{p}n \longrightarrow \rho^+\rho^o;\ 4\ , \tag{IV-45}$$

$$\bar{p}n \longrightarrow \omega\pi^-;\ 5\ . \tag{IV-46}$$

The percentages for the channels (IV-26)-(IV-32), denoted by a)-g) respectively, of the $\bar{n}p$ case are (see Table 8):

$$\text{a)}:\text{b)}:\text{c)}:\text{d)}:\text{e)}:\text{f)}:\text{g)}$$

$$= \underset{34\pm7}{\cancel{33\pm9}} : \underset{12\pm7}{\cancel{20\pm0}} : \underset{16\pm7}{\cancel{27\pm0}} : \underset{10\pm4}{\cancel{7\pm4}} : \underset{5\pm3}{\cancel{3\pm3}} : \underset{20\pm6}{\cancel{0}} : \underset{4\pm1}{\cancel{0}} \tag{IV-47}$$

The values for the $\bar{p}n$ annihilation were those of rough estimates146), while those of the $\bar{n}p$ annihilation may contain considerable background. Therefore quantitative discussion between them would be rather difficult. Effective mass distributions predicted by the fit, thus obtained, are given in Figure 18 by solid curves together with the phase space distributions (dashed curves).

IV-2-iv. $\bar{n}p \longrightarrow 3\pi^+2\pi^-$ Final State.

A sample of 188 events of the final state

$$\bar{n}p \longrightarrow 3\pi^+2\pi^- , \qquad \text{(IV-48)}$$

was obtained. Figure 19 gives the effective mass distributions for various combinations of the channel. The maximum likelihood fit for resonance production in this final state is not carried out yet. Comparing the effective mass distributions with the prediction by phase space (dashed curves in Figure 19), characteristic features are observed as below.

A salient feature observable in Fig. 19 is an identification of the existence of a clear enhancement in the $(\pi^+\pi^-)$ effective mass distribution at

$$M(\pi^+\pi^-) \sim 700 \text{ MeV}/c^2 . \qquad \text{(IV-49)}$$

From the data for $2\pi^+\pi^-$ or $2\pi^+\pi^-\pi^0$ channels, analyzed in IV-2-ii and iii respectively, the ρ meson production in

$$\bar{n}p \longrightarrow \rho^0\pi^+\pi^+\pi^- , \qquad \text{(IV-50)}$$

or

$$\bar{n}p \longrightarrow \rho^0\rho^0\pi^+ , \qquad \text{(IV-51)}$$

is expected to give a significant contribution, but a bump at the position of ρ meson is not observed.

The shift of the ρ Breit-Wigner peak toward lower mass is discussed by Fields and Singer[145). According to their opinion the annihilation proceeds through the formation and subsequent chain decay of a single fireball. In this case the shift toward lower mass takes place when energy conservation forbits the emmision of the higher mass part of the ρ Breit-Wigner.

A branching ratio for to resonance-like enhancement at ∿ 700 MeV/c^2 was estimated by counting the numbers of events in the peak above a dot-dashed curves in Figure 19(a), which was drawn by hand refering the phase-space curve (dashed curve in Figure 19(a)). The result is

$$\bar{n}p \longrightarrow M(700)\pi^+\pi^+\pi^- \ ; \sim 100\ \% \qquad \text{(IV-52)}$$

where M(700) represents the events in the resonance-like enhancement. It should be emphasized that the result is a rough estimate.

Another interesting feature appears in the $(\pi^+\pi^+\pi^-\pi^-)$ effective mass distribution giving significant peaks at

$$M(\pi^+\pi^+\pi^-\pi^-) \sim 1450\ \text{MeV}/c^2\ , \qquad \text{(IV-53)}$$

and at

$$M(\pi^+\pi^+\pi^-\pi^-) \sim 1680\ \text{MeV}/c^2\ . \qquad \text{(IV-54)}$$

The former may correspond to that observed by Bettini et al.[12) in the $(\pi^+\pi^+\pi^-\pi^-)$ effective mass distribution of $2\pi^+3\pi^-$ state in the $\bar{p}d$ experiment. The mass and width of the enhancement determined by Bettini et al. are 1410 MeV/c^2 and 90 MeV/c^2 respectively. The position of the latter is consistent with g meson whose mass and width established in the Particle Data Group[112) are 1686 and 180 MeV/c^2 respectively.

Significant deviations of $(\pi^+\pi^+\pi^-)$ and $(\pi^+\pi^-\pi^-)$ effective mass distributions from the predictions by phase space (see Figure 19 (b),(c)) are observed. It seems that these deviations are not caused by statistics, and we cannot interpret this fact at present.

IV-2-v. $\bar{n}p \longrightarrow \pi^+\pi^+\pi^+\pi^-\pi^-\pi^0$ Final State

309 events for the final state

$$\bar{n}p \longrightarrow 3\pi^+2\pi^-\pi^0 \ , \qquad \text{(IV-55)}$$

were obtained. Figure 20 gives the effective mass distributions for various combinations in this channel. The distributions are reproduced by phase space distributions (dashed curves in Fig. 20) in general except for the $(\pi^+\pi^-\pi^0)$ combinations which shows a sharp peak due to the ω meson production. The ratio of ω $(\longrightarrow \pi^+\pi^-\pi^0)$ production to all 6π events was estimated by counting the number of events in the peak above the phase-space curve (a dashed curve in Figure 20(d)) as

$$\bar{n}p \longrightarrow \omega 2\pi^+\pi^- \ ; \ 45\ \% \qquad \text{(IV-56)}$$

IV-3. ρ-ω Interference

IV-3-i. G-Parity and $\bar{p}n$ System

The ρ-ω interference effect in $(\pi^+\pi^-)$ mass spectra was discussed theoretically by several authors[120),121)], and it was observed in $\bar{p}p$ annihilation experiments.[122),123)] Opat[124)] suggested that this effect could be observable in $\bar{p}n$ annihilation experiment by comparing $(\pi^+\pi^-)$ mass spectra in forward region with that in backward region; the ρ-ω interference causes different $(\pi^+\pi^-)$ mass spectra in forward and in backward directions.

According to Opat's argument, $\bar{p}n$ annihilation is represented as follows.

The operator G which has the following mapping:

$$G|\bar{p}(a),n(b)\rangle = |\bar{p}(b),n(a)\rangle \quad \text{and}$$

$$G|m\pi\rangle = \eta|m\pi\rangle , \qquad \text{(IV-57)}$$

is the G-parity operator

$$G = C \exp i\pi I_2,$$

where a,b denote the momentum-plus-helicity labels $(\vec{p},h)$, $|m\pi\rangle$ the state of m pions and $\eta = (-1)^m$, C denotes the particle-antiparticle conjugation operator, and I_2, the 2nd component of isospin. The scattering matrix element between an initial $\bar{p}n$ state and the final state f is represented as

$$\begin{aligned}\langle f|S|\bar{p}(a),n(b)\rangle &= \langle f|G^+GS|\bar{p}(a),n(b)\rangle \quad \text{as G is unitary,}\\ &= \langle f|G^+SG|\bar{p}(a),n(b)\rangle \quad \text{as G is conserved,}\\ &= \langle f|G^+S|\bar{p}(b),n(a)\rangle \quad \text{by eq. (IV-57)}\end{aligned}$$

If the final state $|f\rangle$ in the above equation is an eigenstate of G (e. g. a final state consisted of only pions), then it follows

$$\langle f|S|\bar{p}(a),n(b)\rangle = \eta_f\langle f|S|\bar{p}(b),n(a)\rangle ,$$

whence, for any differential cross section $d\sigma$,

$$d\sigma\ (a,b) = d\sigma(b,a).$$

This equation means that if G-parity is conserved, angular distributions of non-strange mesons show beam-target reversal symmetry (i.e. forward-backward symmetry).

Consider the interference between two reactions

$$\bar{p}n \longrightarrow \rho^{o}X,\ \rho^{o} \longrightarrow \pi^{+}\pi^{-}. \qquad \text{(IV-58)}$$

$$\bar{p}n \longrightarrow \omega X\ ,\ \ \omega \longrightarrow \pi^{+}\pi^{-},\ \text{(X; anything)}. \qquad \text{(IV-59)}$$

The ω decay into two pions is mediated by electromagnetic interactions, and is G-parity violating. The overall amplitude for the reactions (IV-58),(IV-59) is given by

$$\begin{aligned} A(a,b) &= T(\pi^{+}\pi^{-};\rho^{o})T(\rho^{o}X;\bar{p}(a)n(b)) \\ &\quad + T(\pi^{+}\pi^{-};\omega)T(\omega X;\bar{p}(a)n(b)). \qquad \text{(IV-60)}\end{aligned}$$

Each term in eq. (IV-60) is the product of ρ(or ω) production and decay amplitudes (in selfevident notations).

Let assume X be an eigen-state of G for simplicity. Then remembering that $\eta_{\rho}=1$, $\eta_{\omega}=-1$ it follows that

$$\begin{aligned} A(b,a) &= \eta_{X}(T(\pi^{+}\pi^{-};\rho^{o})T(\rho^{o}X;\bar{p}(a)n(b)) \\ &\quad -T(\pi^{+}\pi^{-};\omega)T(\omega X;\bar{p}(a)n(b))). \qquad \text{(IV-61)}\end{aligned}$$

A comparison of eq. (IV-60) with (IV-61) shows that if the ρ-ω interference is constructive in the forward direction, it will be destructive in the backward direction (and vice versa). So integrated over all directions, the ρ-ω interference should vanish automatically. The amplitude $T(\pi^{+}\pi^{-};\omega)$, being electromagnetic in origin, is small, so that in practice only ρ term and the ρ-ω interference term should be seen, if any. D.E. Caro et al.146) tried to find ρ-ω interference effects in $\bar{p}n$ annihilation between

0.40-0.92 GeV/c. They found that; plotting the difference between the numbers of 4π events with forward dipions (F) and with backward dipions (B) in c.m.s. as a function of $m(\pi^+\pi^-)$, such an effect is not observed. However, dividing each hemisphere into two parts by a cut at $|\cos\theta| = 0.5$, where θ is an angle between the incident $\bar{p}$ and the dipion system, the same plot showed anomalies at the position of the ω mass with 2 standard deviations ($(F-B) < 0$ for the events of $|\cos\theta| > 0.5$ and $(F-B) > 0$ for those of $|\cos\theta| < 0.5$).

IV-3-ii. Dipion Mass Spectra of $\bar{n}p$ Annihilation

The discussion in IV-3-i for $\bar{p}n$ system is also applicable to $\bar{n}p$ system without any change since the relation

$$G|\bar{n}(a),p(b)\rangle = |\bar{n}(b),p(a)\rangle \, , \qquad \text{(IV-62)}$$

holds for $\bar{n}p$ system.

To search for the ρ-ω interference effect in $\bar{n}p$ annihilation, effective mass distributions for dipion system are taken for forward region (angle between incident $\bar{n}$ and dipion system emitted is less than 90° in the production c.m.) and for backward one separately. Figure 21 shows the $(\pi^+\pi^-)$ mass spectra of $(\pi^+\pi^-)$ system in the forward region (solid lines) and in the backward region (dashed lines) in the production c.m.s. for each of the final states. Striking features observed in this figure are:

Feature i) For $2\pi^+\pi^-\pi^0$ samples the enhancement at the position of ω mass in the forward region, and disappearance of it at the same position in the backward region are observed clearly.

Feature ii) For $3\pi^+2\pi^-$ samples the above effect is less conspicuous, and for $2\pi^+\pi^-$ and $3\pi^+2\pi^-\pi^0$ cases statistics is too poor to draw a definite conclusion.

Figure 22 shows the same distributions for $(\pi^+\pi^0)$ and $(\pi^+\pi^+)$ mass spectra of $2\pi^+\pi^-\pi^0$ samples. Since these combinations do not include the G-parity violation process, $\omega \longrightarrow \pi^+\pi^-$, the mass spectra should show forward-backward symmetric distributions. In fact, this point is fulfilled within the statistical errors as seen in Figure 22. We deduced that Feature i) is of high statistical significance with 99.7 % confidence level (3 standard deviations).

To study more details for the structure appearing on the mass spectra of $2\pi^+\pi^-\pi^0$ samples, a distribution of the production angle $\cos\theta$ of $(\pi^+\pi^-)$ system with respect to the incident $\bar{n}$ in c. m. s. was taken as given in Figure 23. The samples in Figure 23 were divided into two parts by a cut at $|\cos\theta| = 0.5$, and the $(\pi^+\pi^-)$ mass spectra for each part were plotted with the same way as done above. Plots, thus obtained for samples of $|\cos\theta| > 0.5$ and for those of $|\cos\theta| < 0.5$ separately, are given in Figure 24. It seems from this figure that the structure at the ω position is more pronounced for the samples of $|\cos\theta| > 0.5$ than for those of $|\cos\theta| < 0.5$. Change of sign of the quantity (F-B) at the ω position between the two parts, which was observed in the $\bar{p}n$ case as mentioned in Section IV-3-i. is not probable in the present case.

IV-3-iii. Description of the Mass Spectra

We have tried to reproduce the Feature i) by a formula of the type ' $\rho + \omega$ + ρ-ω interference + phase space ' as follows. Taking eqs. (IV-60),(IV-61) into consideration, we used the formalism of W. W. M. Allison et al,[122] and fitted the form:

$$dN/dm = dN/dm(\text{forward}) + dN/dm(\text{backward}), \qquad \text{(IV-63)}$$

to the $(\pi^+\pi^-)$ histograms in the forward region and in the backward region simultaneously. Each of the terms in eq. (IV-63) is:

$$dN/dm(\text{forward}) = A_\omega^2 \; |BW_\omega|^2 + A_\rho^2 \; |BW_\rho|^2 + 2\alpha A_\omega A_\rho \mathrm{Re}(e^{i\psi} BW_\omega BW_\rho^*) + B \cdot PS ,$$

$$dN/dm(\text{backward}) = A_\omega^2 \; |BW_\omega|^2 + A_\rho^2 \; |BW_\rho|^2 - 2\alpha A_\omega A_\rho \mathrm{Re}(e^{i\psi} BW_\omega BW_\rho^*) + B \cdot PS ,$$

where N and m are a number of combinations and $(\pi^+\pi^-)$ mass respectively, and PS is a phase-space factor normalized to 1. $BW\omega$ and $BW\rho$ are Breit-Wigner amplitudes for the ω and ρ :

$$BW = \sqrt{\Gamma}_\omega / ((m_\omega^2 - m^2) - i m_\omega \Gamma_\omega) \; , \; BW = \sqrt{\Gamma}_\rho / ((m_\rho^2 - m^2) - i m_\rho \Gamma_\rho)$$

where values m_ω=784, Γ_ω=10, m_ρ=770 and Γ_o=146 in MeV/c^2 were used, and Γ_ρ is the mass-dependent width for the ρ : $\Gamma_\rho = \Gamma_o (m_\rho / m)(q/q_\rho)^3$. Parameters to be obtained by fitting are magnitude of the ω amplitude:A_ω, magnitude of the ρ amplitude:A_ρ, coherence factor: α, relative phase between ω and ρ amplitudes:ψ, measure for phase-space factor:B. Results are:

$$A_\omega = 0.35 \pm 0.03, \; A_\rho = 0.95 \pm 0.19, \alpha = 0.75 \pm 0.33, \; \psi = 1.23 \pm 1.55,$$
$$B = 420 \pm 30 \quad \text{with} \quad \chi^2 = 86 \; (n_D = 61). \qquad \text{(IV-64)}$$

Fitted curves with the above values of the parameters are given in Figure 25 by solid curves for $(\pi^+\pi^-)$ mass spectra of $2\pi^+\pi^-\pi^0$ samples in the forward region (Fig.25(a)) and in the backward region (Fig.25(b)).

To check the influence due to the contaminations of multineutrals over the structure appearing on the mass spectra of $2\pi^+\pi^-\pi^0$ samples, we have done the following procedure:

i) We assume that the above-mentioned multineutrals are mostly due to $2\pi^+\pi^- 2\pi^0$events and furthermore $(\pi^+\pi^-)$ mass spectra of such events show the same behavior as those of $3\pi^+2\pi^-$ samples (see Figure 21(c)).

ii) We take away 40 % of combinations from the mass spectra of the forward (backward) region of $2\pi^+\pi^-\pi^0$ samples with the shape of $(\pi^+\pi^-)$ mass spectra in the forward (backward) region of $3\pi^+2\pi^-$ samples.

iii) For the spectra of $2\pi^+\pi^-\pi^0$ sapmles, thus obtained, we try fitting the form of eq. (IV-63).

Results of such fit are; $A_\omega=0.38\pm0.13$, $A_\rho=0.81\pm0.08$, $\alpha=0.75\pm0.33$,$\psi=1.26\pm0.84$, $B=173.24\pm0.04$ with $\chi^2=175(n_D=61)$, which are not far from those in (IV-64) in essence. Figure 26 gives curves obtained by this fit. The method, employed here, may be unable to dermine the values of A_ω, α and ψ uniquely by the following reason. The structure at the ω mass is reproduced by A_ω, α and ψ seentially, whereas we have about two data points for it. To determine the value of the phase ψ, data points giving the spectra within ω width Γ_ω should be provided, since a structure within Γ_ω is represented by two terms proportional to $A_\omega\alpha\sin\psi$ and $A_\omega\alpha\cos\psi$ which show different behavior as a function of the $(\pi^+\pi^-)$ mass.

IV-4. CŁA Model and $\bar{n}p$ Annihilation

IV-4-i. Description of the Model

a) Amplitude of Multiperipheral Graph

The CŁA model modified by Vaissiere[43),44)] in order to include the resonance production in $\bar{p}p$ annihilation is applied to $\bar{n}p$ annihilation as follows. Let's take a multiperipheral diagram with n particles (pions or resonances) indexed upward from 1 to n as shown in Figure 1(b),

each pair is characterized by 2 invariants;

a sub energy $s_i = (p_i + p_{i+1})^2 - (m_i + m_{i+1})^2$, (IV-65)

the quadri-momentum transfer squared to the nucleon

$$t_i = (p_P - \sum_{j=1}^{i} p_j)^2 \ , \qquad \text{(IV-66)}$$

where p_i, m_i are the quadri-momentum and the mass of the i-th particle. The formula for the amplitude of the graph k is

$$A_k = F \sum_i g(s_i) \left(\frac{s_i + c}{a}\right)^{\alpha_o} \left(\frac{s_i + b_i}{b_i}\right)^{e(t_i)} \ , \qquad \text{(IV-67)}$$

which is slightly different from the usual formula of the original one by Chan Hong-Mo et al[85] (see eq.(II-16)). The meaning of most parameters is unchanged,

a is an energy scale factor which limits the contribution of low- and high-energy region.

b_i is related to the residue of the pole exchanged between particles i and i+1. In the model by Vaissiere an assumption was made for the value of b_i.

$e(t_i)$ describes the t_i dependence of the amplitude. This function is equivalent to βt_i if t_i is small(>0). On the other hand if one neglects the exchange of Δ^{++} trajectory, it is imposible to have a significant amplitude for large negative values of t_i (emission of pions backward) unless the value of parameter b_i is taken large (around 3 $(\mathrm{GeV})^2$). In this model, putting a small value to b_i, βt_i is replaced by the function

$$e(t) = \exp(bt-\gamma t^2) -1 \text{ for } t<0. \qquad \text{(IV-68)}$$

α_0 and β are the intercept and slope of the exchanged nucleon trajectoty respectively.

$g_i(s_i)$ is the coupling constant depending on the nature of particles i, i+1 and of their relative energy s_i.

F is the factor directly related to coupling constants at the external vertices.

The above-mentioned parameters, used in the fit to $\bar{n}p$ annihilation data, are fixed by the values of Vaissiere's usage as given in Table 9(a).

b) Coupling Constants

In the high-energy limit the coupling constant g_i is connected to the individual coupling constants G_i, G_{i+1} of a meson through the nucleon trajectory by

$$g_i = \sqrt{G_i G_{i+1}} \ . \qquad \text{(IV-69)}$$

This expression determines the overall coupling constant which is a product of all G_i in the very high-energy limit (all the s_i>>a) as described below.

It is assumed that the vertex constant G decreases with mass m of meson. This hypothesis is supported[44)] by the fact that; i) primary pions are produced at much higher rate than resonances, ii) when the mass increases resonances are more and more difficult to observe. A suitable expression for G is the exponential decrease

$$G = H\, D_{I,I_Z} \exp(-m/M_o) , \tag{IV-70}$$

where D_{I,I_Z} is the Clebsch-Gordan coefficient connecting the isosopin state I, I_Z of the meson and that of coupled nucleon-antinucleon pair, M_o is the nucleon mass, and H, a parameter to be adjusted.

In the low-energy limit the amplitude for nucleon-antinucleon state giving two mesons with no relative kinetic energy is given by c_i. A crude dependence on the nature of the two consecutive mesons is assumed by putting

$$c_i = D^{'} \lambda^n c , \tag{IV-71}$$

where $D^{'}$ is the isospin amplitude for the process

$$\bar{N}N \longrightarrow \text{two consecutive mesons.} \tag{IV-72}$$

c is a numerical factor which gives less weight to pairs including 0 or 1 pion. λ is smaller than 1 and n is the number of mesons other than pions.

The formulation for $g_i(s_i)$ is

$$g_i(s_i) = \frac{g_i s_i + c_i}{s_i + a} . \tag{IV-73}$$

All the functions $g_i(s_i)$ are described with four parameters H, M_o, λ, c which are given in Table 9(a), and numerical values of g_i and c_i are in Table 9(b).

The factor F is introduced to give the similar weight to the external coupling as to the internal ones;

$$F = \sqrt{G_1 G_n} . \tag{IV-74}$$

c) Generation of Weighted Events

Since it is known that the Δ^{++} trajectory is weaker in coupling strength than the nucleon trajectory by about one order of magnitude[125)], it is neglected.Then in the first approximation, pions coupling to external vertices must be π^o (coupling $p \longrightarrow p\pi^o$) or π^+ (coupling $p \longrightarrow n\pi^+$), having the baryon's charge. Therefore one can see that the following rules must be held in drawing the contributing diagrams; i) the $\pi\pm$ must alternate,ii) the π^o may occupy any position, iii) the charged pions closest to the external vertices must have the charge of the incoming baryon. These rules must be held in the case of resonance couplings too.

Since the CŁA model gives no information about the phase, the squared matrix element for a given intermediate channel v, $|M_v|^2$, is obtained by adding the squares of the amplitudes of all possible diagrams,

$$|M_v|^2 = \sum_k |A_k|^2 . \qquad \text{(IV-75)}$$

The effective weight P_v of the channel is, according to the Fermi rule, the product

$$P_v = |M_v|^2 \, PS_v , \qquad \text{(IV-76)}$$

where PS_v is the statistical phase space relative to the channel. The overall weight is obtained by summing over all channels:

$$W = \sum_v P_v . \qquad \text{(IV-77)}$$

For resonance production, normalized Breit-Wigner function

$$BW(m,m_R,\Gamma) = \frac{1}{\pi} \frac{1}{(m-m_R)^2+\Gamma^2/4} \qquad \text{(IV-78)}$$

is used at each diagram. The parameters of resonances considered here are given in Table 9(c).

All calculations are carried out by using the Monte Carlo program FOWL.116),117) Being given the set of parameters, the total weight is calculated for each generated event. All the distributions obtained by the FOWL are histogramed with the same cuts as the experimental results. In Appendix B the procedure for phase-space calcultion by the FOWL is described in detail.

IV-4-ii. Application of the Model to $\bar{n}p$ Annihilation

With the above-mentioned method, events of $\bar{n}p$ annihilation are generated which are weighted by the squared amplitude of the CLA model. Only 3- and 4-pion final states are considered here, since it is expected that a multi-peripheral component decreases with increasing the multiplicity and furthermore a number of contributing graphs increases rapidly with increasing the multiplicity (for example $3\pi^+2\pi^-\pi^0$ state is described by 65 graphs under the consideration of ρ and ω mesons). Comparisons of the model with the experimental data is focussed on three subjects; i) effective mass distribution and resonance production, ii) angular correlations, iii) single-particle distribution.

a) $2\pi^+\pi^-$ Final State

Inspecting the $(\pi^+\pi^-)$ effective mass distribution (see Figure 29)), the following channels are included in the calculation of the matrix elements;

$$\bar{n}p \longrightarrow 2\pi^+\pi^- , \qquad \text{(IV-78)}$$

$$\bar{n}p \longrightarrow \rho^0\pi^+ , \qquad \text{(IV-79)}$$

$$\bar{n}p \longrightarrow f\pi^+ , \qquad \text{(IV-80)}$$

$$\bar{n}p \longrightarrow g\pi^+ . \qquad \text{(IV-81)}$$

All graphs contributing are shown in Figure 27. The weight for each event is calculated by the incoherent sum of the squared amplitude for each graph in which the effect due to Bose statistics is taken into account. The predictions are given for the effective mass distributions (Figure 29), opening angle distributions between two outgoing pions (Figure 30) by solid curves, and for single-particle distributions (cos θ_{cm}: Fig. 33, P_T: Fig. 34, $|P|$: Fig. 35) by dashed curves.

In the $2\pi^+\pi^-$ case, statistics is poor, hence it is difficult to make a quantitative discussion. It seems that the resonance productions are well represented qualitatively by this model.

b) $2\pi^+\pi^-\pi^0$ Final State

The effective mass distributions (Figure 31) show a strongly produced ρ, while f and ω are produced weakly. The following channels are included in the calculation of the weight

$$\bar{n}p \longrightarrow 2\pi^+\pi^-\pi^0, \qquad \text{(IV-82)}$$

$$\bar{n}p \longrightarrow \rho^+\pi^+\pi^-, \qquad \text{(IV-83)}$$

$$\bar{n}p \longrightarrow \rho^0\pi^+\pi^0, \qquad \text{(IV-84)}$$

$$\bar{n}p \longrightarrow \rho^-2\pi^+, \qquad \text{(IV-85)}$$

$$\bar{n}p \longrightarrow \rho^+\rho^0, \qquad \text{(IV-86)}$$

$$\bar{n}p \longrightarrow f\pi^+\pi^0, \qquad \text{(IV-87)}$$

$$\bar{n}p \longrightarrow f\rho^+, \qquad \text{(IV-88)}$$

$$\bar{n}p \longrightarrow \omega\pi^+. \qquad \text{(IV-89)}$$

All diagrams for the above channels are given in Figure 28. In calculating the weight, the width of ω is kept at the measured value instead of that given in the Particle Data Group.

The effect due to Bose statistics is also taken into account. 36,000 events were generated by the FOWL with the weight for the diagrams in the Fig. 28. The predictions are given for the effective mass distributions (Figure 31) and opening angles (Figure 32) by solid curves, and for single-particle distributions (Figures 33, 34, 35) by dashed curves.

The data not only for the single-particle distributions but also for the two-particle correlations (effective mass and opening angle) are well reproduced by this model. This fact may throw light on the production mechanism of resonances in annihilation processes.

IV-5. Single Particle Distribution of Pions

IV-5-i. Production Angle of Pions in CM System.

The distributions of the angles between (π^+ or π^- or π^0) and the incident antineutron in the production center-of-mass(CM) are given in Figure 33 for $2\pi^+\pi^-$, $2\pi^+\pi^-\pi^0$, $3\pi^+ 2\pi^-$, and $3\pi^+ 2\pi^-\pi^0$ final states. The solid curve in each figure shows the phase space distribution obtained by the Monte Carlo program FOWL. For the $2\pi^+\pi^-$ and $2\pi^+\pi^-\pi^0$ final states, the predictions by the CŁA model (see IV-4) are also given in these figures (dashed curves), where the resonance productions are taken into account. In these Figs. both collimation effect (tendency of the pions to be emmited at small angles) and asymmetry effect (tendency of the pions to follow the line of flight of the baryon with the same charge) are very weak. Table 10 contains the collimation and asymmetry coefficients defined respectively as

$$C = (P-E)/(P+E), \qquad \text{(IV-90)}$$

$$A = (F-B)/(F+B), \qquad \text{(IV-91)}$$

where P is the number of pions with $|\cos\theta| > 0.5$, E the number of pions with $|\cos\theta| < 0.5$, F the number of pions with $\cos\theta > 0$, B the number of pions with $\cos\theta < 0$ (θ being the angle between the (π^+,π^-,π^0) and the antineutron in the production CM).

Small values of C's and A's, thus obtained, imply that the $\bar{n}p$ annihilation at the present energy takes place mostly through statistical mechanism.

Opat[124)] suggested that, if G-parity conserves in $\bar{n}p$ annihilation each distribution of production angles for π^+,π^- and π^0 shows forward-backward symmetry in the production CM. It is explained in IV-3 in detail. The coefficients A for π^+ and π^- in Table 10 do not show any significant deviation from zero, while those for π^0 are far from zero (see Table 10 too).

Such asymmetry for neutral pions was also observed in $\bar{p}n$ annihilation below 1 GeV/c.146) These asymmetries may be caused by contamination due to multi-π^0 final states.

IV-5-ii. Momentum Spectra

Figure 34 gives spectra of the transverse momentum of pions and spectra of absolute values of the momentum are given in Figure 35. The solid and dashed curves in each figure give the distributions by phase space and those predicted by the CŁA model43),44) respectively. The spectra for π^+, π^- and π^0 show the same behavior and they can be well described by a statistical picture.

IV-6. Bose-Einstein Statistics

IV-6-i. Experimental Data

Figures 42 through 45 show the distributions of the dipion angles in the production CM for different pion charge combinations in $2\pi^+\pi^-$, $2\pi^+\pi^-\pi^0$, $3\pi^+ 2\pi^-$, $3\pi^+2\pi^-\pi^0$ final states. Significant deviations of the distributions for like-charge pair from the distributions of phase space (dashed curves) are evident, while those for unlike-charge pair are rather close to the phase space ones. This effect, the distributions of the opening angles of like-charge pair are different from those of unlike-charge one, was first observed by Goldhaber et al.$^{126)}$ (GGLP effect) and was confirmed by later experiments in $\bar{p}p$ annihilation into pions.

To measure the deviations from the phase space predictions, a correlation parameter γ is defined as

$$\gamma = \frac{\text{number of pion pairs with opening angle}>90°}{\text{"} \qquad\qquad\qquad\qquad <90°} \qquad \text{(IV-92)}$$

Values of γ's for various charge pairs of pions are tabulated in Table 11 together with the predictions by phase space.

IV-6-ii. Weighting Function for Bose-Einstein Statistics

A possible explanation for the GGLP effect is to introduce Bose-Einstein statistics into the annihilation process as suggested originally by Goldhaber et al.,$^{46)}$ where phase space distributions are modified by a correlation function (Bose-Einstein symmetrization function) for like-charge pions as follows.

The correlation function for two like-charge pions (1,2) is$^{46)}$

$$\psi(1,2)=1+e^{-\lambda\ x_{12}}\ , \qquad \text{(IV-93)}$$

where

$$x_{12}=(P_1-P_2)^2-(\omega_1-\omega_2)^2\ , \qquad \text{(IV-94)}$$

and that for three like-charge pions (1,2,3) is given by[127)]

$$\Psi(1,2,3)=1+e^{-\lambda\Delta P^2_{12}}+e^{-\lambda\Delta P^2_{13}}+e^{-\lambda\Delta P^2_{23}}+ 2e^{-1/2\lambda(\Delta P^2_{12}+\Delta P^2_{13}+\Delta P^2_{23})}\ , \qquad \text{(IV-95)}$$

where

$$\Delta P^2_{ij} = |P_i-P_j|^2\ . \qquad \text{(IV-96)}$$

In eqs. (IV-93)-(IV-96), P_i and ω_i are the momentum vector and energy of the i-th pion in the CM system respectively, and λ is interpreted as representing the size of an interaction volume. The factor λ is defined as[26)]

$$\lambda=(\rho/2.15)^2 = 6.15(\mathrm{GeV})^{-2}$$

where 3/4 $\hbar/m_\pi c$(3/4 pion Compton wave length) was taken as the radius ρ of the interaction volume. When the pions 1,2 and 3 have the same sign of charge and the pions 4,5 have the opposite sign, for example, the overall correlation function is $\psi(1,2,3)\mathrm{x}\psi(4,5)$.

IV-6-iii. Description of the Data

The phase space distributions for n̄p annihilation are modified by putting the weight (correlation function) due to the Bose-Einstein statistics. Events were generated with the weight for each final state of the n̄p annihilation using the FOWL. The solid curve in each figure of 42-45 is that obtained by this method. The correlation coefficients γ predicted by the Bose-Einstein statistics are given in Table 11.

Figure 46 shows the values of γ plotted against the total charge Q of the pion pair obtained for each final state, in which the dashed line and the solid one represent the predictions by phase space and by the Bose-Einstein statistics respectively (the predictions are connected by the lines in this figure to guide eyes). One can see from Figs. 42-46 that the introduction of the Bose-Einstein statistics improves the description of the data in general. In this analysis, resonance productions were not taken into account which might cause the discrepancies as seen in Figs.42-46 for non-exotic channels.

IV-6-iv. Duality and Multiparticle Final State

Rubinstein had given qualitative predictions such that; in all processes where there are two-body exotic channels and none or at most one neutral pion, threshold-like enhancement in the exotic channels ($\pi^+\pi^+$, or $\pi^-\pi^-$ combination in the present case) and resonance-like peaks near the prominent resonances should appear in the effective mass distributions.30) According to Rubinstein's opinion, these effects are caused by duality mechanism, and should disappear as a function of increasing the number of neutral pions, which increases a number of amplitudes contributing. The above-mentioned threshold-like enhancement is analogous to the GGLP effect since the effective mass m and opening angle θ of a pair of pions (1,2) are related by

$$m = \sqrt{(\omega_1+\omega_2)^2-P_1^2-P_2^2-2P_1P_2\cos\theta}\ , \qquad \text{(IV-97)}$$

where ω_1,ω_2 and P_1, P_2 are energies and absolute values of the momenta respectively. The effect should appear more strongly in

$2\pi^+\pi^-$ and $3\pi^+2\pi^-$ final states of $\bar{n}p$ annihilation since these states are fully charged modes. The effective mass distributions for exotic combinations of the various final states are given in Figs. 36-41 together with the predictions by phase space (dashed curve) and Bose-Einstein statistics (solid curve). Systematic shifts of the effective mass to low-mass region with respect to the phase space are observable in these figures in common. But it is not possible to make quantitative discussion on the Rubinstein's standpoint for the present data, because the statistics is not enough and furthermore combinational background may mask the underlying dynamics with increasing multiplicity.

IV-7. Analysis Using Multiparticle Variables

IV-7-i. Choice of Variables

The search for kinematical variables which would be sensitive to the dynamics of multiparticle production is important to investigate strong interactions. Alexander et al.[45)] had constructed multiparticle variables in such a way as to be more sensitive to the expected underlying dynamical picture. They had analyzed $\bar{p}p$ annihilation at 7 GeV/c using the variables and found some characteristics due to multiperipheral mechanism. The Alexander's method is employed for $\bar{n}p$ annihilation in this section.

The variables are constructed out of two kinematical quantities, the transverse momentum $p_{T\ i}$ and the CM rapidity $y_i=0.5\ \ln((E_i+p_{Li})/(E_i-p_{Li}))$ associated with the i th outgoing particle of an event (E_i and p_{Li} are the CM energy and longitudinal momentum). The other two quantities entering into the calculation are charge q_i of the i th particle and its ordering according to rapidity among the final particles.

The variables employed here are those related to the multiparticle picture of high-energy strong interactions. In this kind of picture the production mechanism is described by a diagram of the type shown in Figure 47. The ordering of the outgoing particle is given by the value of a kinematical quantity such as rapidity, which is adopted in the present work.

Conservation laws at each vertex in the diagram of Figure 47 allow one to calculate the charge q_{ex} and transverse momentum $\vec{p}_{ex}$ exchanged in the j th rung of the multiperipheral ladder, that is

$$\vec{p}^{\,j}_{ex} = \sum_{i=1}^{j} -\vec{p}_{Ti} , \qquad \text{(IV-98)}$$

$$q^{j}_{ex} = q_a - \sum_{i=1}^{j} q_i , \qquad \text{(IV-99)}$$

where q_a is the charge of the incoming particle A. From these exchange quantities the following variables are built;

$$P_{Tex} = \sum_{j=1}^{\nu-1} |\vec{p}^{\,j}_{ex}| , \qquad \text{(IV-100)}$$

and

$$Q_{ex} = \sum_{j=1}^{\nu-1} |q^{i}_{ex}| , \qquad \text{(IV-101)}$$

where ν-1 is the number of rungs in the diagram.

These variables are related to the multiperipheral picture of hadron interactions where the exchanged objects are believed to carry small p^{j}_{ex} and q^{j}_{ex} values. Alexander et al. pointed out that the multiparticle variables , evaluated event by event, eliminated the combinational background at least in part, which was introduced by the presence of identical particles in the final state and expected to mask the underlying properties in the interaction.

IV-7-ii. The Analysis for $\bar{n}p$ Data

The experimental distributions of the multiparticle variables P_{Tex} and Q_{ex} are evaluated for $2\pi^+\pi^-$, $2\pi^+\pi^-\pi^o$, $3\pi^+2\pi^-$, and $3\pi^+2\pi^-\pi^o$ final states. The same quantities for phase space are calculated using the Monte Carlo program FOWL and are compared with those of experimental data as follows.

Distributions of R, the ratio of Q_{ex} of the data to that of phase space, and those of $P_{T\,ex}$ are given in Figs. 48 and 49 respectively. The solid curves in Fig. 49 are the phase-space distributions.

These figures show that the distributions for the final states of various multiplicities are consistent with the phase space distributions. This fact suggests that the contribution of multiperipheral mechanism to $\bar{n}p$ annihilation at the present energy does not differ from that of phase space. Q_{ex} and P_{Tex} of the $2\pi^+\pi^-$ data deviate slightly from the phase space toward the lower values. This feature may be caused by multiperipheral component with small amount.

IV-8. Analysis of $\bar{n}p \longrightarrow 2\pi^+\pi^-$ Reaction by Dual Model

IV-8-i. $\pi\pi$ Scattering and Dual Amplitude

The reaction

$$\bar{n}p \longrightarrow 2\pi^+\pi^- \,, \qquad \text{(IV-102)}$$

can be regarded as a decay process of a heavy particle made of $\bar{n}p$ of the initial state decaying into $2\pi^+\pi^-$ state. Therefore the amplitude to describe the reaction (IV-102) is related to the reaction

$$\pi^+\pi^- \longrightarrow \pi^+ S \,, \qquad \text{(IV-103)}$$

by the line reversal, where S represents the heavy particle of spin S, isospin 1.

The amplitude A(s,t) satisfying the duality for the reaction

$$\pi^+\pi^- \longrightarrow \pi^+\pi^- \,, \qquad \text{(IV-104)}$$

is given by 128)

$$A(s,t) = \frac{\Gamma(1-3(s))\Gamma(1-\alpha(t))}{\Gamma(1-\alpha(s)-\alpha(t))}, \qquad \text{(IV-105)}$$

where $\Gamma(z)$ is the Γ function, $\alpha(t)$ the single exchange degenerated trajectory of the Regge expole ($\alpha_\rho(t)=\alpha_f(t)=\alpha_0+\alpha' t$), and s, t are the Mandelstam variables. The amplitude (IV-105) has the following properties;

a) it is analytic,

b) it has Regge asymptotic behavior for $s \longrightarrow \infty$ determined by $\alpha(t)$,

c) it has resonance poles of zero width at positions determined by $\alpha(s)$.

The pole structure of A(s,t) on the (s,t) plane is shown in Fig. 50. The curve drawn in this figure at $s>0$, $t>0$ region is the boundary for the reaction (IV-102) at 0.65 GeV/c. Inspection of the Figure 50 leads to the following consideration.

The poles at $\alpha(s)=n$, $\alpha(t)=m$ ($n, m=1,2,\ldots$) may coincide in the region $s>0$, $t>0$, which is outside of the physical region of the scattering process (IV-104). No double pole appears, however, since the amplitude $A(s,t)$ vanishes on the lines $\alpha(s)+\alpha(t)=n$, ($n=1,2,\ldots$), so that the double poles of the numerator are reduced to a single pole of $A(s,t)$ only. The poles at $\alpha(s)=n$ lie on the real axis ($\alpha(s)$ is real) and these correspond to resonances of zero width. Phenomenologically, finite-width resonances are introduced into the amplitude by adding an imaginary part to $\alpha(s)$;

$$\alpha(s)=\alpha_0 + \alpha's + i\,\mathrm{Im}\alpha(s) \quad . \qquad \text{(IV-106)}$$

Lovelace had analyzed the Dalitz plot of the annihilation process

$$\bar{p}n \longrightarrow 2\pi^-\pi^+ \ , \qquad \text{(IV-107)}$$

by the dual amplitude for $\pi\pi$ scattering. In this case $\bar{p}n$ state is assumed to have the same quantum number as pion under consideration of the incident energy (at rest), and the amplitude employed is

$$A(s,t) = (0.885(s,t)-0.034)\beta\frac{\Gamma(1-\alpha(s))\Gamma(1-\alpha(t))}{\Gamma(2-\alpha(s)-\alpha(t))} \ , \qquad \text{(IV-108)}$$

with

$$\alpha(s)=0.483 + 0.885s + i0.28\sqrt{s-4m_\pi^2} \ . \qquad \text{(IV-109)}$$

The distribution of events on the $s=M^2_{\pi^+\pi^-_1}$ versus $t=M^2_{\pi^+\pi^-_2}$ Dalitz plot is then given by

$$\frac{\partial^2\sigma}{\partial t\partial s} \propto |A(s,t)|^2 \ . \qquad \text{(IV-110)}$$

Fig. 51(a) shows the Dalitz plot for the reaction (IV-107) at rest together with the prediction by the dual amplitude (Lovelace's method). One can see immediately that the experimental distribution is very much similar to that of the dual model as expected on the basis of Figure 50. The events concentrated at $\alpha(s)=1$, $\alpha(t)=1$; ρ band, and $\alpha(s)=2$, $\alpha(t)=2$; f band, and furthermore there is a hole in the middle corresponding to the line $\alpha(s)+\alpha(t)=3$. In fact this hole is so deep and the depletion of events along the lines $\alpha(s)+\alpha(t)=2$ or 4 is so much weak that a fit to the data will require an additional line of zeros at $\alpha(s)+\alpha(t)=3$.

IV-8-ii. $\bar{n}p \longrightarrow 2\pi^+\pi^-$ Process

Fig. 51 gives the Dalitz plot for the reaction (IV-102) at 0.65 GeV/c based on 90 events (the present experiment) together with those of the reaction (IV-107) at rest(29) and at 1.2 GeV/c(22). $\bar{n}p$ state is related to $\bar{p}n$ state by the CP conjugation, therefore the distribution of $\bar{n}p$ data is expected to show a similar behavior to that of $\bar{p}n$ data. Figure 51(b) shows that; in spite of poor statistics, the $\bar{n}p$ Dalitz plot seems to have a hole at $s \simeq t \simeq 1$ $(\text{GeV}/c^2)^2$ and gives the concentration of events at both ρ and f bands which are observed commonly at the $\bar{p}n$ Dalitz plot at rest (Figure 51(a) and at 1.2 GeV/c (Figure 51(c)). The above-mentioned structure is consistent with the one expected on the basis of Figure 50, that is, concentration of events at $\alpha(s)=1$, $\alpha(t)=1$, $\alpha(s)=2$, $\alpha(t)=2$, and depletion of events corresponding to the line $\alpha(s)+\alpha(t)=3$. More detailed structure is not obvious.

IV-8-iii. Comparison of the $\bar{n}p$ Data with Dual Model

A phenomenological approach for the reaction (IV-102) is made in this section considering each J^P state of the initial states of $\bar{n}p$ system. The J^P values of such states can be grouped in the two sequences;

a) normal parity: $J^P = 2^+, 4^+, \ldots$

b) abnormal parity: $J^P = 0^-, 1^+, 2^-, 3^+, \ldots$

Regarding the $\bar{n}p$ system as being a certain J^P state, the density of the Dalitz plot can be deduced from the amplitude for the reaction (IV-103).

Goebel et al.[129)] applied the Veneziano model to the reaction (IV-103), namely, $\pi\pi$ scattering with arbitrary-spin particle in the final state. Bettini et al.[22)] analyzed the Dalitz plot of the reaction (IV-107) at 1.2 GeV/c based on 818 events following the Goebel's method. Assuming J^P value of $\bar{p}n$ system as given in the above two sequences (up to G waves of $\bar{p}n$ angular momentum), Bettini et al. obtained qualitative agreement of the data with the prediction by the 2^+ amplitude. The 2^+ amplitude is

$$A^{ij}(s,t) = \frac{\Gamma(2-\alpha_\rho(s))\Gamma(1-\alpha_\rho(t))}{\Gamma(3-\alpha_\rho(s)-\alpha_\rho(t))}(p_1^i q^j + p_1^j q^i) - (1 \overset{\leftarrow}{\rightarrow} 2), \tag{IV-111}$$

with

$$\alpha_\rho(s) = 0.65 + 0.84s + i0.26\sqrt{s-4m_\pi^2}\,, \tag{IV-112}$$

where $s = M^2_{\pi^+\pi_1^-}$ and $t = M^2_{\pi^+\pi_2^-}$, p_1 and p_2 are the negative pions' momenta in the CM, $q = p_2 \times p_1$ and $(1 \overset{\leftarrow}{\rightarrow} 2)$ indicates the second term obtained from the first one by interchanging particles 1 and 2.

The amplitude (IV-111) is employed together with the trajectory (IV-112) for the $\bar{n}p$ annihilation at 0.65 GeV/c to describe the Dalitz plot. The density on the Dalitz plot by the amplitude is calculated using the Monte Carlo program FOWL. The contours on the Dalitz plot in Figure 52(a) are the predictions by the above amplitude and the solid curves on the projected histograms are also the predictions by it (dashed curves are the phase space distributions). It is not possible to make a quantitative discussion on the Figure 52 because of the poor statistics, but the structure appearing on the Dalitz plot is consistent with that predicted by the 2^+ amplitude.

IV-9. Inclusive Analysis

We picked up $\bar{n}p$ events with ≥ 3 prongs on a scanning table as mentioned in Section III. Therefore inclusive analyses are not applicable for the annihilation process for lack of 1 prong events in the strict sense of the word. However we have done the analyses for the $\bar{n}p$ annihilation in this section by the following reason; a rate of the 1 prong events to the total of the annihilation is predictable as $\sim$ 15% based on the data of $\bar{p}d$ experiments[18][21] ($\sim$15%) and on the prediction by the Orfanidis Rittenberg model (17%), which is rather small, and furthermore such events have only one charged track. We believe that results of the analyses give good information to investigate the annihilation process.

IV-9-i. Thermodynamical Analysis

In the framework of the Hagedorn model,[47] the primary annihilation process can be treated as a fireball of mass equal to the CM energy, which decays into successive fireballs and/or resonances until the final multipion state is reached. The fireball system is described by the statistical thermodynamics of an unlimited and undetermined number of more or less excited hadrons, in which an idea of the highest temperature (independent of the actual number of particle) is introduced (see II-2-v).

The highest temperature can be determined by fitting the exponential type formula to the data of the transverse momentum distribution as follows.

Concerning to the transverse momentum spectrum p_T, there are two different types of the distribution from thermodynamical aspect, that is, Hagedorn distribution and Boltzmann one;[130),131)]

$$N(p_T)dp_T = N_o p_T{}^{3/2}\ e^{-p_T/T}\ dp_T \text{ (Hagedorn)}, \qquad \text{(IV-113)}$$

$$N(p_T)dp_T = N_o p_T\ e^{-p_T^2/\alpha^2}\ dp_T \text{ (Boltzmann)}\ , \qquad \text{(IV-114)}$$

where $N(p_T)dp_T$ represents a number of particles of p_T within the interval dp_T, N_o is a constant for normalization, T represents the highest temperature (Hagedorn temperature) and α being a parameter. A question then arises which of the two types of the distribution (IV-113),(IV-114) is more adequate to account for experimental data.

Figs. 53(a), (b), and (c) give the inclusive spectra of transverse momenta of π^+, π^- and both of them in the $\bar{n}p$ annihilation at 0.65 GeV/c respectively. Solid and dashed curves in these figures are those obtained by fitting the distributions of Hagedorn type (IV-113) and Boltzmann type (IV-114) for the data respectively. χ^2 value for each fitting is summarized in Table 12 together with the highest temperatures thus obtained.

The highest temperatures for π^+, π^-, and both of them are in good agreement and furthermore they are not far away from the value expected in the Hagedorn's thermodynamical model for strong interactions (∿130 MeV).

IV-9-ii. Müller-Regge Analysis for $\bar{n}p$ Annihilation.

Rittenberg and Rubinstein[34)] proposed an inclusive analysis of $\bar{p}n$ annihilation to study the questions of duality and background correlation to exotic states. They considered the forward amplitude of the scattering of a spinless particle(A) on a spinless particle(B) (their masses being m_a and m_b respectively such that

$m_a > m_b$) below threshold. The discontinuity of the scattering amplitude is then related through unitarity to the decay process

$$A \longrightarrow B + \text{anything}. \qquad \text{(IV-115)}$$

The Lorentz invariant differential cross section for particle B can be written as

$$E_b d\sigma/d^3p_B \sim \text{Disc}_s(A(s,t=0,u=2m_a^2+2m_b^2-s)), \qquad \text{(IV-116)}$$

with $s=(p_A+p_B)^2$, which is the equivalent formula to the Müller expression[132] for an inclusive scattering process.

Assuming the amplitude

$$A(s,t,u)=B(s,t)+B(t,u)+B(u,s), \qquad \text{(IV-117)}$$

as suggested by duality,

$$\text{Disc}_s(A(s,t=0,u=2m_a^2+2m_b^2-s))=S(s)+U(s), \qquad \text{(IV-118)}$$

where

$$S(s)=\text{Disc}B(s,t),\ U(s)=\text{Disc}B(u,s). \qquad \text{(IV-119)}$$

Parametrization of the S(s) term below threshold by means of Regge poles is made considering duality and saturation with a few Regge poles as

$$S(s)=\sum_i \beta_i s^{\alpha_i(0)}. \qquad \text{(IV-120)}$$

The trajectories α_i have quantum numbers of the $\bar{A}A$ and $\bar{B}B$ systems and include the Pomeron.

Following to the above consideration and assuming that $\bar{n}p$ annihilation proceeds via a small number of direct channel resonances, the pion spectrum of the reaction

$$\bar{n}p \longrightarrow \pi^{\pm} + \text{anything}, \qquad \text{(IV-121)}$$

is related to the forward amplitude of the scattering

$$A + \pi^{\mp} \longrightarrow A + \pi^{\mp},\ A=(\bar{n}p)\ \text{system}, \qquad \text{(IV-122)}$$

since the above discussion is available even if the annihilation takes place via higher spin states of s-channel or in flight. The only one restriction is that the $\bar{n}p$ state should be through direct channel resonances. Neglecting the contribution of U(s) in eq. (IV-118), the invariant cross sections of the inclusive process (IV-121) in flight are given by

$$d\sigma^2/dM^2dt = \sum_i \beta_i(t)(M^2)^{\alpha_i(t)}, \qquad \text{(IV-123)}$$

where the variables are the missing mass squared M^2, which corresponds to the variable s in eqs. (IV-116)-(IV-120)), and the momentum transfer t between the incident $\bar{n}$ and each pion of a specific charge. The sum should be made over the relevant Regge trajectories α_i that can be exchanged between the $\bar{n}p$ system and the pion (see scattering (IV-122)) with suitable residue functions $\beta_i(t)$.

Looking at the π^- spectrum in (IV-121), the crossed channel (IV-122) is exotic, hence the only possible trajectory is the (by duality) Pomeron, and the cross section(IV-123) becomes

$$d\sigma^2/dM^2dt = \beta(t)M^2. \qquad \text{(IV-124)}$$

In the π^+ case more terms being expected to contribute to the sum in eq. (IV-123). Then one can expect a difference between the spectra of π^+ and π^-.

Figure 54 gives the spectra of π^+(cross mark) and π^-(closed circle) against M^2 for various t intervals, and Figure 55(a) gives the same quantity for overall t region. It is obvious that the spectra of π^+ and π^- behave similarly in these figures. The data in Figure 55(a),M^2 distribution for overall t, are used in fitting the formula

$$dN/dM^2 = K(M^2)^{\alpha}, \text{ (N: number of pions)}, \qquad \text{(IV-125)}$$

to the spectra of π^+, and π^-, where K and α are left to be free parameter. The α's obtained for π^+ and π^- are

$$\alpha^{\pi^+} = 1.99 \pm 0.07, \qquad \text{(IV-126)}$$

$$\alpha^{\pi^-} = 2.03 \pm 0.10. \qquad \text{(IV-127)}$$

The above two results are in good agreement and are unrealistic for any Regge trajectory, whereas they reproduce the data fairly well (see the dotted curve in Figure 55(a). In conclusion, the predictions by Rittenberg and Rubinstein are in disagreement with the present data. The inclusive analysis of $\bar{p}n$ annihilation at rest[17)] and at 1.0-1.6 GeV/c[25)] had been performed in the similar way of the above-mentioned method, and the both results show also disagreement with the predictions by Rittenberg and Rubinstein. One of the causes of the disagreement may be that the value of missing mass squared M^2 kinamatically allowed is too low to test the model.

A statistical approach is made for the inclusive process (IV-121) with the Orfanidis-Rittenberg model (OR model), which is explained in Appendix A. The branching ratios of

$$\bar{n}p \longrightarrow l\pi^+(l-1)\pi^- m\pi^0, (l,m;\ \text{positive integer}), \qquad \text{(IV-128)}$$

for various (l,m) values were calculated following the OR model. The ratios thus obtained are given in Table 13. The events with fixed l,m are generated without appealing to any dynamical property by the FOWL, and histograms for the missing mass squared are taken at the same time in a similar way of the inclusive analysis. Then the histograms for each (1,m) set are added according to the predicted rates in Table 13. The spectra, thus obtained, for π^+ and π^- show the same behavior, which are given in Fig.55(a) by a solid curve. It reproduces the data well except the highest t region.

Since we did not use the nofit events obtained at Bombay in the present analysis, which corresponded to $\sim$33 % of all $\geq$3-prong events, we chacked the missing-mass spectra for π^+ and π^- of nofit events within Tokyo and Neuchatel data as follows. Figure 55(b) gives the missing-mass spectra for the nofit events. It seems from this figure that π^+ and π^- do not give any significant difference between their missing-mass spectra . We tried fitting the form of eq.(IV-125) to these spectra, and obtained the best-fit values for α as

$$\alpha^{\pi^+} = 1.50 \pm 0.01, \qquad \text{(IV-128)}$$

$$\alpha^{\pi^-} = 1.56 \pm 0.01. \qquad \text{(IV-129)}$$

Both of them are unrealistic for any Regge trajectory. A dotted curve in Fig.55(b) showes the one drawn with α =1.50 . With the above consideration we conclude that the result obtained in this section dose not change in essence even if the nofit events at Bombay are supplied later.

IV-10. Energy Dependence of $\bar{n}p$ Annihilation

Only nucleon antinucleon interactions provide the way to form mesons in the laboratory, besides e^+e^- collisions which couple exclusively to $J^P=1^-$ state. There are obvious quantum number restrictions on nucleon-antinucleon system, namely, strangeness=0, isospin=0 or 1 or mixture of them, and the mass being greater than two nucleon masses.

A lot of experiments had been carried out to search for high-mass mesons in nucleon antinucleon interactions. A review on the formation experiments is given by Astbury58).

Recently Carroll et al.133)measured the total cross sections of $\bar{p}p$ and $\bar{p}d$ reactions between 0.36 and 1.05 GeV/c by electronic counter technique, and observed resonance like structures in the both cross sections at almost the same momenta. Their result is that; the enhancement observed in $\bar{p}p$ total cross sections corresponds to the effective mass 1932 GeV/c^2, the width is 9 MeV/c^2, and it seems to be isospin=1 probably.

We have tried to search for such a signal as found by Carroll et. al. in $\bar{n}p$ reactions as follows.

Figure 56 gives distributions of events of $\bar{n}p$ annihilation in our experiment with respect to the total energy of $\bar{n}p$ system. The same distributions for odd-pion final state (Fig. 56(b)) and even-pion one (Fig. 56(c)) are also given. A position of the enhancement observed by Carroll et al.133) is indicated by arrows in Fig. 56. The normalized cross sections are not obtained in the present case, so that, it is hard to observe enhancements due to direct channel resonances, if any. But if resonances are produced with definite G parity, the distributions of Figs. 51(b) and (c) should show different behavior at the position. It seems from Figs. 56(b) and (c) that the behavior is slightly different around 0.65 GeV/c but the conclusion cannot be drawn yet because of the poor statistics.

V. Antiproton-Proton Annihilation Cross Section

V-1. Beam Details and Two-prong Cross Section

V-1-i. Threshold Energy for Inelastic Reaction

One of the purpose of this experiment is to estimate $\bar{p}p$ annihilation cross section. In other words, it is a main work to estimate the fractions of $\bar{p}p$ charge exchange cross section in the 0-prongs and $\bar{p}p$ elastic cross section in the 2-prongs. The above anlysis is carried out with data on the films of Exposure I only at Tokyo. Beam momenta of the Exposure I were 0.7 GeV/c on the average. At 0.7 GeV/c, the 0-prong should be either

$$\bar{p}p \longrightarrow \bar{n}n\ , \qquad \text{(V-1)}$$

or

$$\bar{p}p \longrightarrow \text{neutral mesons}, \qquad \text{(V-2)}$$

and the 2-prong should be

$$\bar{p}p \longrightarrow \bar{p}p\ , \qquad \text{(V-3)}$$

or

$$\bar{p}p \longrightarrow \text{two charged mesons (plus neutral ones)}, \qquad \text{(V-4)}$$

since the inelastic reactions, such as

$$\bar{p}p \longrightarrow \bar{n}n\pi^0, \qquad \text{(V-5)}$$

and

$$\bar{p}p \longrightarrow \bar{p}p\pi^0, \qquad \text{(V-6)}$$

are not possible because of the higher threshold momenta (0.7852 and 0.7765 GeV/c for the reactions (V-4) and (V-6) respectively).

V-1-ii. Beam Details

In order to calculate the cross section for any reaction, information about a flux of incident beams should be provided. So that, a number of incident tracks and, at the same time, a number of interactions of all topologies were counted within a certain fiducial volume on every twenty frames over 182,000 pictures.

Figure 57(a) shows the reference fiducial marks on the view 2, where the fiducial volume is defined as the region inside the dotted lines. Figure 57(b) gives the spatial fiducial volume and its position in the chamber system. A restriction for the incident $\bar{p}$ tracks was made such that; i) The trajectory or its extrapolated one from the interaction point should cross the two arrows as indicated in Figure 57(a). ii) The angular deviation of the track from the average beam tracks should be less than 5^o at up stream. iii) It does not suffer visible elastic scattering before entering into the fiducial volume.

On searching for all yields in the chamber, events of elastic scattering with a recoil proton track less than 3 mm on a scanning table (20x magnification, on view 2) were not concerned since it was inefficient to pick up such events. Obvious Dalitz pairs comming from the decay $\pi^o \longrightarrow e^+e^-\gamma$, which were characterized by one or two spiralling tracks, were recorded. Beam contamination due to π^- or μ^- background was found to be 9.17 %, since π^- or μ^- tracks were easily distinguishable from $\bar{p}$ ones owing to their lower bubble density (The amount of energy loss of $\bar{p}$ in liquid hydrogen is two times more than that of π^- or μ^- at 0.7 GeV/c).[112)]

About ten tracks of incident $\bar{p}$ per frame were observed on the average. A distribution of momentum at the interaction points of incident $\bar{p}$ beams obtained from THRESH outputs of measured events for $\bar{p}p$ charge exchange is given in Figure 58 for the Exposure I (Tokyo data). Similarly the same distribution is given in Figure 59 for the Exposure II (Bombay's data) to compare the two exposures. Characteristics of the beams are summarized in Table 14.

V-1-iii. Topological Cross Sections

For each topology of $\bar{p}p$ interaction (0-, 2-, 4-, 6-, 8-prong type), the topological cross section σ is calculated as

$$\sigma = \frac{n}{\rho N L} , \qquad \text{(V-7)}$$

where n is the number of events of a certain topology, ρ density of liquid hydrogen, N Avogadro's number, and L total length of effective tracks. To obtain the quantity L, it needs the average track length l_0 within the fiducial volume as defined in Figure 57(b). For this purpose 0-prong tracks measured in this experiment were made use of, and the coordinates of the two points (indicated by characters P and Q in the Figure 57(b)), at which a helix of $\bar{p}$ trajectory intercepted with the planes constituting the fiducial volume, were calculated by Newton-Raphson's method.

The value of l_0, thus obtained, was 39.1 cm. The quantity L is expressed as

$$L = l_0 m(1-\varepsilon), \qquad \text{(V-8)}$$

where m is the number of tracks counted in the all used frames and ε represents the reduction of the average track length due to occurence of all sort of interactions (8.6 % in the present case). The topological cross sections were calculated by the equation (V-7) based on 8,346 frames in which 13,054 interactions were observed, and the result was

$$\sigma(\text{0-prong}) = 12.8 \pm 0.3 \text{ (mb)}, \qquad (\text{V-9})$$

$$\sigma(\text{2-prong}) = 70.3 \pm 0.8 \quad , \qquad (\text{V-10})$$

$$\sigma(\text{4-prong}) = 37.6 \pm 0.6 \quad , \qquad (\text{V-11})$$

$$\sigma(\text{6-prong}) = 3.6 \pm 0.2 \quad , \qquad (\text{V-12})$$

$$\sigma(\text{8-prong}) = 0.04 \pm 0.02 \quad , \qquad (\text{V-13})$$

V-1-iv. Estimation of Lost Events due to Small Angle Scattering

The result in Section V-1-iii does not include the events of elastic scattering with a recoiled-proton length less than 3 mm on the 20x magnifications scanning table, which corresponds to that less than 1.5 mm in real size since the picture itself is reduced from the real event by 1/10. Therefore an amount of the loss of events of elastic scattering with short recoiling or invisible proton should be estimated.

Assuming the view-2 camera being positioned just above the interaction vertex of the elastic scattering, it is possible to draw a picture as Figure 60(a) to represent the relation of recoiled-proton lengths between in the chamber and on the front glass on which tracks are projected. This assumption is right approximately under consideration for position of the camera and the size of the chamber (see Fig.57(b)). In this figure an incident track is perpendicular to the paper which contains the interaction point. A recoil proton is emitted radially in a plane approximately perpendicular to the incident track as shown in Figure 60(a) whenever the scattering takes place forward; for example the range 10 mm of a recoil proton corresponds to the angle 77° between the recoil proton and the incident $\bar{p}$.

The range of a recoil proton (represented by the radious of the circle in Figure 60(a)) is a function of four-momentum transfer t (between incident and scattered $\bar{p}$), so that an event with small $|t|$, such that the projected range of the recoiled proton is smaller than 1.5 mm (shaded area in Figure 60(a)), cannot be picked up. Figure 60(b) shows the ratio of loss of such events as a function of $|t|$, together with the relation between the range and $|t|$ obtained from the data in Particle Data Group.112)

The efficiency, which is equivalent to the ratio $2\theta/\pi$ in Figure 60(a), is almost 100 % at $|t| > 0.04$ $(\mathrm{GeV}/c)^2$. %'s of loss of events due to forward elastic scattering are listed as the result as follows.

$$
\begin{aligned}
0.0 &\le |t| < 0.0085\ (\mathrm{GeV}/c)^2 \ ; && 100\ \%, \\
0.0085 &\le |t| < 0.02\ ; && 24\ \%, \\
0.02 &\le |t| < 0.04\ ; && 4\ \%. \qquad \text{(V-14)}
\end{aligned}
$$

V-1-v. Total Cross Section and Two-Prong Annihilation Cross Section

An experiment of $\bar{p}p$ elastic scattering was carried out based on 2,751 pictures five years ago.73) In this experiment the total elastic cross section was obtained to be

$$\sigma^{el} = 51.2 \pm 1.6 \text{ mb}, \qquad \text{(V-15)}$$

and the differential cross section was also measured. Figure 61 shows the result for the differential cross section at $|t|<0.1(\mathrm{GeV}/c)^2$

in which the solid curve along the data points gives the best fit to the diffraction type formula

$$\frac{d\sigma}{dt} = \frac{A}{|t|} \left(J_1 \left(\frac{a + ƛ}{\hbar} \sqrt{|t|} \right) \right)^2 , \qquad \text{(V-16)}$$

to the data with $A = 59.0 \pm 2.0$ mb and $a = 0.996 \pm 0.023$ fm. According to the result (V-14), the loss of events due to the projected range of recoil proton less than 1.5 mm can be represented schematically as the shaded area in Figure 61, which corresponds to 16.6 % of σ^{el}.

Using the results in Section V-1-iii, the total two-prong cross section, thus obtained, is

$$\sigma^{tot}_{2\text{-prong}} = 78.8 \pm 1.0 \text{ mb}, \qquad \text{(V-17)}$$

and the total cross section is

$$\sigma^{tot} = 132.8 \pm 1.2 \text{ mb}. \qquad \text{(V-18)}$$

This value for σ^{tot} may increase by a few %, since we counted a number of 2, 4, 6 and 8 prongs only once, therefore scanning efficiency for these events was not taken into account. The two-prong annihilation cross section is given by subtracting σ^{el} from $\sigma^{tot}_{2\text{-prong}}$.

$$\sigma^{ann}_{2\text{-prong}} = 27.6 \pm 1.7 \text{ mb} . \qquad \text{(V-19)}$$

V-2. Total Charge Exchange Cross Section

V-2-i. Detection Probability for Charge Exchange Events

A $\bar{p}p$ charge exchange event is identified as a 0-prong vertex associated with an odd-prong star within the restricted fiducial volume. This fact implies that the event could be picked up with detection probability for the emitted $\bar{n}$ giving rise to $\bar{n}p$ annihilation (odd-prong star) within the fiducial volume. Therefore a number of charge exchange events are deducible by putting a weight, inverse of the detection probability, to each observed one. A total number of $\bar{p}p$ charge exchange is then given by the sum of the weight.

The detection probability P(T,L) for $\bar{n}$ with kinetic energy T is given by

$$P(T,L) = (1-\exp(-N\rho L\sigma_{\bar{n}p}^{tot}(T)))\sigma_{\bar{n}p}^{anh}(T)/\sigma_{\bar{n}p}^{tot}(T), \tag{V-20}$$

where N is Avogadro's number, ρ density of hydrogen, and L is a potential-path length of $\bar{n}$ before leaving the fiducial volume (see Fig. 57(b)). $\sigma_{\bar{n}p}^{tot}(T)$ is the total cross section of $\bar{n}p$ reaction and $\sigma_{\bar{n}p}^{anh}(T)$ is the annihilation cross section of that reaction giving ≥ 3 charge prongs.

V-2-ii. Kinematical Ambiguity

The THRESH outputs are used in a calculation of the total charge exchange cross section, because the GRIND outputs don't give a fit for the event of multi-neutral at $\bar{n}p$ vertex even if it is a genuine event (see Section III-7-ii). Therefore the energy and direction of each $\bar{n}$ emitted are calculated from the measured quantities.

Due to the mass difference between $\bar{p}$(or p) and $\bar{n}$(or n), there are two solutions for kinematical quantities in $\bar{p}p$ charge exchange (V-1) although the emission angle of $\bar{n}$ in the laboratory system is known. Figure 62 shows the kinematical scheme. Solving equations of energy and momentum conservation for $\bar{p}p$ charge exchange leads to the following results in lab. system;

$$E(\bar{n}) = \frac{M(p)+\sqrt{A(M(p)^2 - M(n)^2)+A^2M(n)^2}}{(1-A)}, \quad (V-21)$$

or

$$E(\bar{n}) = \frac{M(p)-\sqrt{A(M(p)^2 - M(n)^2)+A^2M(n)^2}}{(1-A)}, \quad (V-22)$$

Where

$$A = \frac{P(\bar{p})^2\cos^2\theta}{(E(\bar{p})+M(p))^2}, \quad E(\bar{n})^2 = p(\bar{n})^2 + M(\bar{n})^2,$$

$p(\bar{p})$; momentum of antiproton in lab., similarly $p(\bar{n})$

$E(\bar{n})$; energy of antineutron in lab., similarly $E(\bar{p})$.

$M(n)=M(\bar{n})$; mass of neutron or antineutron, similarly $M(p)$.

θ ; angle between the directions of the antiproton and antineutron in lab.

Thus, T is given by

$$T = E(\bar{n}) - M(\bar{n}).$$

Kinematical ambiguity for the choice of $\bar{n}$ energy arises from the two possible solutions (V-21) and (V-22), which are called as high-energy solution and low-energy one respectively hereafter.

At the present energy of incident antiprotons, the maximum values of the kinetic energy T and the scattering angle between $\bar{p}$ and $\bar{n}$ in center of mass system $\cos\theta_{cm}$ for the low-energy solution are calculated to be 1.3 MeV and -0.989 respectively, which correspond to the minimum values of those for the high-energy solution. Hence, the events with low-energy solution should distribute having the path lengths of $\bar{n}$ within a few cm and the angles $\cos\theta_{cm}$ in the band $-1.0 \leq \cos\theta_{cm} \leq -0.989$.

The events measured were examined by the aspect pointed above, and the high-energy solution was always taken by the three reasons;

i) The fiducial volume is defined as shown in Fig. 57(b), and an experimental distribution for the ratio of the actual-path length x of $\bar{n}$ to the potential-path length L, x/L, is given in Figure 63. The distribution is compatible with uniformity,hence indicating the mean free path length of $\bar{n}$ larger than the dimension of the chamber.

ii) There were 28 events of 1-C fit having the low-energy solution (momentum of $\bar{n}$ between 4 and 50 MeV/c) in the GRIND outputs. However path lengths of $\bar{n}$'s of these events were rather large (> 3 cm) and values of $\cos\theta_{cm}$ were concentrated to a narrow backward region ($-1.0 \leq \cos\theta_{cm} \leq -0.99997$), indicating that the 1-C fits with low-energy solution were faked ones.

iii) 109 events of 4-C fit were obtained, but none of them had the low-energy solution. This fact implies that the low-energy solution is unlikely with an upper limit 0.9 % for the possible occurence, because the 4-C fit is more reliable than the 1-C fit as explained in III-7-ii.

V-2-iii. Numerical Calculation of Detection Probability

By the charge symmetry, $\sigma_{\bar{n}p}^{tot}$ and $\sigma_{\bar{n}p}^{anh}$ in eq. (V-20) should be equal to $\sigma_{\bar{p}n}^{tot}$ and $\sigma_{\bar{p}n}^{anh}$ of $\bar{p}n$ reaction which can be measurable in an antiproton-deuteron experiment. On the other hand, the choice of the high-energy solution makes it possible to approximate eq. (V-20), the detection probability, as below.

$$P(T,L) \simeq N\rho L\sigma_{\bar{n}p}^{anh}(T), \qquad \text{(V-23)}$$

which includes only $\sigma_{\bar{n}p}^{anh}(T)$ as an unknown quantity.

In practice eq. (V-23) was used instead of eq. (V-20) by the following reason; Data for $\sigma_{\bar{p}n}^{tot}$ at low energies in a deuteron experiment is not enough, because a complete separation of the events of scattering into those on neutrons and on protons is hard because of the kinematical ambiguities in the GRIND outputs and/or the influence of multiple scattering.[18)]

A measurement of $\bar{p}n$ annihilation cross section was made in a deuterium bubble chamber experiment at Roma-Trieste group with incident momenta of $\bar{p}$ beams in the range 0.3-0.6 GeV/c.[18)] They pointed out in the paper that the $\bar{p}p$ annihilation cross section obtained from their deuteron experiment did not show any significant defect in comparison with the same quantity obtained in a hydrogen bubble chamber experiment at low energies.[40)] This fact implies that the measured cross sections for $\bar{p}n$ annihilation with

1-, 3-, and 5-charged mesons at Roma-Trieste group are in good estimate of those on free neutrons. The result for $\bar{p}n$ annihilation is given in Table 15(cited from Table III in ref.18)). $\sigma_{\bar{p}n}^{anh}(T)$, the cross section of $\bar{p}n$ annihilation with ≥ 3 prongs, is nearly equal to the cross section $\sigma_3 + \sigma_5$ in Table 15 (The contribution of σ_7 should be about 1 % as seen in Table 1(a) hence negligible small). The cross sections $\sigma_3 + \sigma_5$ are plotted in Figure 64 at each energy, where a solid curve is the result of fit of an empirical formula to the data as described below, and a dotted one is that used in the previous experiment.[73) The empirical formula which represents the energy dependence of the data fairly well, thus obtained, is

$$\sigma_{\bar{p}n}^{anh}(T) = (747 \pm 10)/\sqrt{T}\ , \text{ in mb}, \qquad (V\text{-}24)$$

with χ^2/n_D=13/8, where T is in MeV. Thus the expression (V-24) is used as $\sigma_{\bar{n}p}^{anh}(T)$ in eq. (V-23), and a weight for each event is obtained by inverse of P(T,L).

To get the average weight, events in the well measured sample were selected following the criteria as below (see Table 1, too).

i) Events whose angle between $\bar{p}$ and $\bar{n}$ in lab. system exceeded the kinematical limit (see Fig. 62) were excluded.

ii) Events out of the fiducial volume were excluded.

iii) Events with more than one zero prong or more than one star in a frame were excluded because of their large fraction of the false association in the combinations between 0-prong vertex and odd-prong star vertex (more than 50 %).

iv) To purify the sample, only events of incident $\bar{p}$ lying within $0.6 < \text{momentum} < 0.8$ (GeV/c) and $-0.2 < \text{dip angle} < 0.2$ (radian) were accepted.

Finally 1,111 events remained (in 223,749 frames) and the average weight for these events was

$$\bar{W} = 24.11 \ . \qquad \text{(V-25)}$$

In the case of well measured events, the number of the charge exchange samples is that remained after cuts of both i) and ii); 1,278 events (see Table 1(a)).

In the case of badly measured events (176 events, see table 1(a)), the number of the samples which should remain after cuts i) and ii) is estimated supposing that the above two cuts reject the events with the same ratio as in the case of well measured events; 167.5 events (= 176x1,278/(1,278+51+14), see Table 1(a)).

The number of the charge exchange events totally observed in the fiducial volume (see Fig. 57(b)) was 1,445.5 as the result, and the sum of weights of these events was

$$W^{tot} = 34,851 \ \text{ in 223,749 frames.} \qquad \text{(V-26)}$$

The cross section corresponding to this number of events is calculated by the same method employed in Section V-1-iii to be

$$\sigma^{tot'}_{chex} = 11.36 \text{ mb.} \qquad \text{(V-27)}$$

V-2-iv. Correction I (Spurious Association)

The result for $\sigma^{tot'}_{chex}$ obtained should be corrected concerning spurious associations. An event of the suprious association is such that, the origin of the antineutron yielding a star within the fiducial volume is not the 0 prong observed in the same frame even if it looks like a genuine event accidentally. Occurence of such events is due to the fact that the antineutron between 0-prong vertex and odd-prong star is invisible. The frequency of the accidental coincidence can be estimated using the known numbers of both isolated stars and 0 prongs as follows

The isolated stars were picked up on scanning which were called 'unassociated stars' as classified in Section III-4-ii, and these events are summarized in Table 16. The number of 0 prongs were obtained in the beam counting as described in V-1-ii. The samples of 5-prong star are used here because these are more detectable than 3-prong stars, and the number of chances of the accidental coincidence N is given by

$$N = \frac{N_1 N_2}{2N_f}, \qquad \text{(V-28)}$$

where

N_f; number of frames used on scanning,

N_1; number of 0 prongs observed in N_f frames without any regard for the stars,

N_2; number of unassociated 5-prong stars observed in N_f frames.

N ; number of the chances of accidental coincidence that a 5-prong star and a 0 prong, which are not connected in truth, appear in the same frame accidentally.

The ratio of the number of the chances of suprious association to that of genuine association for 5-prong events is

$$\varepsilon_1 = N/M, \qquad \text{(V-29)}$$

where M is the number of associated 5-prong events in N_f frames and ε_1 the fraction to be estimated. The result, thus obtained, is

$$\varepsilon_1 = 9.6\ \% , \qquad \text{(V-30)}$$

which should be hold in the 3-prong case, too.

V-2-v. Correction II (Scanning Biases)

The method of scanning employed in this experiment might cause scanning biases and they might distort the data. One of the biases to be taken into account is a scanning loss of events with short-path length of $\bar{n}$. When $\bar{p}p$ and $\bar{n}p$ vertices of these events are very close they are less detectable than the normal ones.

A distribution for the antineutron path length, given in Figure 65(a) shows a dip at the small value (<2 cm), and this feature is also observed in the distribution of x/L, a ratio of an antineutron path length to the potential length (see Fig.63).

This common feature implies the loss of events with short path length of $\bar{n}$, and the loss is estimated by extrapolating the smooth behavior (at $x > 2$ cm) in Fig.65(a) to the dip region ($x \leq 2$ cm). The ratio of the lost events to the observed ones, thus obtained, is

$$\varepsilon_2 = 2.6\ \%, \qquad \text{(V-30)}$$

which is consistent with what obtained from the distribution for x/L.

Another possible bias is a scanning loss of events depending on the location of the vertices on a scanning table. To check this point a weighted distribution for the angle between the scattering plane ($\bar{p}$-$\bar{n}$ plane) and the perpendicular to the front glass of the chamber (approximately parallel to the optical axis) is shown in Figure 65(b). One can see from this Figure that the distribution is not inconsistent with flat one leading to the result of no systematic bias.

The over-all scanning loss explained in III-4-ii should be taken into consideration in calculation of the cross section. After two independent scans over all films the loss was estimated to be

$$\varepsilon_3 = 2.4\ \% \ . \tag{V-31}$$

V-2-vi. Total Charge Exchange Cross Section

Corrections due to ε_1, ε_2, ε_3 should be made on $\sigma^{tot'}_{chex}$ obtained in V-2-iii. The total cross section for $\bar{p}p$ charge exchange is given by

$$\sigma^{tot}_{chex} = \sigma^{tot'}_{chex}(1+\varepsilon_1)(1-\varepsilon_2)/(1-\varepsilon_3)$$

$$= 10.8 \text{ mb} \ . \tag{V-32}$$

Estimation of error is as follows. The statistical error due to the number of observed events is

$$\Delta\sigma^{tot}_{chex} = 0.28 \text{ mb}. \tag{V-33}$$

A systematic error due to the use of the empirical formula for $\sigma^{anh}_{np}(T)$, explained in V-2-iii in detail, is 1.3 %.

The same cross section was also obtained at Bombay group (Exposure II) with essentially the same method employed at Tokyo, and the result was

$$\sigma_{chex}^{tot} = 10.6 \pm 0.24 \text{ mb.} \qquad \text{(V-34)}$$

The two results are in good agreement and the small discrepancy may be caused by a small difference of the incident momenta between two group (Tokyo; 0.7 GeV/c, Bombay; 0.75 GeV/c).

An average value of the two results is

$$\sigma_{chex}^{tot} = 10.7 \pm 0.2 \text{ mb at } 0.73 \text{ GeV/c.} \qquad \text{(V-35)}$$

V-2-vii. Background Contamination

A possible background is the contamination due to $\bar{n}p$ elastic scattering before $\bar{n}p$ annihilation which deflects the direction of $\bar{n}$. The probability of occurence of such events can be estimated making use of the cross section for $\bar{n}p$ elastic scattering at low energies. But there is no data for such reaction, so that, it should be deduced from the data for $\bar{p}n$ elastic scattering by the charge symmetry.

Overcoming the difficulty as pointed out in ref. 18), a measurement of the cross section for $\bar{p}n$ scattering together with that for $\bar{p}p$ scattering was made below 1 GeV/c in a deuterium bubble chamber experiment at Melbourne.[133)] Data of differential cross sections for both $\bar{p}n$ and $\bar{p}p$ scattering were published at 0.735 and 0.940 GeV/c,[133)] where a typical diffractive structure was observed in both $\bar{p}n$ and $\bar{p}p$ data with the same order of magnitude.

From the characteristics of the above-mentioned data, the cross section for $\bar{n}p$ scattering is guessed not far from that for $\bar{p}p$ scattering, therefore it is assumed that at the average momentum of the observed antineutrons (0.6 GeV/c) a $\bar{n}p$ scattering occurs with the same frequency as in the $\bar{p}p$ case (65 mb at 0.6 GeV/c).[134)]

Since the sum of total path length of $\bar{n}$'s was 125m for the samples of 1,111 events, the number of events for $\bar{n}p$ scattering between the 0-prong vertex and odd-prong star is expected to be 30 events, which corresponds to about 3 % of all events.

It is difficult to make a quantitative discussion concerning the effect of such events on the result for $\bar{p}p$ charge exchange cross section. However, since the antineutrons from $\bar{n}p$ scattering are emitted mainly in the forward directions due to the diffraction scattering, the result for $\bar{p}p$ charge exchange could not be changed significantly in conclusion. Only 6 events with heavily ionized tracks between the 0 prong and star were found up on scanning, which were probably the $\bar{n}p$ scattering.

Another contamination is background events due to inelastic charge exchange scattering (V-5), namely

$$\bar{p}p \longrightarrow \bar{n}n\pi^0 \ . \qquad\qquad (V\text{-}5)$$

But the contribution of such events is negligible, because only 0.3 % of all events for the Exposure I (and 22 % for Exposure II) is above the threshold momentum for reaction (V-5), see V-1-i, and furthermore the charge exchange scattering should be dominant over the inelastic charge exchange one by analogy of $\bar{p}p$ elastic (V-3) and inelastic (V-6) cases.[134)]

V-3. Results and Comparison with Other Experiments

V-3-i. Annihilation Cross Sections

Subtracting σ_{chex}^{tot} from the 0-prong cross section and σ_{chex}^{el} from the 2-prong one (see V-2-ii), $\bar{p}p$ annihilation cross sections with 0, 2, 4, 6, and 8 prongs were obtained together with the branching ratios to the total annihilation cross section σ_{anh}^{tot} as follows;

$$\sigma_{anh}^{0\text{-prong}} = 2.0 \pm 0.4 \text{ (mb)}, \quad 2.8 \pm 0.6 \text{ (\%)}, \qquad \text{(V-36)}$$

$$\sigma_{anh}^{2\text{-prong}} = 27.6 \pm 1.7 \quad , 39.0 \pm 2.6 \quad , \qquad \text{(V-37)}$$

$$\sigma_{anh}^{4\text{-prong}} = 37.6 \pm 0.6 \quad , 53.1 \pm 1.7 \quad , \qquad \text{(V-38)}$$

$$\sigma_{anh}^{6\text{-prong}} = 3.6 \pm 0.2 \quad , 5.1 \pm 0.3 \quad , \qquad \text{(V-39)}$$

$$\sigma_{anh}^{8\text{-prong}} = 0.04 \pm 0.02 \quad , 0.06 \pm 0.03 \quad , \qquad \text{(V-40)}$$

$$\sigma_{anh}^{tot} = 70.8 \pm 1.9 \quad . \qquad \text{(V-41)}$$

The average multiplicity for multi-particle production processes is defined as

$$\langle n \rangle = (1/\sigma) \sum_i n_i \sigma_i , \qquad \text{(V-42)}$$

with

$$\sigma = \sum_i \sigma_i ,$$

where subscript i represents each channel and n_i, σ_i are the multiplicity, the cross section of channel i respectively.

The average multiplicity for negatively charged meson $\langle n^- \rangle$ in the $\bar{p}p$ annihilation is calculated from the data (V-36)-(V-41) as follows

$$\langle n^- \rangle = 1.61 \pm 0.03 \ . \qquad \text{(V-43)}$$

A Dalitz pair which might be overlooked on scanning increases the number of charged mesons of the event by 2 by deceit, so that it should be checked on this point. Numbers of obvious Dalitz pairs observed are (5, 31, 23, 3) for (0-, 2-, 4-, 6-prong event) which correspond to (2.5, 1.1, 0.6, 0.8) % of the annihilation cross sections (V-36)-(V-40).

Taking into account π^o partial decay mode

$$\pi^o \longrightarrow e^+e^-\gamma$$

with fraction 1.17 %,[112] the average multiplicity for π^o in the $\bar{p}p$ annihilation can be deduced from eq. (V-42) as

$$\langle n^{\pi^o} \rangle \simeq 0.74 \ . \qquad \text{(V-44)}$$

Comparing the results (V-43) and (V-44), one can guess that half or more of the Dalitz pairs associated to the annihilating events may be overlooked on a scanning table. However percentage of such misidentified events is only 1 %, if any, of the annihilation samples, which is too small to bring a significant bias.

V-3-ii. Minimum Number of Angular Momentum

The knowledge of the elastic cross section σ^{el} and the total cross section σ^{tot} allows us to make a statement on the minimum number of angular momentum partial waves contributing to the annihilation process. According to Rarita et al.,[135] σ^{el} and σ^{tot} are expressed as

$$\sigma^{el} = (\pi/k^2) \sum_{l=0}^{\infty} (L_l^2 + M_l^2)/(2l + 1), \qquad \text{(V-45)}$$

$$\sigma^{tot} = (2\pi/k^2)\sum_{l=0}^{\infty} L_l , \qquad \text{(V-46)}$$

where k is the wave number, L_l and M_l (both real) are related to the usual (complex) phase shift δ_l as

$$L_l + iM_l = (2l+1)(1-e^{2i\delta_l}).$$

For given σ^{el} and σ^{tot}, eqs. (V-45) and (V-46) place certain restrictions on the (L_l,M_l). We are interested in the case in which $L_l=M_l=0$ when $l>\bar{l}$ for given $\bar{l}$. In order to determine the minimum allowable value of $\bar{l}$, the purely formal problem, in which $\bar{l}$ is given, is considered firstly. The condition, that (L_l,M_l) must satisfy for $l \leq \bar{l}$ in order that σ^{el} be a minimum for a given σ^{tot},
is sought. The method of Lagrange multipliers leads to

$$M_l=0, \quad L_l/(2l+1)=L_0 \qquad \text{(V-47)}$$

for $l \leq \bar{l}$. When eq. (V-47) holds, the sum in eq. (V-46) can be carried out to give a relation expressing L_0 in terms of $\bar{l}$ and σ^{tot},

$$L_0 = k^2 \ \sigma^{tot}/(2\pi(\bar{l}+1)^2). \qquad \text{(V-48)}$$

The corresponding value of σ^{el}, designated by σ^{el}_{min}, is the minimum consistent with the assumed values of σ^{tot} and $\bar{l}$. Therefore, for given values of the latter two quantities, σ^{el} must satisfy

$$\sigma^{el} \geq \sigma^{el}_{min} = L_0 \ \sigma^{tot}/2 = k^2(\sigma^{tot})^2/(4\pi(\bar{l}+1)^2), \qquad \text{(V-49)}$$

which is a consequence of eqs. (V-45), (V-47), and (V-48). From (V-49) it follows that for arbitrary σ^{el} and σ^{tot} the summations in (V-45) and (V-46) can be cut off above $l=\bar{l}$ only if $\bar{l}$ satisfies

$$(\bar{l}+1)^2 \geq k^2(\sigma^{tot})^2/(4\pi\ \sigma^{el}). \qquad \text{(V-50)}$$

This provides the restriction on $\bar{l}$ sought at the outset.

With the given values $\sigma^{el} = 51.2$ mb and $\sigma^{tot} = 132.8$ mb (see V-2-ii) for $\bar{p}p$ reactions at 0.7 GeV/c, which corresponds to the wave number $k= 1.676\ \text{fm}^{-1}$ in the center of mass system, $\bar{l}$ is obtained as

$$\bar{l} \geq 2\ . \qquad \text{(V-51)}$$

The present data indicate that at 0.7 GeV/c partial waves with values of the orbital angular momentum l (and total angular momentum J) up to at least $l=2$(and J=2), must contribute to the annihilation process.

V-3-iii. Comparison with Other Experiments

The cross sections (or the branching ratios) for $\bar{p}p$ annihilation below 1 GeV/c were published at rest[4), 0.43,[40),41) 0.55.[40),41) and 0.94[42) GeV/c, all of them are bubble chamber experiments. Figure 66(a) gives the total (kaonic plus pionic) annihilation cross sections of these results together with that at 0.7 GeV/c obtained in this experiment. The solid curve in this figure is the cross section obtained by fitting the data to the formula of the geometrical picture assuming an energy-dependence law of the type

$$\sigma_{anh}^{tot} = \pi(a+\lambda\!\!\!^{-}\ )^2, \qquad \text{(V-52)}$$

where $\lambda\!\!\!^{-}$ being the wave length of the relative motion. The best fit value is

$$a = 0.930 \pm 0.015 \text{ fm.} \qquad \text{(V-53)}$$

In the Koba-Takeda model[75)], the antinucleon-nucleon interaction is considered in terms of absorption and <<shadow>> scattering by a black sphere without any surrounding potential. In this aspect, the annihilation cross section has the form of eq.(V-52) and a is interpreted as the radius of the black sphere.

The branching ratios of the 0-prong, 2-prong, 4-prong, and 6-prong annihilation cross sections to the total annihilation ones below 1 GeV/c are given in Figures 66(b),(c),(d), and (e) respectively. The average multiplicities of negatively charged particles and two-particle correlation coefficients are also given in Figures 66(f) and (g) respectively (see the next section). Curves in these figures are explained in the next section. It seems from the figures that the distribution of annihilation events into various charged multiplicities does not show any appreciable variation below 1 GeV/c.

V-4. Discussion on the Result of Theoretical Models

V-4-i. Comparison with Orfanidis Rittenberg (OR) Model

Orfanidis and Rittenberg[36)] suggested that a statistical contribution is dominated over a multi-peripheral component in $\bar{p}p$ annihilation up to 5.7 GeV/c. They proposed a statistical model where $\bar{p}p$ annihilation occurs through a linear chain of fireballs (with no exotic quantum numbers) with each fireball decaying into a single pion and other fireball. This model is explained in Appendix A in detail. The energy dependence of the annihilation cross section is not given by the model, so that the branching ratios for the topological cross section are considered here.

The solid curves in Fig.66(b)-(e) are the predictions by this model. Assuming the all tracks at each topology to be pions, the agreement between the data and the predictions is satisfactory. The average multiplicity and the two-particle correlation coefficient for negatively charged particles are defined as

$$f_1^- = \langle n^- \rangle \quad , \tag{V-54}$$

$$f_2^- = \langle n^-(n^- - 1) \rangle - \langle n^- \rangle^2 . \tag{V-55}$$

Fig.66(f)-(g) gives the above quantities for the experimental data together with the predictions by OR model (solid curves), where agreement is also good. A salient feature of the data is the large negative correlation coefficient in the momentum range under consideration, which is also reproduced by the statistical model.

V-4-ii. Comparison with Lamb Model

The statistical model for antinucleon-nucleon annihilation, proposed by Lamb, incorporates SU(3) invariance and resonance production.[28)] In this model each particle (hadron) or resonance in both initial and final states is regarded as a member of the SU(3) multiplet in which it belongs. Consequently the transition matrix is built ensuring conservation of hypercharge, isospin, charge, and SU(3)-spin(or unitary spin), and the couplings are accomplished using SU(3) Clebsh-Goldan codfficients. Details for the numerical calculation are described in Appendix C.

The predicted branching ratios of 0-prong, 2-prong, 4-prong, and 6-prong annihilation cross sections to the total annihilation one, $<n^->$ and f_2^- are given in Figures 66(b)-(g) by dashed curves which were read from the figure of ref. 28) by the author. The predictions also reproduce the data well, while these are somewhat different from those by the OR model. It is not conclusive which of the two models is more appropriate to the data.

V-4-iii. Comparison with Goldberg Model

Goldberg136) employed a simple multi-Regge model of Chew and Pignotti137) $\bar{p}p$ annihilation processes and obtained an acceptable fit to the bulk of annihilation data at the incident momentum range 3-7 GeV/c. The Goldberg's method is as follows;

The reaction under consideration is

$$\bar{p}p \longrightarrow m\pi^+ m\pi^- k\pi^o, \qquad \text{(V-56)}$$

where both m and k are integers. The annihilation channel is constructed from baryon-exchange diagram, which resembles Figure 1(a). An assumption is made that only one B=1, I=1/2 trajectory with intercept α_B is present, and only pions are considered in the final state. The SU(2) invariant couplings are taken as $(2/3)^{1/2}g$(for $\pi\pm$) and $(1/3)^{1/2}g$ for (π^o) and the end couplings $(2/3)^{1/2}G$ and $(1/3)^{1/2}G$. The kinematic approximations of Chew and Pignotti lead to the cross section formula

$$\sigma_{m,k} = \left(G^4 e^{(2\alpha_B-2)Y} \frac{(g^2Y)^{2m+k-2}}{(2m+k-2)!} (1/3)^k (2/3)^{2m} \right) \\ \times\left(\frac{(2m+k)!}{k!(2m)!} \right), \qquad \text{(V-57)}$$

where $Y=\ln(s/M^2)$, and s,M are the total energy squared and nucleon mass respectively. The topological cross section is obtained by summing over k as

$$\sigma_m = G^4 e^{(2\alpha_B-2+g^2/3)Y} \left(\frac{4}{9} \frac{(2/3g^2Y)^{2m-2}}{(2m-2)!} + \right. \\ \left. \frac{4}{9} \frac{(2/3g^2Y)^{2m-1}}{(2m-1)!} + \frac{1}{9} \frac{(2/3g^2Y)^{2m}}{(2m)!} \right).$$

(V-58)

The total annihilation cross section $\sigma^{\bar{p}p}_{anh}$ and the charged average multiplicity $<n^{ch}>$ are

$$\sigma^{\bar{p}p}_{anh} = 1/2\ G^4 e^{(2\alpha_B - 2 + g^2)Y}\ , \qquad \text{(V-59)}$$

$$<n^{ch}> = \sum_{m=1}^{\infty} (2m)\sigma_m / \sigma^{\bar{p}p}_{anh} = 2/3g^2 Y + 4/3. \qquad \text{(V-60)}$$

With the above formula for σ_m(V-58) and with the parameters

$$\alpha_B = -0.14, \qquad \text{(V-61)}$$

$$g^2 = 1.68, \qquad \text{(V-62)}$$

$$G_4 = 240.0, \qquad \text{(V-63)}$$

which were obtained by Goldberg, the branching ratios, $<n^->$ and f_2^- are calculated as given in Fig. 66 by dot-dashed curves. One can see that the Goldberg model behaves differently from the statistical models and the data are not reproduced by this model. This fact implies that the Chew-Pignotti type multiperipheral mechanism in $\bar{p}p$ annihilation at low energies is negligibly small.

V-4-iv. $\bar{p}p$, $\bar{K}K$, e^+e^- Annihilations and Statistical Model

Positron-electron(e^+e^-) annihilation process have been[37)-39), 138)-142)] investigated together with $\bar{p}p$ annihilation one by many authors both theoretically and experimentally. The two annihilation processes share a common feature of an absence of a diffractive contribution to the final state. Furthermore the quantum numbers of the both initial states are commonly given as

Q(charge) =0,

B(baryon number) =0,

S(strangeness) =0,

I(isospin) = mixed state of I=1 and I=0.

It is observed[139)] that the e^+e^- annihilation process is dominated by a single photon exchange, namely the initial state is

$$J^{PC} = 1^{--},$$

while the $\bar{p}p$ annihilation in flight occures with a lot of initial J^{PC} state;

$$J^{PC} = 0^{-+},\ 0^{++},\ 1^{+-},\ 1^{++},\ 1^{--},\ 2^{-+},\ \ldots$$

where J=intrinsic angular momentum; P=parity, C=charge conjugation.

Irrespect to whether the e^+e^- annihilation takes place through a mediation of partons (parton model)[138)] or vector mesons such as $\rho°$, ω or ϕ (vector meson dominance model),[138)] statistical model considerations may at least partially describe the process. From a more dynamical point of view, the process may be regarded as a formation of a single fireball of energy.[142)] The decay of that fireball provides an excellent situation for using statistical ideas. In fact, the OR model proposes a description for the decay process of such fireballs on a standpoint of statistical mechanism, therefore it is meaningful to test the OR model to reproduce the data of e^+e^- or $\bar{K}K$ (see below) annihilations although the model is that for $\bar{p}p$ annihilation.

Regardless of the detailed mechanisms occuring in the two processes ($\bar{p}p$ and e^+e^- annihilations), the number of charged pions appearing in the final states are compared with the O-R statistical model in the following. Data for $\bar{K}K$ annihilation, which are also available to be taken into consideration, are presented by Fry et al.[38)] They had analyzed the reaction

$$K^-p \longrightarrow \Lambda + \text{pions}$$

at 8.25 GeV/c and measured the pion multiplicities of the process

$$\bar{K}K \longrightarrow \text{pions} ,$$

with available energy of the pion system defined as

$$s(\pi) = (K^- + p - \Lambda)^2,$$

where K^-, p and Λ are the four-vector momenta.

Figures 67(a), (b), and (c) show e^+e^-, $\bar{K}K$ and $\bar{p}p$ data for the branching ratios of 2-prong, 4-prong, and 6-prong annihilation cross sections to the total ones, respectively, versus s, the available energy squared. Our data for $\bar{p}p$ annihilation at 0.7 GeV/c are indicated by closed circles, and other data are cited from the paper by Fry et al.38) For these data, we extrapolated the calculation of the model below 4 GeV^2 and drew curves of the predictions as given in Figure 67.

A feature in these figures is that: the ratio of 2 prongs for e^+e^- or $\bar{K}K$ annihilation is systematically larger than that for $\bar{p}p$ annihilation and it is reversed for 4-prong case. However behavior of the predictions as a function of s is similar to that of e^+e^- and $\bar{K}K$ data. These facts imply that: the chain decay scheme of fireballs of the OR model is not so suitable for e^+e^- or $\bar{K}K$ annihilations than the $\bar{p}p$ case, but the gross feature of the e^+e^-, $\bar{K}K$ data (energy dependence) may retain the statistical mechanism.

VI. Summary of Results

In this section we summarize the results drawn from our analysis.

A bubble chamber analysis for the antineutron-proton annihilation process

$$\bar{n}p \rightarrow (n_1+1)\pi^+ + n_1\pi^- + n_2\pi^0 \quad , \qquad \text{(VI-1)}$$
$$(n_1=1,2,3, \quad n_2=0,1,2,\ldots)$$

has been made around 0.65 GeV/c based on about 3,500 events in 636,932 pictures. The number of films used at present corresponds to $\sim$11 events/μb of statistics. At the same time topological cross sections of antiproton-proton annihilation process

$$\bar{p}p \rightarrow m(\pi^+ + \pi^-) + (\text{neutrals}) \; , \qquad \text{(VI-2)}$$
$$(m=0,1,2,3,4)$$

have been obtained at 0.7 GeV/c.

The liquid hydrogen density in operating condition of the bubble chamber was deduced by measuring muon ranges of the decay $\pi^+ \rightarrow \mu^+ + \nu_\mu$ (Section III). Checks for measuring devices and for computer processing steps were made by means of evaluation of mass values of K^0 and ω mesons in this experiment, and it was found that the values were in good agreement with those appearing in the Tables of Particle Properties (Section III).

The measured data were processed through the THRESH-GRIND program chain, and contaminations due to background events were checked carefully at several stages of the data handling flow(Section III). Results can be summarized as follows.

$\bar{n}p$ annihilation

(1) The following general features were observed among produced particles in this reaction:

i) Topological branching ratios of $\bar{n}p$ annihilation were obtained as 3 prongs : 5 prongs : 7 prongs = 1 : 0.39 ± 0.03 : 0.013 ± 0.004 . These ratios are in very good agreement with the predicted values 1 : 0.376 : 0.016 by Orfanidis-Rittenberg(OR) statistical model. The ratios also agree with those of $\bar{p}n$ data below 1 GeV/c(Section IV-1).

ii) The branching ratios for pion multiplicities were estimated as given in Tables 5,6 together with those predicted by the OR model and those of $\bar{p}n$ data. It should be noticed that after the missing-mass cut for the samples fitted to $2\pi^+\pi^-\pi^o$ channel we estimated the amount of background events due to multineutrals about 40 % in the samples. The given ratios are in agreement with the predictions and those of $\bar{p}n$ data except that for $2\pi^+\pi^-\pi^o$. This discrepancy may be caused by uncertainty in the estimation of the background(Section IV-1).

iii) It was found that the $\bar{n}p$ annihilation produces resonances (mostly ρ, f and ω) copiously (see Table 8). The $(\pi^+\pi^-)$ effective mass distribution of the reaction $\bar{n}p \rightarrow 3\pi^+ 2\pi^-$ showed an enhancement at $\sim$700 MeV with absence of a bump at the position of ρ meson. This fact may be caused by energy conservation law forbidding the emission of the high-mass part of ρ Breit-Wigner[145)] or by ρ-ω interference effect with destructive interference. This point is not solved yet (Section IV-2).

iv) The $(\pi^+\pi^-)$ effective mass distribution of $2\pi^+\pi^-\pi^0$ samples for forward and backward dipions with respect to the incident $\bar{n}$ in CM system showed a characteristic feature of ρ-ω interference effect based on the G-parity conservation law. The ratio of the magnitudes of the ω amplitude to the ρ one was determined as

$$A(\bar{n}p \to \pi^+\pi^0\omega;\omega \to \pi^+\pi^-)/A(\bar{n}p \to \pi^+\pi^0\rho;\rho\to\pi^+\pi^-) \sim 1/3 \quad \text{(VI-3)}$$

together with the large coherence factor(~ 0.75) between them (Section IV-3).

v) Single-particle distributions of pions($|p|$,p_T momenta, production angles in CM system) were given by the phase space predictions in general. However, among the above distributions the production angle of π^0 for both $2\pi^+\pi^-\pi^0$ and $3\pi^+2\pi^-\pi^0$ samples deviate slightly from a flat distribution which might be caused by contaminations due to multineutrals underlying the samples (Section IV-5).

vi) The GGLP effect between like-charge pions was observed for the 3π, 4π, 5π, and 6π final states. Introduction of the weight due to symmetrized wave functions for like-charge pions could describe the data of opening-angle distributions quantitatively. An effect of the resonance production on the distributions should not be negligible which was not concerned at present(Section IV-6).

vii) Energy dependence of $\bar{n}p$ annihilation rate with odd pions, even pions and the total did not show any significant signals concerning s-channel resonances. A test to search for s-channel resonances in this experiment is difficult because the structure appearing in the differential cross section of $\bar{p}p \to \bar{n}n$ [6)] disturbs a smooth behavior of the rate and furthermore the absolute cross sections of $\bar{n}p$ annihilations at various energy intervals were unable to be evaluated in this experiment(Section IV-10).

(2) Comparison of our data with various models lead to the results:

vii) The CLA model, in which resonances were assumed to have the same kind of coupling with a nucleon trajectory, reproduced the data of single-particle distributions in CM system, opening angles of dipions in CM system, and effective-mass distributions for $2\pi^+\pi^-$, and $2\pi^+\pi^-\pi^0$ samples well. We can emphasize that this model reproduced the rates of resonance productions qualitatively and this fact may throw light on the resonance production mechanism of $\bar{N}N$ annihilation(Section IV-4).

viii) Threshold-like enhancements for exotic combinations of produced particles were observed as predicted by Rubinstein(a dual-dynamical effect).[30)][31)] However quantitative discussion is difficult because of the combinatorial background which increases with increasing multiplicity. Such enhancements were reproduced by the Bose-Einstein statistics fairly well(Section IV-6).

ix) An analysis using multiparticle variables (transverse momentum flow and charge flow quantities along the particles ordering in rapidity) gave the result that the annihilation is taken place mostly through statistical mechanism (Section IV-7).

x) Inclusive analyses with respect to the thermodynamic model and the Müller-Regge model were carried out. For the former case the maximum temperature appearing in the Hagedorn model[47)] was determined as ~ 114 MeV. For the latter case missing-mass spectra for $\bar{n}p \rightarrow \pi^{\pm}$ + ANYTHING were in contradiction with the predictions by the Rittenberg-Rubinstein model,[34)] and were in good agreement with the predictions by the OR model(Section IV-9).

xi) The Dalitz plot for $\bar{n}p \rightarrow 2\pi^+\pi^-$ showed the structure (a hole at $s{\sim}t{\sim}1$ GeV^2 and concentration of events at both ρ and f bands) as observed in the Dalitz plot for $\bar{p}n \rightarrow 2\pi^-\pi^+$. In spite of very poor statistics, the distribution of events in the Dalitz plot was consistent with the prediction on the basis of 4-point Veneziano amplitude for $J^P=2^+$ (Section IV-8).

<u>$\bar{p}p$ annihilation</u>

As for $\bar{p}p$ reaction we found:

i) Topological cross sections for 0 prong, 2 prongs, 4 prongs, 6 prongs and 8 prongs at 0.7 GeV/c were determined together with the total cross section. In evaluation of 0-prong and 2-prong annihilation cross sections, $\bar{p}p$ charge exchange cross section and elastic scattering one were measured and subtracted from 0-prong and 2-prong cross sections respectively(Section V-3).

ii) Under the consideration of unitarity and cutoff of higher partial waves, it was found that the partial waves with orbital angular momentum l (and total angular momentum J) up to at least l=2 (and J=2) must contribute to the annihilation process(Section V-3).

iii) A fit of $\bar{p}p$ annihilation cross sections between 0.4~1 GeV/c to the form $\sigma_{annihi} = \pi(a+\lambda\!\!\!^{-})^2$, where $\lambda\!\!\!^{-}$ being the wave length of the relative motion, gave $a=0.930 \pm 0.015$ fm which could be interpreted as the radius of the black sphere in $\bar{p}p$ scattering (Section V-3).

iv) The topological branching ratios (assuming that all tracks were pions) were compared with predictions by the OR model, Lamb model (SU(3) invariant statistical model)[28)] and Goldberg model (multi-Regge model).[136)] The Goldberg model was ruled out. Both of the OR model and Lamb model reproduced the data well(Section V-4).

v) We extrapolated the OR model below $\sqrt{s} = 2m_N$ and compared the predictions, thus obtained, with topological branching ratios of $\bar{K}K$ and e^+e^- annihilations.[38)] The data of the ratios of 2 prongs for $\bar{K}K$ and e^+e^- annihilations are substantially larger than those for $\bar{p}p$ annihilation and it is reversed for 4-prong case at the same energies up to $s=14$ GeV^2. It seems that the predictions by the OR model reproduce the behavior of energy dependence of the data of $\bar{K}K$ and e^+e^- annihilations well, however the ratios of 2 prongs and 4 prongs are systematically larger and smaller than the predictions respectively (Section V-4).

Finally we give some comments concerning the quality of the data used in the present analysis.

i) The cut on the missing-mass squared distributions for the fitted events was taken into account only for Tokyo data, therefore the contaminations due to multineutrals were not concerned for the events in Bombay and Neuchatel data.

ii) In the inclusive analysis, all of the charge tracks were assumed as pions, Furthermore 1-prong events were not taken into consideration and nofit events obtained at Bombay were not used.

Our opinion is that the results give good information on investigation on the annihilations,even if the data suffer distortions a little by the above reason (explained in the text).

VII. Discussion and Conclusion

In this section we make a discussion on the results, summarized in Section VI, and try to understand the mechanism of $\bar{N}N$ annihilations. For this attempt, we make a discussion concerning (A) study of $\bar{n}p$ annihilation in comparison with $\bar{p}n$ annihilation in a deuterium bubble chamber, (B) study of the dynamics ruling $\bar{N}N$ annihilations.

(A) $\bar{n}p$ and $\bar{p}n$ annihilations

One of the interesting points in this experiment is to compare $\bar{n}p$ data with $\bar{p}n$ ones as mentioned in Section I. Our experiment of $\bar{n}p$ annihilation gives a result, within its statistics, that the data on $\bar{n}p$ annihilation agree in gross feature with those of $\bar{p}n$ annihilation in $\bar{p}d$ reactions for the following points:

i) charged prong multiplicities,
ii) pion multiplicities,
iii) M_x^2 distributions in the inclusive analysis,
iv) structure in the Dalitz plot for the 3π state,
v) rates of resonance productions (for ρ, f, ω).

This fact tells us that the $\bar{p}n$ data for the above points of problem are not distorted although they are extracted in $\bar{p}d$ reactions and they give good information to investigate $\bar{N}N$ annihilations of pure isospin state ($I=1$).

On the other hand we have observed interesting features in the $\bar{n}p$ data as follows:

i) an enhancement at ~ 700 MeV in the $(\pi^+\pi^-)$ mass spectra of 5π samples with absence of the ρ peak,

ii) appearance of a structure at the ω mass position in $(\pi^+\pi^-)$ mass spectra of 4π samples characteristic to ρ-ω interference. For the former feature, which is not observed in p̄n data, we cannot interpret it quantitatively yet. It may be produced by ρ-ω interference effects or some kinematical effects[145], but such explanation seems not powerful.

The latter feature was observed slightly in a p̄d experiment[146] with 2 standard deviations, while our data give it with 3 standard deviations. Furthermore our data show that this feature is more pronounced for the events with the $(\pi^+\pi^-)$ dipion emitted into polar directions with respect to the incident n̄ in CM system. We explain this fact in such a way that the CM system could be defined more precisely in n̄p case than in p̄n case and by this reason the ρ-ω interference effect appears in the n̄p annihilation with high confidence level. We have tried fitting the form 'ρ+ω+ρ/ωint.+PS' to the data and the value of the coherence factor between ρ and ω amplitudes obtained is 0.75 ± 0.33. The large coherence is suggestive that the annihilation may take place overlapping between channels of pure G-parity as pointed out by Allison et al.[122) p̄p experiments have recently reported an evidence for ρ-ω interference in the reaction $\bar{p}p \rightarrow 4\pi$ at 1.26~1.65 GeV/c[122] and 1.6~2.2 GeV/c.[123] This fact together with our result may imply that the 4π final state in N̄N annihilations is sensitive to ρ-ω interference effects. Study of the ρ-ω interference effects in n̄p and p̄p annihilations at low energies varying the incident momenta is interesting for investigation of annihilation dynamics.

(B) Dynamics Ruling $\bar{N}N$ Annihilations

Description of dynamics ruling $\bar{N}N$ annihilations by the information obtained in this experiment is difficult because of the poor statistics, restricted final states and contaminations in the samples. However we can draw pictures concerning $\bar{n}p$ and $\bar{p}p$ annihilations from our results as follows where the data and models suitable for these are contrasted.

i)The topological branching ratios($\bar{n}p$,$\bar{p}p$) and pion multipilcities ($\bar{n}p$) are well represented by the OR statistical model.

ii)The single-particle distributions,correlations,inclusive analyses, multiparticle variable analyses suggest a statistical picture.

iii)The resonance production rates are reproduced by the CŁA model.

iv)The structure on the Dalitz plot is given by the dual model.

Although the models(OR model,CŁA model,dual model) can describe the data as mentioned above and these are not inconsistent each other by duality, each of them has defects as

OR model:	Distributions of produced particles are not predicted, resonances are not taken into account.
CŁA model:	Relative phases between amplitudes for a certain final state are not given, branching ratios are not predicted
dual model:	Branching ratios are not predicted, numerical calculations of the amplitude for many-particle final states are very complicated.

Therefore we cannot describe $\bar{N}N$ annihilation dynamics with one image compensating the above defects at present. However we emphasize that none of our data gives a result inconsistent with the three models within our statistics. This fact implies that $\bar{N}N$ annihilation itself may be ruled by more complex (or more simple) dynamics including these models consistently.

Comparison of topological branching ratios for $\bar{K}K$ and e^+e^- annihilations with the predictions by the OR model shows that energy dependence of the data is well reproduced by this model. We interpret this fact as: $\bar{K}K$ and e^+e^- annihilations are dominated by the statistical mechanism with the multiplicity distribution function employed in the OR model but the distribution function for charged particles should be modified to reproduce the data well, that is, the decay mode of the fireballs may be deformed from that of the linear-chain scheme.

To make further investigation for $\bar{N}N$ annihilations we suggest the following points with experimental aspect.

a) $\bar{n}p$ system (I=1) can produce a channel with fully charge mode, for example $\bar{n}p \rightarrow 2\pi^+\pi^-$, $3\pi^+2\pi^-$, which reduces a background due to the permutation of amplitudes, therefore they may produce data sensitive to the dynamics. Furthermore it is free from the deuteron complication. An experiment with high statistics for such channels is important especially to study the annihilation by means of dual model.

b) Analyses of the data of channels including kaons are attractive since such channels not only reduce the combinatorial background but also give the information for strange-particle productions in the annihilations. Data for branching ratios, effective mass distributions, resonance productions, single-particle distributions of produced particles and inclusive analyses of the channels should give good information to improve the above-mentioned models.

VIII. Appendices

Appendix A

Orfanidis-Rittenberg (OR) Model

In a recent paper[27)] Orfanidis and Rittenberg (hereafter denoted OR) proposed a new statistical model to describe anti-nucleon nucleon ($\bar{N}N$) annihilation. They studied components of statistical behavior and multiperipherality in $\bar{N}N$ scattering both of which may contribute to the annihilation.

At high energies, experimental data indicated that secondary particles distributed with limited transverse momentum and with non-isotropic angular distributions in the CM system, which were characteristic in a multiperipheral picture. Therefore they considered the statistical behavior dominance in the annihilation up to 6-7 GeV/c.

The following assumption is made in the statistical model. Integrated cross sections for $\bar{N}N$ annihilation are represented as

$$\bar{\sigma}_{n,l} = f_{n,l} a_n(s), \qquad \text{(A-1)}$$

for the reaction

$$\bar{p}p \longrightarrow l\pi^- + l\pi^+ + (n-2l)\pi^o, \qquad \text{(A-2)}$$

and

$$\bar{\sigma}_{n,l}^{(-)} = f_{n,l}^{(-)}\, a_n(s), \qquad \text{(A-3)}$$

for

$$\bar{p}n \longrightarrow l\pi^- + (l-\imath)\pi^+ + (n-2l+\imath)\pi^o, \qquad \text{(A-4)}$$

where s is the total energy squared in the CM system and n,l are positive integers. $a_n(s)$ is a factor depending on n-body phase space and $f_{n,l}$($f_{n,l}^{(-)}$) represents the number of configurations in which an initially neutral (negatively charged) fireball decays into n pions of which l have negative charge. To determine the number of $f_{n,l}$ and $f_{n,l}^{(-)}$, it is assumed that $\bar{N}N$ annihilation takes place through a "linear decay chain" of fireballs, that is, only two-body decays occur along the chain which produces always a pion and another fireball at the decaying vertex. Furthermore the fireball retains non-exotic quantum numbers at each stage. Figure 1(a) gives the decaying scheme where solid, dotted and thick lines represent charged pions, neutral pions and fireballs respectively.

$f_{n,l}$ and $f_{n,l}^{(-)}$ thus obtained are

$$f_{n,l} = \alpha^{2l} \binom{n}{2l} , \left(0 \leq l \leq \begin{matrix} n/2 (n \text{ even}) \\ (n-1)/2 \ (n \text{ odd}) \end{matrix}\right), \qquad \text{(A-5)}$$

$$f_{n,l}^{(-)} = \frac{1}{\alpha}\alpha^{2l-1} \binom{n}{2l-1}, \left(1 \leq l \leq \begin{matrix} n/2 \ (n \text{ even}) \\ (n+1)/2 \ (n \text{ odd}) \end{matrix}\right), \qquad \text{(A-6)}$$

with $\alpha = \sqrt{2}$.

From equations (A-1) through (A-6), the ratio of $\bar{p}p$ annihilation cross section to $\bar{p}n$ one is estimated as

$$R = \frac{\bar{\sigma}_{\bar{p}p,\mathrm{ann}}}{\bar{\sigma}_{\bar{p}n,\mathrm{ann}}} = \alpha = \sqrt{2}. \qquad \text{(A-7)}$$

This result suggests that the ratio R should be approximately energy independent if the statistical component dominates the annihilation processes, which is true at low energies.

Comparison of experimental data with the OR model can be made with those of branching ratios instead of annihilation cross sections which are not given by the model. The branching ratios of the model are represented as

$$\sigma_{n,1} = \frac{\bar{\sigma}_{n,1}}{\bar{\sigma}_{\bar{p}p,ann}} \quad : \quad \sigma_{n,1}^{(-)} = \frac{\bar{\sigma}_{n,1}}{\bar{\sigma}_{\bar{p}n,ann}} \quad . \qquad \text{(A-8)}$$

Using eqs. (A-1) and (A-3), eq. (A-8) becomes

$$\sigma_{n,1} = P_{n,1}\, P_n(s) \quad : \quad \sigma_{n,1}^{(-)} = P_{n,1}^{(-)} P_n(s), \qquad \text{(A-9)}$$

where $P_{n,1}$ and $P_n(s)$ are probabilities

$$P_{n,1} = \frac{2\alpha^{21}\binom{n}{21}}{(1+\alpha)^n + (1-\alpha)^n} \quad : \quad P_{n,1}^{(-)} = \frac{2\alpha^{21-1}\binom{n}{21-1}}{(1+\alpha)^n - (1-\alpha)^n} \quad . \qquad \text{(A-10)}$$

$P_n(s)$ is assumed as a Gaussian form which is expected from the central-limit theorem;

$$P_n(s) = \frac{1}{\sqrt{2\pi}\,\sigma} e^{-\frac{1}{2}\frac{(n-\langle n\rangle)^2}{\sigma^2}} \quad , \qquad \text{(A-11)}$$

with

$$\sigma^2 = a\langle n\rangle, \qquad \langle n\rangle \sim s^b \quad , \qquad \text{(A-12)}$$

where a and b are unknown parameters which should be determined by other theoretical models or experimentally. From eqs. (A-9)-(A-12) one obtains the following expression for the correlation coefficients for negatively charged pions;

$$f_1^- = f_1^{-(-)} = \beta\langle n\rangle \quad (\equiv \langle 1\rangle), \qquad \text{(A-13)}$$

$$f_2^- = f_2^{-(-)} = (-1/2 - \beta(1-a))f_1^- \quad (\equiv \langle 1(1-1)\rangle - \langle 1\rangle^2), \qquad \text{(A-14)}$$

$$f_3^- = f_3^{-(-)} = (3/4 - \beta^2 + 3/2(1-a)\beta(1+2\beta))$$
$$(\equiv \langle 1(1-1)(1-2)\rangle - 3(\langle 1(1-1)\rangle - \langle 1\rangle^2)\langle 1\rangle - \langle 1\rangle^3), \qquad \text{(A-15)}$$

with

$$\beta = \frac{\alpha}{2(1+\alpha)} \quad .$$

From eq. (A-13) the average number of π^o's in $\bar{p}p$ annihilation is

$$\langle n_{\pi^o} \rangle = \langle n \rangle - 2f_1^- = \frac{2}{\alpha} f_1^- , \qquad \text{(A-15)}$$

which indicates that $\langle n_{\pi^o} \rangle$ is substantially larger than $\langle n_{\pi^-} \rangle$ or $\langle n_{\pi^+} \rangle$.

The parameters a and b are essentially free as mentioned above, and Orfanidis-Rittenberg took $a={}^1/4$ and $b={}^1/3$ from other theoretical models$^{147),148)}$ such that

$$\langle n \rangle = 5.05\left(\frac{s}{4M^2}\right)^{1/3}, \quad \text{(M=nucleon mass)}. \qquad \text{(A-16)}$$

The constant in eq. (A-16) was adjusted by OR to get the observed multiplicity for $\bar{p}p$ annihilation at rest. The value of α in eq. (A-10) should be $\sqrt{2}$ if only two-body decays occur along the fireball decay chain. Orfanidis-Rittenberg took α=1.5 in order to effectively take into account the multi-body decays and a small multiperipheral component.

Appendix B

Monte Carlo Method for Phase Space Integral

i) Method for the Integration

An important problem in the investigation of multiparticle production processes is the computation of the integral

$$I_n = \int^{4n} T\delta^4(P-\sum_{j=1}^{n} p_j)\prod_{i=1}^{n} \delta(p_i^2 - m_i^2)d^4p_i \ , \qquad \text{(A-17)}$$

where

P is the total four-momentum vector of the n-body system,

p_i is the four momentum vectors of the individual particles

m_i is the mass of the particles,

T is the matrix element squared.

The region of the integral is the whole physical region. The total cross section is evaluated by multiplying a flux factor to I_n, and the differential cross sections are obtained by integrating over the subspace of the entire phase space. T describes the interactions between the particles, and if there is no interaction between outgoing particles, namely T=1, I_n gives the n-body phase space integral.

As before, it is necessary to eliminate the δ functions in the integral (A-17) and to write I_n in the form[143)]

$$I_n = \int_V d\phi \ \rho_n(\phi)T(\phi)$$

$$= \int_V d\phi f_n(\phi). \qquad \text{(A-18)}$$

Here ϕ stands for the coordinate of a point in the 3n-4 dimentional phase space. The domain of integration V is the domain of integration in eq. (A-17) expressed in term of the phase space variables. The integrand $f_n(\phi) = \rho_n(\phi)T(\phi)$ is a product of the matrix element squared $T(\phi)$ and the phase space density $\rho_n(\phi)$. The dinsity $\rho_n(\phi)$ is the product of certain factors arising from the transformation of variables (the Jacobian) and from integration over delta functions.

When one applies the Monte Carlo methods to particle physics one does not evaluate the integrand $f_n(\phi)$ at a predetermined set of points, but rather chooses these points at random with a given density in phase space and evaluates $f_n(\phi)$ at these events. An event here is a set on n momentum vectors $p_1 \,..p_n$ in any given frame satisfying four-momentum conservation and the mass shell conditions $p_i^2 = m_i^2$, $i=1,\ldots,n$.

To be able to generate the events using a fast standard computer routines, the integral (A-18) is further transformed until each of the 3n-4 variables in ϕ has a simple range of variation. In fact one will find a set

$$\phi' = (r^{(1)} \ldots r^{(3n-4)}) , \tag{A-19}$$

so that the 3n-4 dimensional hypercube V'

$$0 \le r^{(i)} \le 1 , \; i=1, \ldots , 3n-4 , \tag{A-20}$$

and the physical region V corresponds to each other one-to-one. Now, the Jacobian from ϕ to ϕ' is $\partial\phi'/\partial\phi$, and the intergral (A-18) becomes

$$\begin{aligned} I_n &= \int_{V'} d\phi' \, \frac{\rho_n(\phi(\phi'))T'(\phi')}{\partial\phi'/\partial\phi} \\ &= \int_{V'} d\phi' \, \frac{T'(\phi')}{g_n'(\phi')} , \end{aligned} \tag{A-21}$$

with

$$g_n'(\phi') = \frac{\partial\phi'/\partial\phi}{\rho_n(\phi)} . \tag{A-22}$$

If the values of ϕ'_1, ..., ϕ'_N for N events are generated evenly in the hypercube (A-20), then the Monte Carlo estimate of I_n is

$$\bar{I}_n = \frac{1}{N} \sum_{k=1}^{N} w_k \quad , \tag{A-23}$$

$$w_k = \frac{T'(\phi'_k)}{g'_n(\phi'_k)} \quad . \tag{A-24}$$

If the distribution in some variable v or the derivative $\partial I_n/\partial v$ is requested, the range of v is devided in bins of width Δv, and the derivative is estimated by

$$\frac{\partial I_n}{\partial v} \cong \frac{\Delta I_n}{\Delta v} \quad . \tag{A-25}$$

Here $\bar{I}_n$ is given by eq. (A-23) with restriction that only events with v inside the given bin are included.

ii) Generation of Events by the FOWL

The phase space integral (T=1 in eq. (A-17)) R_n can be described by the two-body phase space factor R_2, as[144),116)]

$$R_n = \frac{1}{2M_1} \int \cdots \int \prod_{i=1}^{n-1} (2M_i \ R_2(M_{i+1} \ ; M_i, m_{i+1})) dM_{n-1} \cdots dM_2 \ , \tag{A-26}$$

with

$$R_2(M_{i+1}; M_i, m_{i+1}) = \frac{2\pi}{M_{i+1}} \sqrt{M_{i+1}^2 + (\frac{M_i^2 - m_{i+1}^2}{M_{i+1}})^2 - 2(M_i^2 + m_{i+1}^2)} \ , \tag{A-27}$$

where $R_2(M_{i+1}; M_i, m_{i+1})$ represents the invariant two-body phase space of mass M_{i+1} decaying into M_i and m_{i+1}. In the other words, n-body production process can be regarded as a chain process of two-body decay

$$M_{i+1} \longrightarrow M_i + m_{i+1} , \qquad \text{(A-28)}$$

where M_i and m_{i+1} are the masses of the trunk and branch (produced particle) in the i th decay process (similar to the scheme of Figure 1(a)).

M_j (j=2...n-1) is chosen so as to satisfy the physical condition using random numbers r_i.

$$M_j = r_j (M_n - \sum_{i=1}^{n} m_i) + \sum_{i=1}^{j} m_i , \qquad \text{(A-29)}$$

with

$$0<r_1<r_2<\ldots< r_j<r_{j+1}< \ldots<r_{n-2} <1 , \qquad \text{(A-30)}$$

where M_n and M_1 are the invariant mass of the initial state and the mass of the decay particle in the last stage(=m_1) respectively. The weight in eqs. (A-23), (A-24), which is proportional to

$$WT(M_k,m_k) = \prod_{i=2}^{n-1} (M_i R_2(M_{i+1};M_i,m_{i+1})) R_2(M_2;m_1,m_2) , \qquad \text{(A-31)}$$

is calculated in the FOWL.

For n-body final state, there are 3n-4 independent variables satisfying the energy- and momentum-conservation laws, therefore 3n-4 random numbers should be used for generation of an event. n-2 random numbers are spent to determine the invariant masses M_i in the chain decay process. Other 2n-2 are used to generate angles.

Since the two-body phase space is isotropic in angular space, polar angle θ_i and azimuthal one ϕ_i of m_{i+1} in the decay (A-28) are chosen to be isotropic in M_{i+1} frame as

$$\cos\theta_i = (2\bar{r}^{(i)}-1), i=1,\ldots,n-1\ , \qquad \text{(A-32)}$$

$$\phi_i = 2\pi r^{(i)}\ , \quad i=1,\ldots,n-1\ , \qquad \text{(A-33)}$$

where $\bar{r}^{(i)}$ and $r^{(i)}$ are random numbers with uniform distribution between 0 and 1. The final description of the event in the overall center of mass system is obtained by successive Lorentz transformations of each momentum.

iii) Test of the Random Numbers

Sequences of random numbers are classified into three types;116)

A; Truly random numbers are those which are chosen in such a way that at any given point in the sequence all numbers are equally probable and independent of the preceding numbers.

B; Pseudo-random numbers are those which are generated according to an arithmetic prescription so that each number depends on the preceding ones, but in such a way that any finite sequence (up to a certain maximum length) satisfies (nearly) the same statistical tests as a true random sequence.

C; Quasi-random numbers are generated according to an arithmetic prescription which results in certain strong correlations between the numbers in any short sequence, but in such a way that certain asymptotic properties of the distributions are more advantageous than the corresponding properties of truly or pseudo-random sequences.

The principle of quasi-random number generators is that certain correlations are harmless (depending of cource on the problem) and indeed they can sometimes be helpful. For an integration of k dimensions, sets of k random numbers are required, each set giving rise to a point in the space. The k numbers must be uncorrelated within each set. However certain correlations between successive sets of numbers do not cause any trouble. Therefore a subset of quasi-random numbers which have the property that the density of points is more uniform than that of truly random numbers is useful for the integration and it improves the convergence of the Monte Carlo estimate.

The random number generator employed in the FOWL is of the "shuffled quasi-random" type. It is based on the simple formula

$$R_{ij} = K_i * C_j \text{ , modulo 1,} \qquad \text{(A-34)}$$

where R_{ij} is the i th number ($i=1\sim 20$) generated for j th kinematical variables (3n-4 variables are required for an n-body event), C_j is the square root of the j th prime number (in fact it could be almost any irrational number), and K_i is a factor increasing with the number of events generated.

In order to eliminate the correlations between the random numbers, thus generated, the "shuffling" stage is accomplished in the following way; Before the first event, a matrix R_{ij} (i=1 ...20, j=1...3n-4) is filled using the first 20 numbers from each of the 3n-4 generators. Then for each event, a random choice among the 20 numbers is made for each variable, and the numbers used are replaced by the next number produced by each generator. An ordinary pseudo-random generator (supplied by the system library) is required for the "shuffling".

Events are generated by the FOWL using HITAC 8700 computer at KEK where one word is composed with 32 bits. Tests for the random numbers generated in the FOWL are made as follows.

50,000 random numbers are generated by the above-mentioned method and they are devided into five equal parts following the sequential order. Figure 68 gives distributions of the random numbers falling between 0 and 0.05 for each sequence of the five parts (each part contains 10,000 random numbers in a sequence). It is obvious from the figure that except the first sequence the uniformity is destroyed drastically. This fact implies that good estimate of the phase space integral cannot be given as long as one uses the FOWL at 32 bits machine. When the FORTRAN arguments in the generator of the FOWL are used with the double precision declaration (64 bits), the above defect is remedied and the uniformity is preserved (the distributions are given in Figure 69).

The non-uniformity in the case of 32 bits machine may be caused by the small number of the significant figures per word (7 significant figures), that is, the number K_i in eq. (A-34) increases with increase of the number of generated events which leads to the result that the number of significant figures of R_{ij} produced by "modulo 1" are not enough to cover the 3n-4 dimensional space uniformly.

In the present work, the "shuffling" type generator in the FOWL is replaced by a pseudo-random number generator supplied by the HITAC 8700 system library. The generator is

```
      SUBROUTINE RANDUN(IX,X)
      DATA IX/27561413/
      IX=IX*48828125
      IF(IX) 10,10,20
   10 IX=(IX+2147483647)+1
```

```
   20 X=FLOAT(IX)*0.4656613E-9
      RETURN
      END
```

Figure 70 gives the same quantity as given in Figures 68 and 69 using the random numbers generated by the above generator. The uniformity shown in this Figure 70 is not so good as that of Figure 69, which implies that the "shuffling" type generator gives more uniform random numbers than the pseudo-random gemerator. The reason why the "shuffling" type generator is not used in the present work is to avoid the trouble caused in the 32 bits case, which may arise in the 64 bits case when a number of generated events grows up large.

Appendix C

Lamb Model

Lamb model is a SU(3) invariant statiatical model proposed by Lamb to describe $\bar{N}N$ annihilation processes.[28)] Following to the model the annihilation cross section σ_i giving rise to a certain final state is represented by

$$\sigma_i = N_\sigma \, P_{\alpha,\beta,\ \ldots\gamma} S_n A^2_{SU(3)} \, \Omega_{1,m} \, R_n. \qquad \text{(A-35)}$$

Each factor of the above formula is explained in the following.

N_σ is the normalization factor defined by

$$N_\sigma = \frac{N}{P_{CM} E_{CM}} \ , \qquad \text{(A-36)}$$

where P_{CM} and E_{CM} are the incident momentum and total energy in the CM system, and N is a constant(independent of energy) which converts the final statistical weights into absolute cross sections. The denominator gives the incident particle flux. The constant N is found by normalizing the sum of all the final-state statistical weights at a given energy to the experimental cross section. Lamb obtained the value considering data at four different energies as

$$N = (4.61 \pm 0.27) \times 10^{-2} \ \mathrm{GeV}^3 \mathrm{mb}. \qquad \text{(A-37)}$$

$P_{\alpha,\beta,..\gamma}$ is the permutation factor defined by

$$P_{\alpha,\beta,..\gamma} = \frac{n!}{n_\alpha! \ n_\beta! \ \ldots \ n_\gamma!} \ , \qquad \text{(A-38)}$$

where $n_\alpha, n_\beta, ..n_\gamma$ are the numbers of identical particles of kind of α, β, ..γ respectively appearing in the final state, and n is the total number.

S_n is the spin weighting factor. Spin states of j th particle of spin S_j are

$$-S_j,\ -S_j+1,\ \ldots\ S_j. \qquad \text{(A-39)}$$

Regardless of the other quantum number eigen values of the final state, the above states are equally probable and will be equally populated. Thus the angular momentum "phase space" of the final state is given by the spin weighting factor

$$S_n = \prod_{j=1}^{n} (2S_j+1). \qquad \text{(A-40)}$$

$\underline{R_n}$ is the invariant phase space defined as

$$R_n = \int\ldots\int (2m_\pi)^n (2\pi)^4 \ \delta^4(k_f-k_i) \prod_{j=1}^{n} (2\pi)\ \delta(k_j^2-m_j^2)\frac{d^4k_j}{(2\pi)^4}, \qquad \text{(A-41)}$$

where k_f, k_i and k_j are four-momentum vectors of final state, initial state and j th particle respectively. The factor in eq. (A-41)

$$\prod_{i=1}^{n} m_\pi \quad , \qquad \text{(A-42)}$$

is introduced to retain the concept of an interaction volume. $\underline{\Omega_{1,m}}$ represents the interaction volume of $\bar{N}N$ interaction defined by

$$\Omega_{1,m} = \Omega^{1-1}(\pi)\Omega^m(K), \qquad \text{(A-43)}$$

$$\Omega(K) = R\Omega(\pi), \qquad \text{(A-44)}$$

$$\Omega(\pi) \sim \gamma\Omega_\pi \ . \qquad \text{(A-45)}$$

Here 1 is the number of non-strange and m is the number of strange particles; thus

$$1+m=n, \qquad \text{(A-46)}$$

where n is the total number of the particles. γ is the Lorentz contraction factor. $\Omega(\pi)$ and $\Omega(K)$ are the interaction volumes for non-strange and strange particles respectively, which are introduced under consideration that the strange particles are created close to the core of the pion cloud surrounding the incident particle and hence they reach statistical equilibrium only within a somewhat smaller volume than do non-strange particles.

Lamb obtained the values for the radius of the pion interaction volume R_π and the ratio R of $\Omega(K)$ to $\Omega(\pi)$ by the least square fit to experimental data as

$$R_\pi = (1.75 \pm 0.020) - (0.337 \pm 0.001) E_{CM} \lambda, \qquad \text{(A-47)}$$

$$R = (0.48 \pm 0.03), \qquad \text{(A-48)}$$

where λ and E_{CM} are the pion Compton wave length and the total energy in CM respectively.

$\underline{A_{SU(3)}}$ describes the SU(3) invariant amplitude, which is an essential quantity in the Lamb model. The amplitude is built by the following procedure.

The SU(3) invariance of the transition matrix T is introduced into the model by expanding each initial and final state over SU(3) eigenstates. Having expanded the states in this way, T will be automatically invariant if it is a scalar quantity and connects only identical SU(3) eigenstates.

Each particle participating the annihilation is considered as a member of an SU(3) representation or supermultiplet, and the wave function for a state is given by

$$\Phi_f = \phi_1(d_1, i_1, i_{31}, y_1) \ldots\ldots \phi_n(d_n, i_n, i_{3n}, y_n), \qquad \text{(A-49)}$$

which is a product of individual particle wave functions. Here i, i_3, and y denote the isospin, isospin third component and hypercharge respectively. d (≡ D(p,q) denotes the SU(3) representation to which the particle belongs, and is related to SU(3) spin or unitary spin which is now conserved in the interaction. SU(3) invariance states that not only isospin

$$I^2=(\sum_{j=1}^{n} i_j)^2, \tag{A-50}$$

but also unitary spin

$$D^2=(\sum_{j=1}^{n} \otimes\, d_j)^2 , \tag{A-51}$$

are good quantum numbers. In order to exhibit this property, a system of basis states must be used in which both I and D are diagonal. The basis states of such a scheme can be denoted by

$$\phi(i_1 i_2(i_{12})i_3(i_{123})\ldots d_1 d_2(d_{12})d_3(d_{123})\ldots), \tag{A-52}$$

where

$$\begin{aligned} i_{12}^2 &=(i_1+i_2)^2, \\ i_{123}^2 &=(i_1+i_2+i_3)^2, \\ &\vdots \\ d_{12}^2 &=(d_1+d_2)^2, \\ d_{123}^2 &=(d_1+d_2+d_3)^2, \\ &\vdots \end{aligned} \tag{A-53}$$

Then the following unitary transformation can be written.

$$\begin{aligned} \Phi_f &=\phi_1(i_{31},y_1)\phi_2(i_{32},y_2)\ldots\phi_n(i_{3n},y_n) \\ &= \sum_{D_2,D_3,\ldots D_{n-1}} \sum_{I_2,I_3,\ldots I_{n-1}} R(D_1,D_2,\ldots D_{n-1} ; \\ &\quad I_2,I_3,\ldots I_{n-1};i_{31},i_{32},\ldots i_{3n};y_1,y_2,\ldots y_n) \\ &\quad \Phi(D_2,D_3,\ldots D_n;I_2,I_3,\ldots I_n), \end{aligned} \tag{A-54}$$

where the coefficient R is the unitary spin recoupling coefficient which is a product of SU(3) C-G coefficients, and I_j, D_j are

$$I_j = i_{123..j} \, , \tag{A-55}$$

$$D_j = d_{123..j} \, . \tag{A-56}$$

Finally eq. (A-54) becomes

$$\Phi_f = \sum_{D_2,D_3,\ldots D_{n-1}} \; \sum_{I_2,I_3,\ldots I_{n-1}} \; \prod_{j=1}^{n} C^{d_{j-1} d_j D_j ; i_{j-1} i_j I_j}_{y_j Y_j ; i_{3j} I_{3j}}$$

$$\Phi(D_2,D_3,\ldots D_n ; I_2,I_3,\ldots I_n)$$

$$= A_{D_n,I_n} \; \Phi(D_2,D_3,\ldots D_n ; I_2,I_3,\ldots I_n) . \tag{A-57}$$

Describing both initial state Φ_i and final state Φ_f by the same expression of eq. (A-57), the SU(3) invariant matrix element can be written as

$$|\langle\Phi_f|T|\Phi_i\rangle|^2 = \bar{T}^2 \delta_{B'B} \ldots \; \delta_{I_{32}',I_{3n}} |\langle\Phi_f|\Phi_i\rangle|^2$$

$$= \bar{T}^2 \delta_{B'B} \ldots \delta_{I_{32}',I_{3n}} |A_{D_n I_n} A_{D_2' I_2'}|^2$$

$$= \bar{T}^2 \delta_{B'B} \ldots \delta_{I_{32}',I_{3n}} \; A^2_{SU(3)} \, . \tag{A-59}$$

Here primes denote the initial state. Also, in this expression all external quantum numbers are neglected. Typical values for $A^2_{SU(3)}$ are given in Lamb's thesis.

References

1) Proceedings of the Symposium on Antinucleon-Nucleon Annihilations, Chexbres (1972), CERN 72-10 (1972).

2) Proceedings of the Symposium on Nucleon-Antinucleon Interactions, Prague (1974), CERN 74-18 (1974).

3) Proceedings on $\bar{p}p$ Interactions, Helsinki (1975).

4) L. Montanet, Lund Conference on Elementary Particles, (1969), CERN/D. Ph. II 69-30 (1969).

5) P. K. Malhotra, CERN 74-18 (1974), (see ref. 2)).

6) M. Bogdanski, T. Emura, S. N. Ganguli, A. Gurtu, S. Hamada, R. Hamatsu, E. Jeannet, I. Kita, S. Kitamura, J. Kishiro, H. Kohno, M. Komatsu, P. K. Malhotra, S. Matsumoto, U. Mehtani, L. Montanet, R. Raghavan, A. Subramanian, K. Tadahashi, and T. Yamagata, Phys. Lett. ~~B63~~ 62B (1976) 117.

7) E. Castelli, CERN 72-10 (1972), (see ref. 1)).

8) S. P. Denison, S. V. Donskov, Yu. P. Gorin, A. I. Petrukhin, Yu. D. Prokoshkin, R. S. Shuvalov, and D. A. Stoyanova, Phys. Lett. 34B (1972) 167.

9) A. Colebourn, Ph. D. Thesis (Liverpool), (1970).

10) W. Chinowsky, G. Kojoian, Nuovo Cim. 43A (1966) 684.

11) P. Anninos, L. Gray, P. Hagerty, T. Kologeropoulos, S. Zenone, R. Bizzarri, G. Ciapetti, M. Gaspero, I. Laakso, S. Lichtman, and C. Moneti, Phys. Rev. Lett. 20 (1968) 402.

12) A. Bettini, M. Cresti, S. Limentani, A. Loria, L. Peruzzo, R. Santagelo, L. Bertanza, A. Bigi, R. Carrara, R. Casali, E. Hart, and P. Lariccia, Nuovo Cim. 42A (1966) 695.

13) A. Bettini, M. Cresti, S. Limentani, L. Peruzzo, R. Santangelo,
S. Sartori, L. Bertanza, A. Bigi, R. Carrara, R. Casali,
and P. Lariccia, Nuovo Cim. 47A (1967) 642.

14) A. Bettini, M. Cresti, S. Limentani, L. Peruzzo, R. Santangelo,
S. Sartori, L. Bertanza, A. Bigi, R. Carrara, R. Casari,
P. Lariccia, and C. Petri, Nuovo Cim. 62A (1969) 1038.

15) R. Bizzarri, G. Ciapetti, U. Dore, M. Gastero, P. Guidoni,
I. Laakso, F. Marzano, G. C. Moneti, L. Gray, P. Hagerty,
and T. Kalogeropoulos, Phys. Rev. Lett. 25 (1970) 1385.

16) J. Roy and G. Tzanakos, Phys. Rev. Lett. 33 (1974) 1631.

17) Th. Parapopoulou, T. A. Filippas, L. Gray, E. Simopoulou,
P. Tsilimigras, A. Vayaki, M. Dris, T. E. Kalogeropoulos,
and J. Roy, Phys. Lett. 43B (1973) 401.

18) R. Bizzarri, P. Guidoni, F. Marcelja, F. Marzano, E. Castelli,
and M. Sessa, Nuovo Cim. 22A (1974) 225.

19) R. D. Burrows, D. E. Caro, F. Gold, A. G. Klein,
C. E. MacDowell, J. L. Olney, G. I. Opat, J. Starr,
J. W. Wignall, and D. C. Peaslee,
Austral. J. Phys. 23 (1970) 819.

20) J. L. Atitchison, D. E. Caro, E. Gold, A. G. Klein, G. I. Opat,
J. F. Langdon, P. R. Lamb, C. E. MacDowell, J. Starr,
and W. G. Wignall, Lett. Nuovo Cim. 2 (1971) 1009.

21) D. E. Caro, E. Gold, A. G. Klein, G. I. Opat, and
J. G. Wignall, Nucl. Phys. B90 (1975) 221.

22) A. Bettini, M. Cresti, M. Mazzucato, L. Peruzzo, S. Sartori,
G. Zumerle, M. Alston-Garnjost, R. Huesman, R. Ross,
F. T. Solmitz, L. Bertanza, R. Carrara, R. Casali, P. Lariccia
R. Pazzi, G. Borreani, B. Quassiati, G. Rinaudo, M. Vigone,

and A. Werbrouck, Nuovo Cim. 1A (1971) 333.

23) L. Bertanza, A. Bigi, R. Casali, P. Lariccia, P. Pazzi, A. Bettini, M. Mazzucato, G. Sartori, S. Sartiri, G. Zumerle, G. Borreani, B. Quassiati, G. Rinaudo, and M. Vigone, Nuovo Cim. 23A (1974) 209.

24) R. H. Huesman, M. Alston-Garjost, R. R. Ross, F. T. Solmitz, A. Bettini, M. Cresti, M. Mazzucato, L. Peruzzo, G. Sartori, S. Sartori, G. Zumerle, L. Bertanza, A. Bigi, R. Casali, P. Lariccia, R. Pazzi, G. Borreani, B. Quassiati, G. Rinaudo, and M. Vigone, Nuovo Cim. 25A (1975) 91.

25) G. Borreani, V. Manetta, B. Quassiati, G. Rinaudo, M. Vigone, A. E. Werbrouck, A. Bettini, M. Mazzucato, R. Carrara, R. Casali, and R. Pazzi, Lett. Nuovo Cim. 10 (1974) 529.

26) P. S. Eastman, Z. Ming ma, B. Y. Oh, D. L. Parker, G. A. Smith, and J. Sprafka, Nucl. Phys. B51 (1973) 29.

27) S. J. Orfanidis and V. Rittenberg, Nucl. Phys. B59 (1973) 570.

28) D. Q. Lamb, M. Sc. Thesis, University of Liverpool (1969).

29) C. Lovelace, Phys. Lett. 28B (1968) 264.

30) H. R. Rubinstein, Phys. Lett. 32B (1970) 370.

31) H. R. Rubinstein, CERN 74-18 (1974), .(see ref. 1)).

32) G. P. Gopal, R. Migneron and H. Rothery, Phys. Rev. D3 (1971) 2262.

33) L.E. Nicholas, Phys. Rev. D9 (1974) 1330.

34) V. Rittenberg and H. R. Rubinstein, Phys. Lett. 40B (1972) 257.

35) H. R. Rubinstein, Phys. Lett. 33B (1970) 478.

36) S. J. Orfanidis and V. Rittenberg,
Nucl. Phys. B56 (1973) 561.

37) D. Everett, P. Grossman, P. Mason and H. Muirhead,
Phys. Lett. 47B (1973) 541.

38) J. R. Fry, H. Muirhead, A. Apostolakis, M. Kakoulidon, H. Michaelidou, P. Michaelidis, G. Vasiliadis, T. A. Filippas, G. Grammatikakis, T. Papadopoulou, E. Simopoulou, A. Vayaki, P. Gortler, and M. Markytan, Nucl. Phys. B95 (1975) 365.

39) H. Muirhead, Symp. on $\bar{p}p$ Interactions, Helsinki (1975).

40) U. Amaldi, B. Conforto, G. Fidecaro, H. Steiner, G. Baroni, R. Bizzarri, P. Guidoni, V. Rossi, G. Brautti, E. Castelli, M. Ceschia, L. Chersovani, and M. Sessa,
Nuovo Cim. 46A (1966) 171.

41) R. Bizzarri, B. Conforto, G. C. Gialanella, P. Guidoni, F. Marcelja, E. Castelli, M. Ceschia, M. Sessa,
Nuovo Cim. 54A (1968) 456.

42) R. R. Burns, P. E. Gondon, J. Donahue, M. A. Mandelkern, L. R. Price, J. Schultz, and D. W. Smith,
Phys. Rev. D12 (1975) 638.

43) CH. DE. LA Vaissiere, Nuovo Cim. 11A (1972) 185.

44) CH. DE. LA Vaissiere, Nuovo Cim. 19A (1974) 118.

45) G. Alexander, S. Dagan, A. Fridman, J. Grunhause, S. Nussinov, and Y. Oren, Phys. Rev. D9 (1974) 649.

46) G. Goldhaber, S. Goldhaber, W. Lee, and A. Pais,
Phys. Rev. <u>120</u> (1960) 300.

47) R. Hagedorn, Suppl. Nuovo Cim. <u>3</u> (1965) 147.

48) C. Bricman, M. Ferro-luzzi, J. M. Perreau, J. K. Walker,

G. Bizerd, Y. Declais, J. Duchon, J. Seguinot,
Phys. Lett. 29B (1969) 457.

49) J. Storer, D. Cutts, M. L. Good, P. D. Grannis, D. Green, Y. Y. Lee, R. Pittman, A. Benvenuti, G. C. Fischer, and D.D. Reeder, Phys. Rev. Lett. 32 (1974) 950.

50) M. Alston-Garnjost, R. Kenny, D. Pollard, R. Ross, R. Tripp, and H. Nicholson, Phys. Rev. Lett. 35 (1975) 685.

51) A. Colebourne, R. A. Donald, D. N. Edwards, M. Bogdanski, E. Jeannet, and M. Gailloud, Nucl. Phys. B70 (1974) 205.

52) W. Atwood, B. Barish, H. W. Nicholson, J. Pine, A. V. Tollestrup, J. K. Yoh, A. S. Carroll, F. Lobkowicz, A. Melissinos, and Y. Nagashima,
Phys. Rev. D2 (1970) 2519.

53) P. Le Du, O. Guisan, W. Beusch, M. Borghini, E. Polgar, D. Websdale, L. Fluri, F. X. Gentit, P. Astbury, J. Gallivan, J. Jafan, and J. A. Wilson, Phys. Lett. 44B (1973) 390.

54) P. Astbury, G. Brautti, G. Finocchiaro, A. Michelini, D. Websdale, C. H. West, E. Polgar, W. Beush, W. E. Fisher, B. Gobbi, and M. Pepin, Phys. Lett. 23 (1966) 160.

55) J. G. Lee, A. Harckham, M. Letheren, W. Beush, F. Bourgeois, E. Polgar, W. Websdale, K. Freudenreich, R. Frosch, F. X. Gentit, and P. Mühlemann,
Nucl. Phys. B52 (1973) 292.

56) V. N. Bolotov, V. V. Isakov, D. B. Kakauridge, V. A. Kachanov, V. E. Postoev, and Yu. D. Prokoshkin,
Nucl. Phys. B73 (1974) 401.

57) V. N. Bolotov, M. I. Grachev, V. V. Isakov, D. B. Kakauridze,

G. V. Khaustov, V. E. Postoev, Yu. D. Proshkin, S. A. Sadovsky, V. A. Senko, A. V. Starzev, and L. M. Vasiljev, Study of Antiproton Charge Exchange on Protons at Momenta 18 and 40 GeV/c; Presented at the Palermo Conference on High Energy Physics (1975).

58) A. Astbury, CERN 74-18 (1974), (see ref. 2)).

59) J. Froyland and G. A. Winbow, Nucl. Phys. B35 (1971) 351.

60) R. A. Bryan and R. J. N. Phillips, Nucl. Phys. B5 (1968) 201.

61) B. Diu, Nuovo Cim. 20A (1974) 115.

62) E. Leader, Preprint, BNL 20431 (1975).

63) R. J. N. Phillips, Nucl. Phys. B2 (1967) 394.

64) G. L. Kane, F. Henyey, D. R. Richards, Marc Ross, and G. Williamson, Phys. Rev. Lett. <u>23</u> (1970) 1519.

65) J. Geicke, and K. H. Mütter, Phys. Rev. 184 (1969) 1151.

66) Farzam Arbab and Jan Dash, Phys. Rev. 163 (1967) 1603.

67) J. Engler, F. Mönnig, K. Runge, and H. Schopper, Nuovo Cim. 9A (1972) 311.

68) R. E. Mischke, P. F. Shepard, and T. J. Devlin, Phys. Rev. Lett. <u>23</u> (1969) 542.

69) M. B. Davis, B. G. Gibbard, M. N. Kreisler, T. Dobrowolski, M. J. Longo, D. D. O'Brien, and T. Toohig, Phys. Rev. Lett. <u>29</u> (1972) 139.

70) G. Bizard, F. Bonthonneau, J. L. Laville, F. Lefebvres, J. C. Malherbe, and R. Regimbart, Nucl. Phys. B85 (1975) 14.

71) T. Ohsugi, M. Fujisaki, S. Kaneko, Y. Murata, K. Okamura,

H. Kohno, R. Hamatsu, T. Hirose, S. Kitamura, T. Mamiya,
T. Yamagata, T. Emura, I. Kita, K. Takahashi, and M. Fukawa,
Nuovo Cim. 17A (1973) 456.

72) W. E. Frahn and R. H. Venter,
Ann. of Phys. 27 (1964) 135,385,401.

73) H. Kohno, S. Kaneko, Y. Murata, T. Ohsugi, K. Okamura,
M. Fukawa, R. Hamatsu, T. Hirose, T. Mamiya, T. Yamagata,
T. Emura, I. Kita, and K. Takahashi,
Nucl. Phys. B41 (1972) 485.

74) E. Fermi, Prog. Theor. Phys. 5 (1950) 570.

75) Z. Koba, and G. Takeda, Prog. Theor. Phys. 19 (1958) 269.

76) J. McConnell and J. Shapiro, Nuovo Cim. 28 (1963) 1272.

77) H. W. Atherton, W. M. R. Blair, L. M. Celnihier, V. Domingo,
B. R. Fiench, J. B. Kinson, K. Myklebost, B. Nellen,
E. Quercigh, R. Schäfer, J. Bartke, J. A. Danysz, J. Debray,
J. Laberrigue-Frolow, G. Pichon, M. Rumpf, C. De La Vaissiere,
and T. P. Yion, Nucl. Phys. B18 (1970) 221.

78) J. Debray, J. Laberrigue-Frolow, C. De La Vaissiere, and
T. P. Yion, Nucl. Phys. B62 (1973) 13.

79) R. R. Burns, P. E. Condon, J. Donahue, M. A. Mandeldern,
and J. Schultz, Nucl. Phys. B27 (1971) 109.

80) Y. Oren, W. A. Couper, T. Fields, D. S. Rhines, J. Whitmore,
and W. W. M. Allison, Nucl. Phys. B71 (1974) 189.

81) G. P. Fisher, and C. M. Libby, Nucl. Phys. B16 (1970) 450.

82) R. A. Donald, D. N. Edwards, R. S. Moore, E. J. Read,
S. Reucroft, T. Buran, A. G. Frodesen, S. Sire, P. Saetre,
A. Bettinni, S. Limentani, L. Peruzzo, R. Santangelo,
and S. Sartori, Nucl. Phys. B11 (1969) 551.

83) M. A. Ijaz, B. A. Munir, and E. J. B. Terrault,
Nucl. Phys. B42 (1972) 85.

84) D. E. Caro, E. Gold, A. G. Klein, G. I. Opat, and J. W. G. Wignall, Nucl. Phys. B90 (1975) 221.

85) Chan Hong-Mo, J. Loskiewicz, and W. W. M. Allison,
Nuovo Cim. 57A (1968) 93.

86) Fong-Ching Chen, Nuovo Cim. 62A (1969) 113.

87) T. F. Hoang, E. Yen, and D. Phines,
Nucl. Phys. B38 (1972) 62.

88) J. Clayton, P. Mason, H. Muirhead, K. Whiteley, R. Rigopoulos, P. Tsilimigras, and A. Vayaki-Serafimidou,
Nucl. Phys. B22 (1970) 85.

89) J. Clayton, P. Mason, H. Muirhead, K. Whiteley, R. Rigopoulos, P. Tsilimigras, and A. Vayaki-Serafinidou,
Nucl. Phys. B30 (1971) 605.

90) G. Ranft, Nuovo Cim. 58A (1968) 425.

91) E. Plahte and R. G. Roberts, Nuovo Cim. 60A (1969) 33.

92) A. S. Carroll, I-H. Chiang, T. F. Kycia, K. K. Li, P. O. Mazur, D. N. Michael, P. Mockett, D. C. Rahm, and R. Rubinstein,
Phys. Rev. Lett. 32 (1974) 247.

93) R. Bizzarri, CERN 72-10 (1972), (see ref. 1)).

94) G. Veneziano, Nuovo Cim. 57A (1968) 190.

95) H. Müller, Phys. Rev. D2 (1970) 2963.

96) R. Hagedorn and J. Ranft, Nucl. Phys. 48B (1972) 191.

97) J. Duboc, A. G. Mintenard, and S. G. Wojucki,
CERN report, CERN 65-2(1965).

98) I. Kita, lecture at Tokyo Metropolitan Univ. (1974).

99) I. Kita, private communication.

100) Y. Shimano, T. Hirabayashi, and I. Oshinomi, Proceedings of the Symposium on the Bubble Chamber Physics in Japan, Osaka, (1975).

101) P. H. Garbincius and L. G. Hyman, Phys. Rev. A2 (1970) 1834.

102) M. Derrick, T. Fields, L. G. Hyman, G. Keys, J. Fetkovich, M. McKenzie, and I. T. Wang, Phys. Rev. A2 (1970) 7.

103) D. H. Hill and R. B. Palmer, Rev. Sci. Instruments 40 (1969) 878.

104) T. Emura, I. Kita, K. Kurihara, K. Takahashi, N. Ugamura, and A. Yamasaki, Proceedings of the Symposium on the Bubble Chamber Physics in Japan, Sendai (1972).

105) T. Yamagata, Institute for Nuclear Study report, SJC-T-70-4(1970), unpublished.

106) R. Hamatsu, M. Kimura, A. Kurokawa, S. Waguri, and T. Yamagata, Proceedings of the Symposium on the Bubble Chamber Physics in Japan, Tokyo University of Agriculture and Technology(1973).

107) Bombay Bubble Chamber Group,'Study of the Properties of $\bar{p}$ Beam from the THRESH Output', report, January 1973.

108) M. Bogdanski, Ph. D. Thesis, Neuchatel Univ. (1971).

109) CERN Computer 6000 Series Program Library, THRESH (1969).

110) CERN Computer 6000 Series Program Library, GRING (1969).

111) 'Kinematical Identification of Bubble Chamber Events' published by E. Fett in Method in Subnuclear Physics, Vol. I edited by M. Nickolic.

112) V. Chaloupka et al., Review of Particle Properties, Phys. Lett. 50B (1974).

113) D. G. Coyne, W. R. Butler, G. Fang-Landau, and J. MacNaughton, Nucl. Phys. B32 (1971) 333.

114) R. R. Burns, P. E. Condon, J. Donahue, M. A. Mandelkern and J. Shultz, Nucl. Phys. B27 (1971) 109.

115) J. D. Jackson, Nuovo Cim. 34 (1964) 1644.

116) F. James, CERN report, CERN 68-15 (1968).

117) CERN Computer 6000 Series Program Library, FOWL (1970).

118) CERN Computer 6000 Series Program Library, MINUIT (1971).

119) R. R. Burns, P. E. Condon, J. Donahue, M. A. Mandeldern, and J. Schultz, Nucl. Phys. B73 (1974) 219.

120) M. Gourdin, L. Stodolsky, and M. Renard, Phys. Lett. 30B (1969) 347.

121) A. S. Goldhaber, G. C. Fox and C. Quigg, Phys. Lett. 30B (1969) 249.

122) W. W. M. Allison, W. A. Cooper, T. Fields, and D. S. Rhines, Phys. Rev. Lett. 24 (1970) 618.

123) J. W. Chapman, J. C. Vander Velde, Nucl. Phys. B24 (1970) 445.

124) G. I. Opat, preprint, University of Melbourne, UM-P-73/12.

125) V. Barger and D. Cline, Phys. Rev. Lett. 21 (1968) 392.

126) G. Goldhaber, W. B. Fowler, S. Goldhaber, T. F. Hoang, T. E. Kalogeropoulus and W. M. Powell, Phys. Rev. Lett. 3 (1959) 181.

127) Y. Oren, W. A. Cooper, T. Fields, D. S. Rhines, and W. W. M. Allison, Nucl. Phys. B71 (1974) 189.

128) K. Kajantie, Proceedings of the CERN School of Physics, CERN 71-7 (1971)

129) C. J. Goebel, M. L. Blackmon, and K. C. Wali,
Phys. Rev. 182 (1969) 1487.

130) T. F. Hoang, Nucl. Phys. B38 (1972) 333.

131) M. A. Ijaz, B. A. Munir, and E. J. B. Terrault,
Nucl. Phys. B42 (1972) 85.

132) W. R. Frazer, L. Ingber, C. G. Poon, D. Silverman,
K. Stowe, P. D. Ting, and H. J. Vasian,
Rev. Mod. Phys. 44 (1972) 284.

133) D. E. Caro, E. Gold, A. G. Klein, C. E. MacDowell,
G. I. Opat, J. W. G. Wignall,
Nucl. Phys. B52 (1973) 301.

134) J. E. Enstrom et al., $\bar{N}N$ and $\bar{N}D$ Interactions-A Complilation,
Particle Data Group, LBL-58, May 1972.

135) W. Rarita and P. Schwed, Phys. Rev. 112 (1958) 271.

136) H. Goldberg, Phys. Rev. D6 (1972) 2542.

137) G. F. Chew, and A. Pignotti, Phys. Rev. 176 (1968) 2112.

138) G. J. Feldman and M. L. Perl,
Phys. Report 19C (1975) 233.

139) M. Bernardini, D. Bollini, P. L. Brunini, E. Fiorentino,
T. Masson, L. Monari, F. Palmonari, F. Rimondi, and
A. Zichichi, Phys. Lett. 51B (1974) 200.

140) C. A. Nelson, Lett. Nuovo Cim. 11 (1974) 517.

141) B. Richter, Proceedings of XVII International Conference
on High Energy Physics, London 1974, page IV-37.

142) P. Gregory, P. Mason, H. Muirhead, G. Warren, C. J. Hamer,
G. Ekspong, R. Carlsson, S. O. Holmgren, S. N. Nilsson,
R. Stenbacka, and Ch. Walk, Nucl. Phys. B102 (1976) 189.

143) E. Bycling and K. Kajantie, Particle Kinematics,
(Wiley, N. Y. 1973).

144) R. Hagedorn, Relativistic Kinematics (Benjamin, N. Y., 1964).

145) T. Fields and R. Singer, Proc. of the fourth Int. Symposium on $\bar{N}N$ Interactions, Syracuse, 1975.

146) D. E. Caro, E. Gold, A. G. Klein, G. I. Opat, and W. G. Wignall, Proc. of the fourth Int. Symposium on $\bar{N}N$ Interactions, Syracuse, 1975.

147) I. Montvay, CERN preprint TH 1572 (1972),
CERN preprint TH 1580 (1972).

148) A. Jabs, Nucl. Phys. B34 (1971) 177.

Table 1 (a)

TOKYO DATA

Scanning for Associated Events

number of rolls	233 rolls
number of frames	223,749 frames
scanning efficiency after double scanning	97.6 %

LIST OF EVENTS

TYPE	3-P	3-P+V	5-P	7-P	total
(Scanning)					
events found	1,253	7	437	14	1,711
one 0-P and one odd-P in a frame	1,153	7	406	14	1,580
two 0-P or two odd-P in a frame	100	0	31	0	131
(Measuring)					
well reconstructed events*)	1,134	5	368	10	1,517
[cut] π-p elastic scattering**)	174				174
[cut] cos $\theta^{lab.} <$ cos $\theta^{lab.min.}$	11	0	3	0	14
[cut] out of fiducial volume***)	33	0	17	1	51
events remained after these cuts	916	5	348	9	1,278
one 0-P and one odd-P in a frame	821	5	318	9	1,153
two 0-P or two odd-P in a frame	95	0	30	0	125
events which failed in reconstruction	119	2	69	4	194
[cut] π-p elastic scattering****)	18				18
events left after this cut	101	2	69	4	176
one 0-P and one odd-P in a frame	96	2	68	4	170
two 0-P or two odd-P in a frame	5	0	1	0	6

*) All of points and tracks passed criteria of $\Delta X < 0.03$, $\Delta Y < 0.03$, $\Delta Z < 0.15$, track error < 1000 and residual $< 30\mu$ after THRESH outputs.

**) 3-prong events with one heavy ionized track and a cubic volume< 0.04.

***) see Fig. 57.

****) 3-prong events with one heavy ionized track.

cuts on 1,153 events

P(incident); 0.6 - 0.8 GeV/c

dip angle of $\bar{p}$; -0.2 - 0.2 rad.

1,111(3-P,3-P+V,5-P,7-P = 793,5,305,8) events passed.

path length of $\bar{n} > 1$ cm

1,063(3-P,3-P+V,5-P,7-P = 753,5 298,7) events passed.

Table 1(b)

BOMBAY DATA

Scanning for associated events

number of rolls	320 rolls
number of frames	336,080 frames
scanning efficiency from 2 scans of 50 rolls	98 %

LIST OF EVENTS

	number of events
(Scanning)	
events found	2,860
one 0-p(prong) and one odd-p in a frame	2,685
§) odd-p associated with more than one 0-p	175
(Measuring)	
well reconstructed events after 4 measurements*)	2,543
(cut) CUB <0.025	270
(cut) beam momentum < 0.6 or > 0.9 (GeV/c)	29
(cut) failure in kinematics	19
(cut) path length cf $\bar{n}$ < 1 cm	76
events remained after these cuts	2,055
topology of 2,055 events	
1-p+V, 3-p+V, 3-p, 5-p, 7-p = 7, 16.5,**) 1393.83,***) 617.67,20	

*) All of points and tracks passed criteria of $\Delta X < 0.03$, $\Delta Y < 0.03$, $\Delta Z < 0.15$(cm) , track error < 1000 after THRESH outputs.

**) Decimal fractions appear because the events denoted by §) were counted with the weight (e.g. 1/2, 1/3, etc.,).

***) In addition to this number, Bombay group estimated 53.5 3-prong stars lost by the cut on coplanarity(CUB< 0.025).

Table 1 (c)

NEUCHÂTEL DATA

Scanning for Associted events	
number of rolls	70 rolls
number of frames	77,103 frames

LIST OF EVENTS

	type	3-P	5-P	7-P	total
	(Scanning)				
	events found in scanning	321	124	1	446
	one 0-P and one odd-P in a frame	301	118	1	420
	two 0-P or two odd-P in a frame	20	6	0	26
	(measuring)				
	one 0-P and one odd-P in a frame	301	118	1	420
	lost:				
	unmeasurable	15	4	-	9
	tape manipulation	-	1	1	2
	fiducial vol. cut by program	7	1	-	8
	momentum cut(0.6<P<0.8 GeV/c)	2	-	-	2
	events remained	277	112	-	389
	EVENTS CONTAINED IN DST (SENT TO TOKYO)				
	No. of events in DST				~~414~~
	one 0-P and one odd-P in a frame§)	250	113	-	363
	events remained after cuts on $\bar{p}$ *)	245	104	-	349

§) We identified these events in DST with the value of location 25 (=1.0) .

*) We used these events in the calculation of the differential cross sections. 'cuts on $\bar{p}$' means $-0.2<\mathrm{dip}<0.2$, $0.6<P<0.8$ GeV/c and path length of $\bar{n} > 1$ cm.

Table 2(a)

Contents of CONS block of THRESH

Significance	Value
1. Tolerance for fiducial marks	0.04 cm
2. Constant for multiple scattering	0.000675
3. Tolerance on $(\Delta x^2 + \Delta Y^2 + (\Delta z/\text{stereo ratio})^2)^{1/2}$ for labelled point reconstruction	0.1 cm
4. Minimum curvature for quasi-straight tracks	0.00001 cm^{-1}
5. Maximum length for a track image with only 3 measurements	10 cm
6. Stereo ratio	3.8
7. Maximum length for a track that one may try to fit again as quasi-straight when the helix fit does not converge	10
8. Length unit for sagitta cutoff	0.2
9. Measurement error on film	0.002 cm
13. Multiplier of CONS 8.	A
15. Multiplier of the current tolerance for the track measurement	3
16. Number of near corresponding points used as reference for certain tests	5
17. Lowest letter for the second label of a track imposed as straight	W
18. Distance film lens	10 cm
19. Upper tolerance	0.5 cm
20. Lower tolerance	0.05 cm
21. Reference radius of curvature R	400 cm
22. X max	45
23. X min	-45
24. Y max	30
25. Y min	-30
26. Maximum relative angular gap acceptable between consequtive measurements	5
27. Maximum amount of extrapolation for near corresponding point reconstruction	0.8
29. Maximum acceptable variation for the Z coordinate of the start point during the helix fit	1.5 cm
30. Idem for the mass fit	0.5 cm
31. Maximum acceptable mean residual after helix fit or mass fit	100
32. Maximum acceptable Stretch coefficient	0.005
33. Maximum acceptable mean residual after the circle fit of the first approx.	1 cm

Table 2 (b)

Contents of CONS block of GRIND

	Significance	Value
1.	Bubble density for $\lvert\beta\rvert = 1$ (bubbles/cm)	22.
2.	Relative error on bubble density	1.
3.	Range error, if not calculable	0.1 cm
4.	Maximum projected length for zero-range tracks	0.1 cm
5.	Constant for multiple scattering	0.000495
6.	Measurement error on film coordinates	0.008 cm
7.	Number of standard deviations allowed in comparisons	5
8.	ΔX	0.0002 cm
9.	ΔY minimum error on space points	0.0002 cm
10.	ΔZ	0.001 cm
11.	$\Delta\lambda_{max}$ maximum errors on neutral track	0.5 radian
12.	$\Delta\phi_{max}$ angles	0.18 radian
13.	Maximum length of a track in chamber	60 cm

Table 3

Number of Fitted Events

Channel	Tokyo	Bombay	Neuchatel	Total	Accepted Events*)
$2\pi^+\pi^-$	39	47	15	101	90
$2\pi^+\pi^-\pi^0$	225	347	141	713	529
$3\pi^+2\pi^-$	67	122	25	214	188
$3\pi^+2\pi^-\pi^0$	122	182	60	364	309

*) see Section IV-1-i

Table 4

Contents of the Data Summary Tape (54 words)

Location	Contents
1	Identification of the event (film-frame-event number).
2	Number of tracks of the associated star.
3	Number of particles of the associated star (including π^0). Set to 0 for nofit and 0-C fit.
4	Number of constraints in the fit of the associated star. Set to 10 for nofit events.
5,6,7	X,Y,Z coordinates of the primary vertex ($\bar{p}p$ vertex).
8,9,10	X,Y,Z coordinates of the secondary vertex ($\bar{n}p$ vertex).
11,12,13	p(GeV/c), λ, and ϕ (rad.) of the incident $\bar{p}$.
14,15,16	p, λ, and ϕ of the antineutron.
17	θ(lab): emission angle of the $\bar{n}$ in the laboratory.
18	θ(cm) emission angle of the $\bar{n}$ in the $\bar{p}p$-cm.
19	cos θ(cm).
20	-t: four-momentum transfer between $\bar{p}$-$\bar{n}$.
21	Distance between primary and secondary vertices.
22	Potential length for the antineutron.
23	$\bar{n}p$ annihilation cross section: computed from $747/\sqrt{T}$(mb).
24	Weight for the event (inverse of the detection eff.).
25	Weight due to the presence of several events on the same frame (value 1,1/2 or 1/3).
26	Probability of the fit (o if nofit or 0-C fit).
27	Coplanarity angle for the 3-prong associated star: $0 - 1$ (-1 for 5- or 7-prong stars).
28-54	9 times 3 variables (p, λ,ϕ) for the particles of the associated star. Sequence:positive, negative and neutral psrticles. (Completed with 0 for the rest of the banks.).

Table 5

Branching Ratios for $\bar{n}p$ Annihilation*)

type	no. of events	MM cut**)	%	cross section
3 prongs	679	679	71.4±3.6	38.2±3.9 (mb)
$2\pi^+\pi^-$	(32	32	3.4±0.6	1.8±0.3)
$2\pi^+\pi^-\pi^o$	(168	93***)	9.8±1.1	5.2±0.6)
$2\pi^+\pi^- m\pi^o$ (m>1)	(-	554	58.3±3.1	31.1±1.7)
5 prongs	262	262	27.6±1.9	14.7±1.0
$3\pi^+2\pi^-$	(53	50	5.3±0.8	2.8±0.4)
$3\pi^+2\pi^-\pi^o$	(99	98	10.3±1.1	5.5±0.6)
$3\pi^+2\pi^- m\pi^o$(m>1)	(-	114	12.0±1.2	6.4±0.6)
7 prongs	9	9	0.9±0.3	0.5±0.2

*) derived from Tokyo data.
**) see Section III-7-iii.
***) This number is deduced by symmetrizing the $(MM)^2$ distribution (see Sec.III-7-iii) around the axis $(MM)^2=(m_\pi)^2$.

Table 6

Comparison of the result with $\bar{p}n$ data and with the OR model

type	$\bar{n}p$ (%)	$\bar{p}n$ (%) ref.21)	OR model (%)
3 prongs	71.4±3.6	73.5±5.3	71.89
3π	3.4±0.6	2.9±0.4	2.66
4π	9.8±1.1	15.0±1.4	16.46
$>4\pi$	58.3±3.1	55.7±5.1	52.77
5 prongs	27.6±1.9	22.9±3.8	26.94
5π	5.3±0.8	7.4±1.8	6.43
6π	10.3±1.1	11.6±2.8	12.62
$>6\pi$	12.0±1.2	7.4±1.8	7.89
7 prongs	0.9±0.3	-	1.17

Table 7

Resonance Parameters

	mass(GeV)	width(GeV)
ρ	0.77	0.15
ω	0.78	0.05
f	1.27	0.17
g	1.68	0.18

Table 8

Percentages of Resonance Productions

channel	%
$2\pi^+\pi^-$	
$\rho^o\pi^+$	40 ± 12
$f\pi^+$	47 ± 12
$g\pi^+$	8 ± 6
$2\pi^+\pi^-\pi^o$	
$\rho^o\pi^+\pi^o$	~~26±6~~ 11.6 ±6.7
$\rho^+\pi^+\pi^-$	~~21±6~~ 15.8 ±6.6
$\rho^-\pi^+\pi^+$	~~11±4~~ 9.6 ±3.8
$f\pi^+\pi^o$	~~5±3~~ 4.8 ±2.7
$\rho^+\rho^o$	~~0~~ 20.2 ±5.7
$\omega\pi^+$	~~0~~ 4.4 ±1.4
$3\pi^+2\pi^-$	
$M(700\rightarrow\pi^+\pi^-)$	~100
$3\pi^+2\pi^-\pi^o$	
ω production	~45

Table 9

Parameters Used in the CLA Model

(a) Values of model parameters

$\alpha=-0.38$,	$H=3.50(\mathrm{GeV})^{-1}$,
$\beta=0.88(\mathrm{GeV})^{-2}$,	$M_0=0.94\mathrm{GeV}$,
$a=0.88(\mathrm{GeV})^2$,	$\lambda=0.5$,
$b=1.25(\mathrm{GeV})^2$,	$c=1.40(\mathrm{GeV})^{-1}$.
$\gamma=0.25(\mathrm{GeV})^{-4}$,	

(b) Sample values of coupling constants g_i and c_i(in $(\mathrm{GeV})^{-1}$)

	g_i	c_i		g_i	c_i
$\pi^+\pi^-$	3.02	1.27	$\omega\pi^+$	1.80	0.7
$\pi^+\pi^0$	2.54	0.99	$f\pi^+$	1.39	0.7
$\pi^+\ {}^0$	1.81	0.50	$f\pi^0$	1.17	0.49
$\pi^-\rho^+$	2.16	0.64	$f\rho^+$	0.99	0.35
$\rho^+\rho^0$	1.30	0.25	π^+g^0	1.11	0.50
$\rho^0\pi^0$	1.53	0.29			

(c) Masses and widths in GeV

$\rho^{\pm 0}$: 0.77,0.15 .

f : 1.27,0.17 .

g : 1.68,0.18 .

ω :0.783,0.05 .

Table 10

Colimation Paramaters C

and Asymmetry Parameters A

		C(=(P-E)/(P+E))	A(=(F-B)/(F+B))
$2\pi^+\pi^-$;	π^+	0.044±0.074	-0.196±0.072
	π^-	0.019±0.099	0.304±0.099
$2\pi^+\pi^-\pi^0$;	π^+	0.002±0.031	0.030±0.031
	π^-	0.027±0.044	-0.018±0.044
	π^0	0.122±0.043	-0.170±0.043
$3\pi^+2\pi^-$;	π^+	0.011±0.042	-0.064±0.042
	π^-	-0.048±0.052	0.106±0.051
$3\pi^+2\pi^-\pi^0$;	π^+	0.077±0.033	0.064±0.033
	π^-	-0.010±0.040	0.016±0.040
	π^0	-0.023±0.059	-0.314±0.054

Table 11

Correlation Coefficients γ

		$(\pi^-\pi^-)$	$(\pi^-\pi^0)$	$(\pi^+\pi^-)$	$(\pi^+\pi^0)$	$(\pi^+\pi^+)$
$2\pi^+\pi^-$	PS:	-	-	3.51	-	3.51
	BE:	-	-	3.73	-	2.71
	EXP:	-	-	4.26±0.80	-	3.38±0.84
$2\pi^+\pi^-\pi^0$	PS:	-	2.30	2.30	2.30	2.30
	BE:	-	2.21	2.46	2.31	1.65
	EXP:	-	2.31±0.22	2.41±0.16	3.22±0.23	1.39±0.12
$3\pi^+2\pi^-$	PS:	1.80	-	1.80	-	1.80
	BE:	1.51	-	1.98	-	1.66
	EXP:	1.09±0.16	-	2.84±0.19	-	1.32±0.11
$3\pi^+2\pi^-\pi^0$	PS:	1.62	1.62	1.62	1.62	1.62
	BE:	1.27	1.54	1.61	1.98	0.93
	EXP:	1.19±0.14	1.34±0.11	2.02±0.10	1.82±0.12	1.18±0.08

PS:Phase Space, BE:Bose-Einstein statistics, EXP:Experiment

Table 12

Transverse Momentum Spectra

model		χ^2	n_D	max.T or α (GeV)
Hagedorn	π^+	221	36	0.1138
	π^-	179	36	0.1146
	total	351	36	0.1139
Boltzmann	π^+	107	36	0.3326
	π^-	86	36	0.3312
	total	126	36	0.3333

Table 13

Branching Ratios of $\bar{n}p$ annihilation at 0.6 GeV/c for Various Multiplicities Calculated Following the OR model (%)

no. of π^0 / π^+,π^-	0	1	2	3	4	5	6	7	8
$2\pi^+\pi^-$	2.2	13.6	23.7	15.3	4.1	0.5	0.0	0.0	0.0
$3\pi^+2\pi^-$	5.3	10.4	5.5	1.0	0.0	0.0	0.0	0.0	0.0
$4\pi^+3\pi^-$	0.6	0.3	0.05	0.0	0.0	0.0	0.0	0.0	0.0

Table 14

Beam Characteristics

Exposure	average momentum (GeV/c)	μ^-, π^- contamination (%)	no. of $\bar{p}$'s per frame
I(Tokyo)	0.704 ±0.039	9.17±0.11	10.23±0.04
II(Bombay)	0.760 ±0.025	9.9 ±0.18	10.10±0.04

Table 15

$\bar{p}n$ annihilation cross sections at low energies18)

Laboratory kinetic energy(MeV)	Laboratory incident momentum(MeV/c)	Cross sections(mb)	
		3 prongs	5 prongs
57.4±13.2	333. ± 40.	70.6± 3.9	23.3±2.1
79.8 10.0	395. 26.	56.9 3.0	21.5 1.7
98.1 8.5	440. 20.	48.3 2.5	22.6 1.6
109.3 8.8	466. 20.	52.9 2.6	19.2 1.5
124.1 8.1	498. 17.	45.3 2.1	18.6 1.3
137.7 7.5	527. 16.	46.3 2.0	19.1 1.2
146.6 7.1	545. 14.	48.0 2.1	17.6 1.2
158.8 6.7	569. 13.	43.5 1.8	18.6 1.1
170.5 6.4	591. 12.	42.7 1.7	16.1 1.0

Table 16

Numbers of unassociated stars

3 prong	5 prong	7 prong
650	313	13

Figure Captions

Fig. 1. (a) Linear chain decay scheme of $\bar{N}N$ system in the Orfanidis-Rittenberg model. (b) Multi-Regge-pole exchange scheme of the CŁA model by Chan Hong-Mo et al.[85)] (c) Schematic description of the Müller-Regge analysis of $\bar{p}n$ annihilation.

Fig. 2. Layout of the K_4-beam in the North Hall of the CERN P.S.

Fig. 3. (a) Whole aspect of the Saclay 81 cm hydrogen bubble chamber. (b) Alignment of cameras and flashes of the Saclay 81 cm hydrogen bubble chamber.

Fig. 4. Histogram of the μ range in the Saclay 81 cm hydrogen bubble chamber.

Fig. 5. Typical events of the charge exchange scattering associated with $\bar{n}p$ star of (a) 3 prongs, (b) 5 prongs, and (c) 7 prongs. The cross marks are reference marks (called fiducial marks). The 0-prong and odd-prong vertices correspond to $\bar{p}p$ charge exchange and $\bar{n}p$ annihilation respectively.

Fig. 6. (a) Schematic diagram of the Super Mangiaspago type measuring device (SMP). (b) Block diagram of the Computer Aided Measuring Projector (CAMP).

Fig. 7. Distribution of the stretch parameter ST (defined by eq.(III-6)) for (a) view 1, (b) view 2, (c) view 3 of the photograph (Tokyo data).

Fig. 8. Point errors in THRESH outputs for the odd-prong vertex; (a) ΔX, (b) ΔY, and (c) ΔZ. The arrows indicate the criteria for acceptance (Tokyo data).

Fig. 9. Track errors in the THRESH outputs of the incident $\bar{p}$; (a) $\Delta(1/\rho)$, (b) $\Delta\lambda$, (c) $\Delta\phi$,(d) residuals (ρ, λ and ϕ are radius, dip angle, and azimuthal angle respectively.). The arrows indicate the criteria for acceptance (Tokyo data).

Fig.10. Distributions of (a) coplanarity angle COP and (b) cubic volume CUB for the 3-prong stars, which are defined by eqs. (III-7) and (III-8) respectively. The shaded areas correspond to the events of which one of the three tracks was heavily ionized. These events were rejected in the present analysis (Tokyo data).

Fig.11. Distributions of pulls (as defined in eq. (III-20)) for the incident $\bar{p}$. (a) 1/p, (b) λ, (c) ϕ(Tokyo data).

Fig.12. χ^2 probability distributions of the GRIND outputs for (a) $\bar{n}p \longrightarrow 2\pi^+\pi^-$, (b) $2\pi^+\pi^-\pi^o$, (c) $3\pi^+2\pi^-$, and (d) $3\pi^+2\pi^-\pi^o$ final states (Tokyo data).

Fig.13. Distributions of missing-mass squared for (a) $\bar{n}p \longrightarrow 2\pi^+\pi^-$, (b) $2\pi^+\pi^-\pi^o$ (The dot lines represent a histogram symmetrised around $MM^2=m_\pi^2$.), (c) $3\pi^+2\pi^-$, and (d) $3\pi^+2\pi^-\pi^o$ final states (Tokyo data).

Fig.14. Block diagram of the experimental procedure employed at Tokyo. Events flow along the arrows.

Fig.15. Determination of the effective width of ω meson. (a) Effective mass squared distribution of $(\pi^+\pi^-\pi^o)$ combinations of the $3\pi^+2\pi^-\pi^o$ final state. (b) Mass and width of ω meson determined. Events used are those within the region indicated by the arrows in (a) (Tokyo data).

Fig.16 Momentum distribution of the antineutrons. The two arrows indicate the momentum criterion imposed for acceptance of events.

Fig.17. $(\pi^+\pi^-)$ effective mass distribution for $\bar{n}p \longrightarrow 2\pi^+\pi^-$ reaction.The solid and dashed curves are the fitted curve of (resonances+ phase space) and the prediction by phase space respectively.

Fig.18. Effective mass distributions of various combinations for resonance productions in $\bar{n}p \longrightarrow 2\pi^+\pi^-\pi^0$ reaction.The solid and dashed curves are the fitted curve of (resonances + phase space) and the prediction by phase space respectively.

Fig.19. The same distributions as Fig.18 for $\bar{n}p \longrightarrow 3\pi^+2\pi^-$ reaction.The dot-dashed curve in the $(\pi^+\pi^-)$ mass spectrum is explained in Section IV-2-iv.

Fig.20. The same distributions as Fig.18 for $\bar{n}p \longrightarrow 3\pi^+2\pi^-\pi^0$ reaction.

Fig.21. $(\pi^+\pi^-)$ effective mass distributions for (a) $2\pi^+\pi^-$, (b) $2\pi^+\pi^-\pi^0$,(c) $3\pi^+2\pi^-$ and (d) $3\pi^+2\pi^-\pi^0$ samples. The solid and dotted histograms represent those for the events with $(\pi^+\pi^-)$ dipion system emitted in the forward and backward directions with respect to the incident $\bar{n}$ in c.m. system respectively.

Fig.22. The same distributions as Fig.21 for (a) $(\pi^+\pi^0)$ and (b) $(\pi^+\pi^+)$ combinations of $2\pi^+\pi^-\pi^0$ samples .

Fig.23. Production angle, $\cos\theta$, distribution of $(\pi^+\pi^-)$ dipion system with respect to the incident $\bar{n}$ in c.m. system for $2\pi^+\pi^-\pi^0$ samples.

Fig.24. $(\pi^+\pi^-)$ effective mass spectra of $2\pi^+\pi^-\pi^0$ samples for the events with production angle θ of $(\pi^+\pi^-)$ dipion system (a) $|\cos\theta| > 0.5$ and (b) $|\cos\theta| < 0.5$.

Fig.25. $(\pi^+\pi^-)$ effective mass spectra of events with $(\pi^+\pi^-)$ dipion system emitted (a) in the forward direction and (b) in the backward direction for $2\pi^+\pi^-\pi^0$ samples. The solid curves are those obtained by fitting the histograms with the form defined in eq (IV-63).

Fig.26. $(\pi^+\pi^-)$ effective mass spectra of events with $(\pi^+\pi^-)$ dipion system emitted (a) in the forward direction and (b) in the backward direction for $2\pi^+\pi^-\pi^0$ samples. These histograms are those obtained by subtracting events from the histograms in Fig.25 by the amount of 40% following the shapes of the $(\pi^+\pi^-)$ mass spectra of $3\pi^+2\pi^-$ samples (see IV-3-iii).The solid curves are those obtained by fitting the histogram with the form defined in eq. (IV-63).

Fig.27. Graphs of the CłA model contributing to the reaction $\bar{n}p \longrightarrow 2\pi^+\pi^-$.

Fig.28. Graphs of the CłA model contributing to the reaction $\bar{n}p \longrightarrow 2\pi^+\pi^-\pi^0$.

Fig.29. $(\pi^+\pi^-)$ effective mass distribution for $2\pi^+\pi^-$ final state.The solid curve is the prediction by the CłA model.

Fig.30. $(\pi^+\pi^-)$ opening angle distribution in the production c.m. system for $2\pi^+\pi^-$ final state.The solid curve is the prediction by the CłA model.

Fig.31. Effective mass distributions for $2\pi^+\pi^-\pi^0$ samples. (a) $(\pi^+\pi^-)$ combination, (b) $(\pi^+\pi^0)$ combination (c) $(\pi^-\pi^0)$ combination, (d) $(\pi^+\pi^-\pi^0)$ combination.The solid curves are the predictions by the CŁA model.

Fig.32. Opening angle distributions of dipions in the production c.m. system for $2\pi^+\pi^-\pi^0$ samples. (a) $(\pi^+\pi^+)$ combination, (b) $(\pi^+\pi^0)$ combination,(c) $(\pi^+\pi^-)$ combination,(d) $(\pi^-\pi^0)$ combination.The solid curves are the predictions by the CŁA model.

Fig.33. Distributions for production angles of π^+, π^-, and π^0 for various final states in the production c.m. system.The solid and dashed curves are the predictions by phase space and by the CŁA model respectively.

Fig.34. Distributions for transverse momenta (P_T) of π^+, π^-, and π^0 for various final states.The solid and dashed curves are the predictions by phase space and by the CŁA model respectively.

Fig.35. Distributions for absolute values of momentum of π^+, π^-, and π^0 for various final states in the production c.m. system.The solid and dashed curves are the predictions by phase space and by the CŁA model respectively.

Fig.36. $(\pi^+\pi^+)$ effective mass distribution for $2\pi^+\pi^-$ final state. The solid and dashed curves are the predictions by the Bose-Einstein statistics and phase space respectively. This notation is kept up to Fig.41.

Fig.37. $(\pi^+\pi^+)$ effective mass distrivution for $2\pi^+\pi^-\pi^0$ final state.

Fig.38. $(\pi^+\pi^+)$ effective mass distribution for $3\pi^+2\pi^-$ final state.

Fig.39. $(\pi^-\pi^-)$ effective mass distribution for $3\pi^+2\pi^-$ final state.

Fig.40. $(\pi^+\pi^+)$ effective mass distribution for $3\pi^+2\pi^-\pi^0$ final state.

Fig.41. $(\pi^-\pi^-)$ effective mass distribution for $3\pi^+2\pi^-\pi^0$ final state.

Fig.42. Distributions of the dipion opening angles in the production c.m. system for $2\pi^+\pi^-$ final state.The solid and dashed curves are the predictions by the Bose-Einstein statistics and phase space respectively. This notation is kept up to Fig.45.

Fig.43. The same distribution as Fig.42 for $2\pi^+\pi^-\pi^0$ final state.

Fig.44. The same distribution as Fig.42 for $3\pi^+2\pi^-$ final state.

Fig.45. The same distribution as Fig.42 for $3\pi^+2\pi^-\pi^0$ final state.

Fig.46. Correlation parameters γ (defined by eq.(IV-92)) as a function of the dipion charge mode in the reactions (a) $\bar{n}p \longrightarrow 2\pi^+\pi^-$, (b) $2\pi^+\pi^-\pi^0$, (c) $3\pi^+2\pi^-$, and (d) $3\pi^+2\pi^-\pi^0$. The solid and dashed lines are the predictions by the Bose-Einstein statistics and phase space respectively, which are the ones obtained by connecting the predicted points to guide eyes.

Fig.47. A ladder diagram of $\bar{n}p \longrightarrow$ pions showing the flow of charge and transverse momentum along the t-channel.

Fig.48 Distributions of R, the ratio of Q_{ex}(defined in eq. (IV-101)) of the data to that of the prediction by the phase space for (a) $2\pi^+\pi^-$, (b) $2\pi^+\pi^-\pi^0$, (c) $3\pi^+2\pi^-$, and (d) $3\pi^+2\pi^-\pi^0$ final states.

Fig.49 Distributions of P_{Tex} (defined in eq.(IV-100)) for (a) $2\pi^+\pi^-$, (b) $2\pi^+\pi^-\pi^0$, (c) $3\pi^+2\pi^-$, and (d) $3\pi^+2\pi^-\pi^0$ final states together with the predictions by phase space.

Fig.50. The physical regions on the s,t plane of the three different channels of $\pi^+\pi^- \longrightarrow \pi^+\pi^-$. The straight lines marked $\alpha(s)=1$, etc., show the positions of the poles in s and t; the dashed lines marked $\alpha(s)+\alpha(t)=1$, etc., are the lines of zeros of the amplitude. The curve in the region $s>0$, $t>0$ is the boundary of the Dalitz plot for $\bar{n}p \longrightarrow 2\pi^+\pi^-$ at 0.65 GeV/c.

Fig.51. Dalits plots of the reactions (a) $\bar{p}n \rightarrow 2\pi^-\pi^+$ at rest,[29)] (b) $\bar{n}p \rightarrow 2\pi^+\pi^-$ at 0.65 GeV/c, and (c) $\bar{p}n \longrightarrow 2\pi^-\pi^+$ at 1.2 GeV/c[22)]. The contours in (a) show the prediction by the Veneziano model[29)].

Fig.52. (a) Dalitz plot for the reaction $\bar{n}p \rightarrow 2\pi^+\pi^-$ at 0.65 GeV/c.The contours give the prediction by the 2^+ amplitude which is given by eq. (IV-111) explicitly. (b) The projected distribution of the Dalitz plot for $(\pi^+\pi^-)$ effective mass squared. (c) The projected distribution of the Dalitz plot for $(\pi^+\pi^+)$ effective mass squared.The solid and dashed curves in both (b) and (c) are the prediction by the 2^+ amplitude and phase space respectively.

Fig.53. Inclusive spectra of the transverse momentum for (a) π^+, (b)π^- and (c) total pions. The solid and dashed curves represent the fitted ones of the Hagedorn distribution (eq.(IV-113)) and the Boltzmann distribution (eq.(IV-114)) respectively. The best fit parameters are given in Table 12.

Fig.54. M_X^2 spectra of π^+ (cross mark) and π^- (closed circle) for various t intervals of the inclusive reaction $\bar{n}p \longrightarrow \pi^{\pm} + X$.

Fig.55. (a) The same distribution as Fig.54 over whole t region. The solid and dashed curves are the prediction by the OR model and the fitted curve by eq.(IV-125) respectively. (b) The same distribution as (a) for nofit events.

Fig.56. Distributions of events of $\bar{n}p$ annihilation with respect to the total energy; (a) all events, (b) odd-pion final states ($3\pi+5\pi$), (c) even-pion final states ($4\pi+6\pi$). The dashed arrows indicate the position at which Carroll et al. observed an enhancement in the spectrum of the total cross section of $\bar{p}d$ reaction.92)

Fig.57. (a) Fiducial marks (cross marks) projected on the view 2 screen of a scanning table (20x magnification). The arrows indicate the entrance and exit for the incident beams to be accepted. The camera is placed in this side of the sheet (98.5 cm from the two-folded circle). The dashed lines indicate the fiducial volume for the present experiment. (b) Fiducial volume difined in the bubble chamber coordinate.

Fig.58. Momenta of the incident $\bar{p}$ at $\bar{p}p \longrightarrow \bar{n}n$ scattering vertex of the Exposure I (Tokyo data).

Fig.59. The same distribution as Fig.58 of the Exposure II (Bombay data).

Fig.60. (a) Schematical representation of the range of a recoil proton of elastic scattering in a bubble chamber. An incident $\bar{p}$ is assumed to be perpendicular to the sheet which contains the interaction point. The radius represent the range. The projected length of the range of the recoil proton falling within the shaded area is smaller than 1.5 mm. (b) Rate of loss of events of short-recoiled elastic scattering on a scanning table (solid curve) and the range of the recoil proton (dashed curve) as a function of t (between incident and scattered $\bar{p}$) in a hydrogen bubble chamber.

Fig.61. Differential cross section for $\bar{p}p \longrightarrow \bar{p}p$ with $|t|<0.1$ $(GeV/c)^2$ at 0.7 GeV/c. The solid curve along the data points gives the prediction by the diffraction model (see eq.(V-16)). The shaded area represents loss of events due to the small projected range of the recoil proton (< 1.5 mm in the bubble chamber).

Fig.62. Kinematical scheme for $\bar{p}p \longrightarrow \bar{n}n$ scattering.

$\theta_1^* \theta_2^*$: possible angles of emission of antineutron in cms.

θ_L: measured angle between $\bar{p}$-$\bar{n}$ in lab. system.

P_L, P_H: momenta of antineutron with low-energy and high-energy solutions in lab. system respectively.

P_S: momentum for which $P_L=P_H$.

Figures are exaggerated concerning the $\bar{p},\bar{n}$ mass difference for the sake of clarity.

Fig.63. Ratios of the path length of $\bar{n}$ (X) to the potential length (L). Definition for each quantity is given in Fig.57.

Fig.64. A fitted curve of the empirical formula (eq.(V-24)) to the cross sections $\sigma_3+\sigma_5$ of $\bar{p}n$ annihilation at low energies (solid curve).The dashed curve is the one used in the previous experiment$^{73)}$.

Fig.65. (a) Path lengths of the $\bar{n}$, (b) Angles between the scattering plane ($\bar{p}$ - $\bar{n}$ plane) and the perpendicular to the front glass of the chamber (approximately parallel with the optical axis).

Fig.66. Data for $\bar{p}p$ annihilation below 1 GeV/c. The data obtained in this experiment are indicated by open circles. (a) Annihilation cross sections.The solid curve is that obtained by fitting the formula of eq.(V-52) to the data. (b) Branching ratios of 0-prong annihilation cross section to the total one.The solid and dashed curves are the predictions by the OR model and Lamb model respectively. (c) Branching ratios for 2-prong annihilation.The solid, dashed and dot-dashed curves are the predictions by the OR model, Lamb model and Goldberg model respectively, and this notation is kept up to (g). (d) The ratios for 4-prong annihilation. (e) The ratios for 6-prong annihilation. (f) Average multiplicities of negatively charged particles. (g) Two-particle correlation coefficients for the $\bar{p}p$ data (see eq.(V-55)).

Fig.67. Branching ratios of (a) 2-prong, (b) 4-prong, and (c) 6-prong annihilation cross sections to the total annihilation cross sections for e^+e^-, $\bar{K}K$, and $\bar{p}p$ annihilations. The data in the present analysis are indicated by closed circles and other data are cited from ref. 38). The solid curves are the predictions by the OR model.

Fig.68. Distributions of random numbers generated by the "Shuffling" method that is employed in the FOWL. 50,000 random numbers are generated using HITAC 8700 computer (32 bits per word), and they are divided into five equal parts following the sequential order. The distributions are taken for the numbers of each part distributing within the interval 0.0-0.05.

Fig.69. The same distribution as Fig.68. Random numbers are generated by the "Shuffling" method where FORTRAN areguments in the generator are used with DOUBLE PRECISION declaration (64 bits per word).

Fig.70. The same distribution as Fig.68. Random numbers are generated using a generator supplied by the HITAC 8700 system library.

Fig. 1.

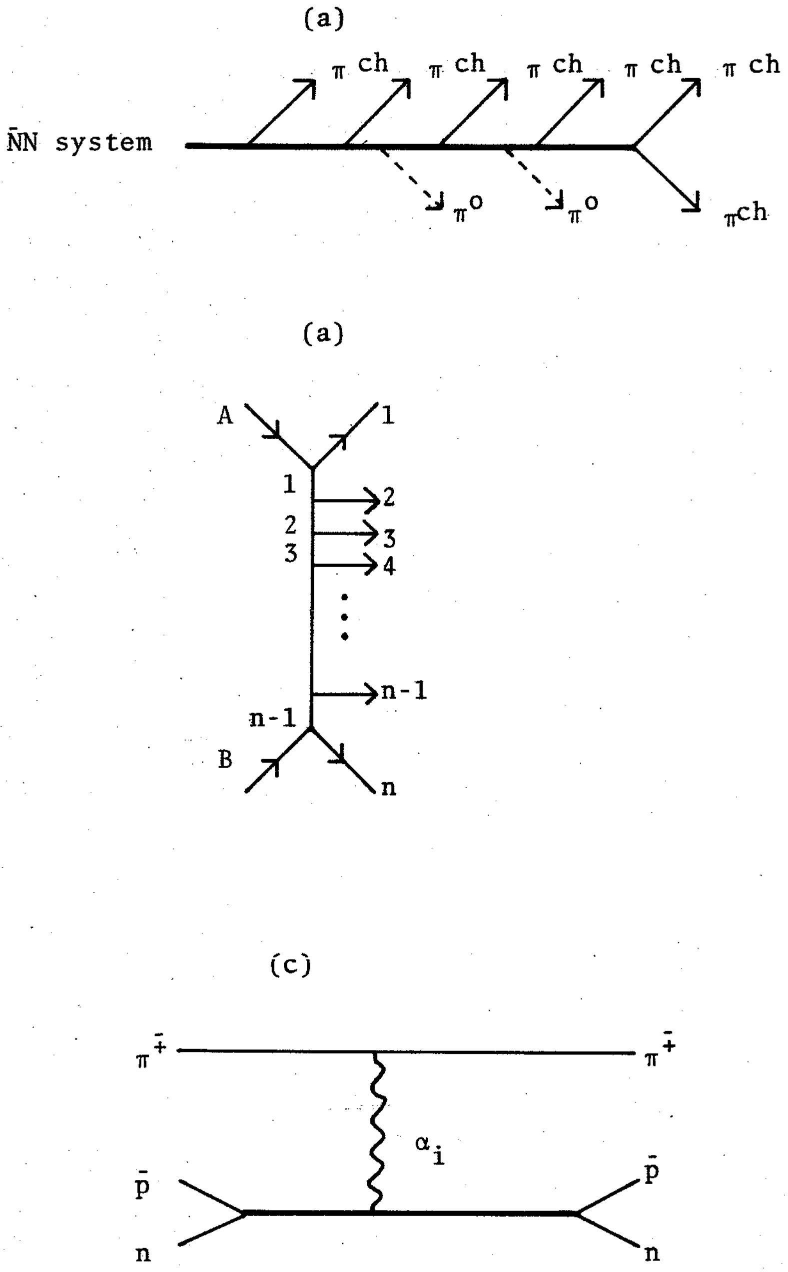
(a)
π ch
π ch
π ch
π ch
π ch
N̄N system
π o
π o
πch
(a)
A
1
1
2
2
3
3
4
n-1
n-1
B
n
(c)
π∓
π∓
α_i
p̄
n
p̄
n

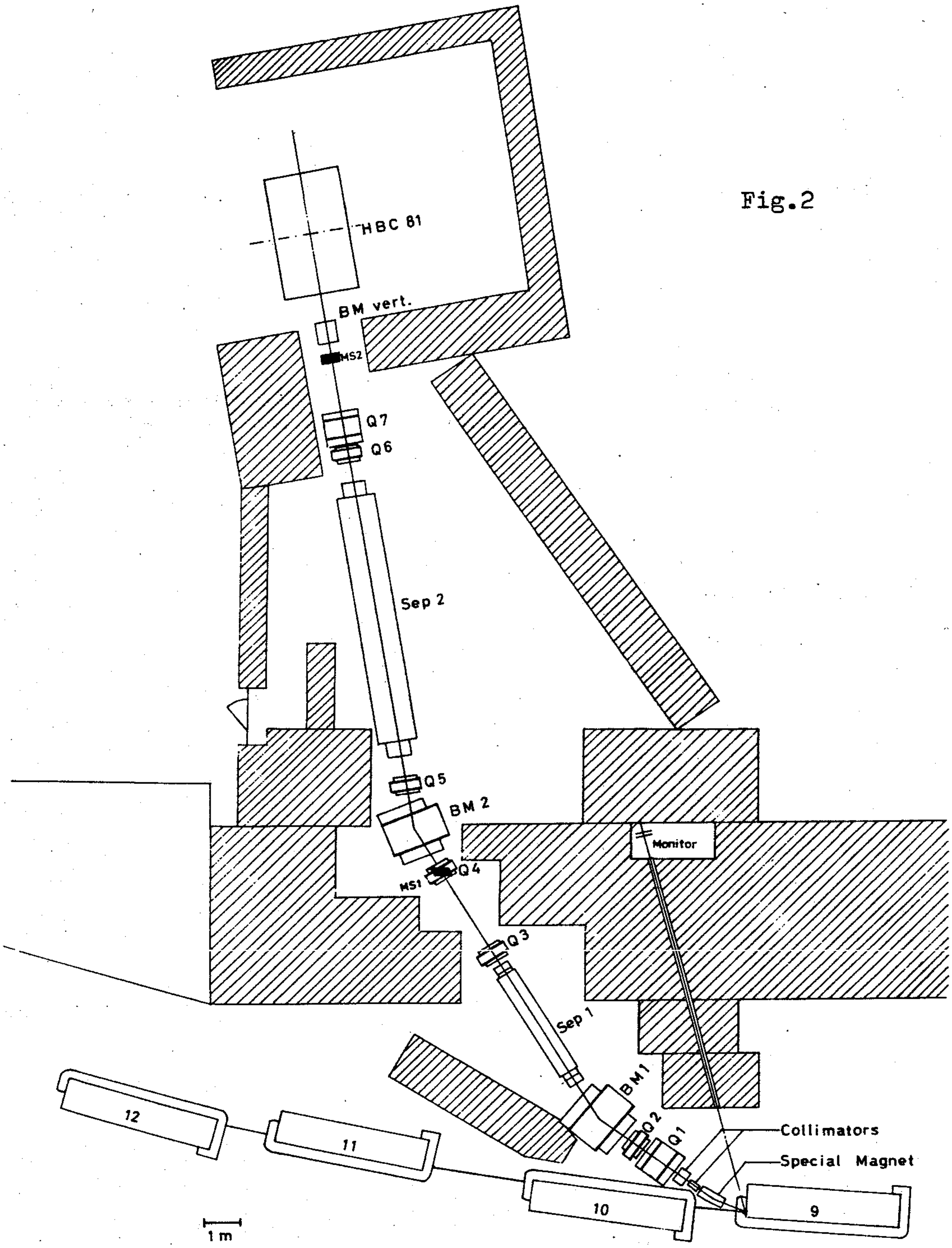
HBC 81
BM vert.
MS2
Q7
Q6
Sep 2
Q5
BM 2
Q4
MS1
Monitor
Q3
Sep 1
BM1
Q2
Q1
Collimators
Special Magnet
12
11
10
9
1 m

Fig.2

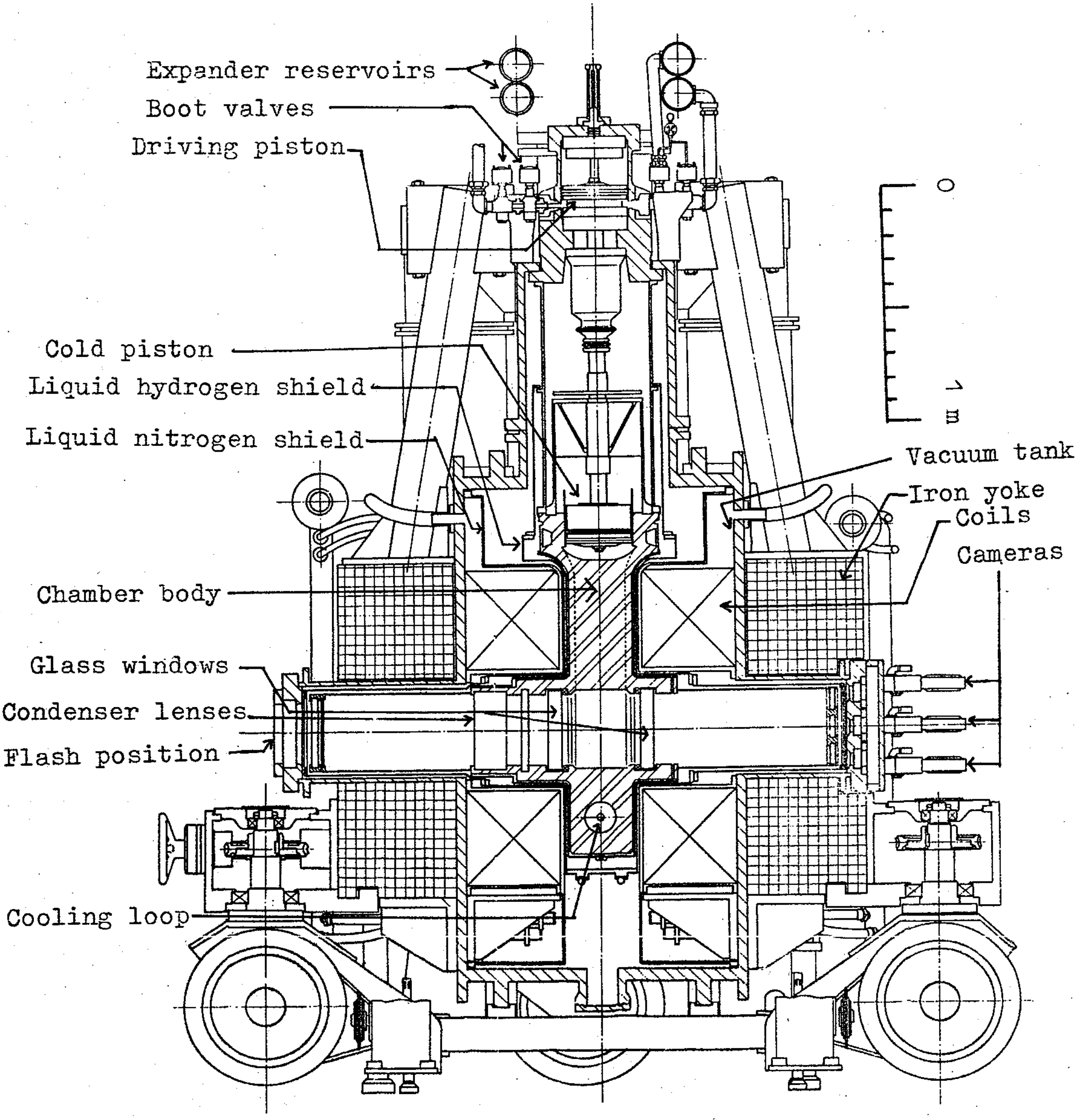

Fig.3 (a)
Saclay-CERN 81 cm Hydrogen Bubble Chamber

Fig.3.(b)

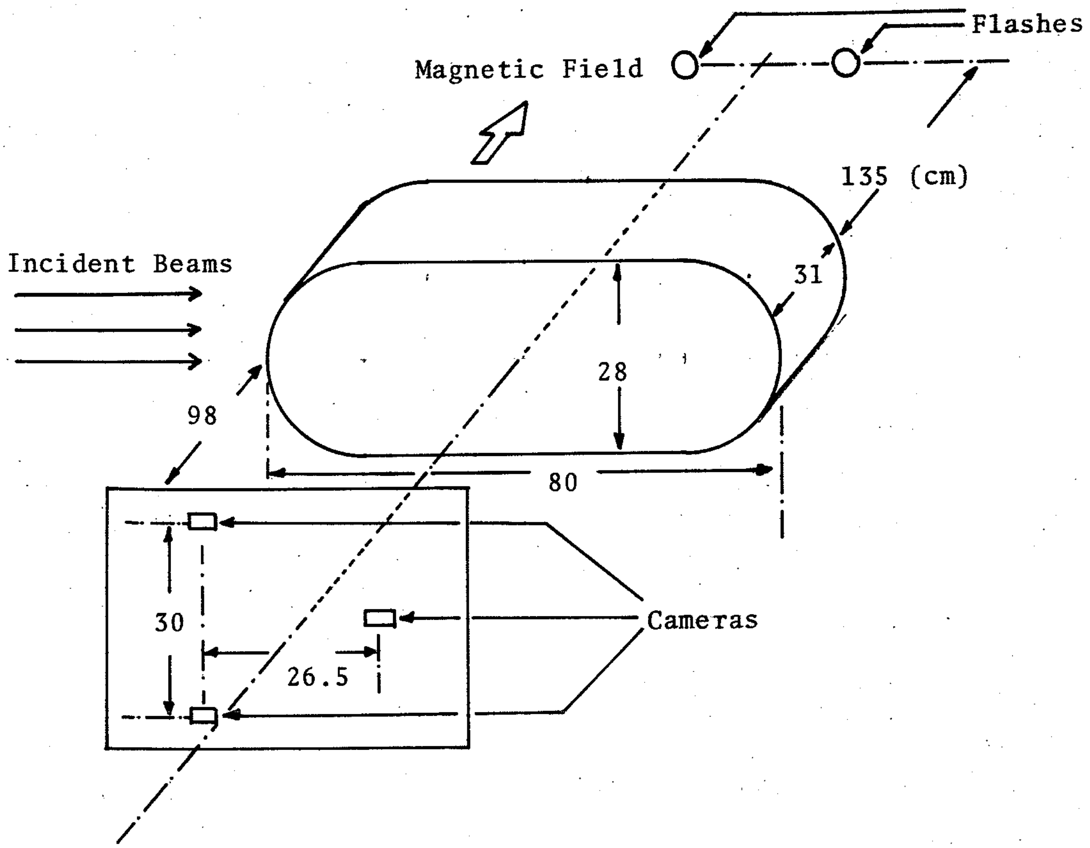
Flashes
Magnetic Field
135 (cm)
Incident Beams
31
28
98
80
30
26.5
Cameras

Fig. 4.

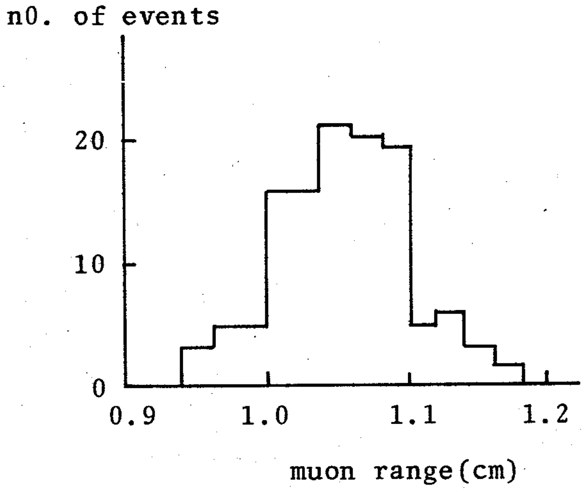
n0. of events
20
10
0
0.9
1.0
1.1
1.2
muon range(cm)

Fig.5.(a) 3-prong Event

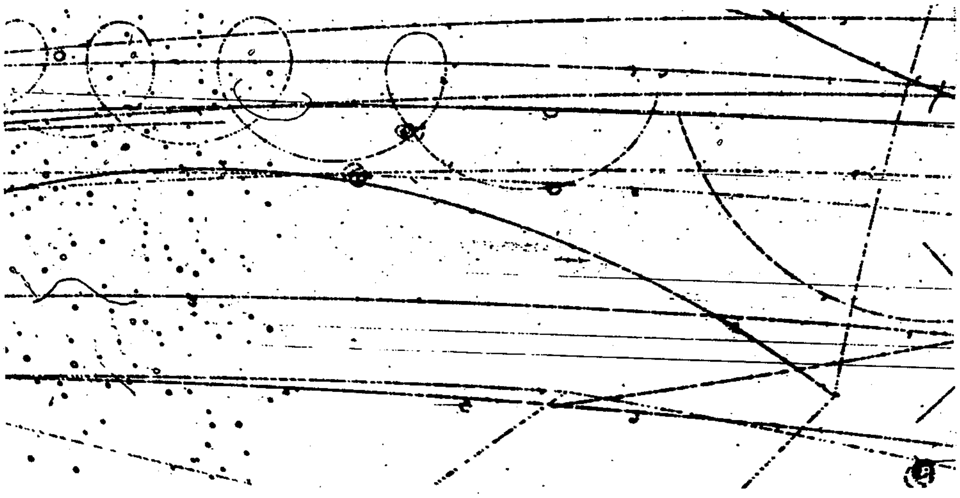

(b) 5-prong Event

(c) 7-prong Event

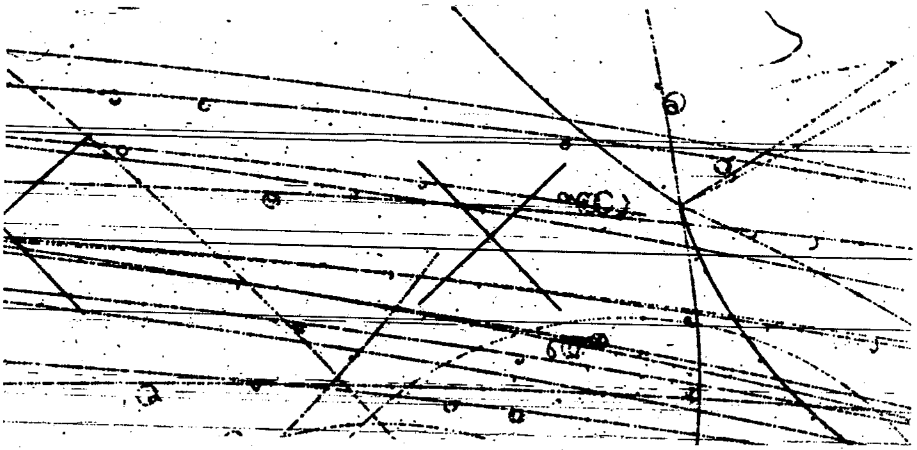

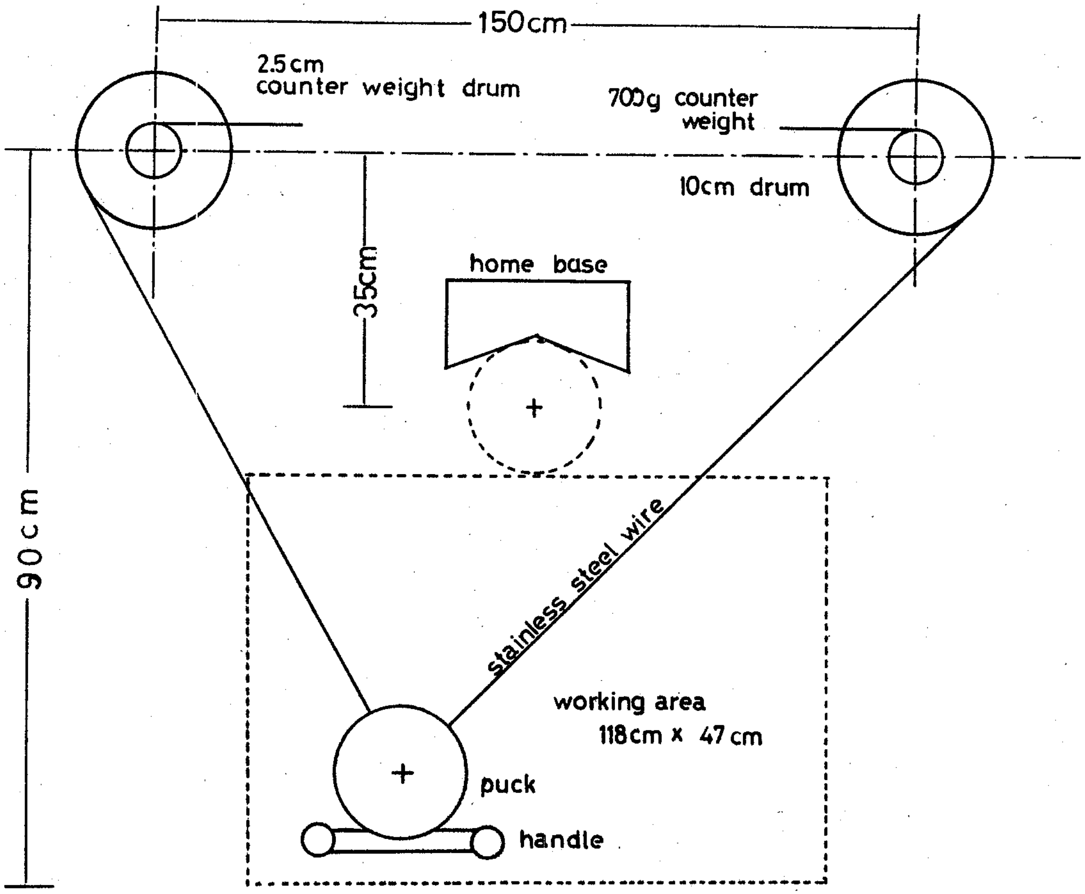

Fig.6(a) Hand-measuring Device SMP .

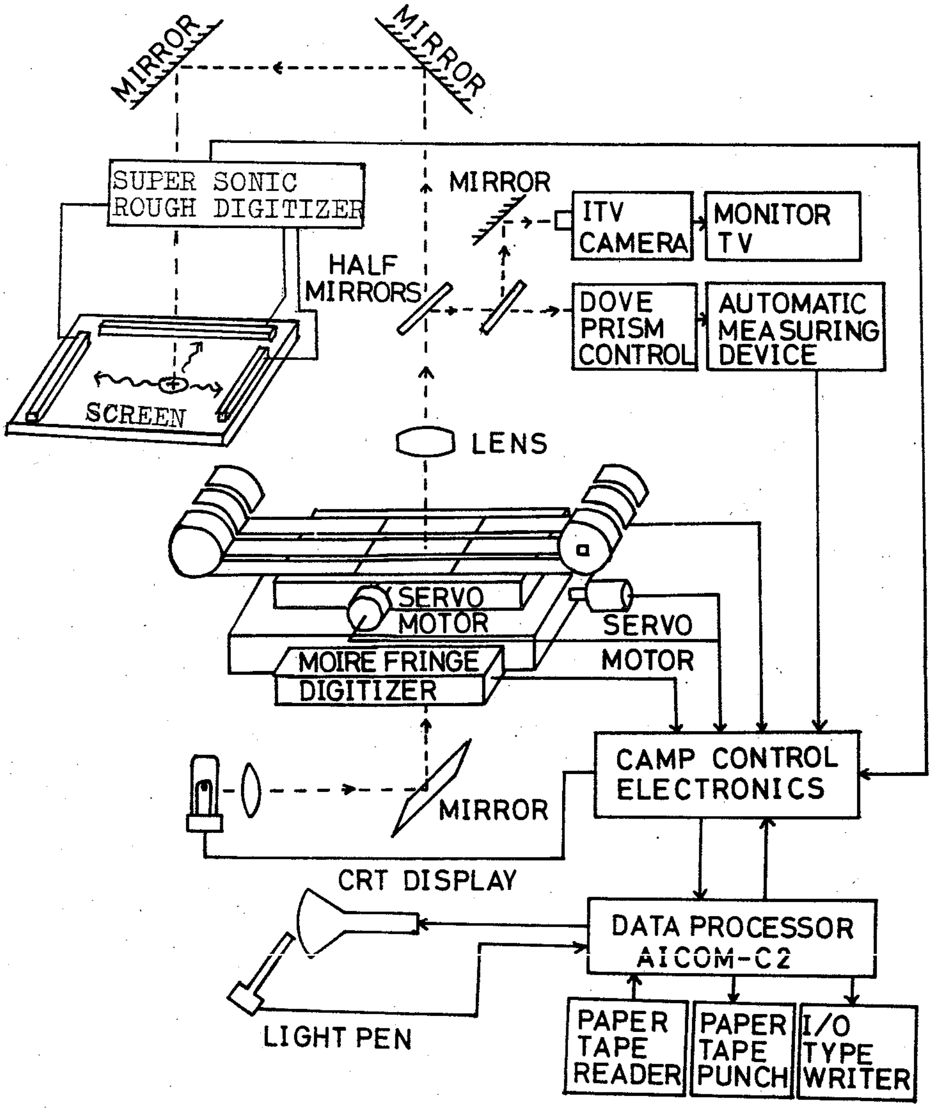

Fig.6 (b) Block diagram of CAMP.

Fig. 7.

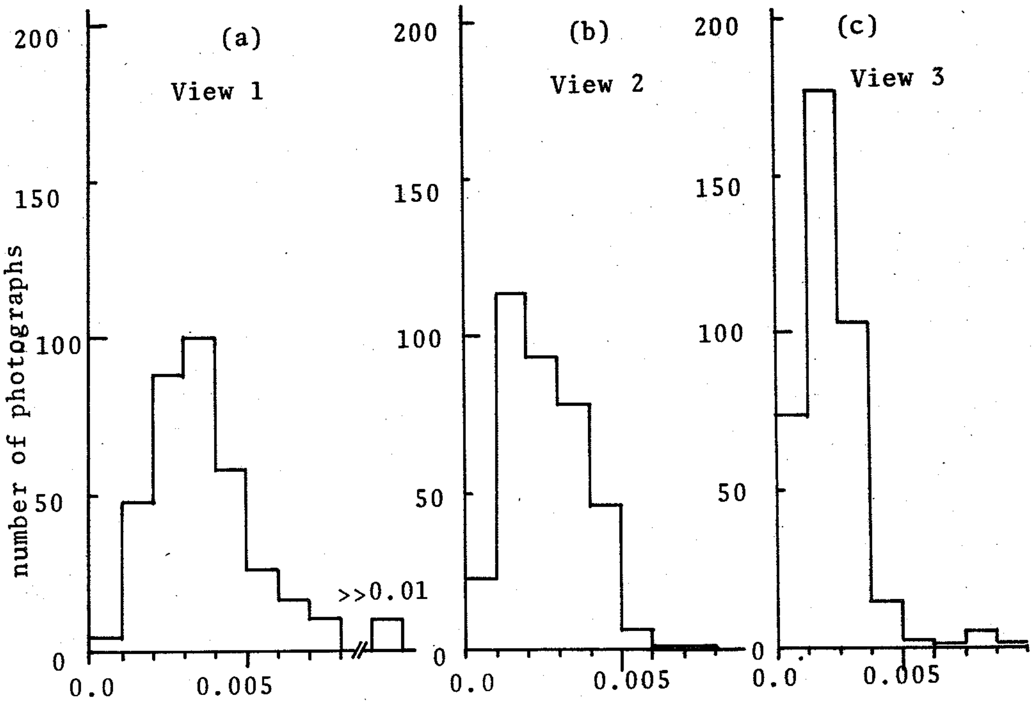
(a)
View 1
(b)
View 2
(c)
View 3
number of photographs
200
150
100
50
0
0.0
0.005
>>0.01

Fig.8.

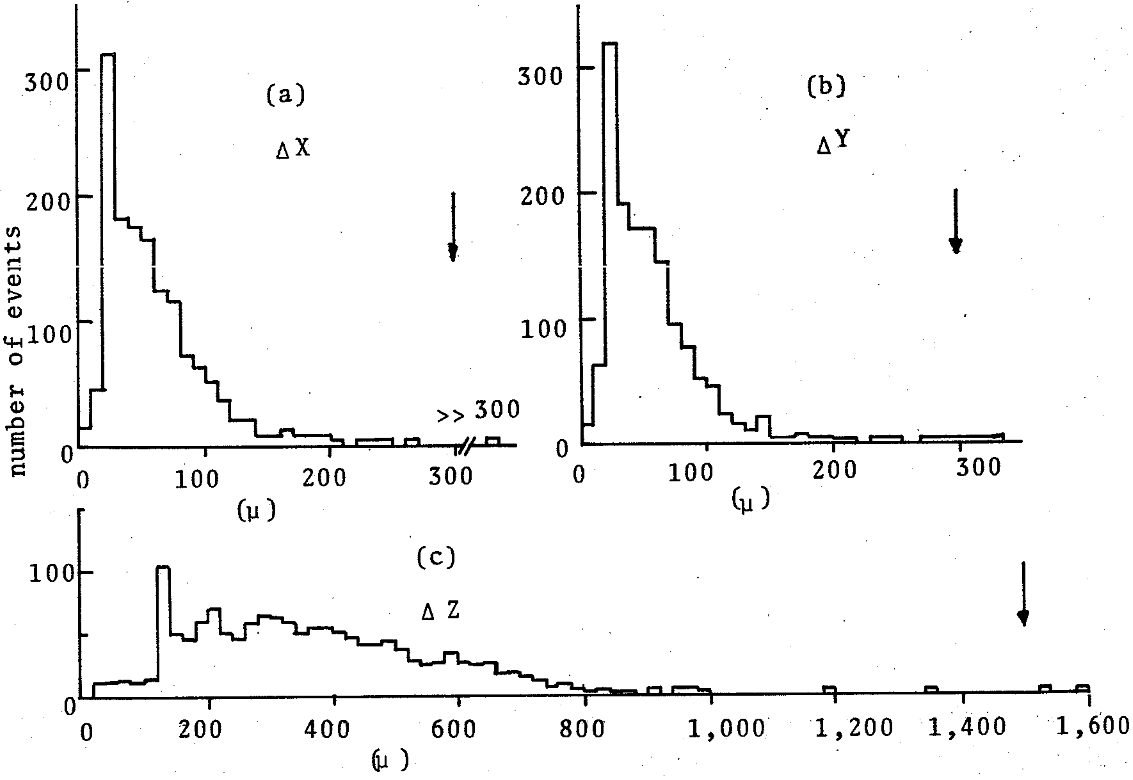
(a)
ΔX
(b)
ΔY
(c)
ΔZ
number of events
300
200
100
0
100
200
300
>> 300
(μ)
400
600
800
1,000
1,200
1,400
1,600

Fig. 9.

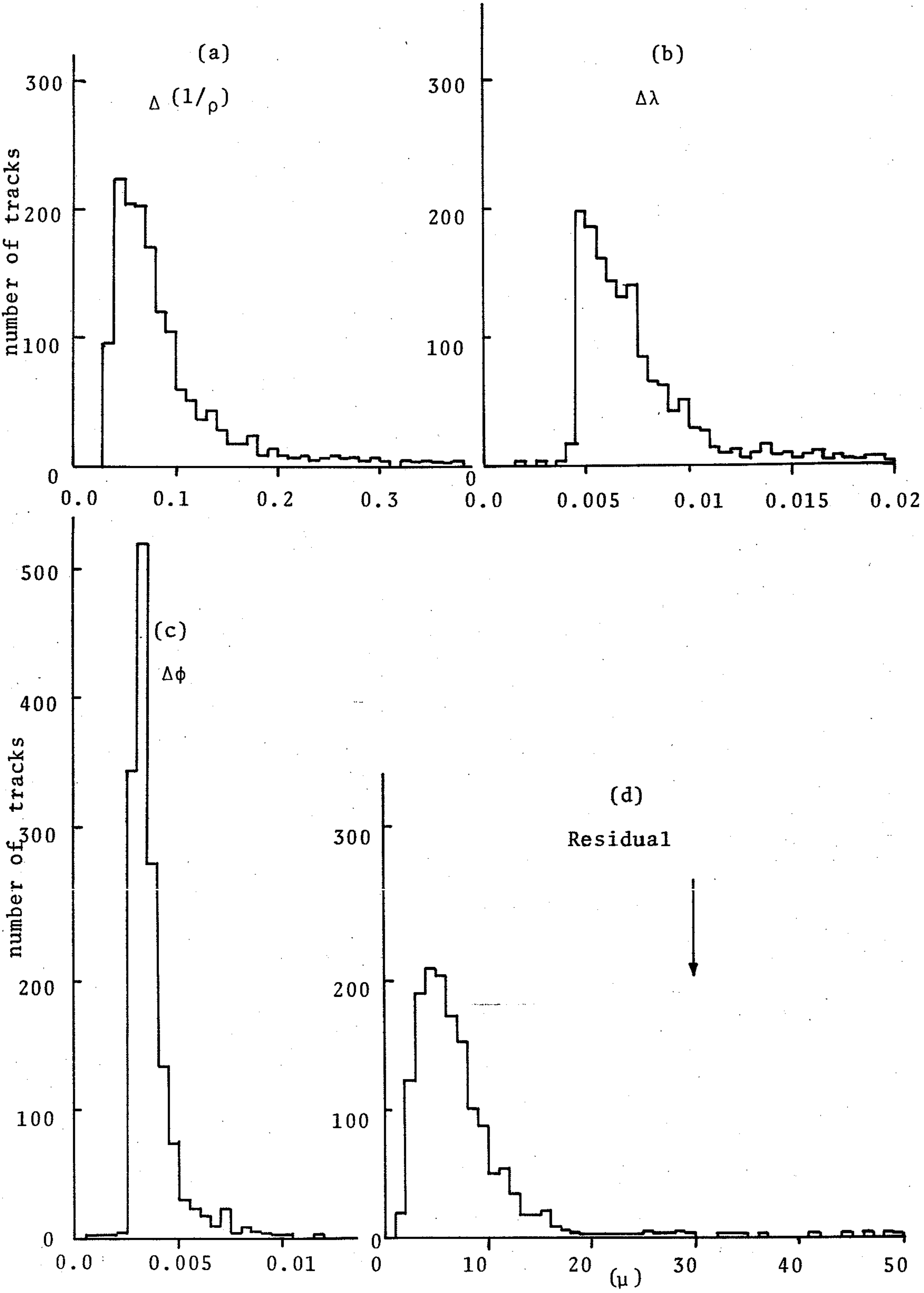
(a)
Δ (1/ρ)
number of tracks
300
200
100
0
0.0
0.1
0.2
0.3
(b)
Δλ
300
200
100
0
0.0
0.005
0.01
0.015
0.02
(c)
Δϕ
number of tracks
500
400
300
200
100
0
0.0
0.005
0.01
(d)
Residual
300
200
100
0
0
10
20
30
40
50
(μ)

Fig.10.

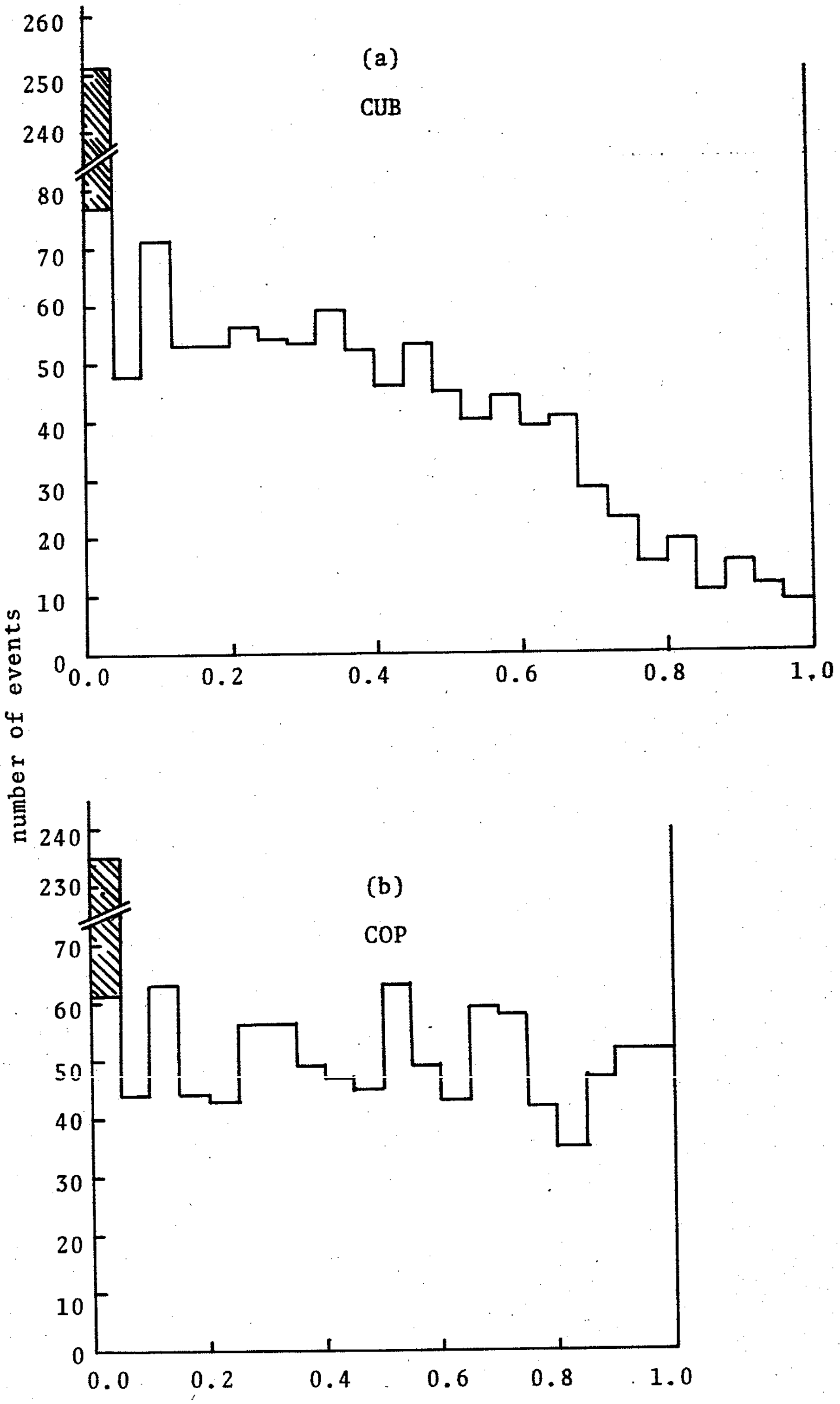
(a)
CUB
260
250
240
80
70
60
50
40
30
20
10
0
0.0
0.2
0.4
0.6
0.8
1.0
number of events
(b)
COP
240
230
70
60
50
40
30
20
10
0
0.0
0.2
0.4
0.6
0.8
1.0

Fig.11.

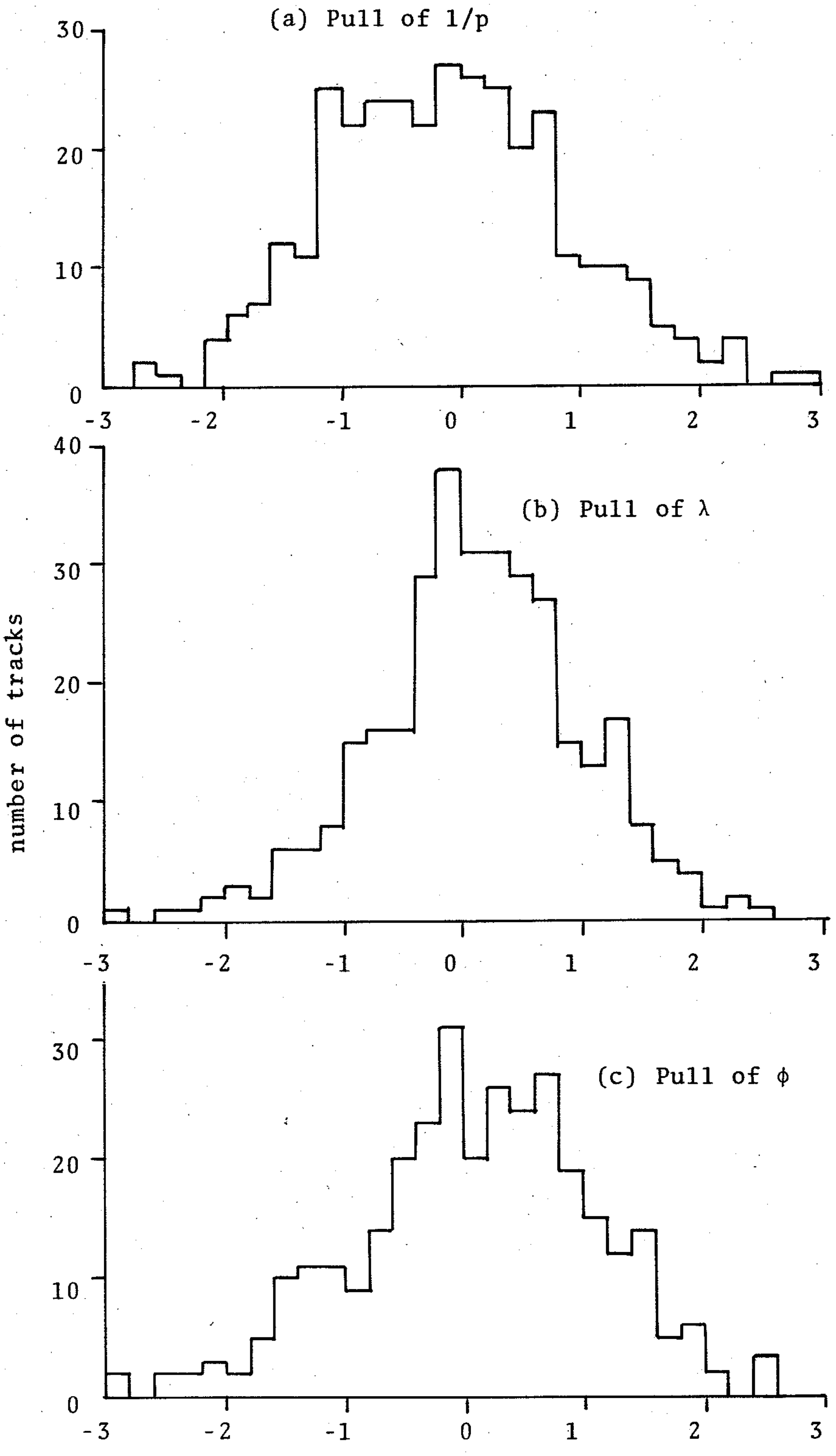
(a) Pull of 1/p

(b) Pull of λ

(c) Pull of ϕ

Fig.12.

χ^2 Probability

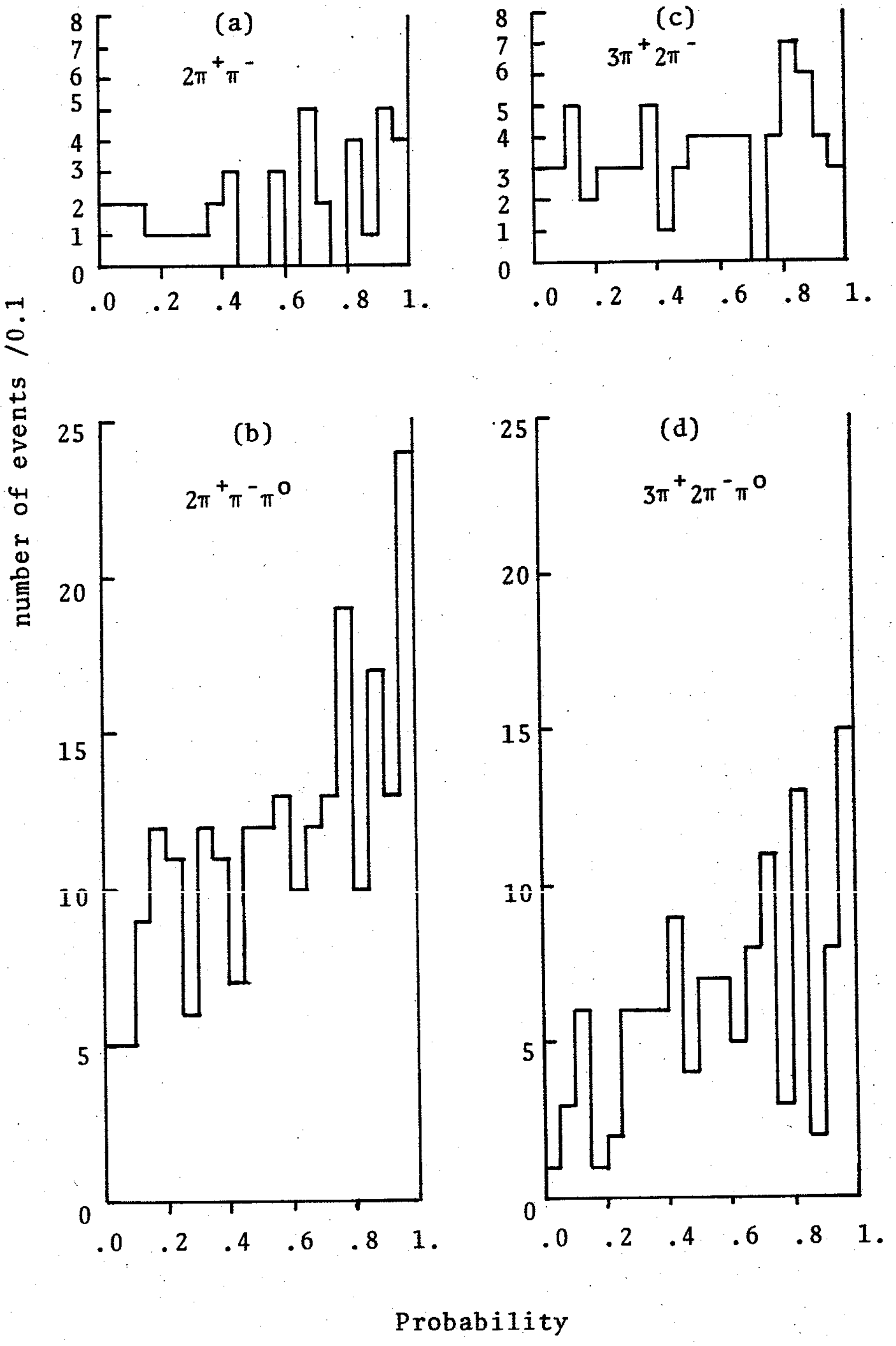

Fig.13.

Missing-Mass Squared

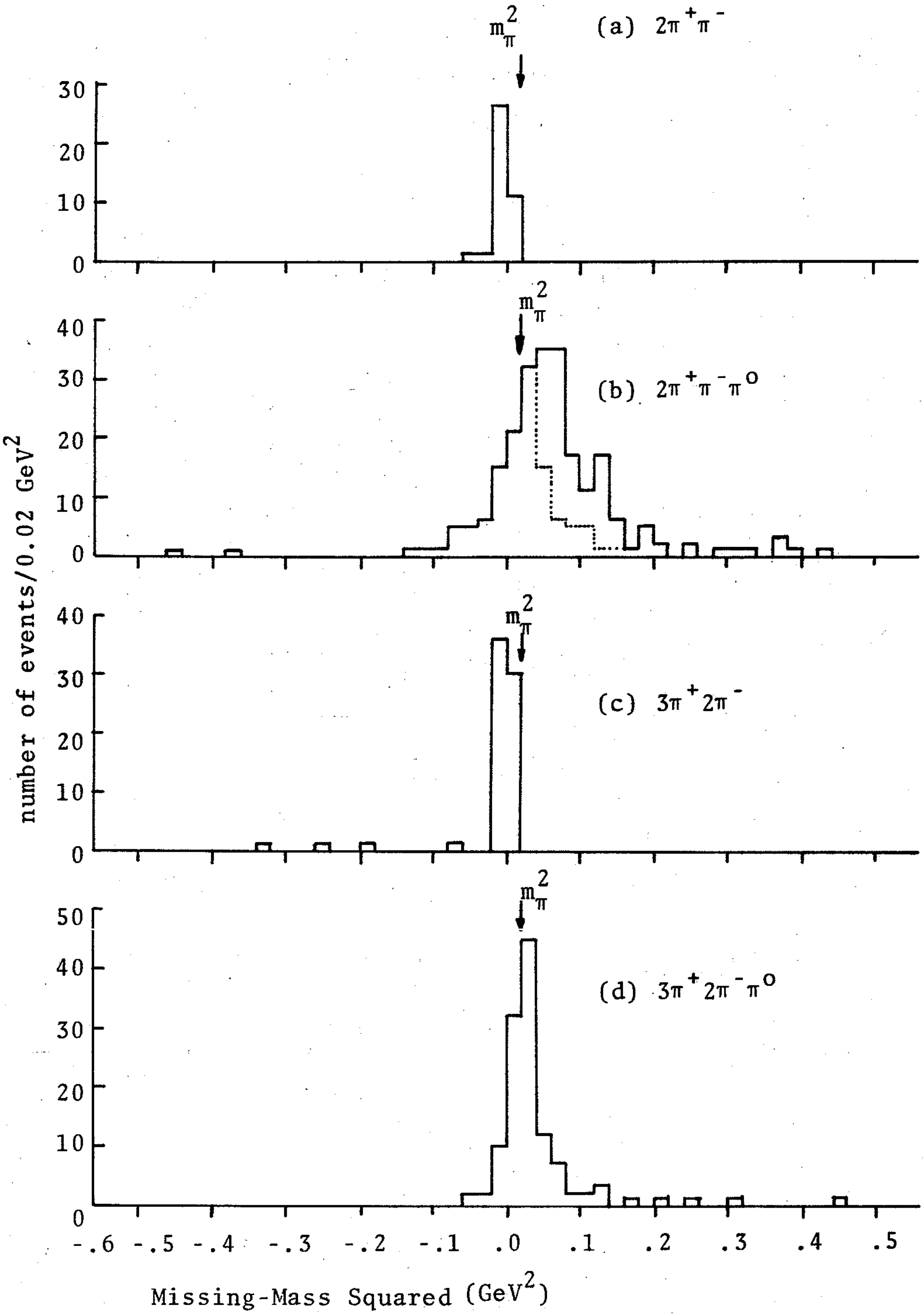

Figure 14

Experimental Procedure

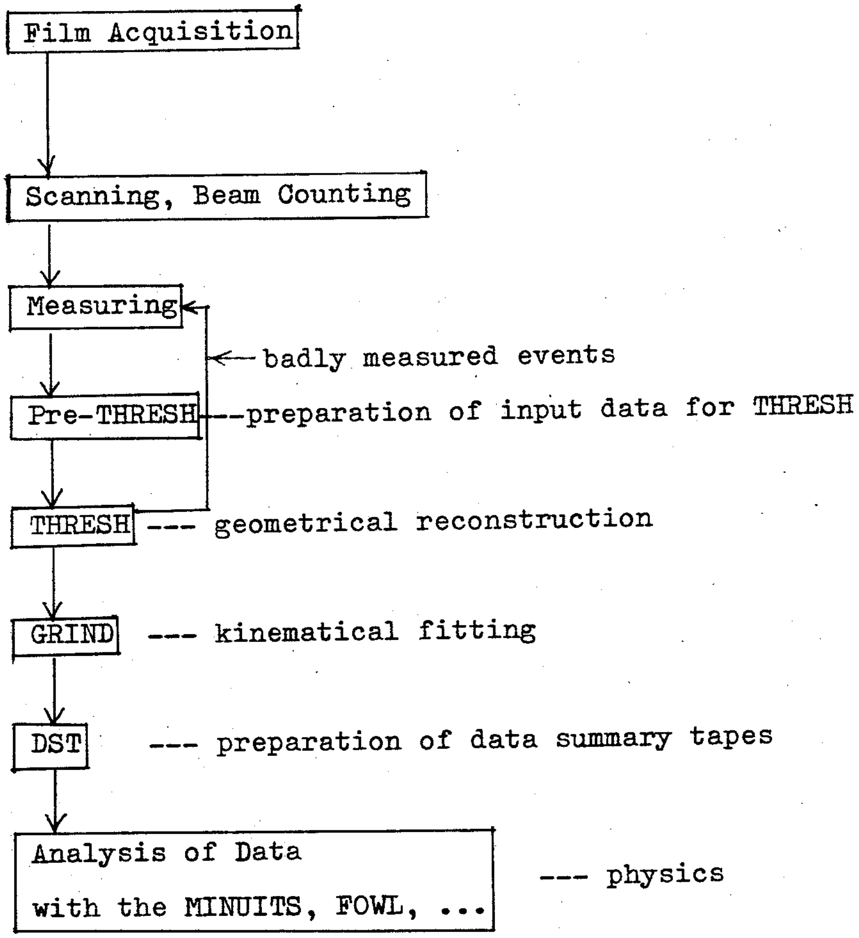

Fig.15.

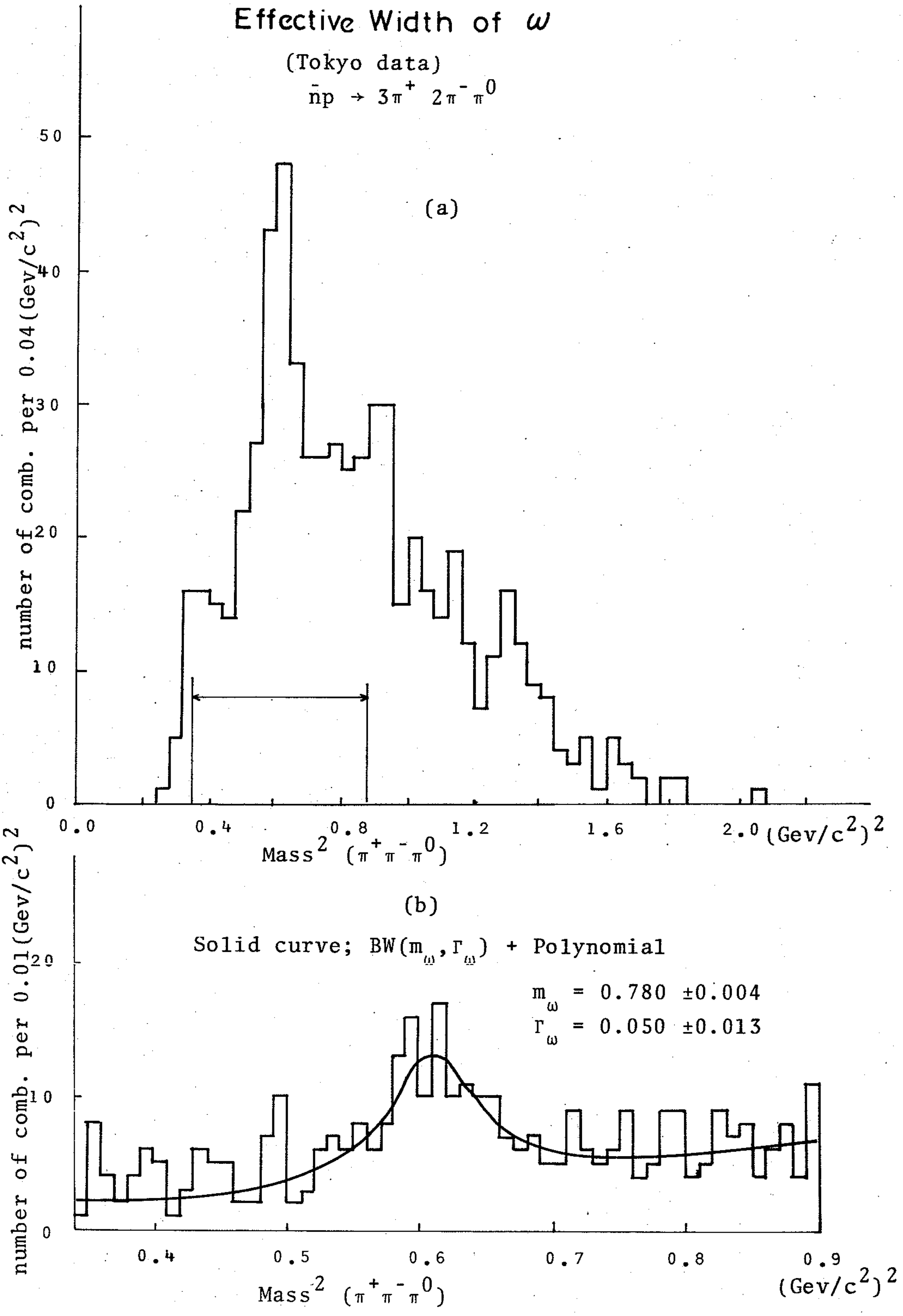
Effective Width of ω
(Tokyo data)
n̄p → 3π⁺ 2π⁻ π⁰
(a)
number of comb. per 0.04 (Gev/c²)²
0
10
20
30
40
50
0.0
0.4
0.8
1.2
1.6
2.0
(Gev/c²)²
Mass² (π⁺π⁻π⁰)
(b)
Solid curve; BW(m_ω, Γ_ω) + Polynomial
m_ω = 0.780 ±0.004
Γ_ω = 0.050 ±0.013
number of comb. per 0.01 (Gev/c²)²
0
10
20
0.4
0.5
0.6
0.7
0.8
0.9
(Gev/c²)²
Mass² (π⁺π⁻π⁰)

Fig.16.

Antineutron Momenta

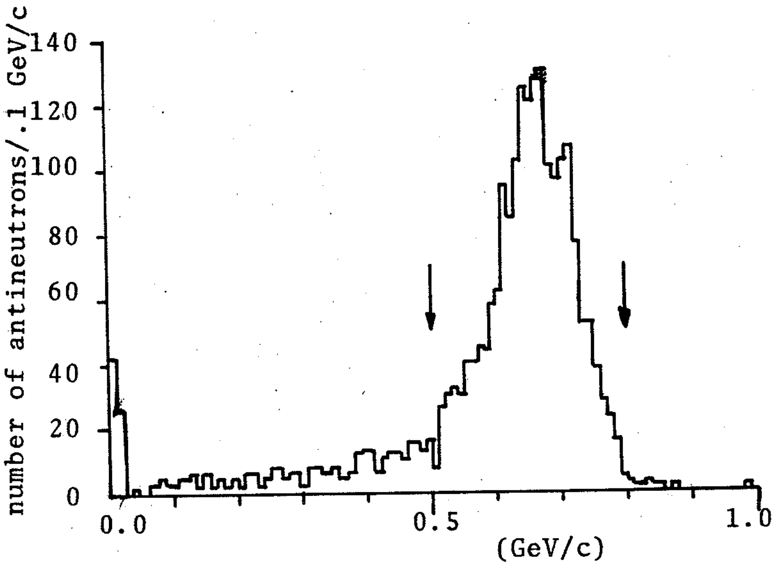

Fig.17.

Resonance Productions in $2\pi^+\pi^-$ Samples

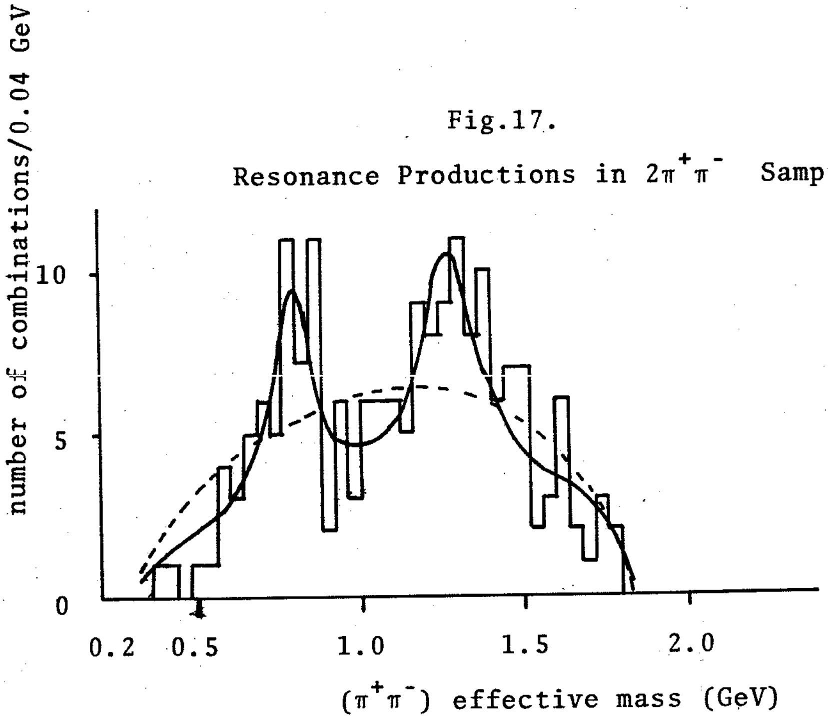

Fig.18.

Resonance Productions in $2\pi^+\pi^-\pi^0$ Samples

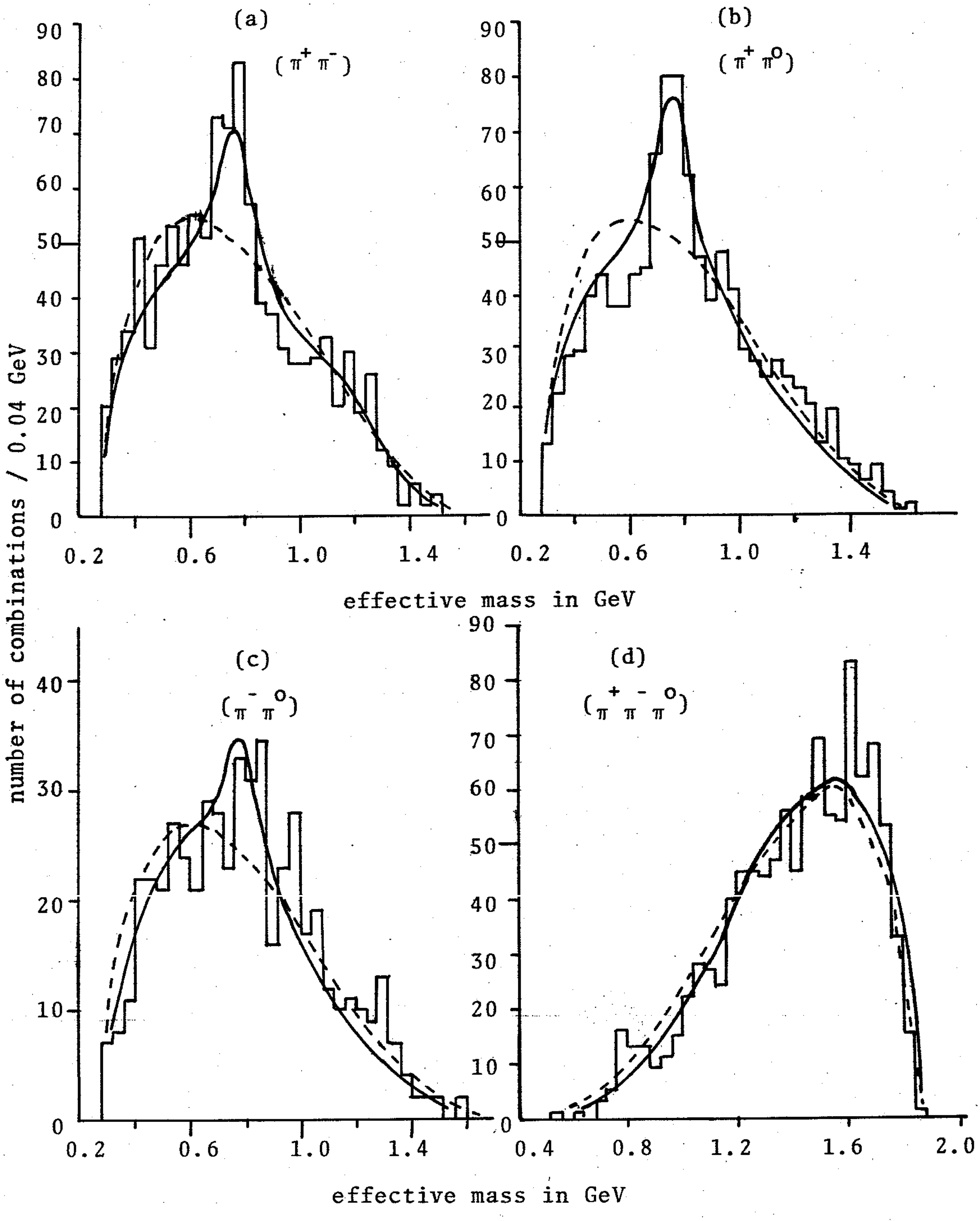

Fig.19.

Resonance Productions in $3\pi^+2\pi^-$ Samples

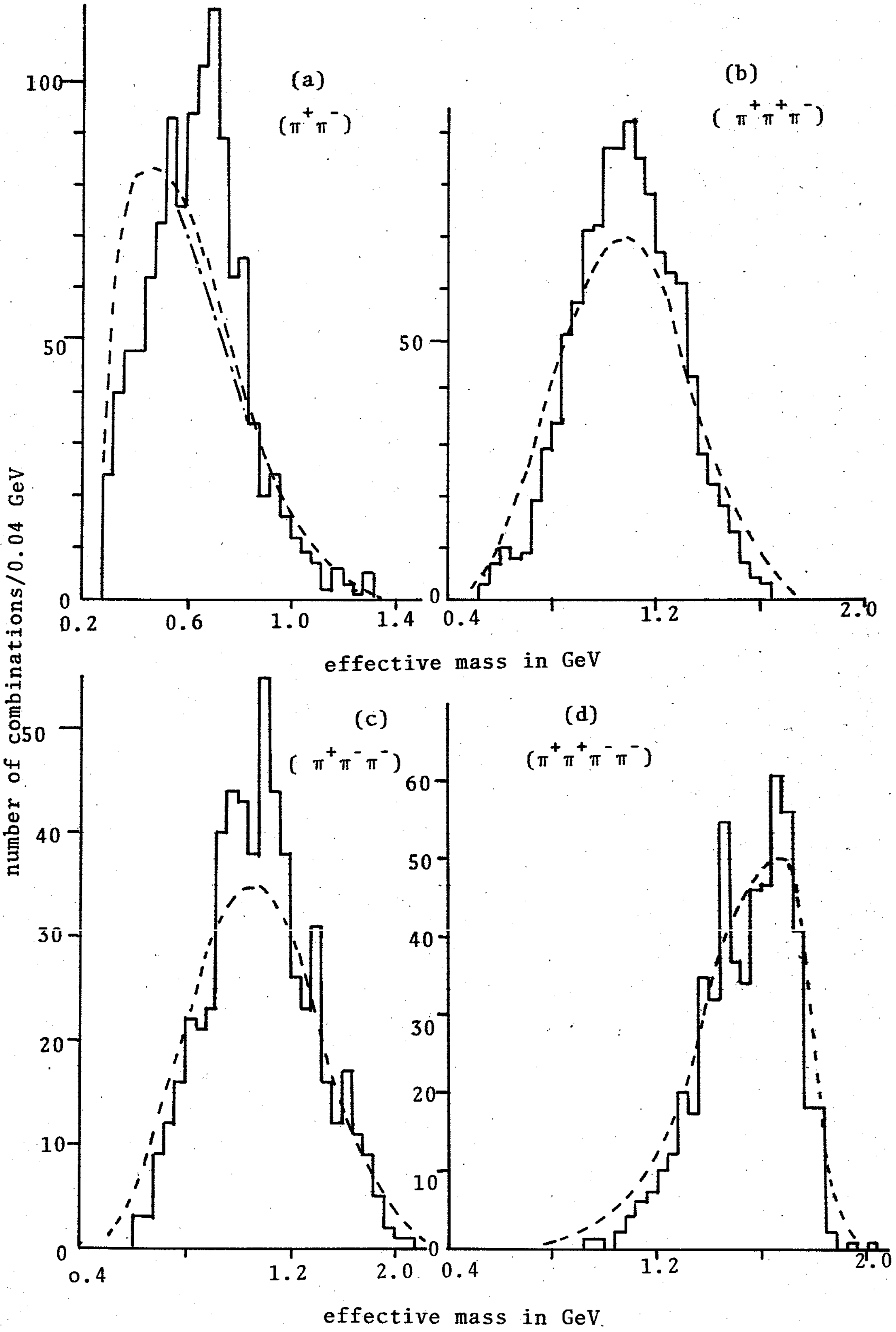

Fig.20.

Re sonance Productions in $3\pi^+2\pi^-\pi^o$ Samples

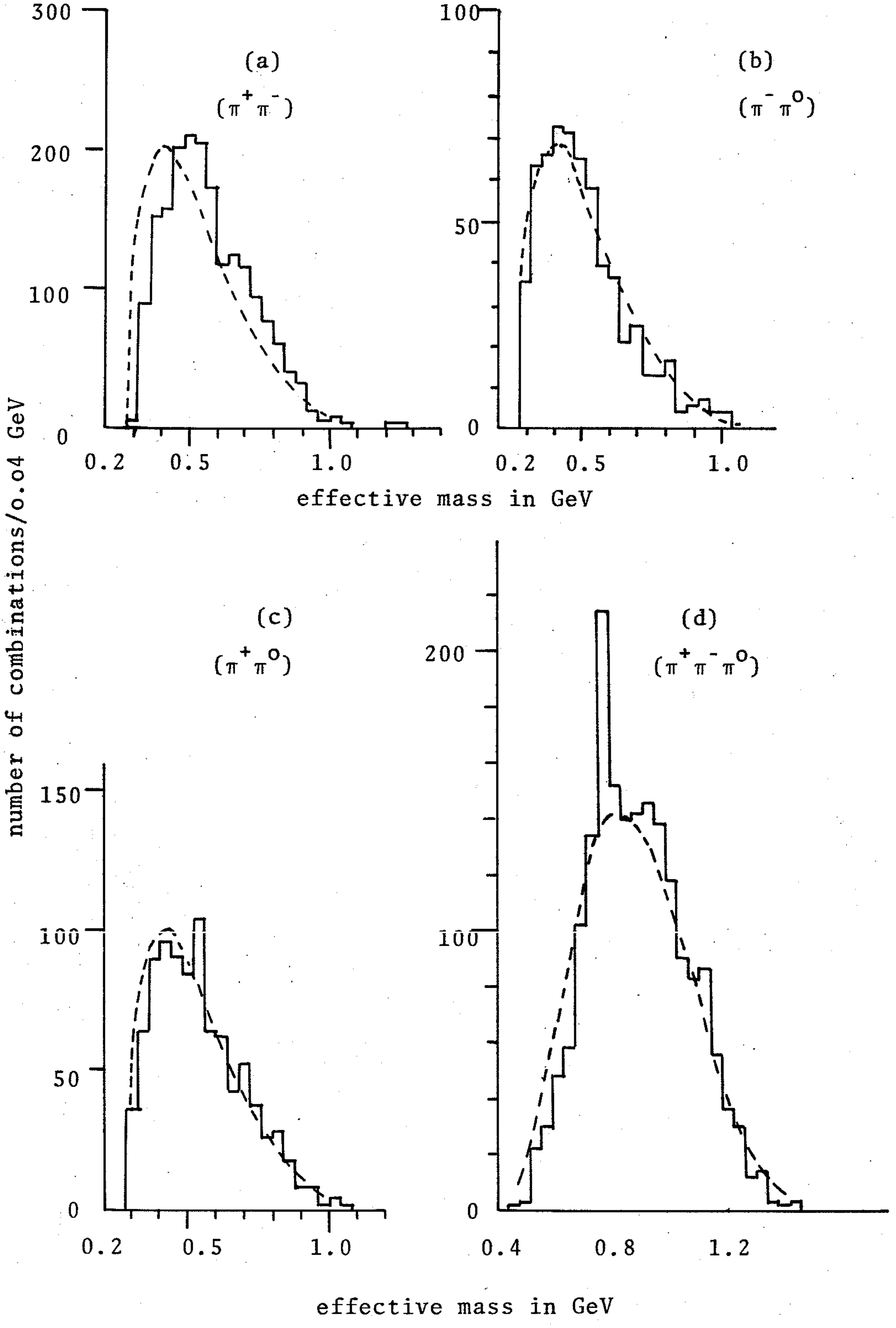

Fig.21.

($\pi^+\pi^-$) Effective Mass Spectra

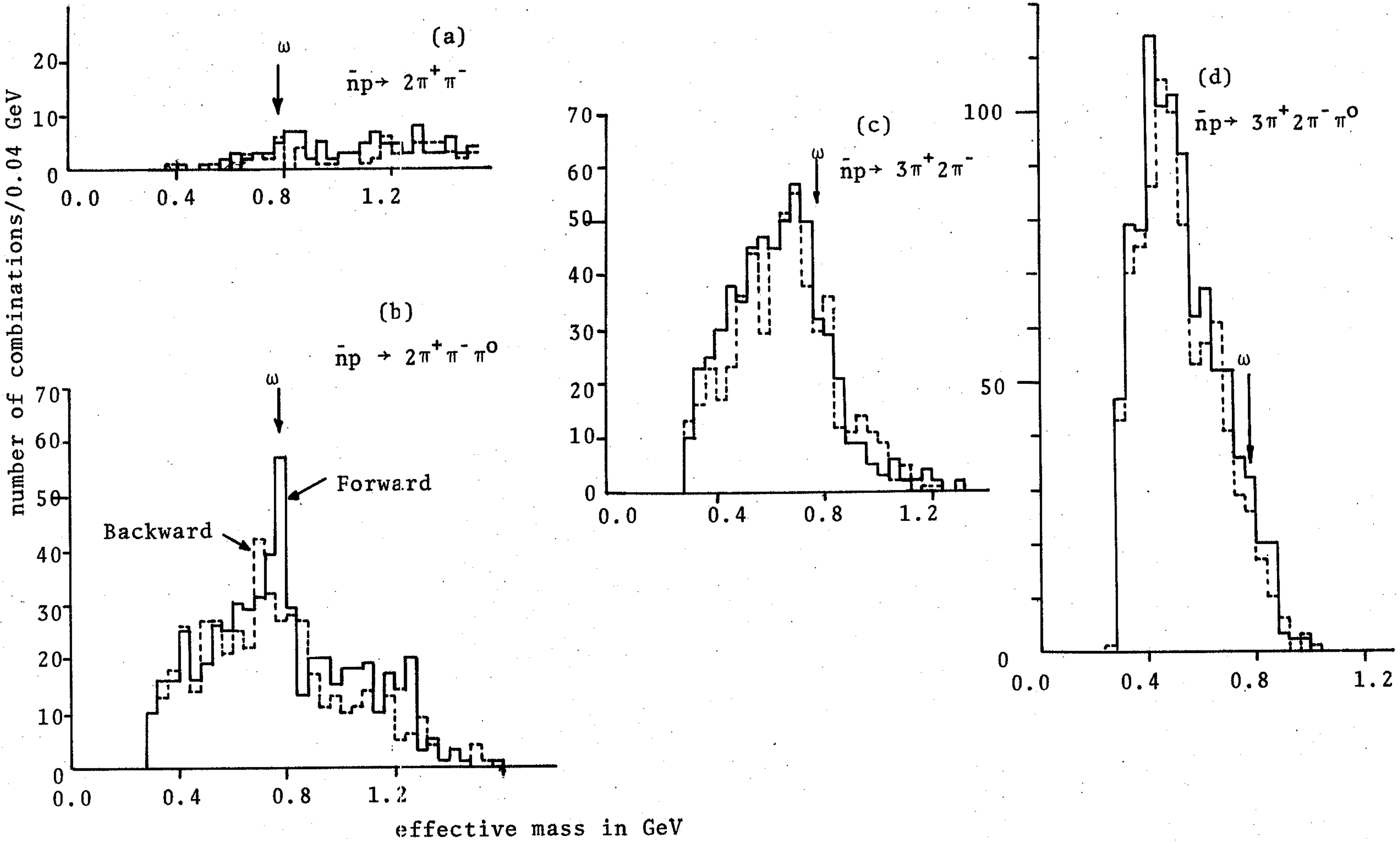

Fig.22.

$(\pi\ \pi)$Mass Spectra of $\bar{n}p \rightarrow 2\pi^+\pi^-\pi^o$ Samples

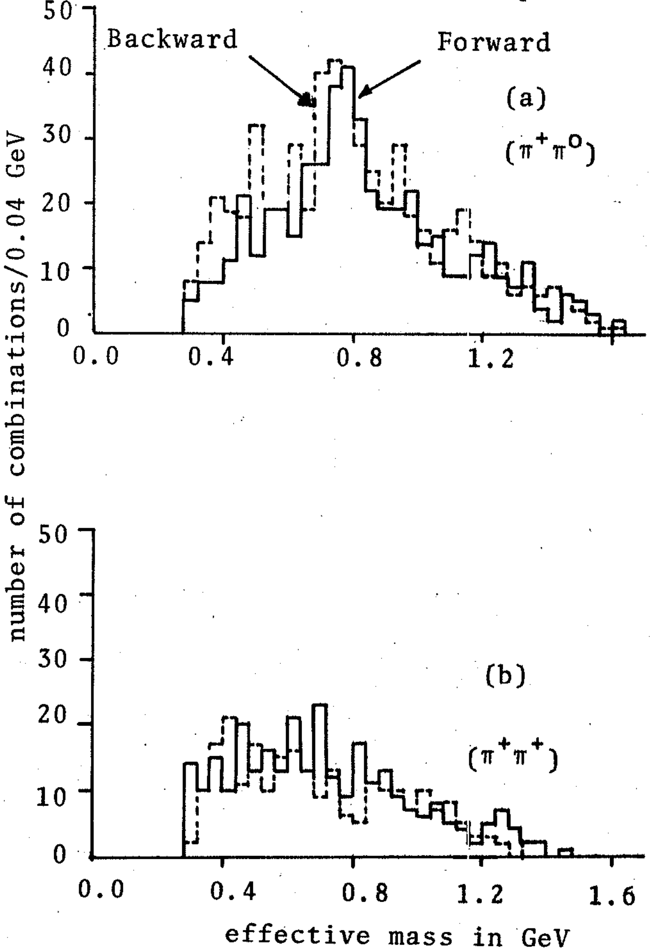

Fig.23.

Production Anglesof$(\pi^+\pi^-)$ Dipions

$\bar{n}p \rightarrow 2\pi^+\pi^-\pi^o$

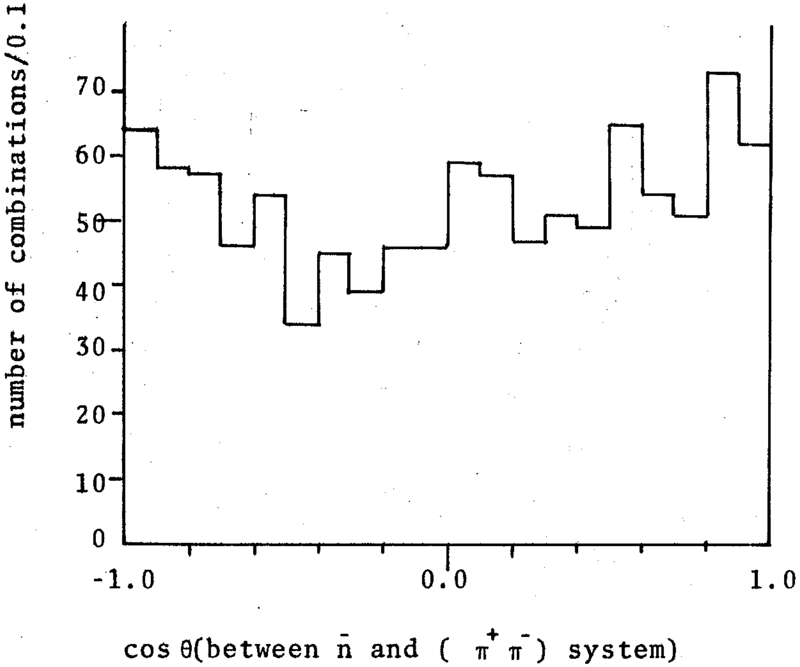

Fig.24.

$(\pi^+\pi^-)$ Mass Spectra of $\bar{n}p \rightarrow 2\pi^+\pi^-\pi^0$

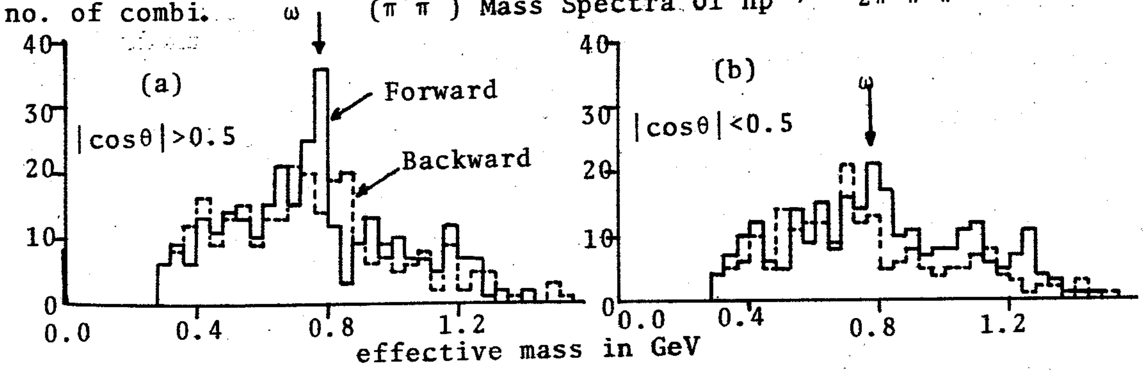

Fig.25.

Fit of $(\pi^+\pi^-)$ Mass Spectra to 'ρ+ω + ρ/ωint.'

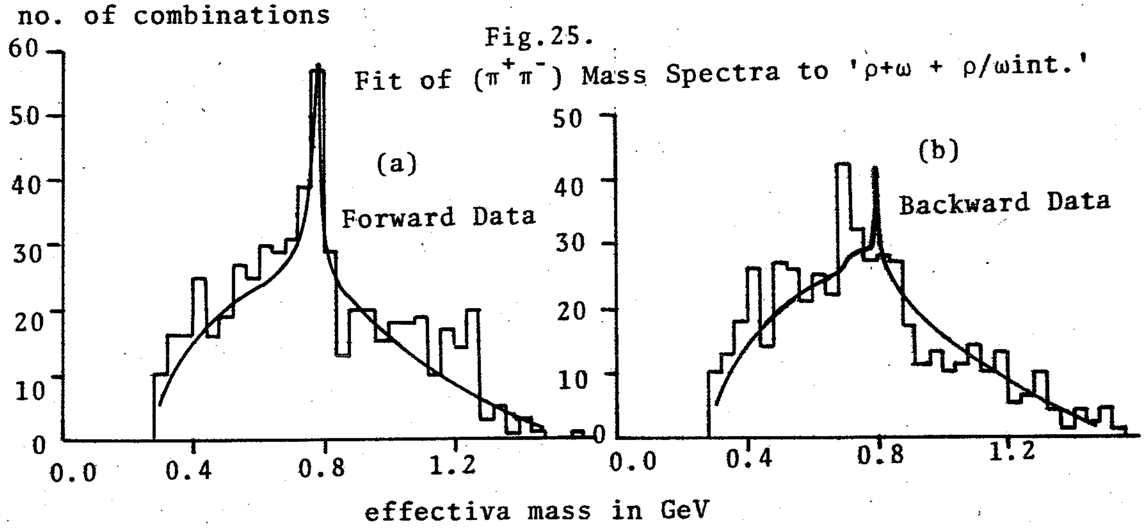

Fig.26.

Fit of $(\pi^+\pi^-)$ Mass Spectra to ' ρ + ω + ρ/ωint.'

(see the text)

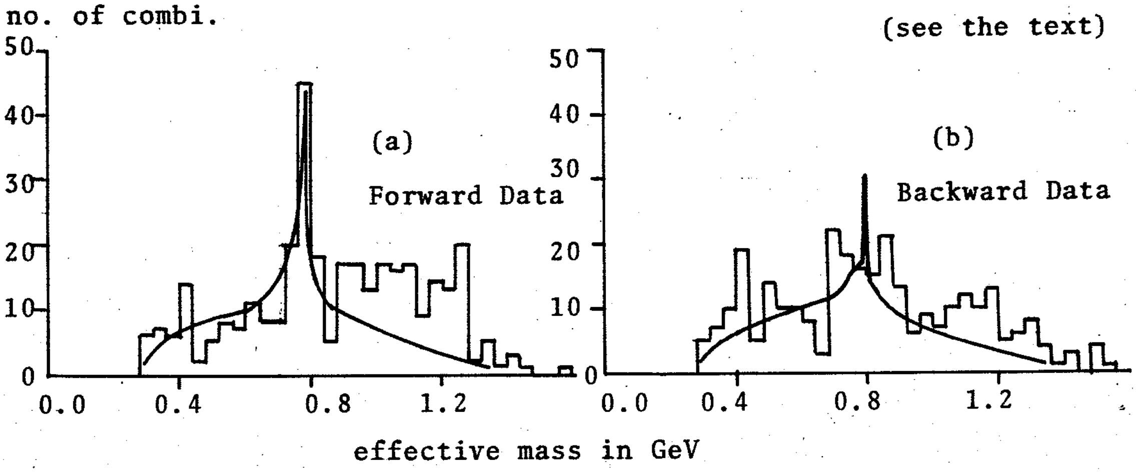

Fig.27.

Graphs of CLA model for $\bar{n}p \longrightarrow 2\pi^+\pi^-$

three body state

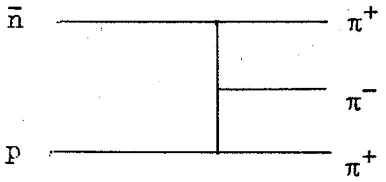

two body states

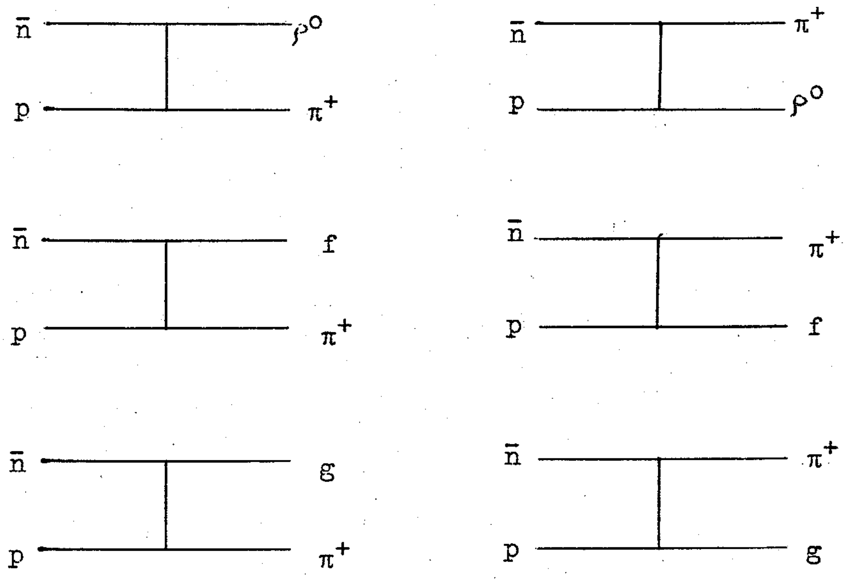

Fig.28.

Graphs of CLA model for $\bar{n}p \longrightarrow 2\pi^+\pi^-\pi^0$

two body states

three body states

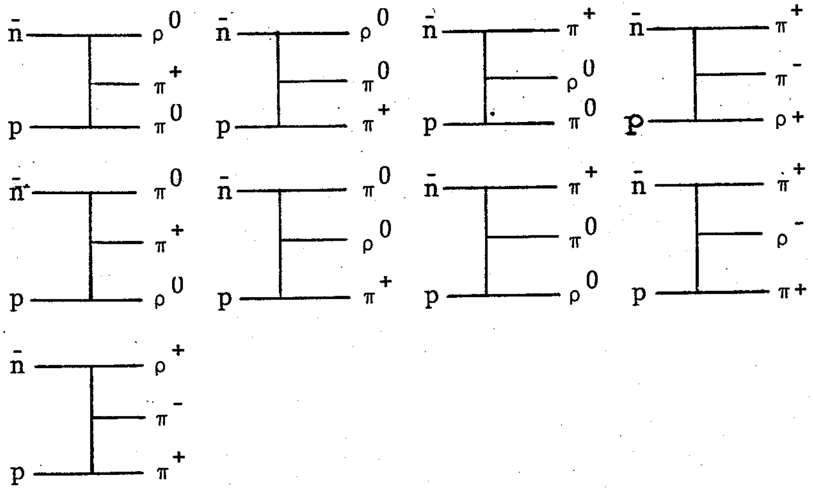

four body states

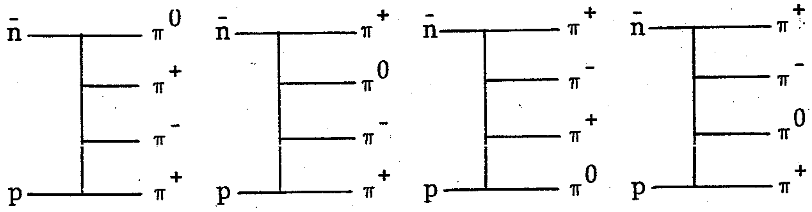

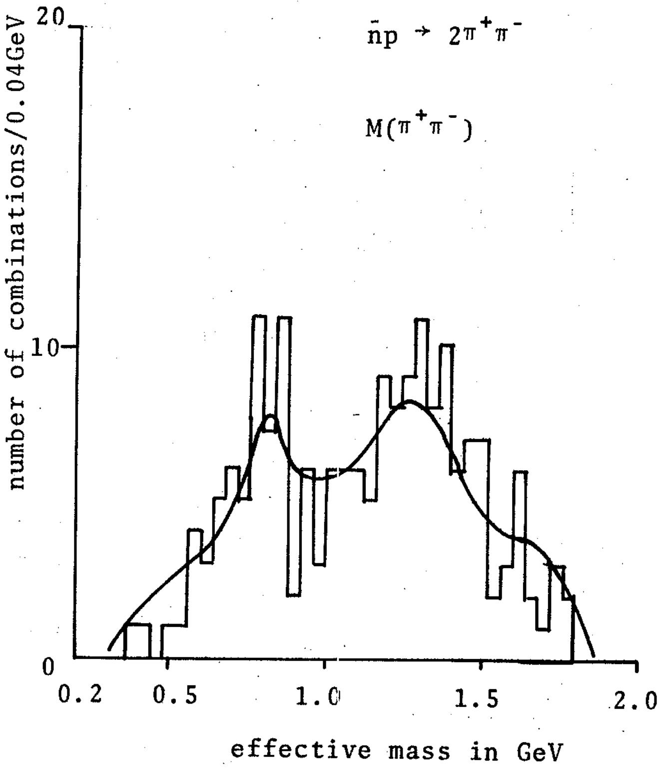

Fig.29.

$\bar{n}p \rightarrow 2\pi^+\pi^-$

$M(\pi^+\pi^-)$

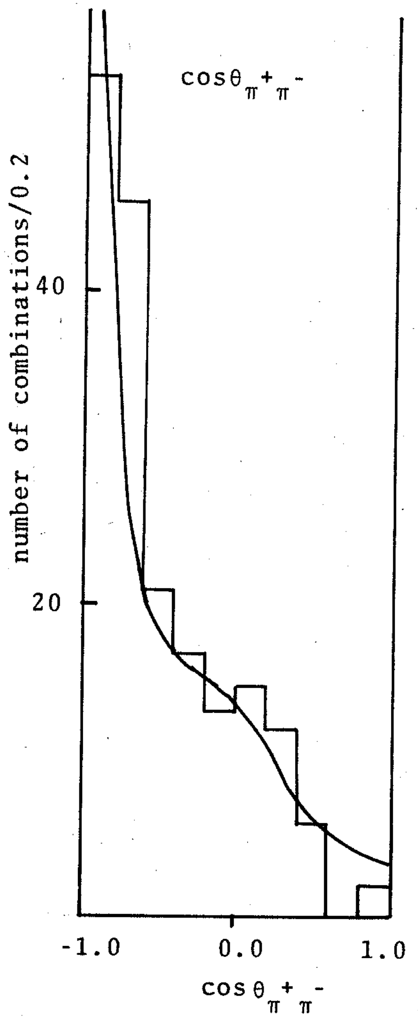

Fig.30.

$\bar{n}p \rightarrow 2\pi^+\pi^-$

$\cos\theta_{\pi^+\pi^-}$

Fig.31.

$\bar{n}p \rightarrow 2\pi^+\pi^-\pi^0$

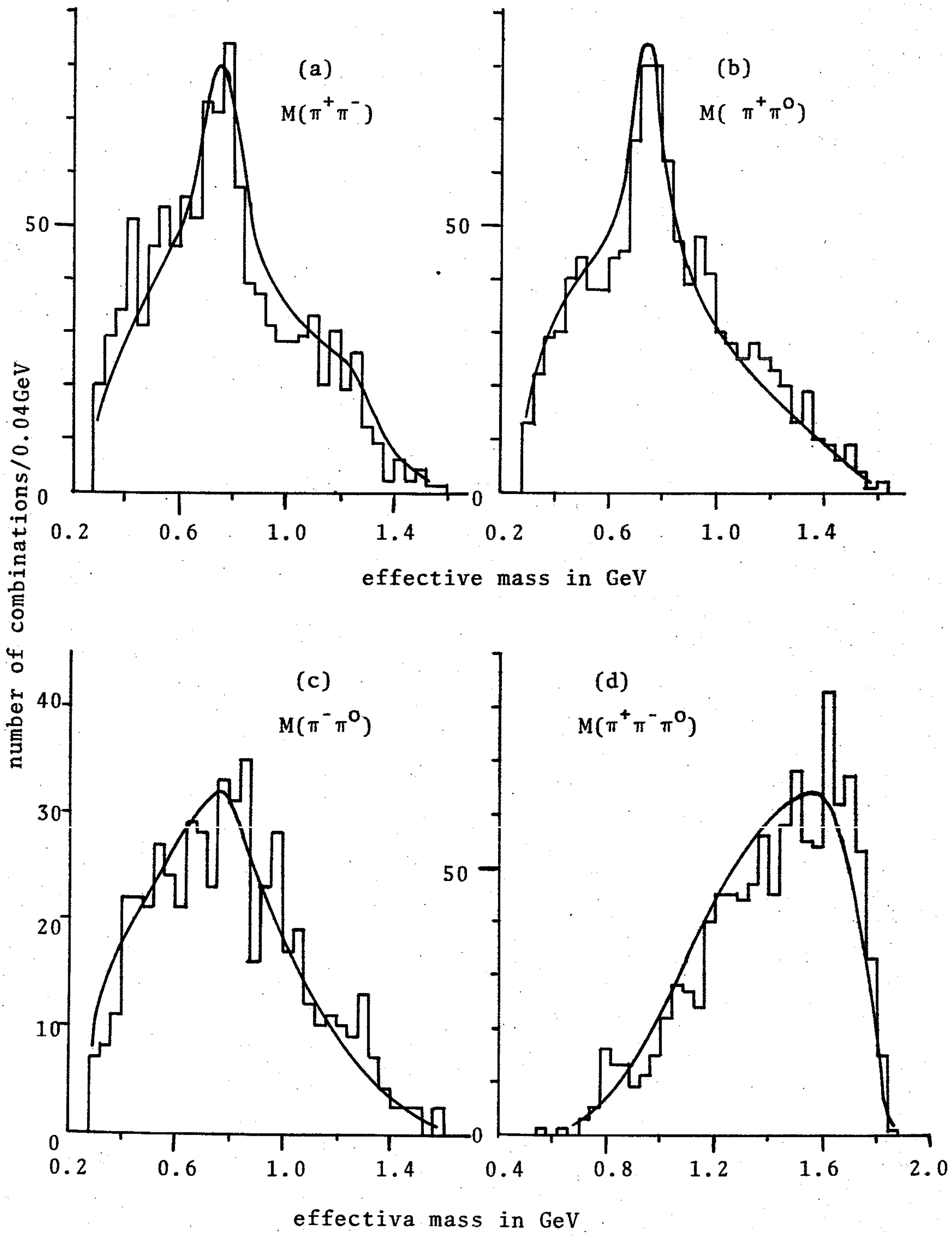

Fig.32.

$\bar{n}p \rightarrow 2\pi^+\pi^-\pi^o$

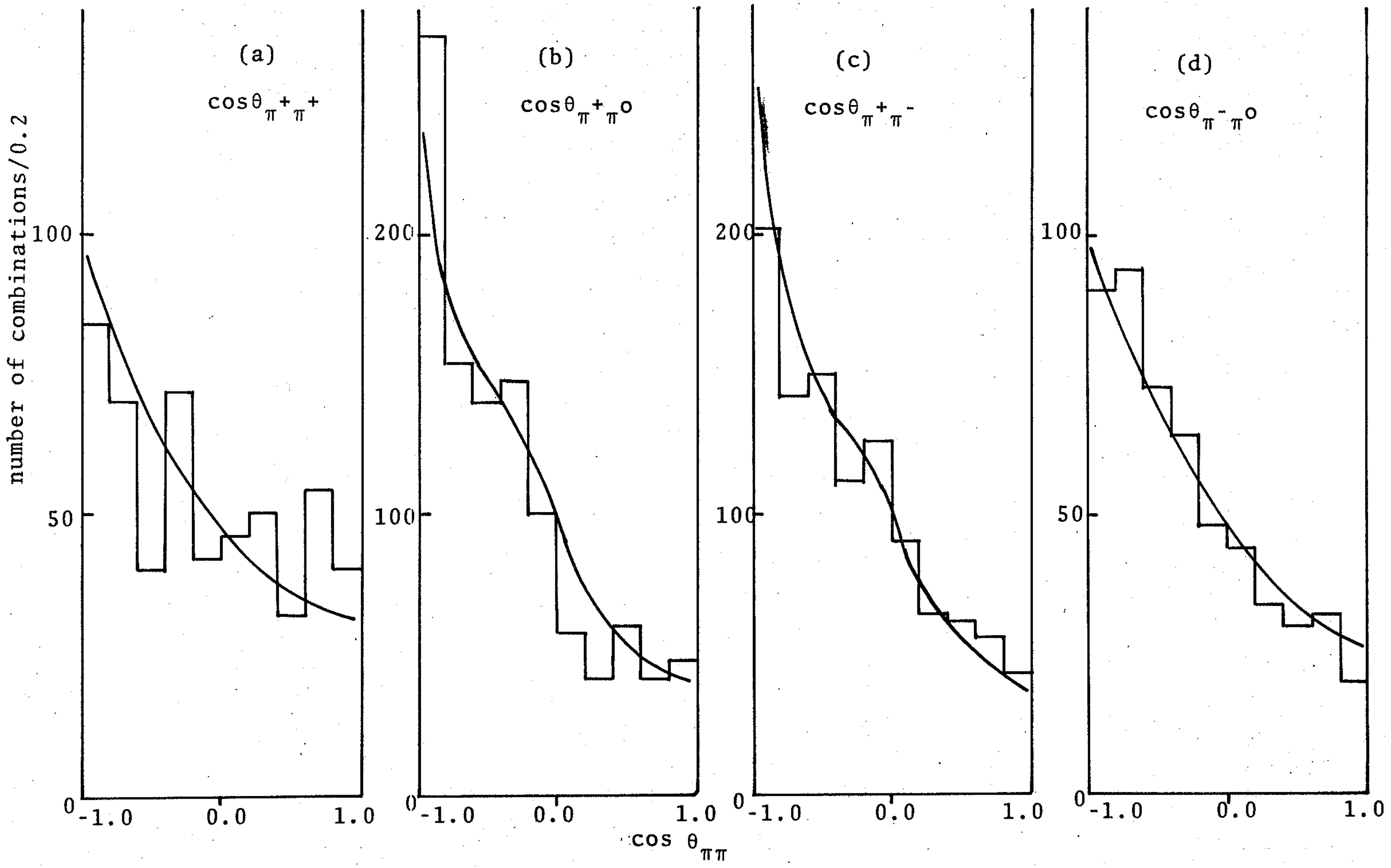

Fig.33.

Production Angles in c.m.s

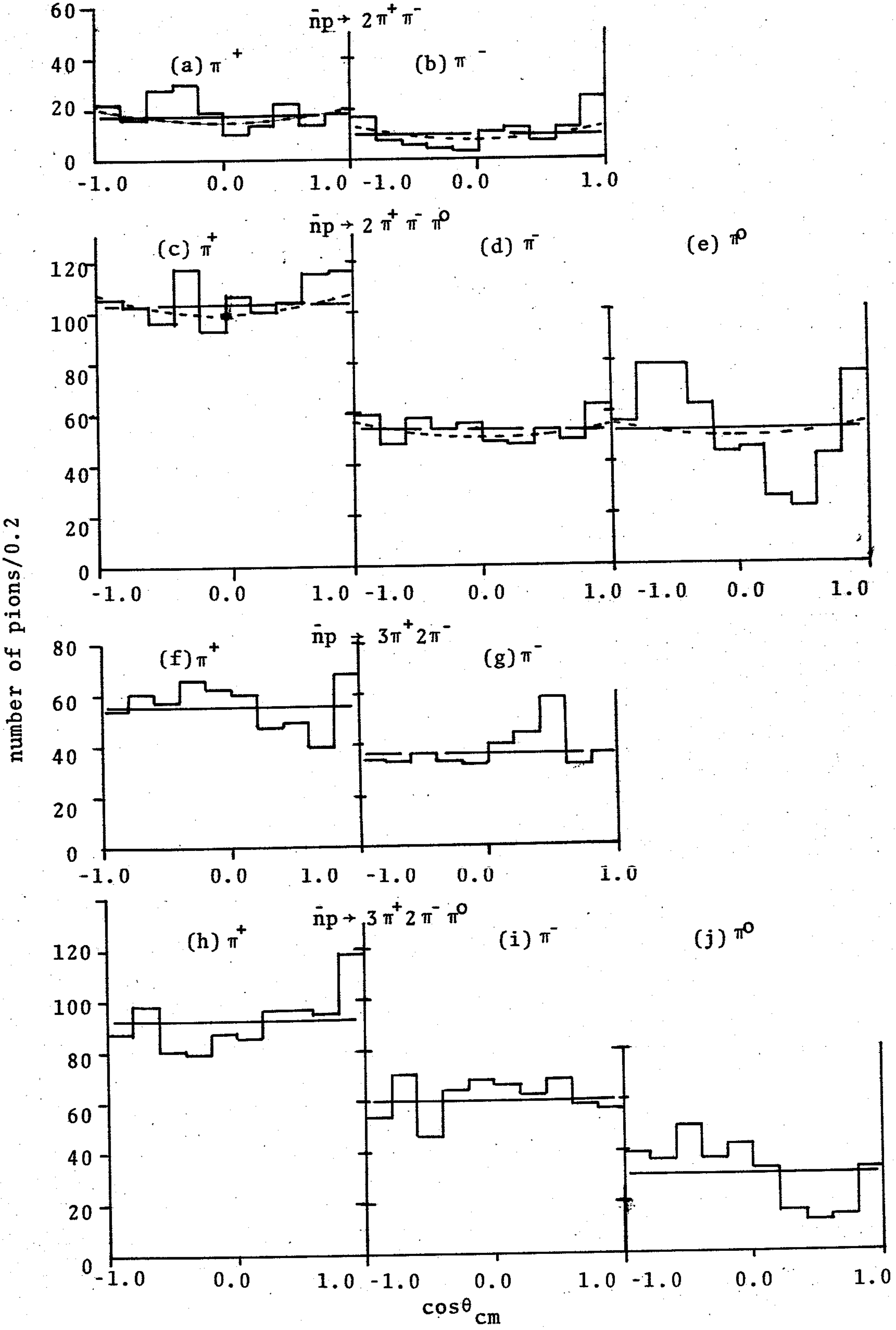

Fig.34. P_T Distributions

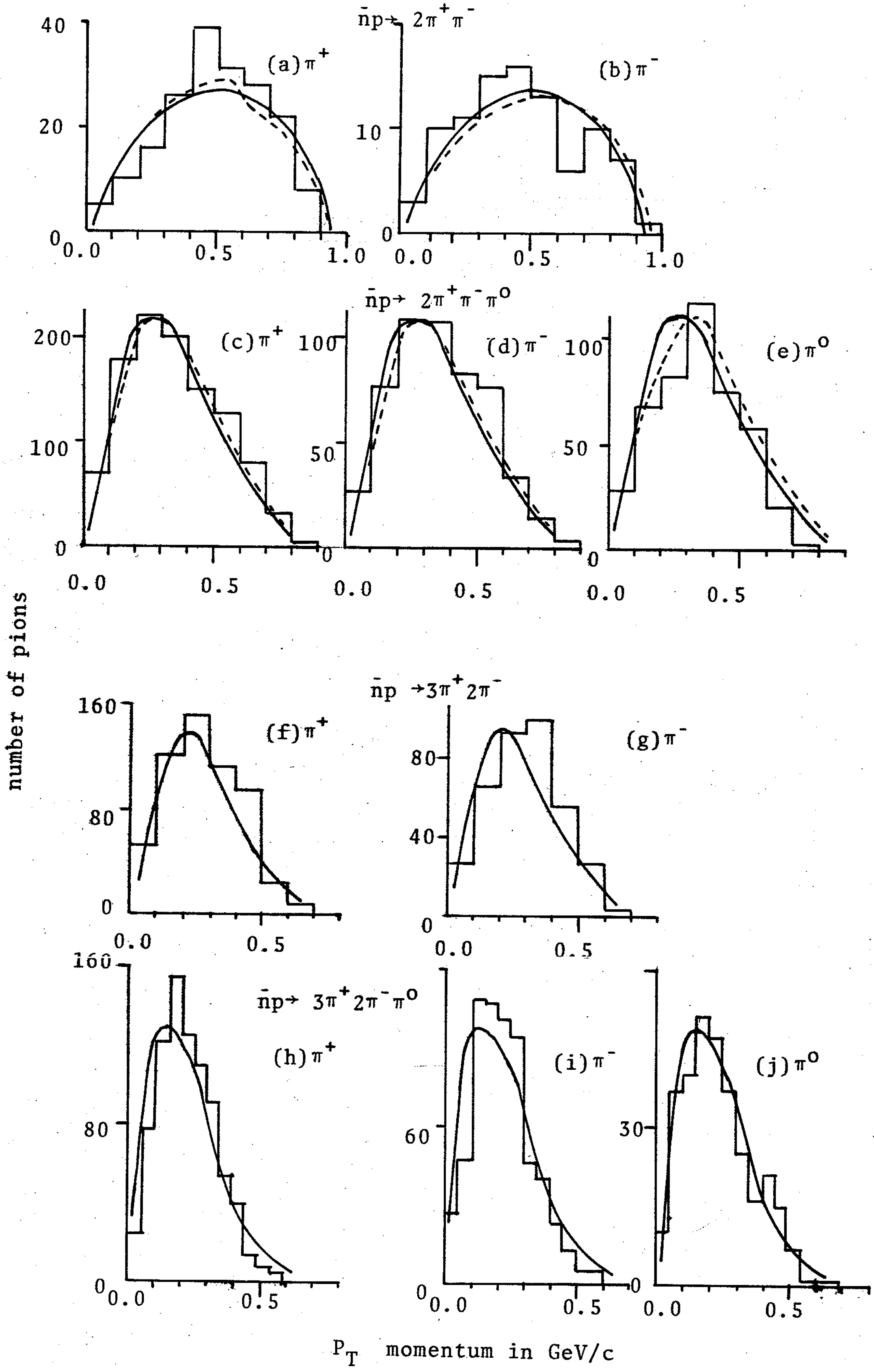

Fig.35. |P| Distributions

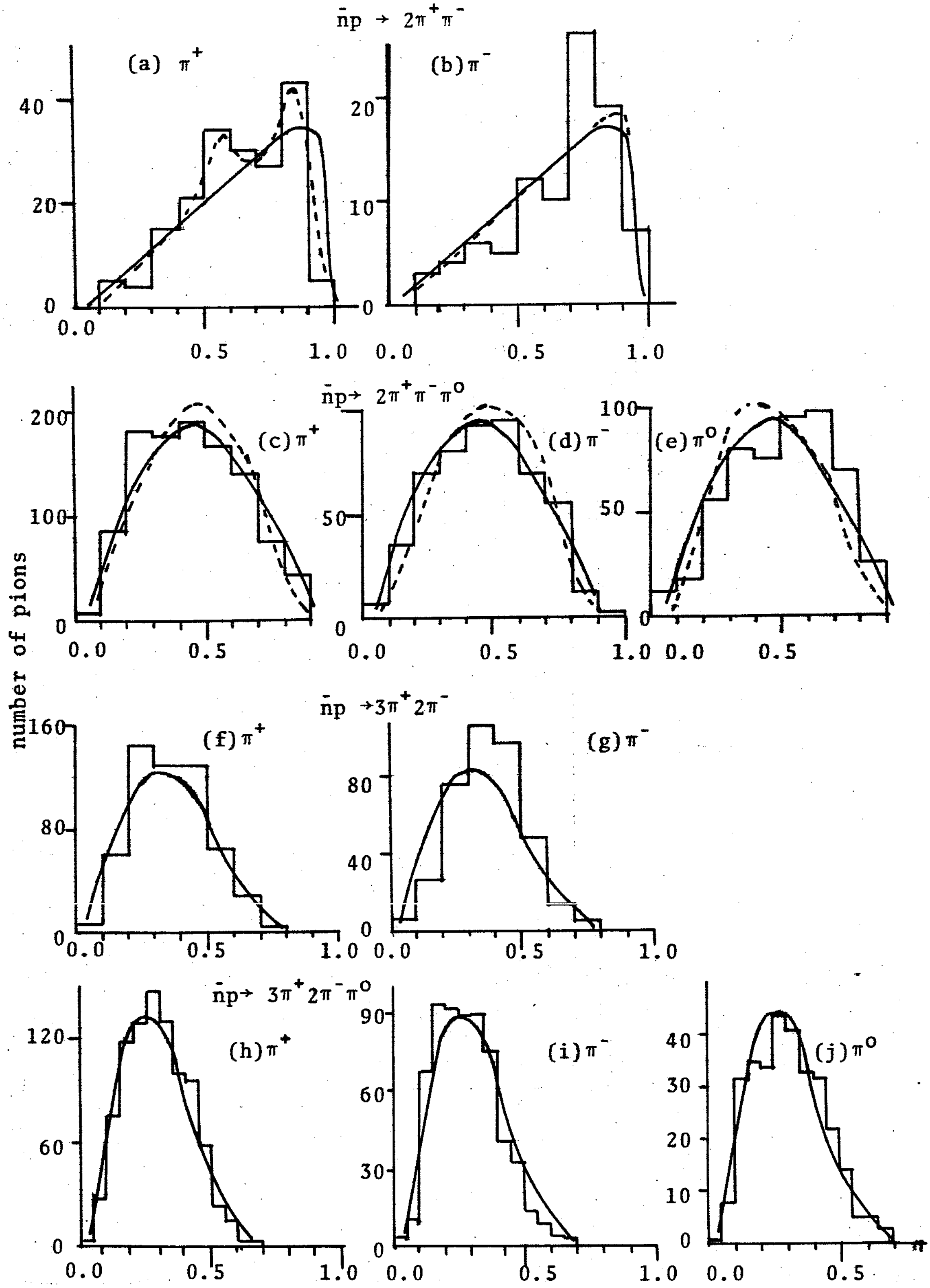

Fig.36

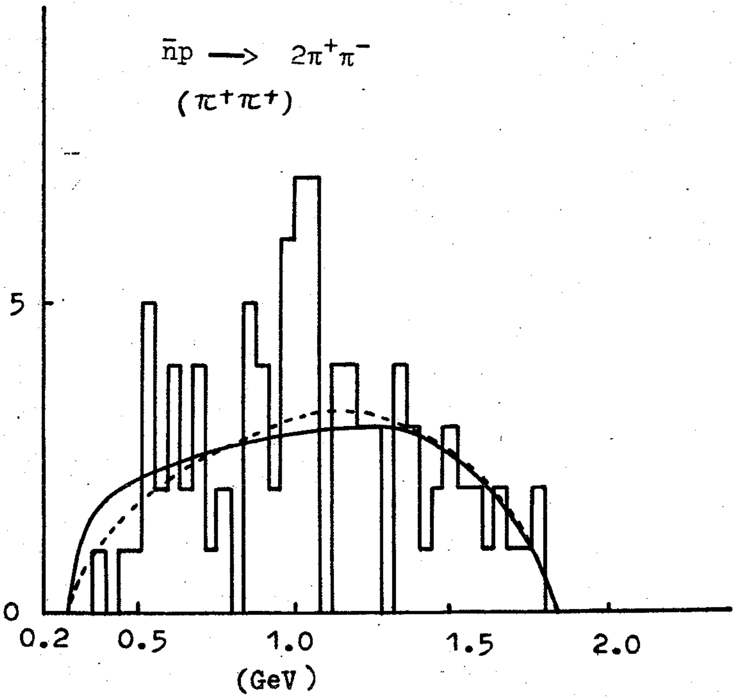
$\bar{n}p \longrightarrow 2\pi^+\pi^-$
$(\pi^+\pi^+)$
5
0
0.2
0.5
1.0
1.5
2.0
(GeV)
number of combinations / 0.04 GeV

Fig. 37

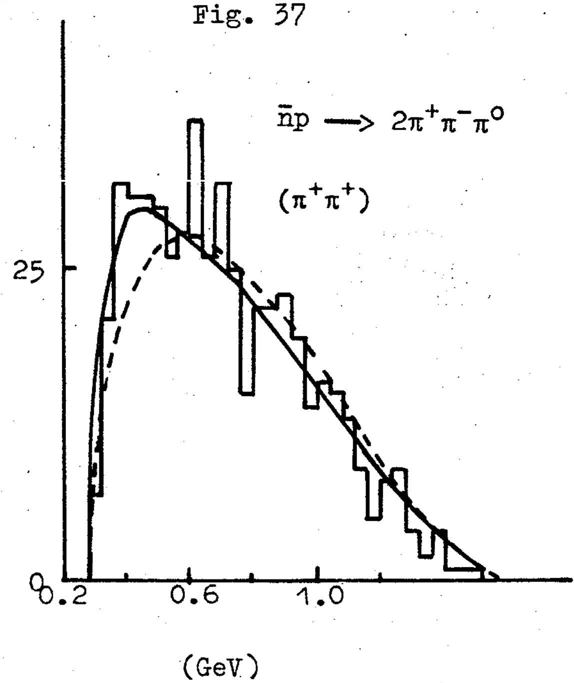
$\bar{n}p \longrightarrow 2\pi^+\pi^-\pi^0$
$(\pi^+\pi^+)$
25
0
0.2
0.6
1.0
(GeV)

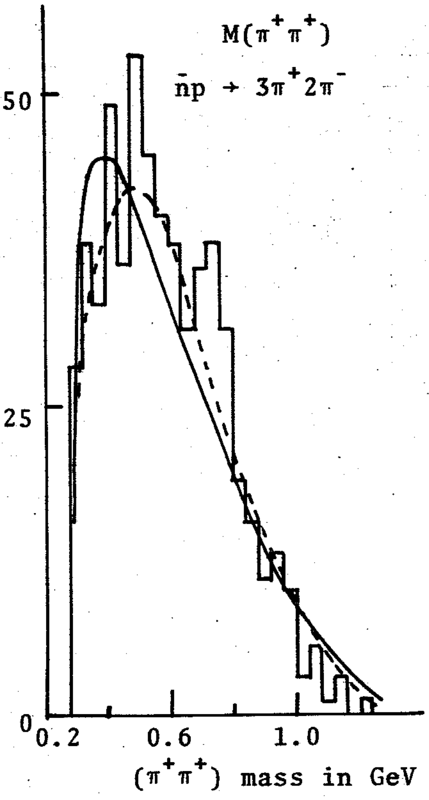
Fig.38.

$M(\pi^+\pi^+)$

$\bar{n}p \rightarrow 3\pi^+2\pi^-$

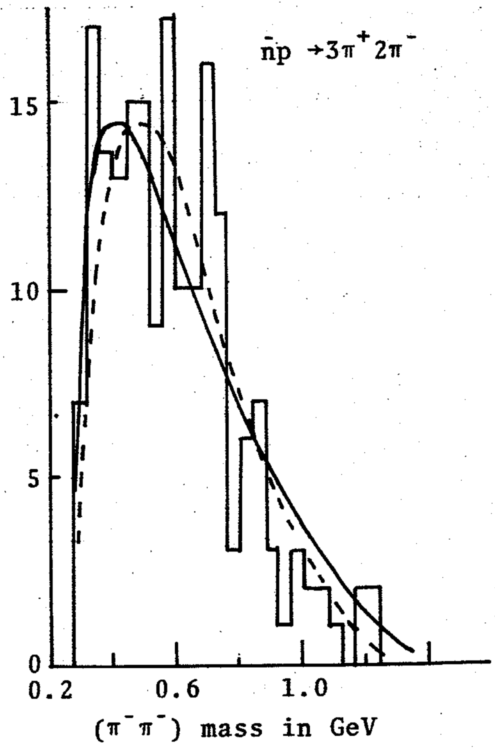
Fig.39.

$M(\pi^-\pi^-)$

$\bar{n}p \rightarrow 3\pi^+2\pi^-$

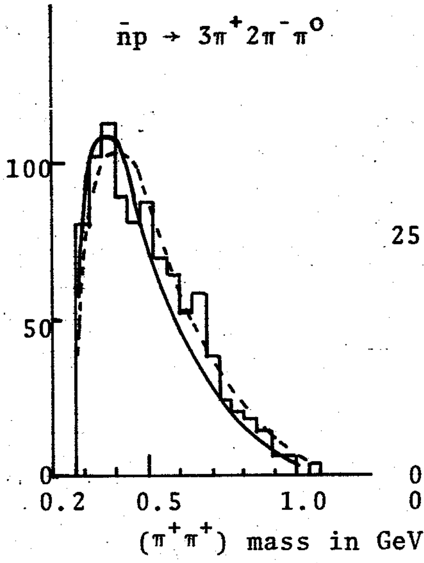
Fig.40.

$M(\pi^+\pi^+)$

$\bar{n}p \rightarrow 3\pi^+2\pi^-\pi^0$

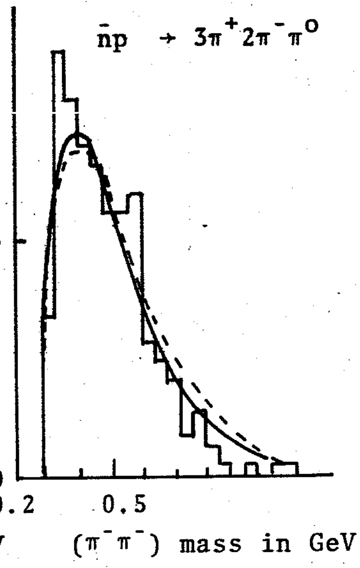
Fig.41.

$M(\pi^-\pi^-)$

$\bar{n}p \rightarrow 3\pi^+2\pi^-\pi^0$

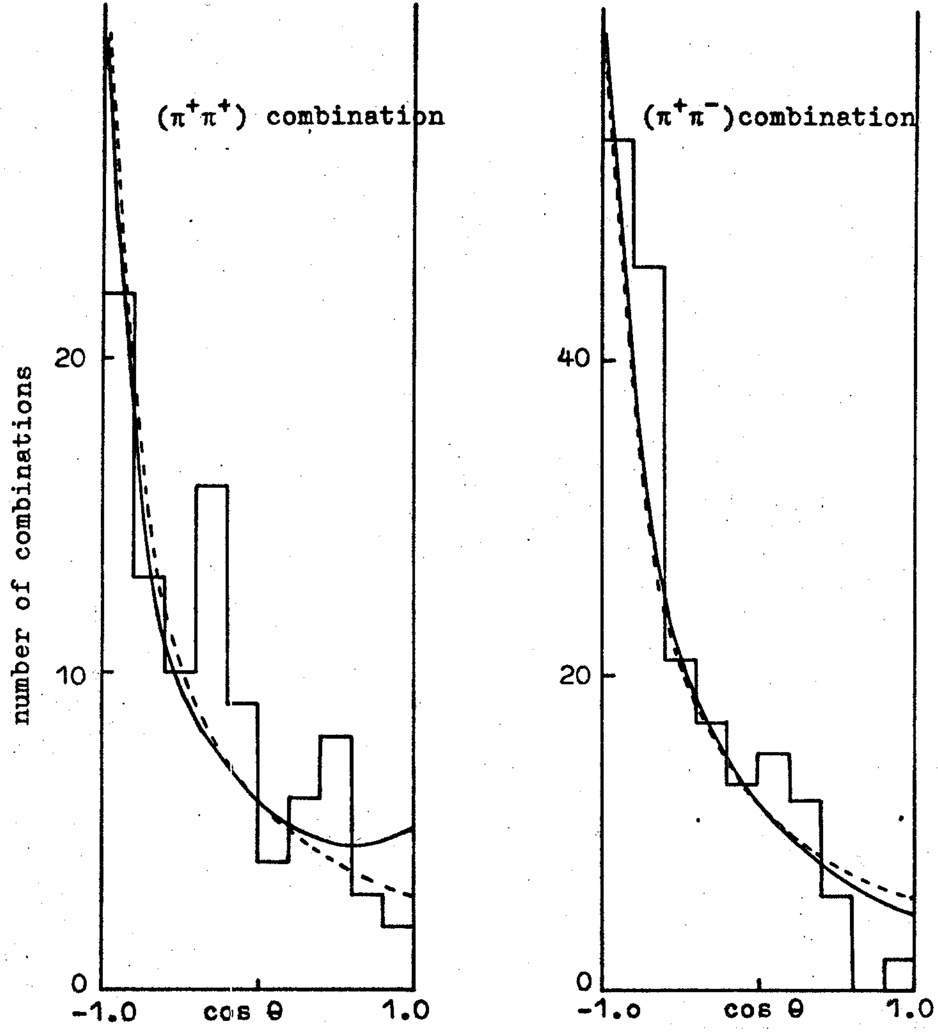

Figure 42 Dipion openimg angle in $\bar{n}p \longrightarrow 2\pi^+\pi^-$

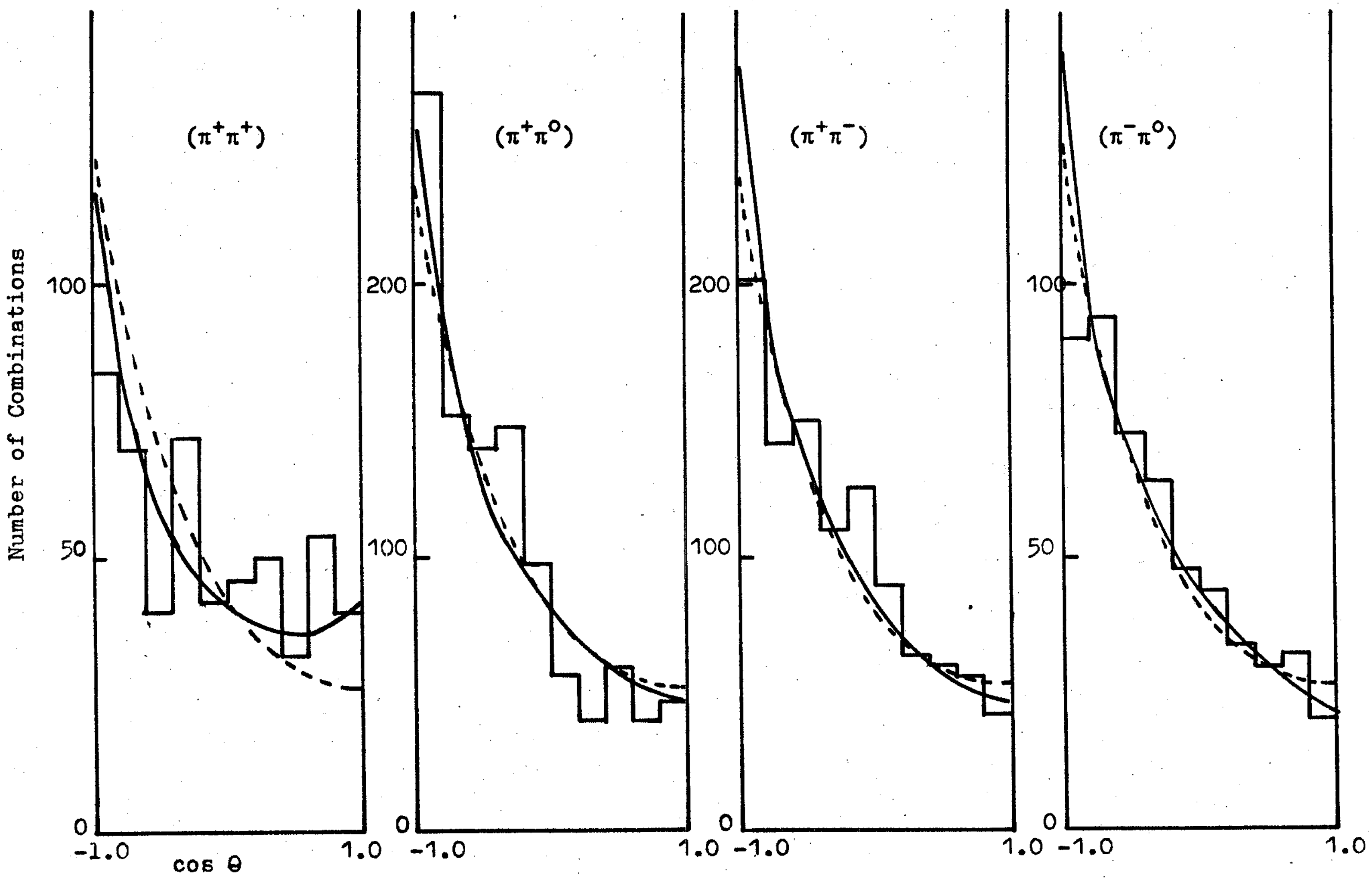

Figure 43 Dipion opening angle in $\bar{n}p \longrightarrow 2\pi^+\pi^-\pi^0$

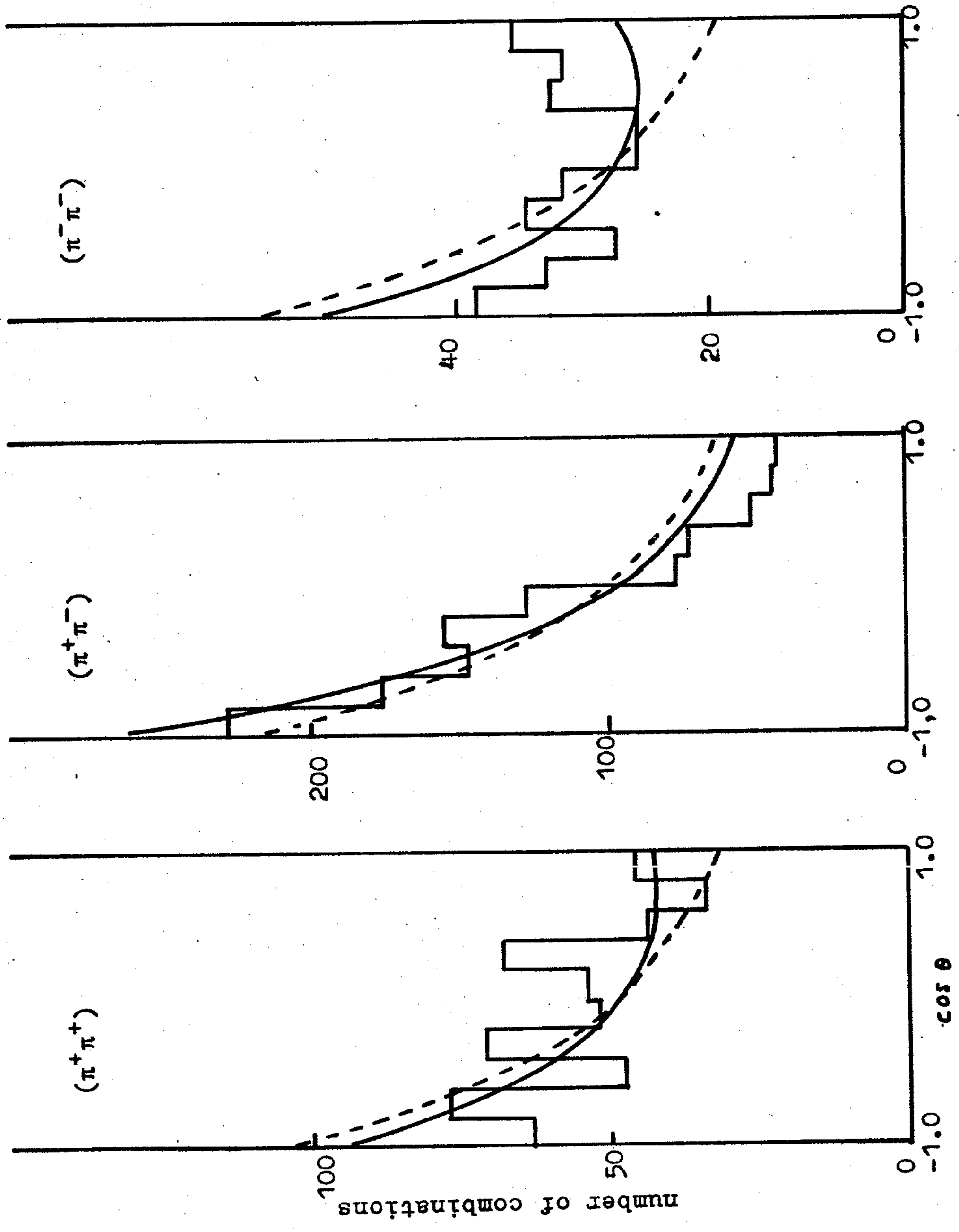

Figure 44 Dipion opening angle in $\bar{n}p \to 3\pi^+2\pi^-$

Fig.45.

Dipion Opening Angles in $\bar{n}p \to 3\pi^+2\pi^-\pi^0$

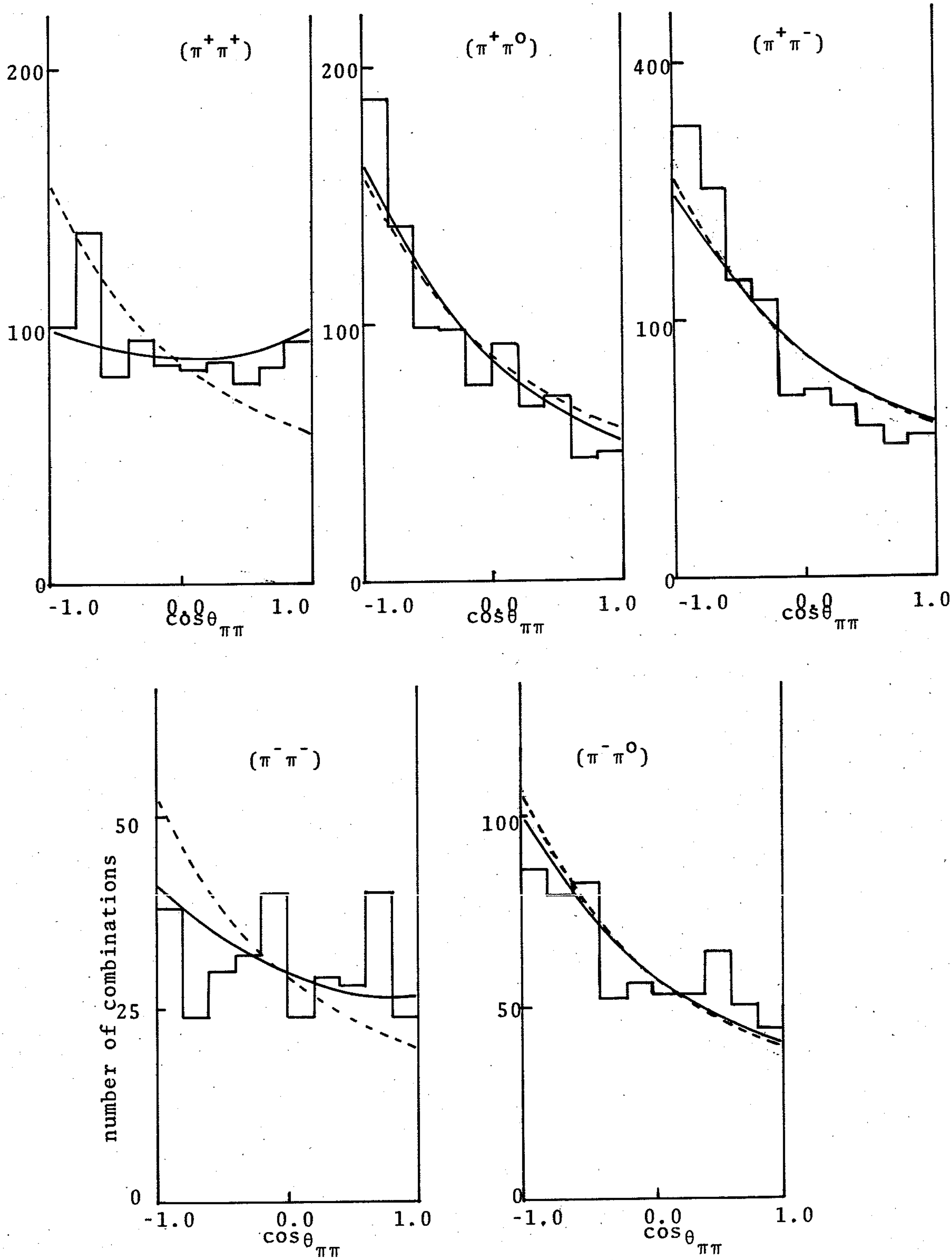

Fig.45.

Correlation Parameters γ

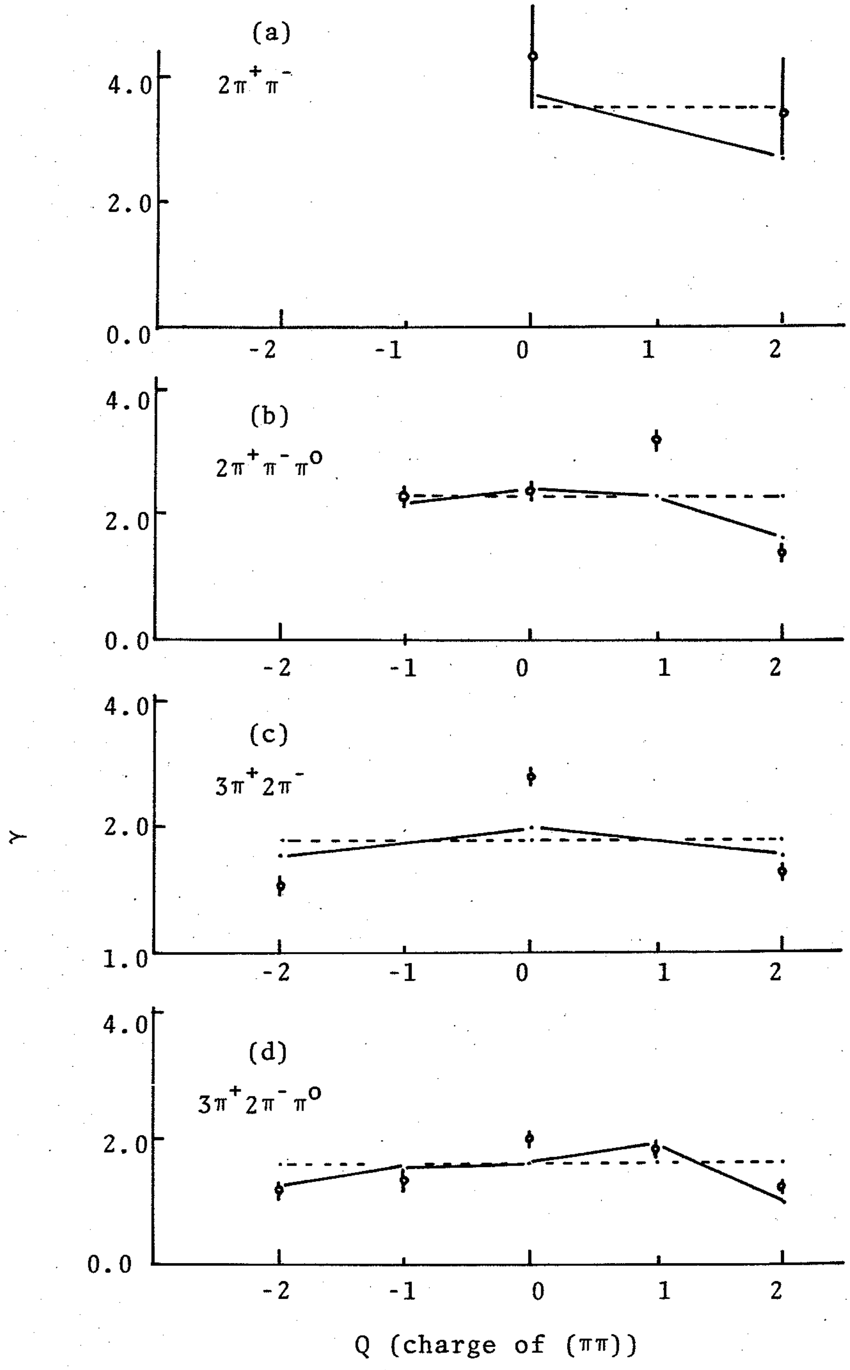

Fig.47. Multi-Particle Variables

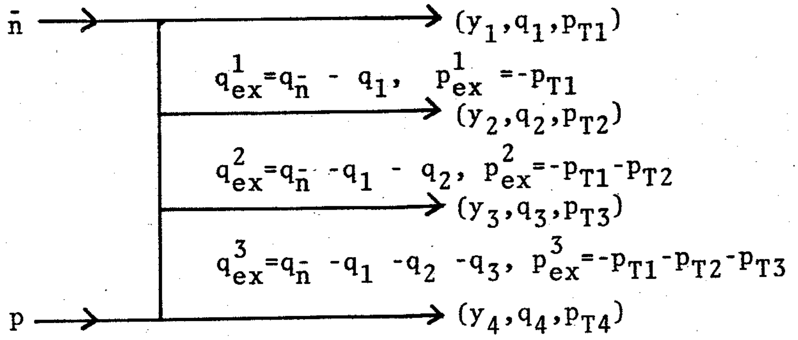

$$Q_{ex}=\sum_{j=1}^{3}|q^j_{ex}|\ ,\qquad P_{Tex}=\sum_{j=1}^{3}|p^j_{ex}|$$

Fig.48.

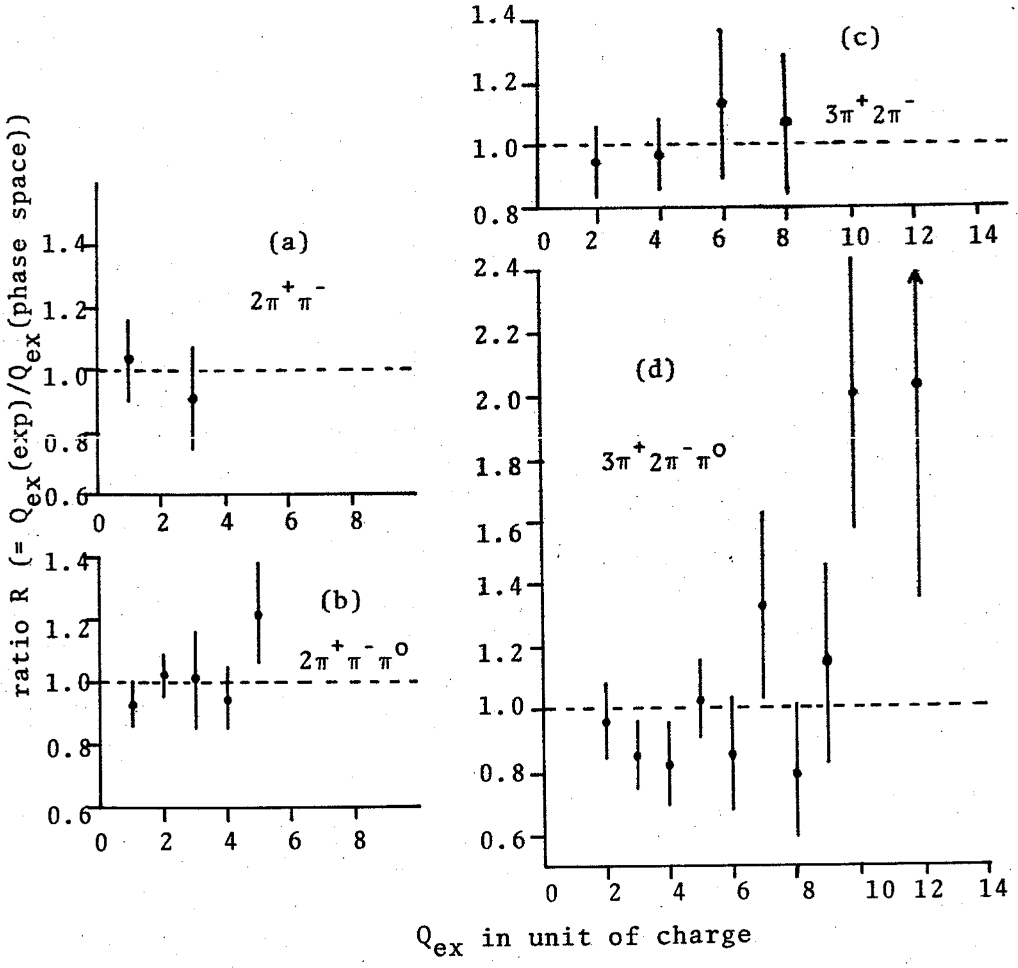

Fig.49,

P_{Tex} Distributions

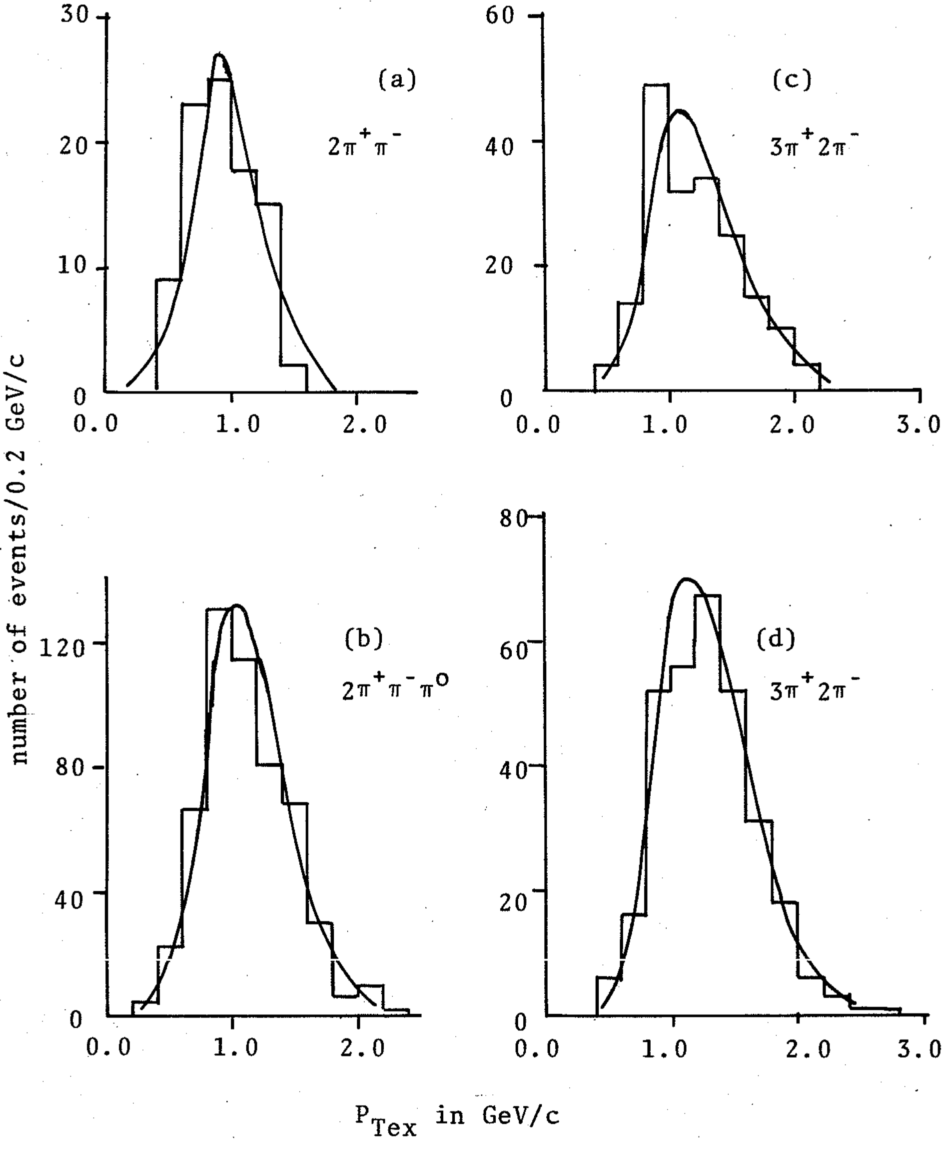

Fig.50.

Pole Structure on the Dalitz Plot

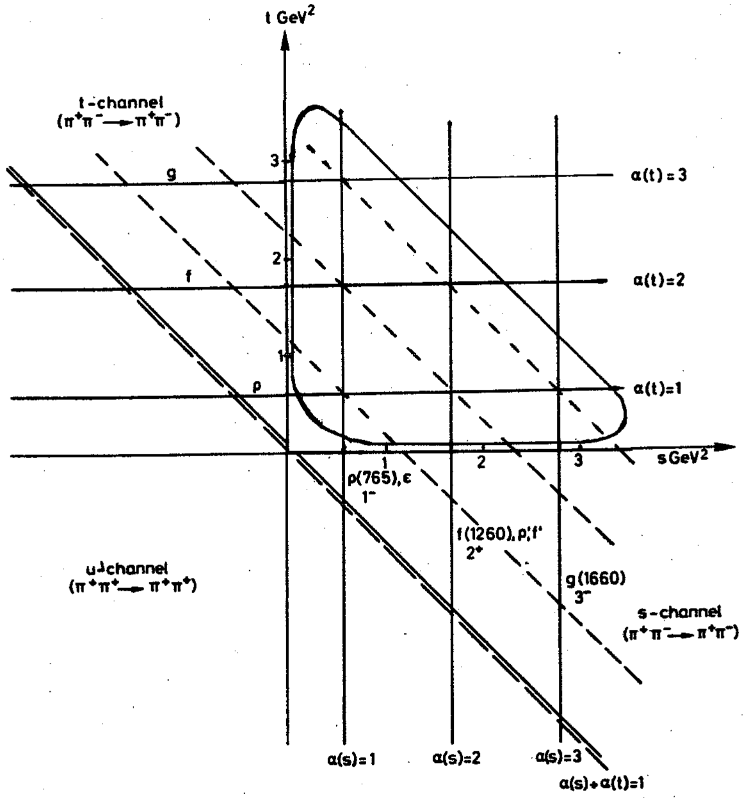

Figure 51

Dalitz plots of 3π final state

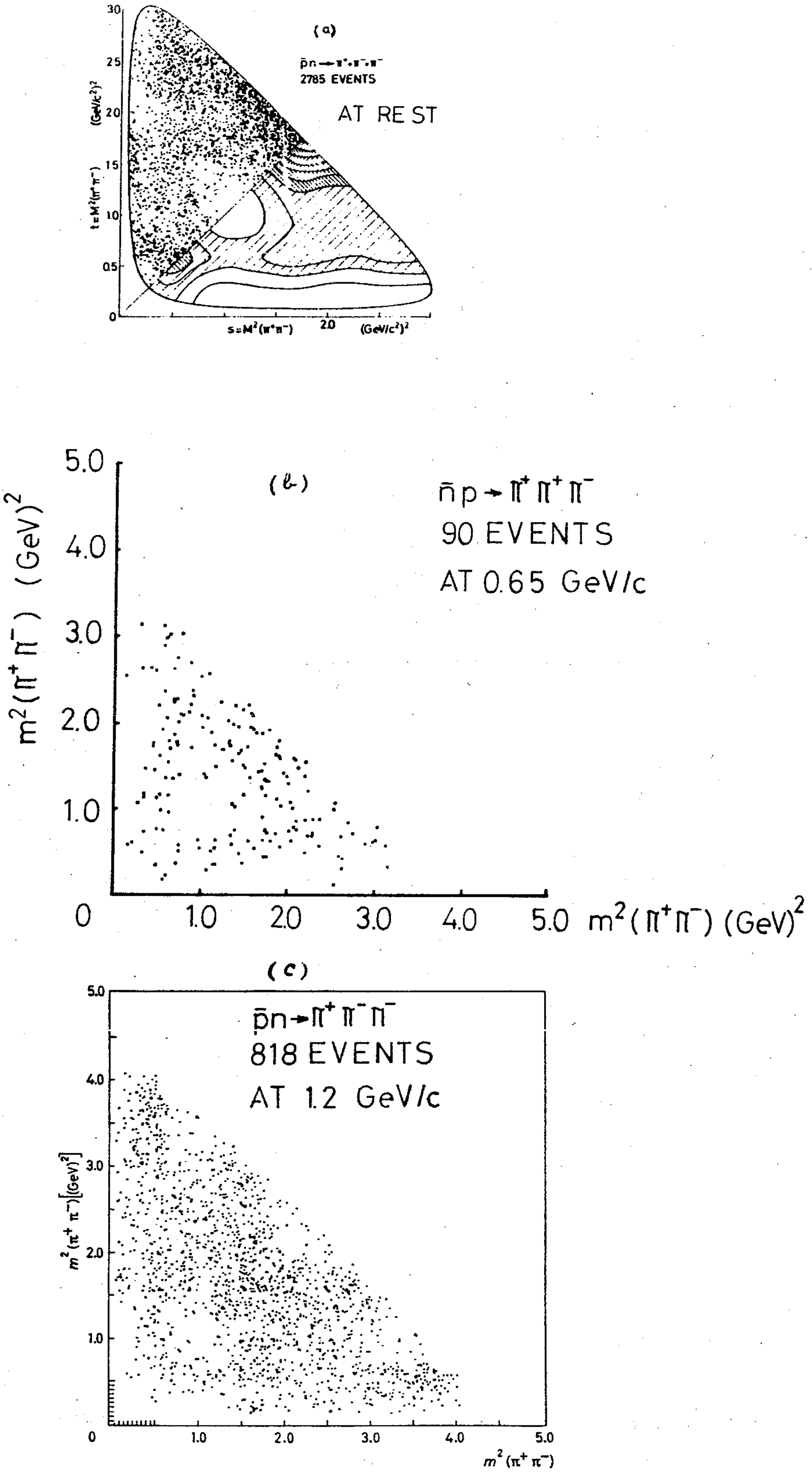

Figure 52

Dalitz plot of the reaction $\bar{n}p \longrightarrow 2\pi^+\pi^-$

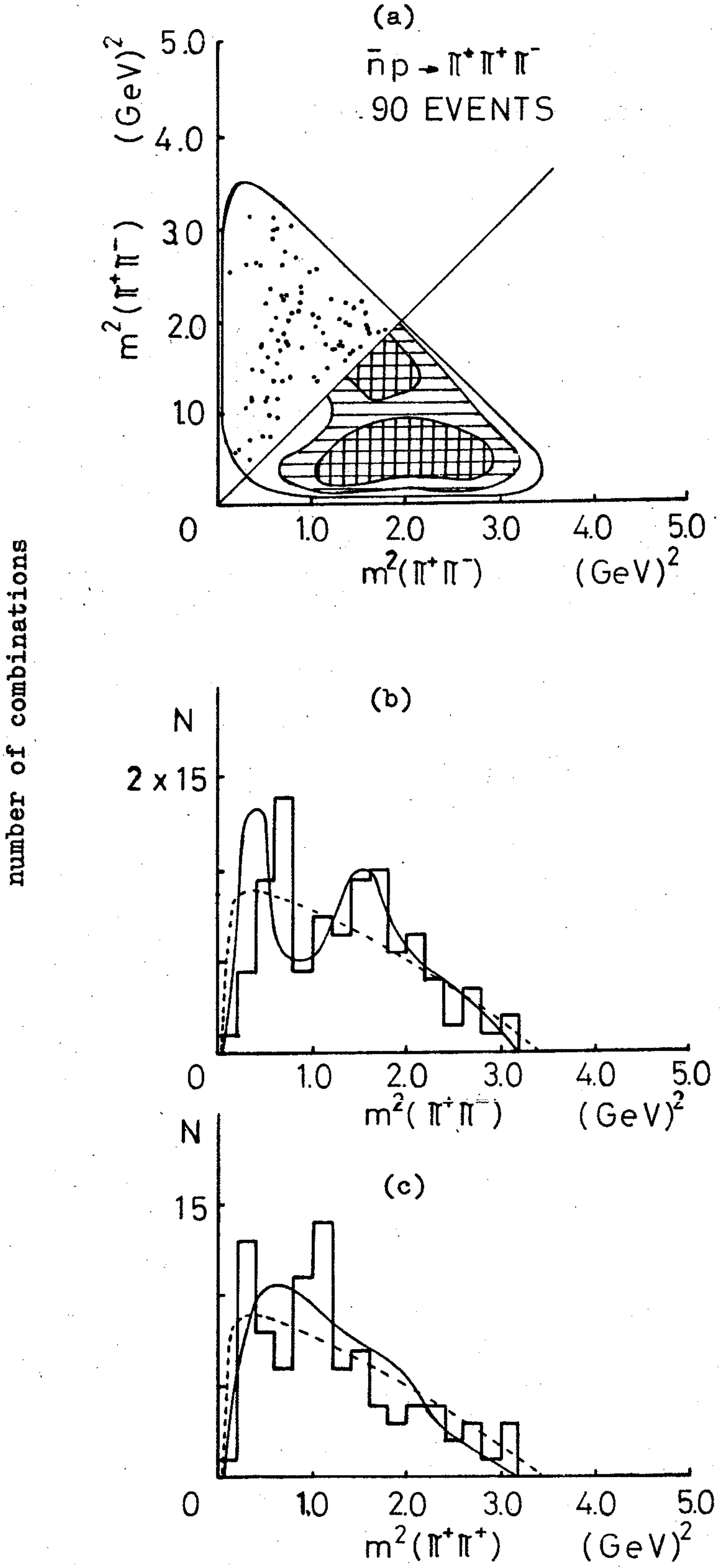

Fig.53.

Transverse Momentum Spectra

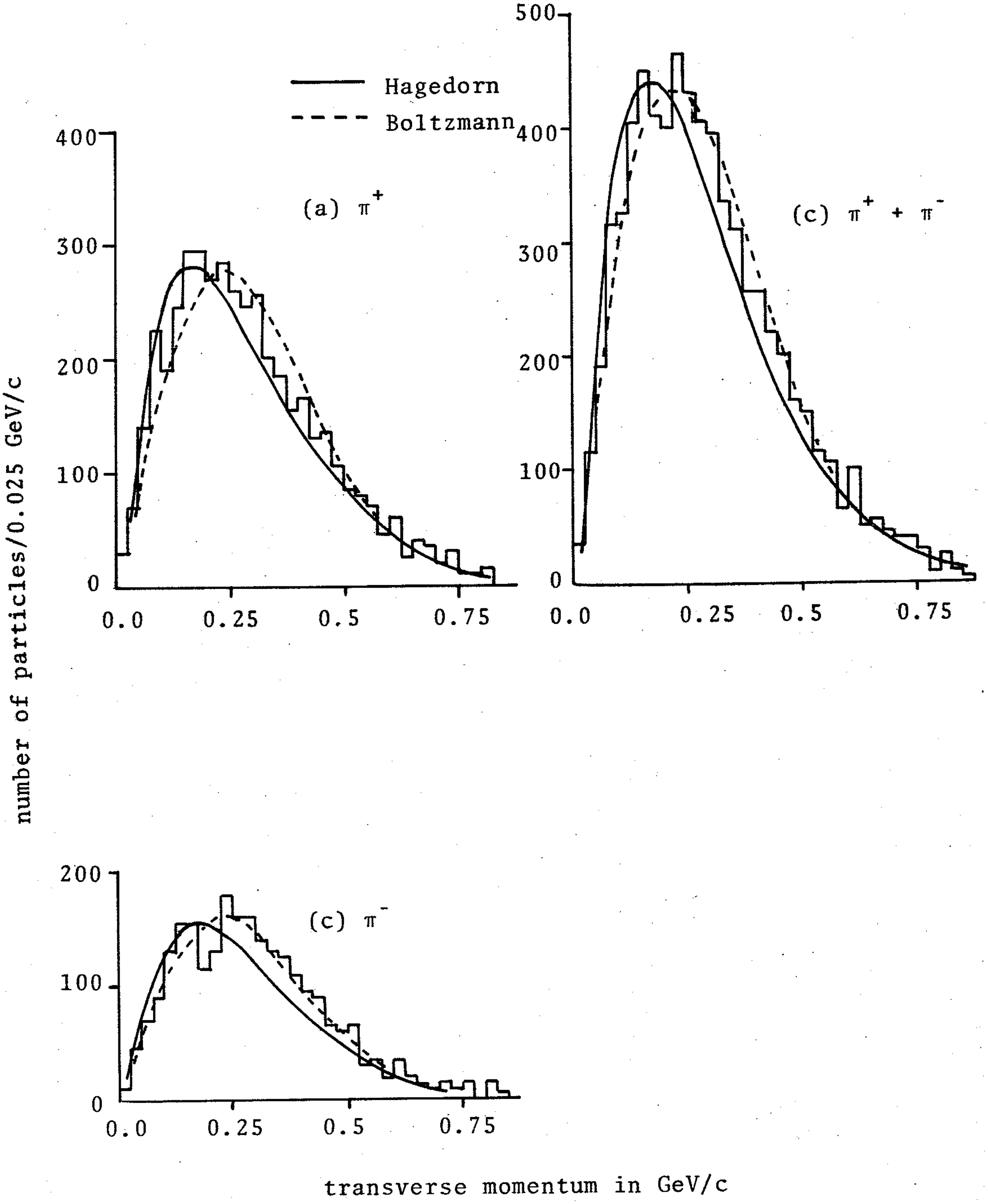

Fig.54.

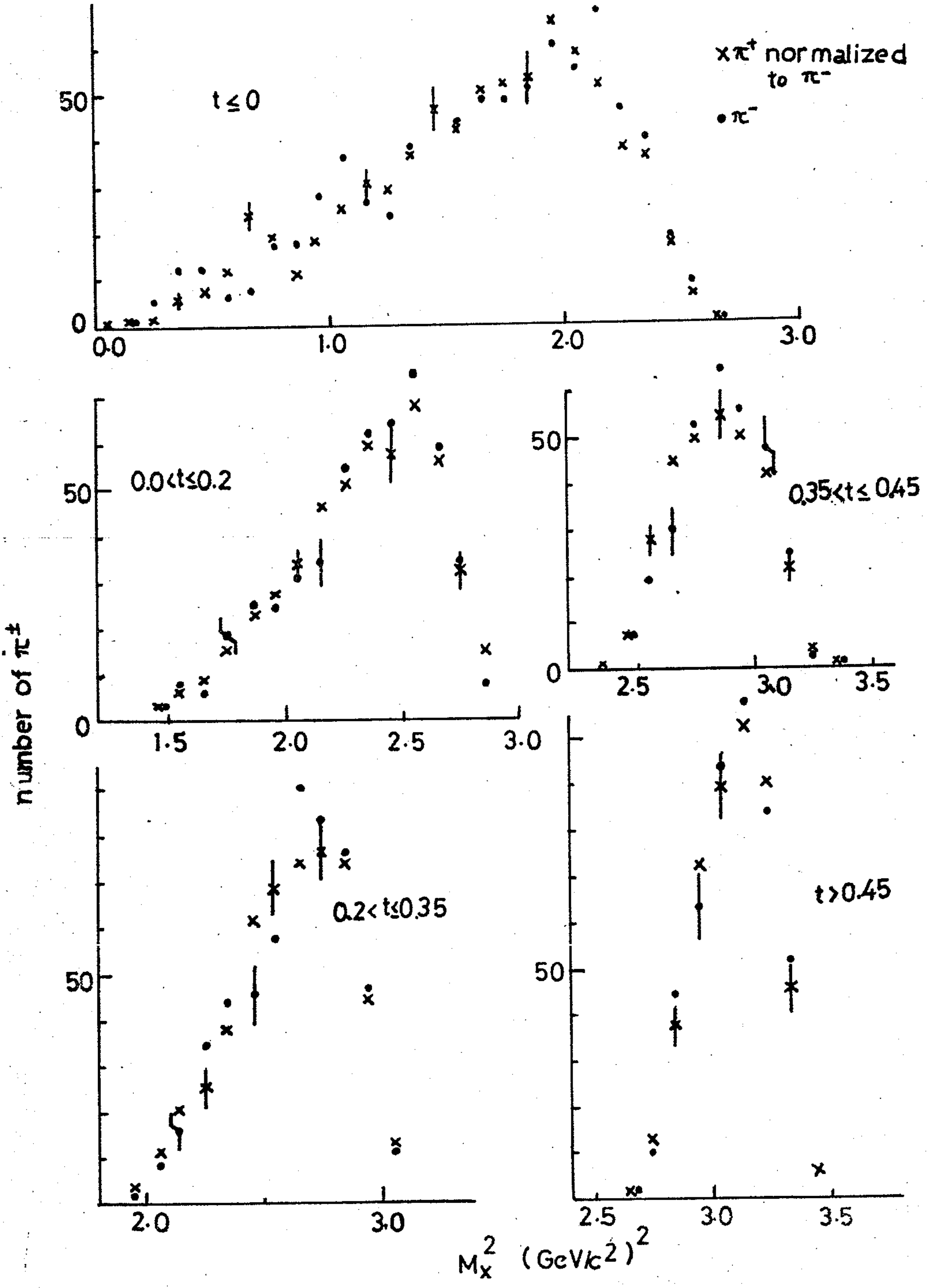
×π⁺ normalized to π⁻
• π⁻
t≤0
0.0<t≤0.2
0.35<t≤0.45
0.2<t≤0.35
t>0.45
number of π±
Mx² (GeV/c²)²
0
50
0.0
1.0
2.0
3.0
1.5
2.0
2.5
3.0
2.5
3.0
3.5

Fig.55. (a)

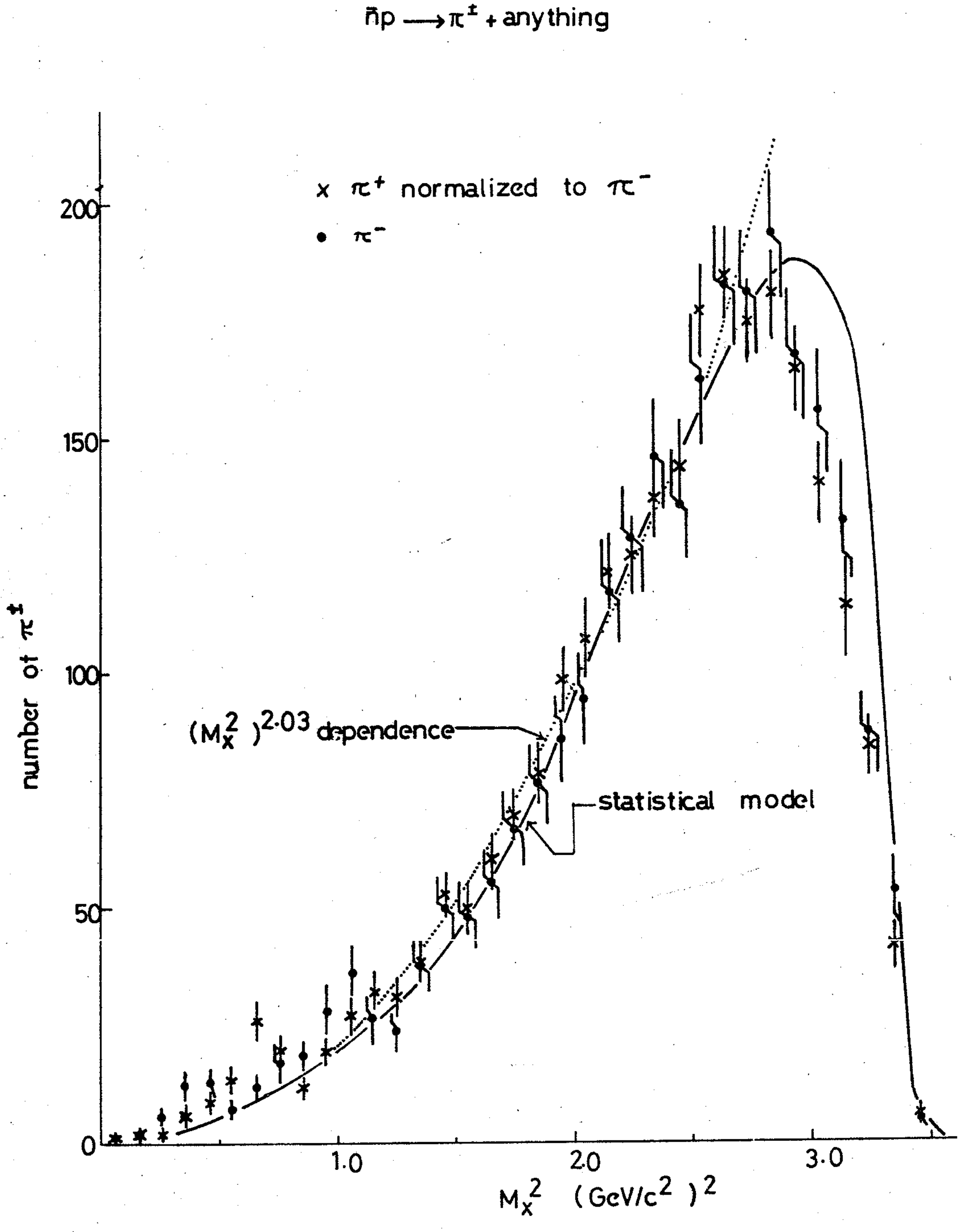
$\bar{n}p \longrightarrow \pi^{\pm}$ + anything
x π^+ normalized to π^-
● π^-
$(M_X^2)^{2.03}$ dependence
statistical model
number of $\pi^{\pm}$
0
50
100
150
200
1.0
2.0
3.0
M_X^2 $(GeV/c^2)^2$

Fig.55(b)

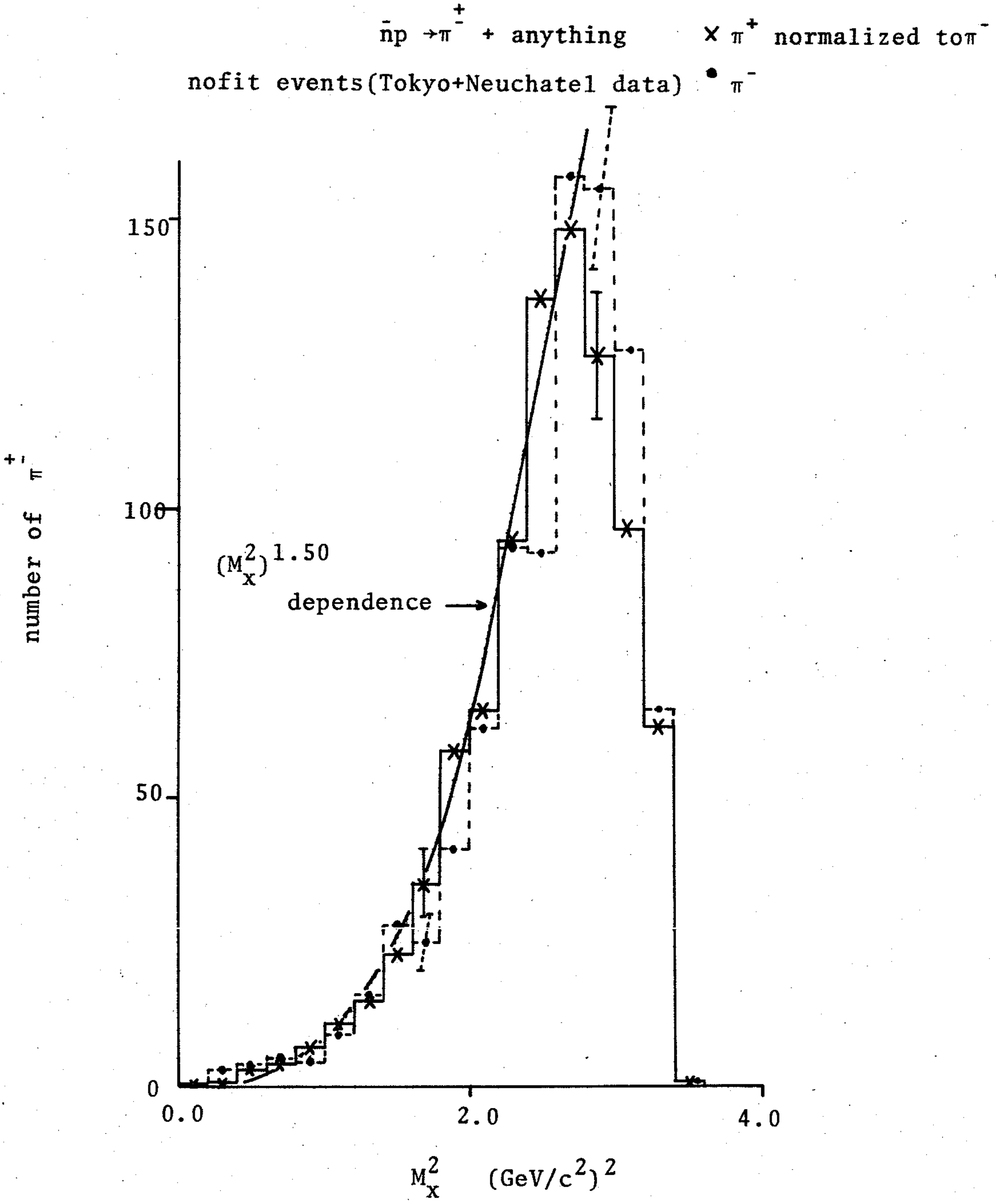
$\bar{n}p \to \pi^{\pm}$ + anything
× π^+ normalized to π^-
nofit events(Tokyo+Neuchatel data)
● π^-
number of $\pi^{\pm}$
150
100
50
0
$(M_x^2)^{1.50}$
dependence
0.0
2.0
4.0
M_x^2 $(GeV/c^2)^2$

Fig.56.

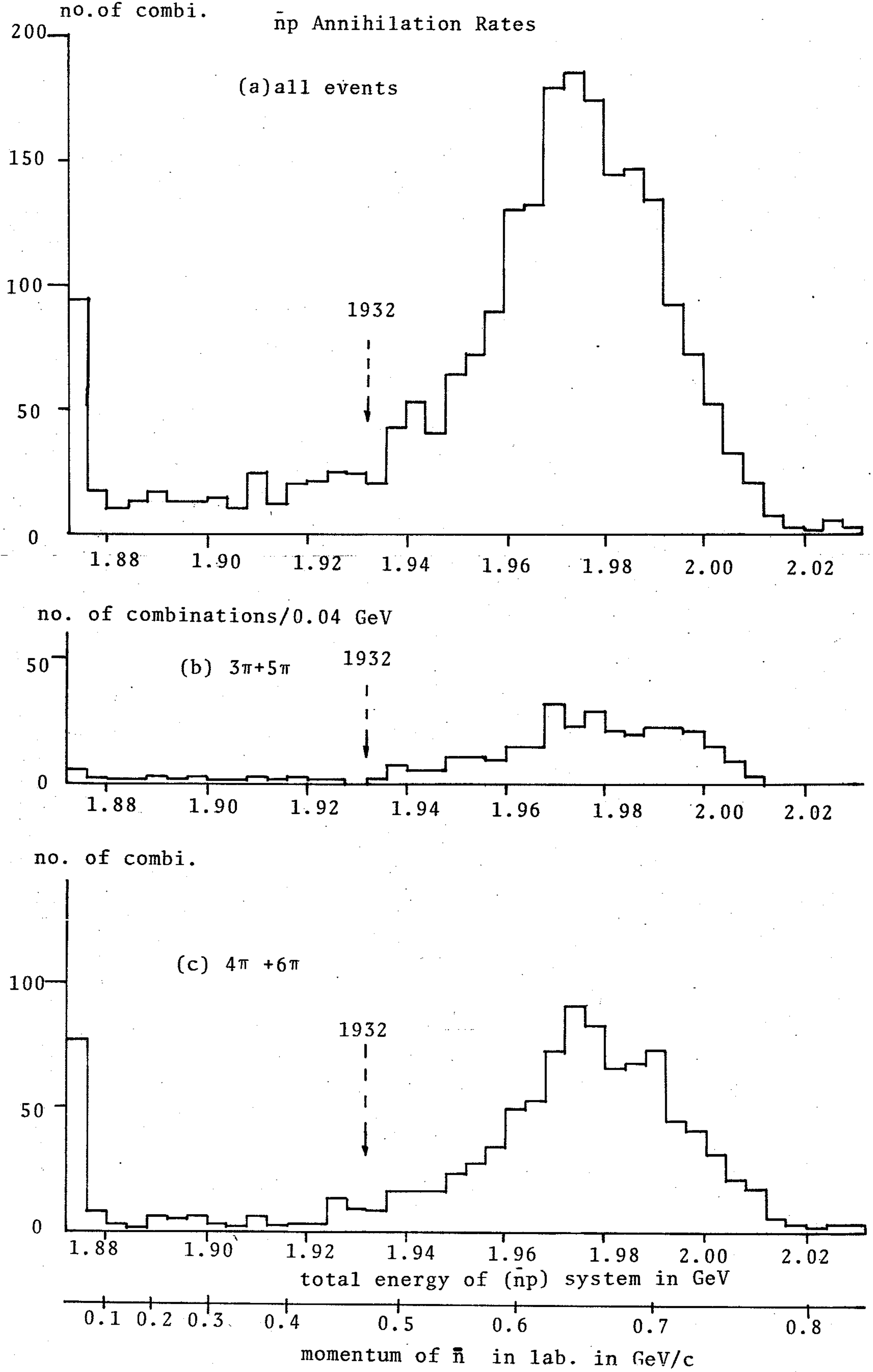
no.of combi.
n̄p Annihilation Rates
(a)all events
1932
200
150
100
50
0
1.88
1.90
1.92
1.94
1.96
1.98
2.00
2.02
no. of combinations/0.04 GeV
(b) 3π+5π
1932
50
0
1.88
1.90
1.92
1.94
1.96
1.98
2.00
2.02
no. of combi.
(c) 4π +6π
1932
100
50
0
1.88
1.90
1.92
1.94
1.96
1.98
2.00
2.02
total energy of (n̄p) system in GeV
0.1
0.2
0.3
0.4
0.5
0.6
0.7
0.8
momentum of n̄ in lab. in GeV/c

Fig.57.

(a)

Fiducial Marks Projected on a View 2 Screen

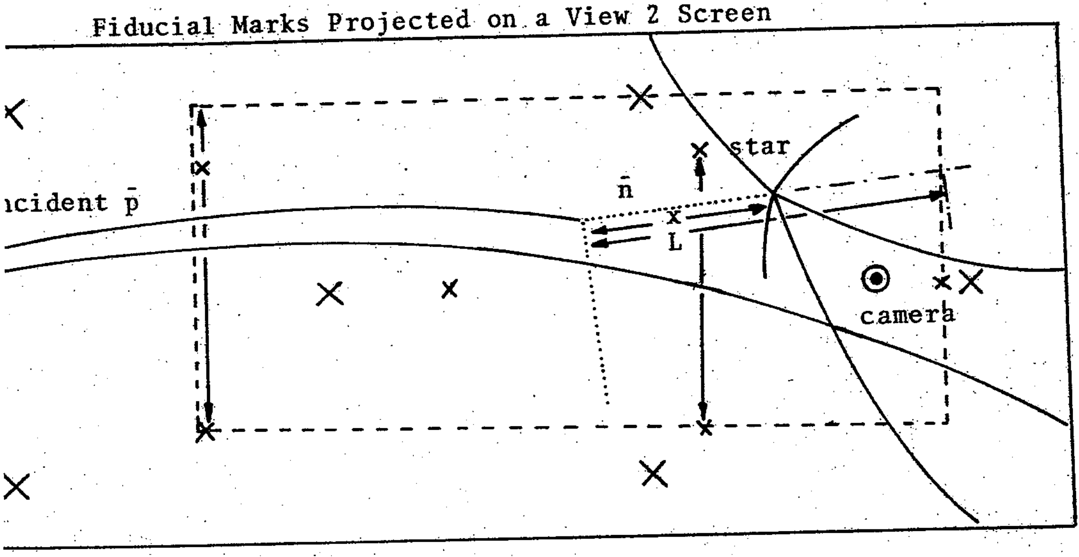

(b)

Spatial Coordinates of the Fiducial Volume

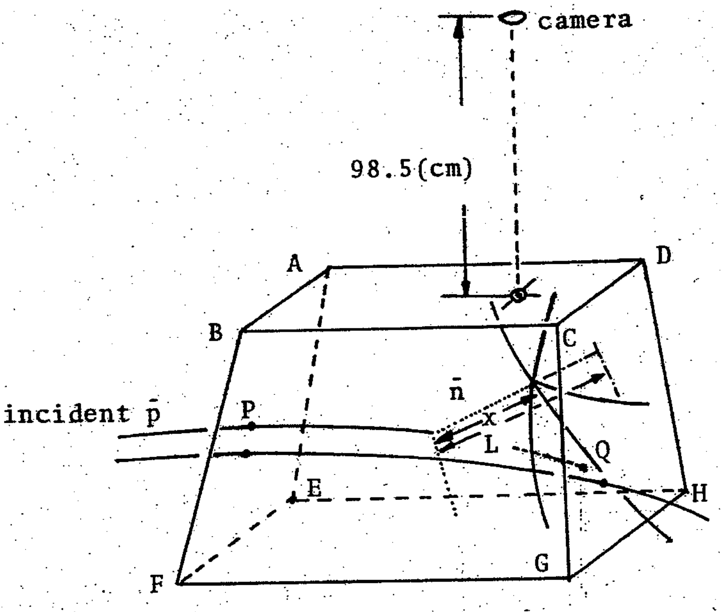

	X	Y	Z
A	-5.7	8.8	0.0
B	-5.7	-6.6	0.0
C	28.9	-6.6	0.0
D	28.9	8.8	0.0
E	-15.0	11.5	-31.0
F	-15.0	-8.6	-31.0
G	30.0	-8.6	-31.0
H	30.0	11.5	-31.0

Fig.58.

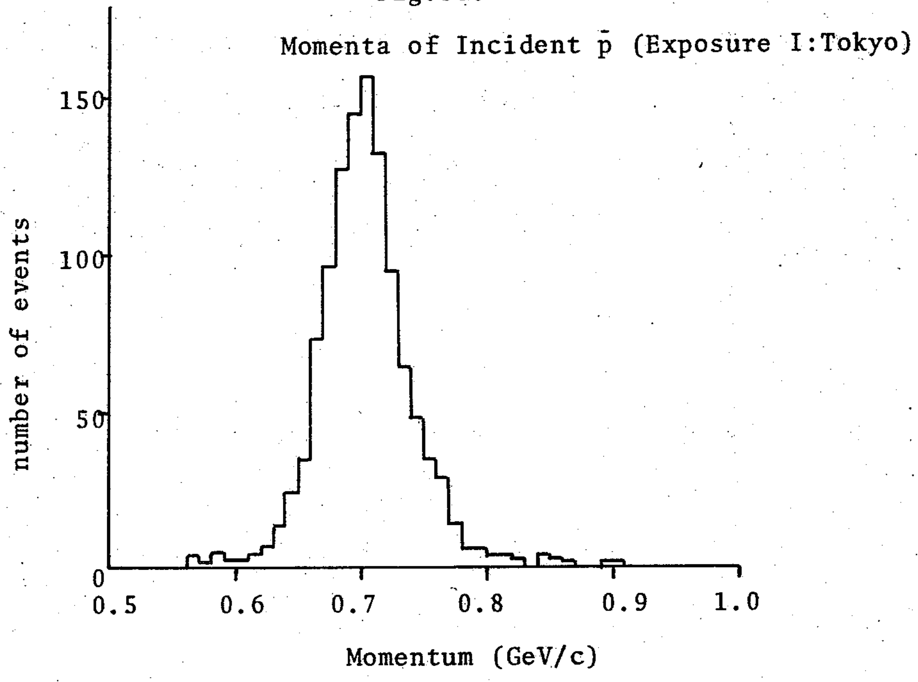
Momenta of Incident $\bar{p}$ (Exposure I:Tokyo)
number of events
150
100
50
0
0.5
0.6
0.7
0.8
0.9
1.0
Momentum (GeV/c)

Fig.59.

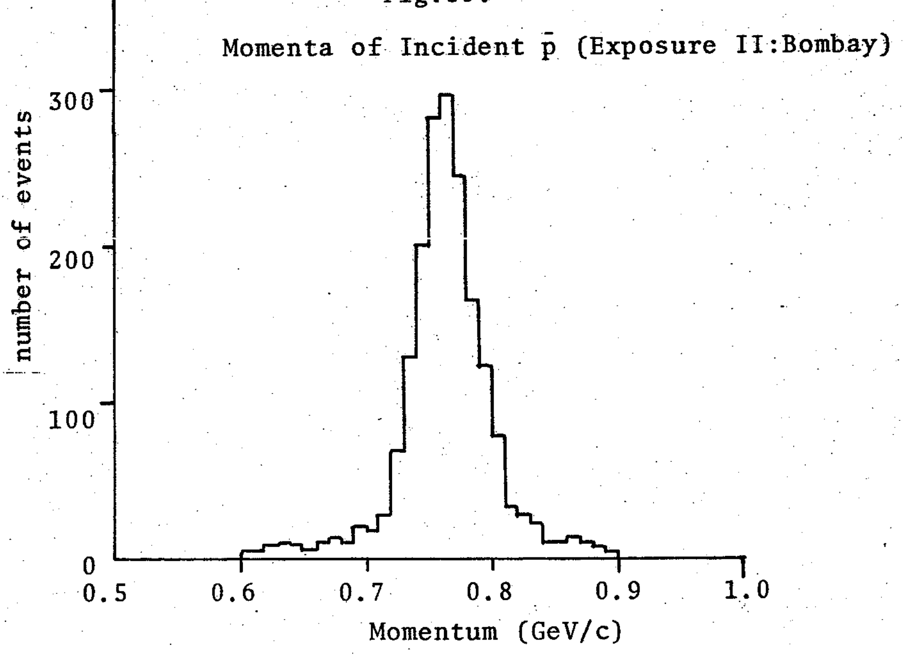
Momenta of Incident $\bar{p}$ (Exposure II:Bombay)
number of events
300
200
100
0
0.5
0.6
0.7
0.8
0.9
1.0
Momentum (GeV/c)

Fig.60.

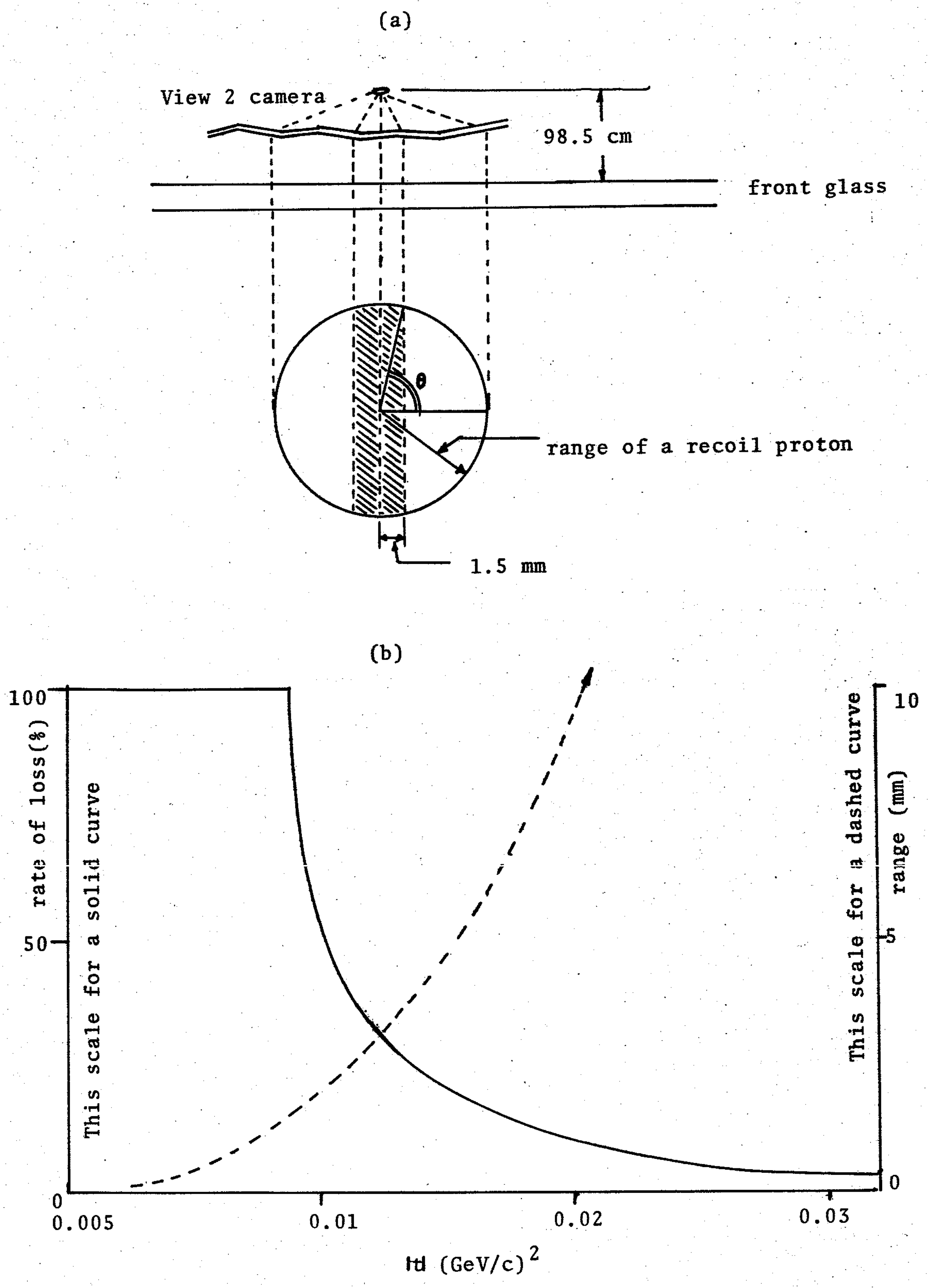
(a)
View 2 camera
98.5 cm
front glass
θ
range of a recoil proton
1.5 mm
(b)
100
50
0
rate of loss(%)
This scale for a solid curve
10
5
0
range (mm)
This scale for a dashed curve
0.005
0.01
0.02
0.03
|t| (GeV/c)^2

Fig.61.

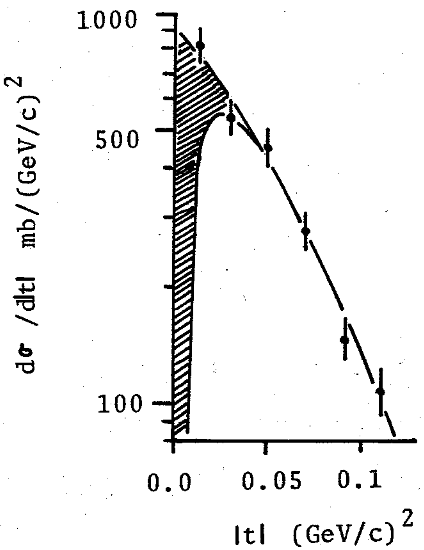

Fig.62.

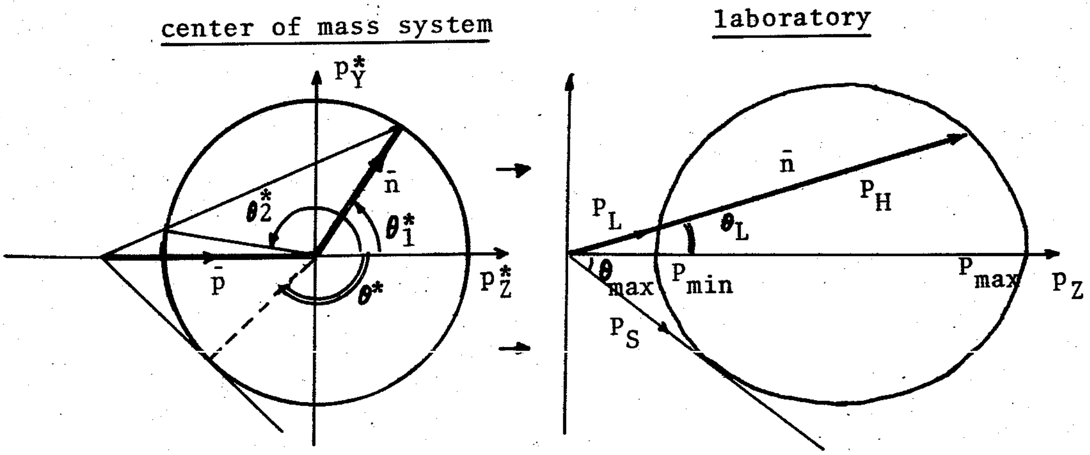

if $P_{incident}$=720 MeV/c,

P_{max}=716.2 MeV/c,

P_{min}= 3.8 MeV/c,

P_S = 49.3 MeV/c,

θ_{max}=81.1° .

Fig.63.

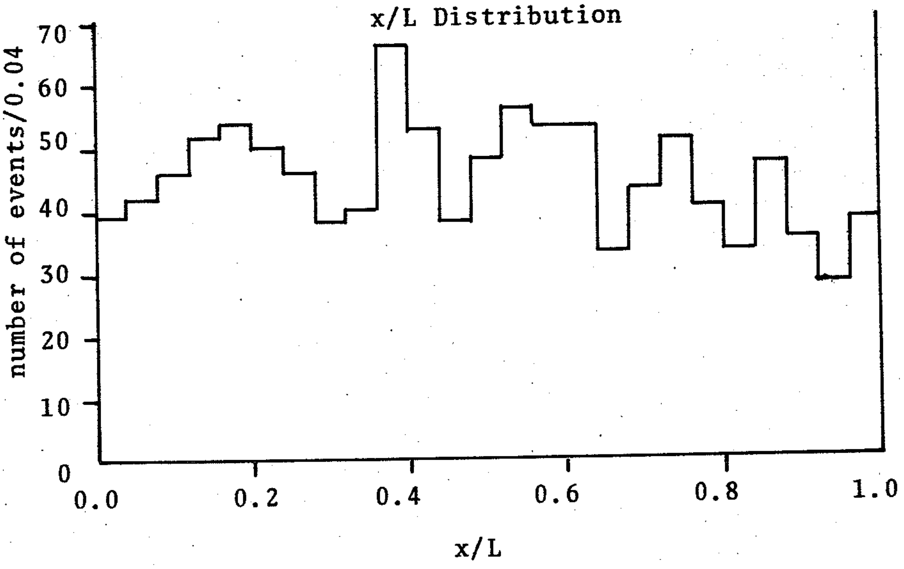

Fig.64.

Cross Sections $\sigma_3 + \sigma_5$ of $\bar{p}n$ Annihilation

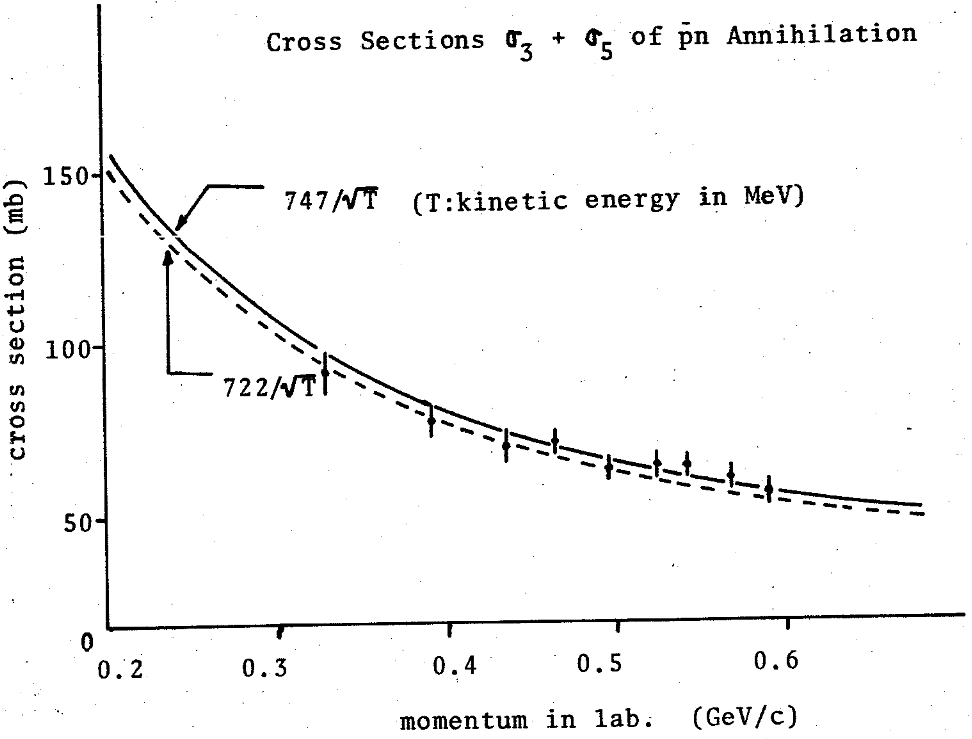

Fig. 65.

(a)

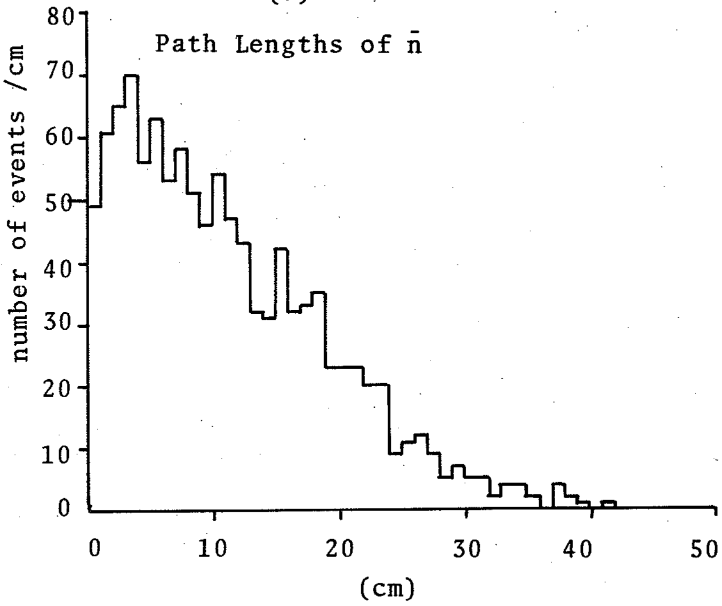
Path Lengths of $\bar{n}$
number of events /cm
80
70
60
50
40
30
20
10
0
0
10
20
30
40
50
(cm)

(b)

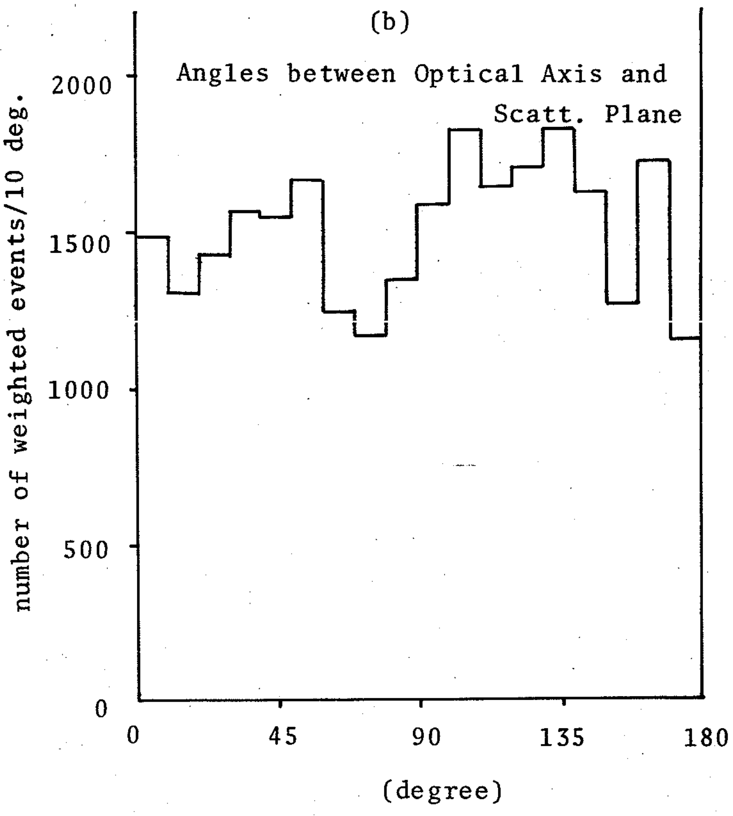
Angles between Optical Axis and Scatt. Plane
number of weighted events/10 deg.
2000
1500
1000
500
0
0
45
90
135
180
(degree)

Fig.66.

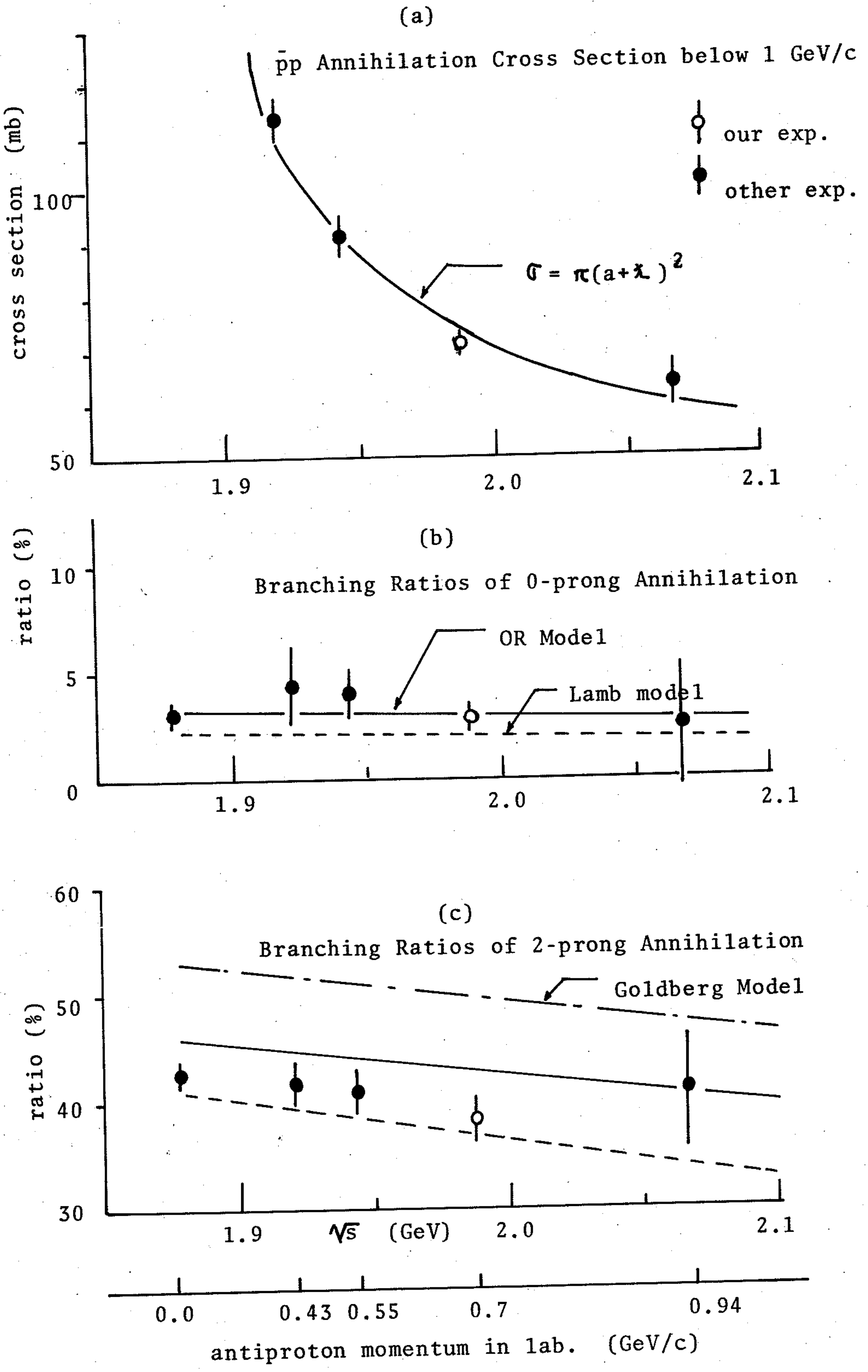
(a)
p̄p Annihilation Cross Section below 1 GeV/c
our exp.
other exp.
$\sigma = \pi(a+\lambda)^2$
cross section (mb)
100
50
1.9
2.0
2.1
(b)
Branching Ratios of 0-prong Annihilation
OR Model
Lamb model
ratio (%)
10
5
0
1.9
2.0
2.1
(c)
Branching Ratios of 2-prong Annihilation
Goldberg Model
ratio (%)
60
50
40
30
1.9
$\sqrt{s}$ (GeV)
2.0
2.1
0.0
0.43
0.55
0.7
0.94
antiproton momentum in lab. (GeV/c)

Fig.66.

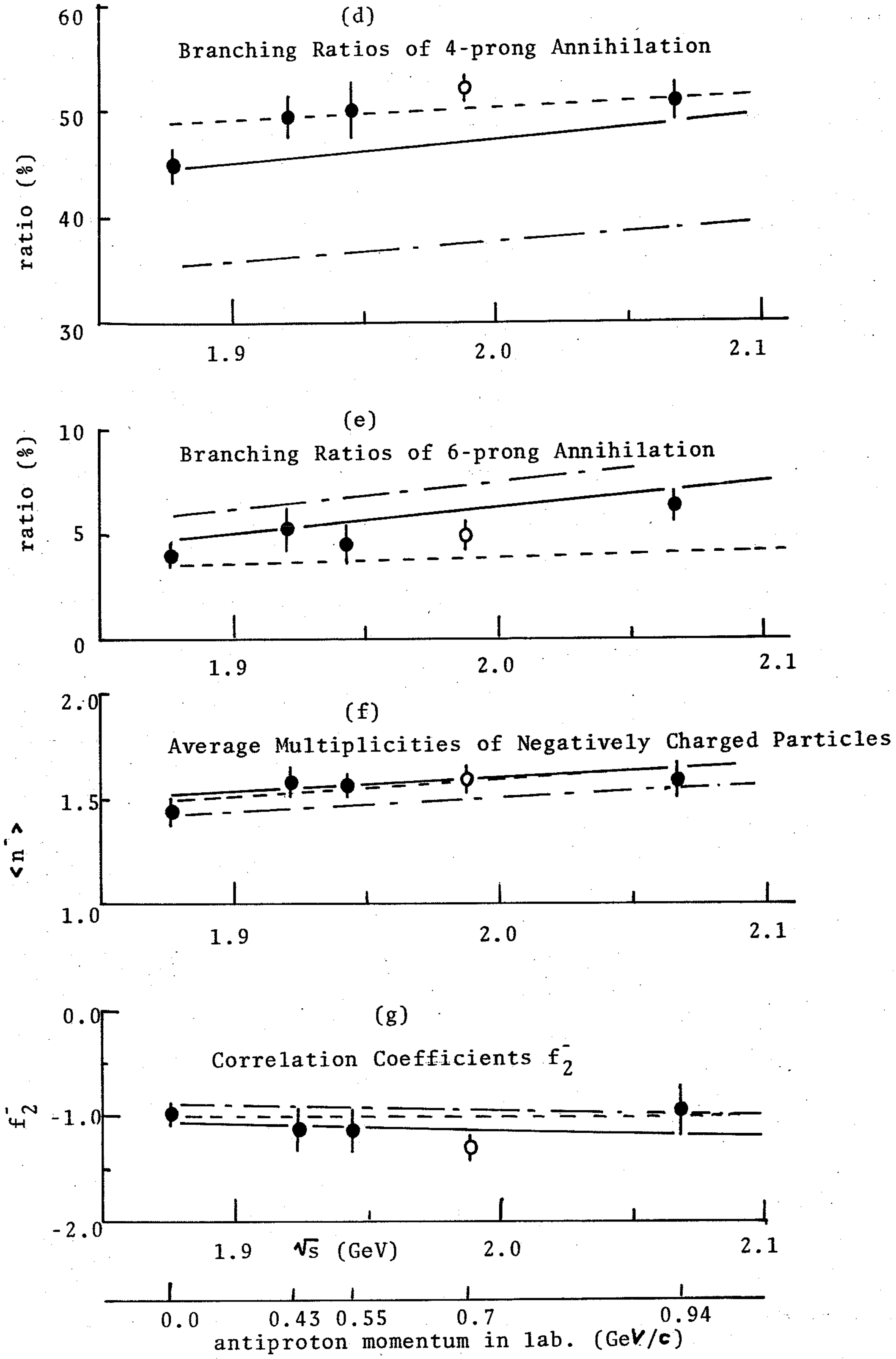
(d)
Branching Ratios of 4-prong Annihilation
ratio (%)
60
50
40
30
1.9
2.0
2.1
(e)
Branching Ratios of 6-prong Annihilation
ratio (%)
10
5
0
1.9
2.0
2.1
(f)
Average Multiplicities of Negatively Charged Particles
<n⁻>
2.0
1.5
1.0
1.9
2.0
2.1
(g)
Correlation Coefficients f⁻₂
f⁻₂
0.0
-1.0
-2.0
1.9
√s (GeV)
2.0
2.1
0.0
0.43
0.55
0.7
0.94
antiproton momentum in lab. (GeV/c)

Fig. 67.

Data of e^+e^-, $\bar{K}K$, and $\bar{p}p$ Annihilations and Predictions by the OR Statistical Model

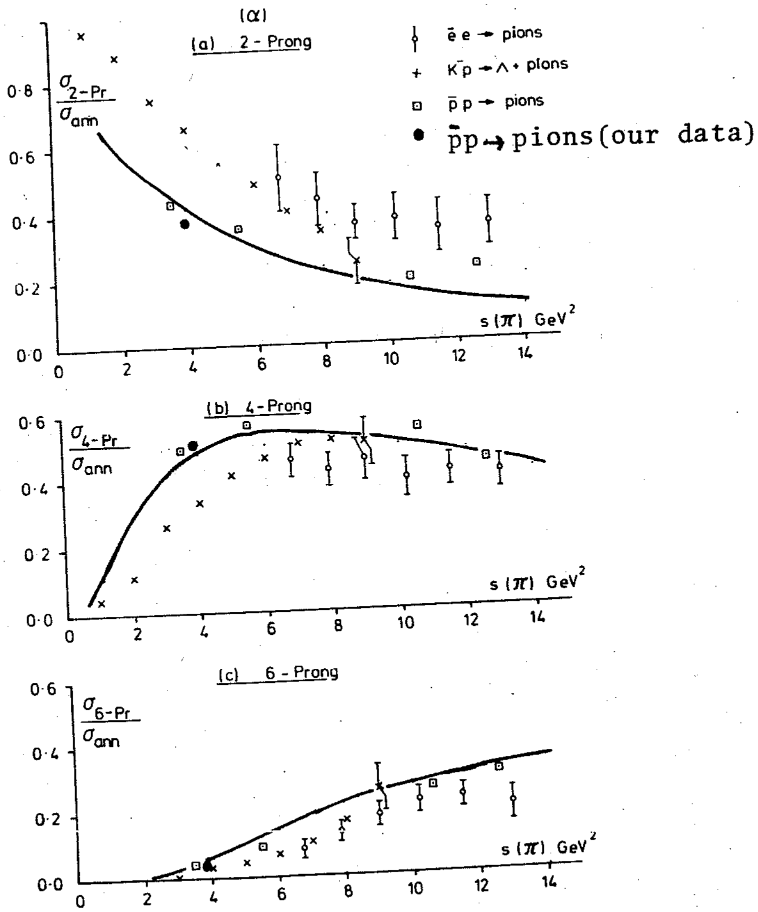

Fig.68.

Random Numbers in the FOWL

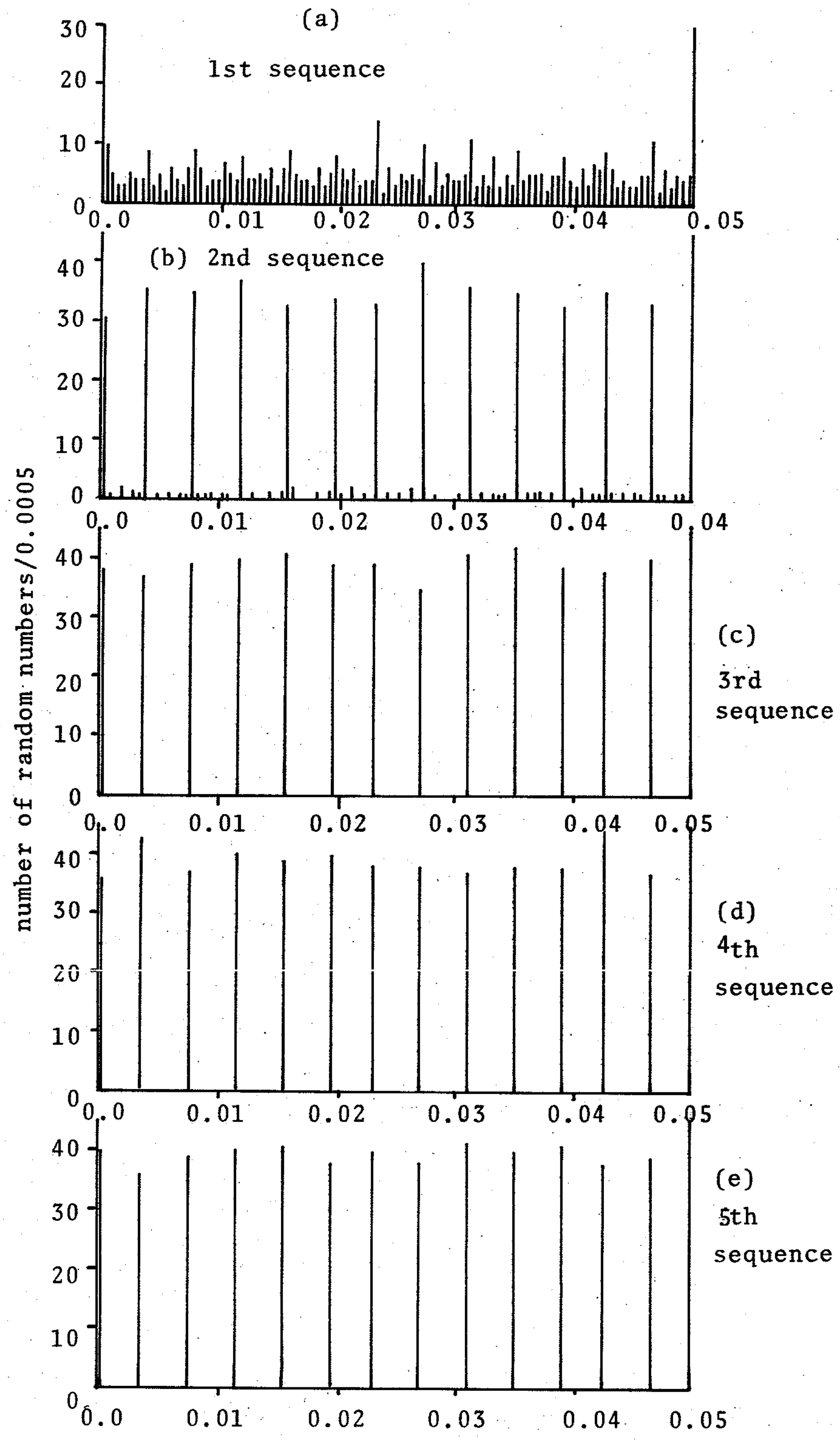

Fig.69.

Random Numbers in the FOWL

(DOUBLE PRECISION)

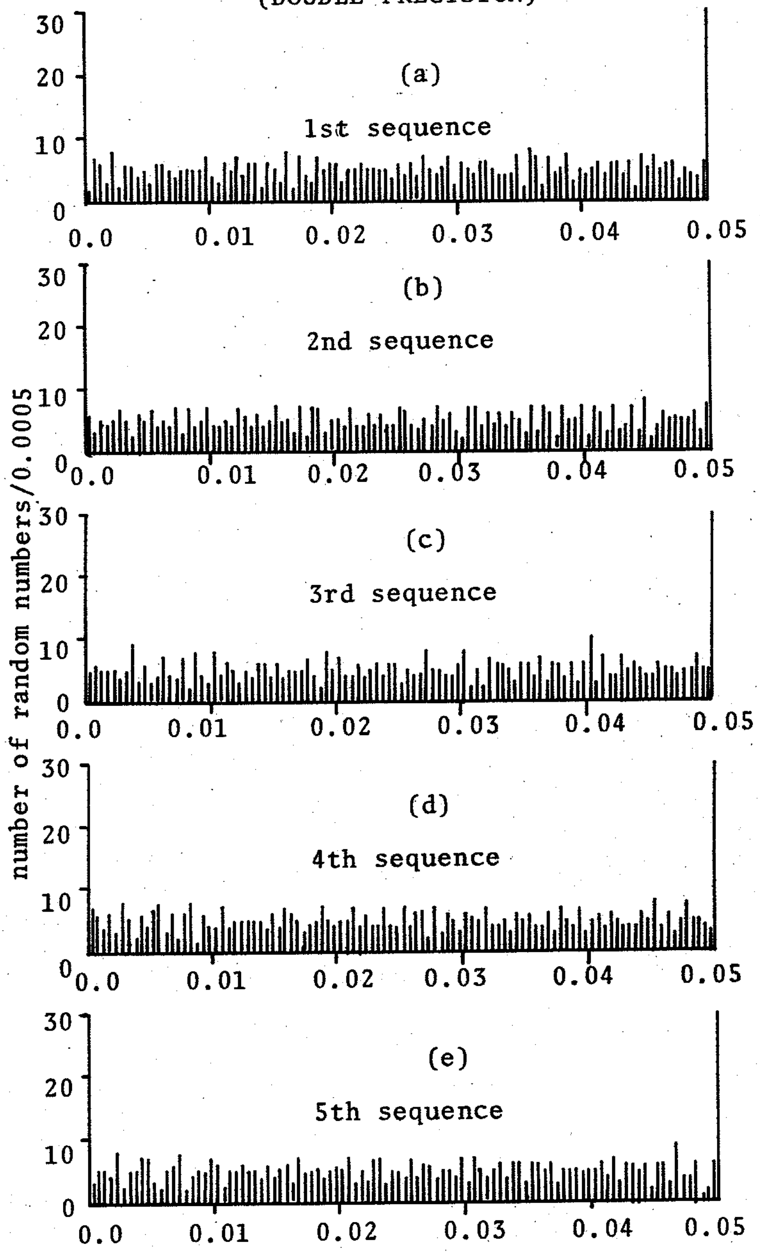

Fig.70.

Random numbers by the System Library